Polymer-gold nanoparticulate formulations for combinational photochemotherapy of pancreatic cancer

Mina Emamzadeh

Department of Pharmaceutics

School of Pharmacy

University College London

PhD thesis

2018

This thesis is dedicated to my wonderful parents
Mr. Seyed Masoud Emamzadeh and Ms. Mehri Hamidi
For their endless love, support and encouragement

Declaration

I, Mina Emamzadeh confirm that the work presented in this thesis is my own. Where information has been derived from other sources, I confirm that this has been indicated in the thesis.

Presentations

- European University Consortium for Pharmaceutical Sciences in Paris-Sud University.   4-11 July 2015

- UCL Doctoral School Research day.   1-2 March 2016

- Micro- and Nanotechnologies for Medicine: Emerging Frontiers and Applications, in Massachusetts Institute of Technology Harvard-MIT Health Sciences & Technology, Cambridge, Massachusetts, USA.   25-29 July 2016

- 4th Symposium on Innovative Polymers for Controlled Delivery (SIPCD 2016) in Suzhou, China.   23–26 September 2016

- International Conference and Exhibition on Nanomedicine and Drug Delivery in Osaka, Japan.   29-31 May 2017

- PhD research day in UCL School of Pharmacy.   20 April 2017

Impact

Pancreatic cancer is a devastating malignancy with an extremely poor prognosis, with 5-year survival rate of around 8% for all stages of the disease. Hence, the identification of effective systemic anti-cancer drugs against pancreatic cancer will have transformative implications. In fact, the efficacy of Gem, the chemotherapeutic agent presently used for pancreatic tumors, is very limited due to insufficient accumulation and activation in the tumor cells. This study has demonstrated the ability of GNPs to deliver chemotherapeutic agents and to simultaneously exert red-light induced hyperthermia. Interestingly, the designed nanoformulation increased the therapeutic index of Gem, which could potentially lead to improved pharmacokinetics of Gem, reducing its non-specific side effects and enabling higher dose drug delivery to the site of action. Furthermore, targeting the Gem-loaded GNShells locally with light irradiation can produce sufficient heat in order to enhance the cellular uptake and bioactivity of the nanoformulation. In the longer term, synergistic photothermal therapy and chemotherapy could provide minimally invasive cancer therapy modalities for patients with pancreatic cancer and improve their quality of life by considerable decrease of systemic cytotoxicity without compromising the therapeutic efficacy.

This research has been awarded four grants from the UCL School of Pharmacy (April 2016); Royal Society of Chemistry (January 2017) and School of Life and Medical Sciences (June 2016; February 2017) for travelling and conference attendance, which created the opportunities to boost the visibility of our work in diverse audiences comprising both academics and industrial delegates in internationally recognised scientific meetings such as the European University Consortium for Pharmaceutical Sciences, Paris, France; Liposome Advances: Progress in Drug and Vaccine Delivery' conference, London, UK; Micro- and Nanotechnologies for Medicine: Emerging Frontiers and Applications, in Massachusetts Institute of Technology Harvard-MIT Health Sciences & Technology, Cambridge, Massachusetts, USA; 4th Symposium on Innovative Polymers for Controlled

Delivery (SIPCD 2016), Suzhou, China; International Conference and Exhibition on Nanomedicine and Drug Delivery, Osaka, Japan 2017.

Overall, the proposed multi-functional nanosystem provides future directions for improving the therapeutic outcomes and shows that combinational chemo- and photothermal therapy has promising potential in future cancer therapeutics and hence I anticipate that our findings will be inspirational to a wide range of researchers from pure formulation scientists to oncologists, biomedical engineers and nanoscience experts.

Acknowledgments

Table of Contents

CHAPTER 3 FORMULATION AND CHARACTERISATION OF GEM-LOADED GNSHELLS FOR TREATMENT OF THE PANCREATIC CANCER

CHAPTER 4 INCREASING THE CYTOTOXIC POTENCY OF GEM WITH LASER-INDUCED HYPERTHERMIA MEDIATED BY GNSHELLS+SH-P(PEGMA)100+GEM

List of Tables

23

List of Abbreviation

τ_s	Time constant for heat transfer from the system
θ	Dimentionless driving force temperature
η	Photothermal conversion efficiency
$\Delta\psi_m$	Transmembrane potential
ζ	Zeta
anti-EGFR	Anti-epidermal growth factor receptor
anti-IgG	Anti- immunoglobulin G
ATP	Adenosine triphosphate
ATCC	American Type Culture Collection
ATRP	Atom Transfer Radical Polymerisations
BE	Binding energy
BET	Brunauer–Emmette– Teller
BH	Bcl-2 homology
C_t	Mass of drug released at time t
C_∞	Mass of drug
C_D	Heat capacity of the deionised water used as a solvent
CRP	Controlled/Living Radical Polymerisation
Cyt c	Cytochrome c
dATP	2'-deoxyadenosine triphosphate
dCK	Deoxycytidine Kinase
dCMP deaminase	Deoxycytidine monophosphate deaminase
dCTP	Deoxycytidine
DD	Death domain
DED	Death effector domain
dFdC	2',2'-difluorodeoxycytidine
dFdCDP	Gemcitabine diphosphate (2',2'-difluorodeoxycytidine diphosphate)
dFdCMP	2',2'-difluorodeoxycytidine monophosphate
dFdCTP	Gemcitabine triphosphate (2',2'-difluorodeoxycytidine triphosphate)

dFdUMP	2',2'-difluorouridine monophosphate
D_h	Hydrodynamic size
DISC	Death-inducing signaling complex
DLS	Dynamic Light Scattering
EC50	Half maximal effective concentration value.
ESCA	Electron spectroscopy for chemical analysis
EM	Electromagnetic radiation
ER	Endoplasmic reticulum
ETC	Electron transport chain
FADD	Fas-Associated Death Domain
fs	Femtosecond
GNPs	Gold nanoparticles
GNRs	Gold nanorods
GNShells	Gold nanoshells
GPC	Gel permeation chromatography
HSPs	Heat shock proteins
HT	Hyperthermina
HPLC	High Performance Liquid Chromatography
JNK	c-Jun N-terminal kinase
KE	Kinetic energy
LE	Loading efficiency
m_D	Mass of the deionised water used as a solvent
MAM	Mitochondria-associated ER membranes
MOMP	Mitochondrial outer membrane permeability
MPTP	Mitochondrial permeability transition pore
MTT	3-(4,5-dimethylthiazol-2-yl)-2,5 diphenyltetrazoliumbromide
MWCO	Molecular weight cut-off
NCT	National Clinical Trial
NDP	Diphosphate kinase
NMP	Nitroxide Mediated Living Free Radical Polymerisations
NMR	Nuclear Magnetic Resonance

PEGMA	Poly(ethylene glycol) methacrylate
PBS	Phosphate-buffered saline
PE	Plating efficiency
RAFT	Reversible Addition Fragmentation Chain Transfer polymerisation.
Q_0	Heat dissipation from the light absorbed by the quartz sample cell
ROS	Reactive oxygen species
RR	Ribonucleotide reductase
SERS	Surface-enhanced Raman scattering
SF	Survival fraction
SPR	Surface plasmon resonance
T_{max}	Maximum steady temperature
T_{amb}	Ambient temperature
TCA cycle	Tricarboxylic acid cycle
TEM	Transmission Electron Microscopy
TMS	Tetramethylsilane
TGA	Thermogravimetric Analysis
TRADD	TNF-receptor associated protein with death domain
UPR	Unfolded Protein Response
UV-Vis	Ultraviolet–visible spectroscopy
VDAC	Voltage-dependent anion channel
XPS	X-ray photoelectron spectroscopy

Abstract

Pancreatic cancer is one of the most deadly of all types of cancer, with a yearly incident that equals its mortality. Gemcitabine (Gem) is currently the first-line chemotherapeutic drug used to treat pancreatic cancer. The major deficiencies of Gem therapy are poor cell membrane permeability, short plasma half-life and toxic side effects. In order to improve the pharmacokinetic characteristics and overcome the obstacles to achieve effective drug delivery, a nanoparticulate drug delivery system can be utilised; gold nanoparticles (GNPs) have been investigated as carriers for drug delivery due to their appealing physicochemical and optical properties.

This research project concerns the development of a new generation of GNPs for cancer treatment by co-delivering anti-cancer drugs in combination with laser-induced photothermal effects confined at the diseased areas.

Gold nanoshells (GNShells) were synthesised with the capability to carry and deliver Gem and exert phototherapeutic properties. Protein repellent thiol capped poly (ethylene glycol) methyl ether methacrylate polymers were synthesised by RAFT polymerisation and used as efficient particle stabilising ligands. Significant stability enhancement was achieved allowing for the co-functionalisation of GNShells with Gem for applications in *in vitro* assays against pancreatic cancer cells. GNShells mediated strong photothermal effect owing to their strong surface plasmon absorption in the red/NIR region. This property was exploited to enhance the toxicity of Gem using laser light as the external stimulus.

The concerted antitumor activity of Gem with the photothermal effect of the GNShells upon irradiation with a continuous wave laser, increase the cellular uptake and efficacy of Gem-loaded GNShells against MiaPaCa-2 cells. Therefore, the proposed nanoformulation might provide an active strategy for synergistic chemo-photothermal combined therapy.

Chapter 1

Introduction

Over the last decade, laser-induced tissue hyperthermia mediated by gold nanoparticles has shown an immense potential to enhance the efficiency of cancer treatment. This research includes the elucidation of the unique plasmonic radiative and non-radiative properties of gold nanoparticles, their use in nanomedicine as carriers for enhancing the delivery ofgemcitabine against pancreatic cancer cells and also as photothermal agents for the selective killing of cancer cells under irradiation by NIR laser light. This is followed by the overview of the work of active groups in the field of phototherapy of cancer with different shapes of gold nanoparticles (nanorods, nanoshells, nanostars, nanospheres, etc.); in particular, gold nanoshells are advantageous over other particle shapes owing to their unique optical properties.

1.1 Pancreatic cancer

Pancreatic cancer is one the most aggressive human malignancies, with an extremely dismal prognosis due to absence of symptoms and lack of reliable screening tests for early diagnosis. The incidence of pancreatic cancer is almost equal with the mortality rate, with less than 5% five-year survival (Affram *et al.*, 2015). Pancreatic cancer comprises both endocrine and exocrine type, according to the origin of the tumors. Ductal adenocarcinoma is an exocrine and the most common type of the pancreatic cancer (more than 90%) and originates in the cell lining of the pancreatic duct. On the contrary, pancreatic endocrine tumors, also called as neuroendocrine tumors, are rare and start in the islet cells of the pancreas (Figure 1.1) (Patra *et al.*, 2010).
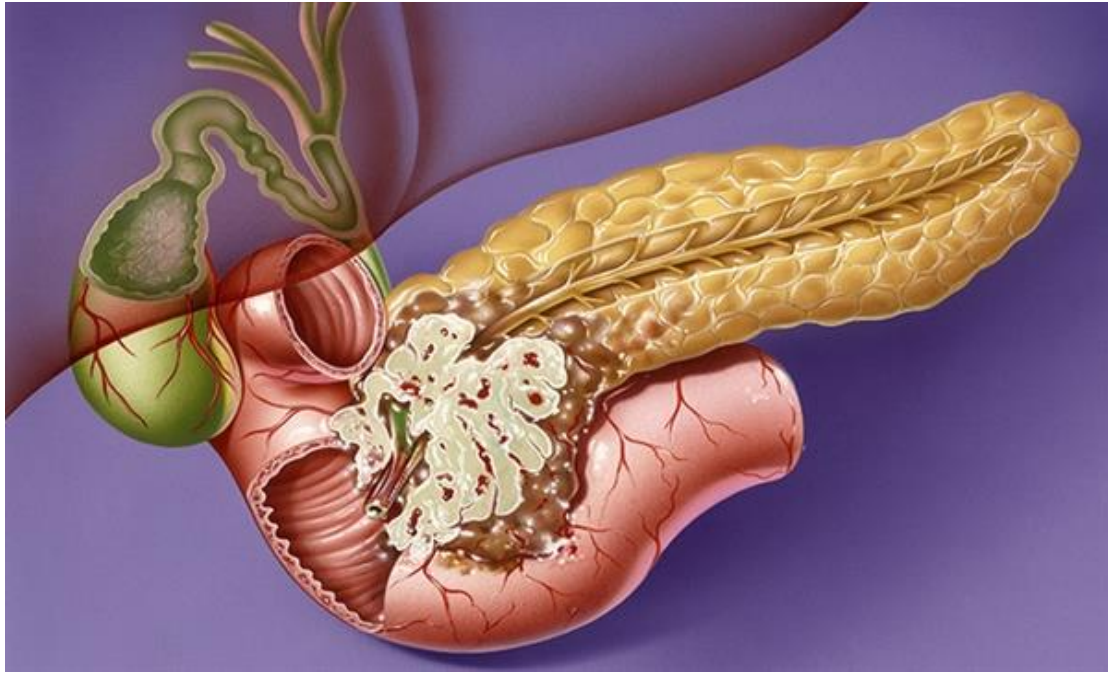
Figure 1.1. Illustration of pancreatic cancer (Shroff *et al.* 2011). The pancreas is a 6 inches long glandular organ that is located across the back of the abdomen, behind the stomach (Drake *et al.*, 2005). The vast majority of the pancreatic cancers are ductal adenocarcinoma (exocrine tumors) that originates from the epithelium lining pancreatic ducts (Patra *et al.*, 2010). Due to fibrotic and hypovascular microenvironment of pancreatic cancer, efficient drug delivery to the tumor site remains a major challenge (Li *et al.*, 2010).

Among solid tumors, pancreatic tumors are highly chemo-resistant to cytotoxic anti-cancer agents due to their desmoplastic reaction (DR). A dense desmoplastic reaction surrounding malignant epithelial cells is composed of extracellular matrix (ECM) proteins, fibroblasts, stellate cells, endothelial cells, immune cells, and neurons. This unique microenvironment along with frequent genetic alterations and insufficient drug delivery can cause pancreatic tumor growth, invasion, and resistance to therapy (Li *et al.*, 2010). Considering the number of obstacles for effective and penetrating treatment, novel strategies are desperately needed for the treatment of this deadly disease.

1.2 Gemcitabine

Gemcitabine (Gem) is currently the leading therapeutic for pancreatic cancer therapy, which was first synthesised by Hertel *et al.* (Hertel *et al.*, 1988). It is normally sold as its hydrochloride salt. Gem has a short plasma half-life (<20 min) due to the rapid conversion to the inactive metabolite (2',2'-difluorouridine, dFdU) by plasma deaminase deoxynucleotide which severely limits its efficacy. Also, the hypovascular and poorly perfused nature of pancreatic tumors cause inadequate delivery of the drug to cancer cells (Cavalcante and Monteiro, 2014). Therefore, drug delivery strategies are needed to improve the chemotherapeutic action of Gem.

1.2.1 Uptake and metabolism

Gemcitabine (dFdC, 2',2'-difluorodeoxycytidine) is a deoxycytidine analogue with anti-tumor activity against many solid tumors including pancreatic cancer (Figure 1.2). It augments its own cytotoxicity by self-potentiation mechanisms that are attributed to the inhibition of ribonucleotide reductase (RR) and deoxycytidine monophosphate deaminase (dCMP deaminase) by Gem diphosphate and triphosphate, respectively (Figure 1.3) (Heinemann *et al.*, 1992). The uptake of Gem into the cell is accomplished through the human nucleoside transporters (hNTs). Once inside the cell, Gem undergoes through successive intracellular phosphorylation in order to exert its action. Gem is first phosphorylated into its monophosphate form (2',2'-difluorodeoxycytidine monophosphate, dFdCMP) by deoxycytidine kinase (dCK) in the rate limiting step, then phosphorylated to Gem diphosphate (2',2'-difluorodeoxycytidine diphosphate, dFdCDP) and Gem triphosphate (2',2'-difluorodeoxycytidine triphosphate, dFdCTP) by pyrimidine nucleoside monophosphate (NMP) and diphosphate kinase (NDP), respectively.
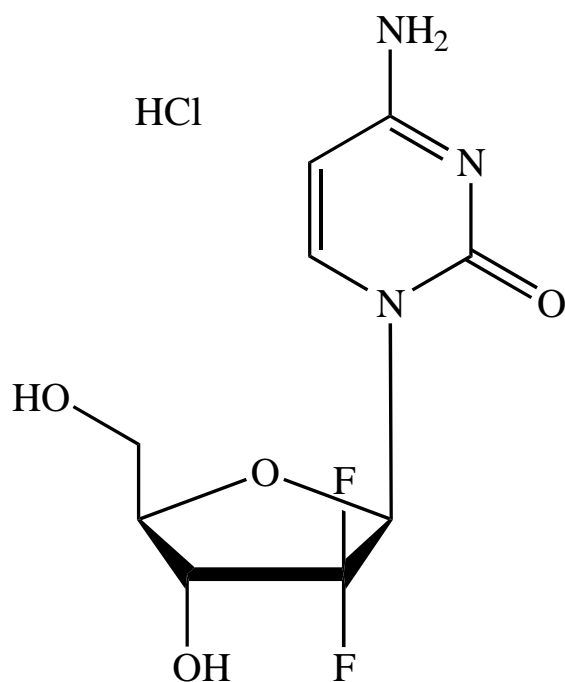
Figure 1.2. Chemical structure of Gem.

dFdCDP inhibits ribonucleotide reductase (RR) and this reduces the pool of competing deoxycytidine (dCTP) necessary for DNA replication. dFdCTP (cytotoxic form of dFdC) is an active metabolite that promotes cell apoptosis by being incorporated into the DNA strand and terminating DNA polymerisation. Also, dFdCTP inhibits deoxycytidine monophosphate deaminase (dCMP deaminase), which transforms dFdCMP into 2',2'-difluorouridine monophosphate (dFdUMP) and causes Gem inactivation (Mini *et al.*, 2006; Gesto *et al.*, 2012; Andersson *et al.*, 2009; Binenbaum *et al.*, 2015). All these steps benefit the cytotoxicity effect of Gem.
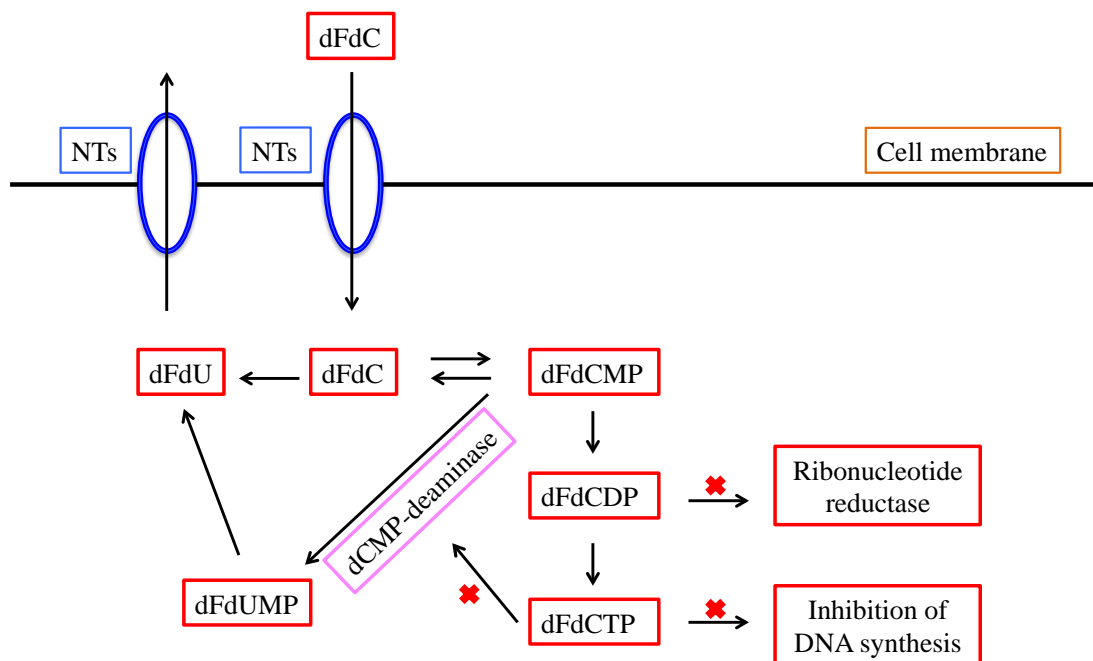
NTs　　　→　nucleoside transporters

dFdC　　　→　2',2'-difluorodeoxycytidine

dFdCMP　　→　2',2'-difluorodeoxycytidine monophosphate

dFdCDP　　→　2',2'-difluorodeoxycytidine diphosphate

dFdCTP　　→　2',2'-difluorodeoxycytidine triphosphate

dFdUMP　　→　2',2'-difluorouridine monophosphate

dFdU　　　→　2',2'-difluorouridine

dCMP deaminase　→　Deoxycytidine monophosphate deaminase

Figure 1.3. The cellular metabolism of Gem.

1.3 Cancer Nanomedicine

Nanotechnology is a multidisciplinary research field that involves optimal engineering of functional materials at the nanoscale (1-100 nm) (Ferrari, 2005). Short drug circulation times, non-specific drug delivery, drug toxicity and tumor resistance are the challenges associated with current existing cancer treatments. Therefore, applying nanotechnology in medicine (Nanomedicine) to overcome these impediments is under development over the past two decades (Pedrosa *et al*, 2015). Nanomedicine is being applied to cancer therapy by developing innovative nanovectors, such as nanoparticles, which show significant improvement in cancer detection, diagnosis, imaging, and non-invasive therapy by altering the pharmacokinetic properties of chemotherapeutic agents (Khare *et al*., 2014).

1.4 Gold Nanoparticles

Gold nanoparticles (GNPs) are currently possessing broad potential utilisation in cancer therapy, including drug delivery, bio-imaging and bio-diagnostics (Cai *et al*., 2008). GNPs have unique physicochemical properties that brought them to the forefront of cancer research (Patra *et al*., 2010; Huang and El-Sayed, 2010; Shukla *et al*., 2010; Fan *et al*., 2008; Murphy *et al*., 2008; Link and El-Sayed, 2000), such as:

- Accessible synthesis of GNPs in different sizes and shapes (spheres, rods, shells, stars, etc.).
- GNPs compositions with tunable optical properties and bigger surface to mass ratio.
- GNPs with the ability to bind, absorb and carry compounds such as drugs, biomolecules, surfactants, polymers, etc. (surface modification).
- Exceptional stability against oxidation along with their non-cytotoxic, non-immunogenic and biocompatible nature.

Tunable optical properties of GNPs in the visible and near-infrared regions in particular distinguish them from other nanoplatforms (polymeric and magnetic nanoparticles, or semiconductor quatum dots); their optical properties arise from the surface plasmon resonance (SPR), a unique optical phenomenon that enhances the radiative (light scattering) and non-radiative (conversion of absorbed light into heat) properties of GNPs due to the existence of strong electromagnetic field on the NPs' surface. Therefore, these metal NPs can act as a powerful theranostic tool with applications in electronics, sensing, imaging, and photothermal therapy (Huang and El-Sayed, 2010; Link and El-Sayed, 2000; Jain *et al.*, 2008; Huang *et al.*, 2007).

1.5 Surface plasmon resonance (SPR)

In 1957, Michael Faraday published the first systematic study on the dependence of colloidal GNPs color variation to their size alteration (Faraday, 1957). In 1908, Gustav Mie reported the fundamental theory for the prediction of optical properties of spherical GNPs in non-absorbent media, using Maxwell's electromagnetic equations. Mie computed the elastic scattering of light from the surface of spherical GNPs (30-100 nm) and detected the scattered light with a commercial microscope under dark-field illumination conditions (Mie, 1908; Grodzinski *et al.*, 2006; Wriedt, 2012). The scattering of electromagnetic waves by spherical particles as described by Mie, was later interpreted in terms of surface plasmon resonance. The interaction of oscillating electromagnetic field of light at specific wavelengths with metal nanoparticles (e.g. GNPs) causes the collective coherent oscillation of the conduction band electrons on the metal surface with respect to the positive metallic lattice. This dipole oscillation is resonant along the direction of electromagnetic field of light and reaches its amplitude at a specific frequency, called surface plasmon resonance (SPR) (Figure 1.4).
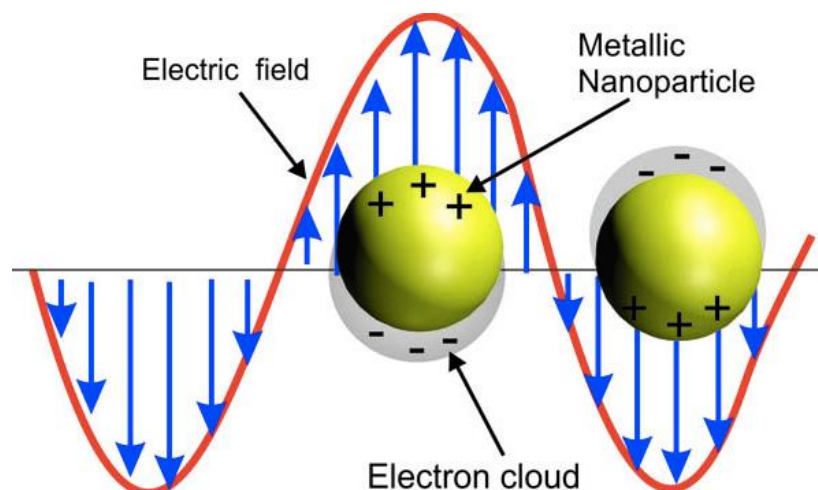
Figure 1.4. Scheme of the collective oscillation of conduction electrons on the surface of GNPs interacting with resonant electromagnetic radiation of an appropriate wavelength (Camacho, 2015).

The plasmon band intensity and frequency depends on the nanoparticle's size (redshift with larger size), the shape (shells, rods, spheres, stars, etc.), the aggregation state (inter-particle distance lower than the GNP size) and the environment (i.e. the dielectric properties of the solvent) and can be tuned from visible to near infrared region (NIR) by altering each of these factors (Huang and El-Sayed, 2010; Jain *et al.*, 2008; Huang *et al*, 2007; Boisselier and Astruc, 2009).

Illumination of metallic nanostructures (e.g. GNPs) at room temperature, using visible light or NIR laser with a photon energy equal to the metal's work function, excites surface plasmons on the nanoparticle surface (Brongersma *et al.*, 2015). Plasmons can damp their accumulated energy on a femtosecond (fs) timescale (electromagnetic decay) either radiatively through re-emitted photons or non-radiatively by converting the energy into heat through a cascade of photo-physical processes (Figure 1.5). Radiative and nonradiative properties of SPR can be selected or combined depending on the specific biomedical application of metal nanoparticles (Clavero, 2014).
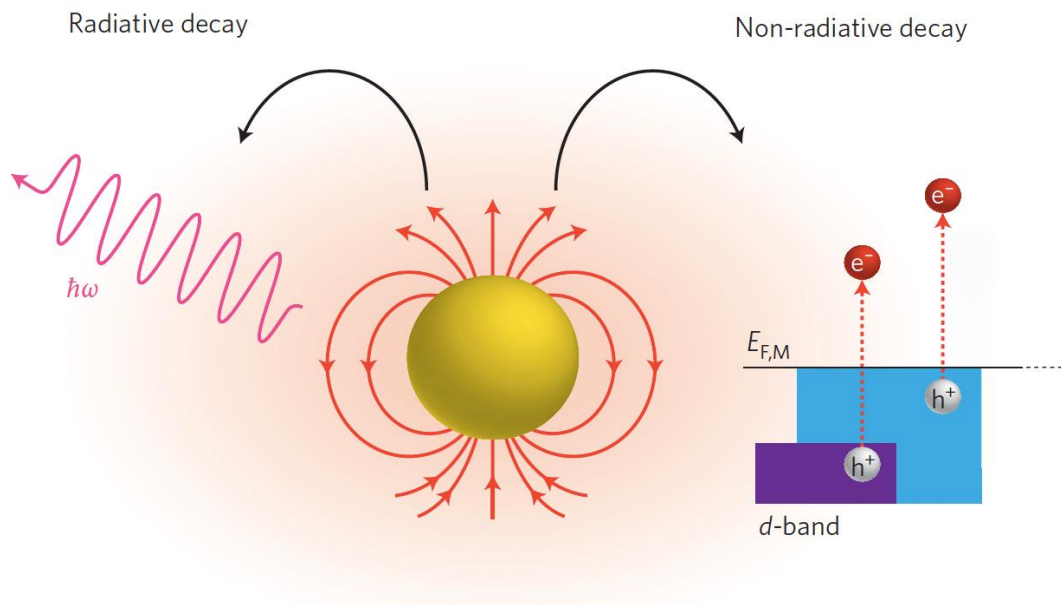
Figure 1.5. Localised surface plasmons can decay radiatively via re-emitted photons or non-radiatively via excitation of hot electrons. In metal nanoparticles, non-radiative decay can occur through intraband/or interband excitation of electrons above the Fermi level (Clavero, 2014).

1.6 Tunable radiative properties

As mentioned above, collective *oscillation* of free electrons on metal surfaces that resonate with the frequency of incident light (i.e. SPR) can undergo relaxation radiatively by emitting photons in the form of scattered light (elastic /or inelastic electron scattering) (Huang and El-Sayed, 2011; Clavero, 2014). SPR radiative decay strongly depends on the optical characteristics of the material (i.e. nanoparticle size, shape, composition, dielectric constant and surrounding medium) (Kim *et al*., 2016; Schatz, 1984; Jackson and Halas, 2004). According to Mie theory, the frequency of the plasmon band varies from spherical to various shapes and structures of non-spherical nanoparticles (e.g. rods, stars, shells etc.) For instance, spherical GNPs exhibit plasmon band around ~530 nm (Link and El-Sayed, 1999) whereas for gold nanoshells (GNShells), the plasmon band absorption shifts to the near-IR region by decreasing in the shell thickness-to core radius ratio (Prashant and El-Sayed, 2007). Due to the anisotropic shape of gold nanorods (GNRs), there are transverse and longitudinal SPRs that correspond to electron

oscillations perpendicular and parallel to the rod length direction, respectively. Their longitudinal surface plasmon wavelengths are tunable from visible to infrared regions by increasing their aspect ratio (Eustis and El-Sayed, 2006). The plasmon resonance absorption and scattering coefficient (extinction coefficient) of GNPs is up to 10^{11} M^{-1} cm $^{-1}$ i.e. several orders of magnitude larger than the absorbing organic dye molecules or fluorescence molecules. This high extinction coefficient along with GNPs photo-stability can enhance the Raman signal of molecules on the particles surface, light scattering and fluorescence of metal itself, and therefore, render GNPs useful in cellular imaging, spectroscopy and optical labelling of (cancer) biomarkers (Link and El-Sayed, 2000; Huang *et al.*, 2007; Huang *et al.*, 2006; Eustis and El-Sayed, 2006; Sordillo *et al.*, 2014).

1.6.1 Cancer imaging

GNPs are excited by light at the wavelength that matches their surface plasmon frequency and because of their high scattering efficiency, can be seen as bright spots under the dark-field microscopy (Huang *et al.*, 2006, Chang *et al.*, 2012). An increase in SPR scattering-to-extinction ratio of GNPs by red shifting the plasmon band to NIR region minimises the light extinction by tissue media and enhances the optical imaging (Sordillo *et al.*, 2014; Taruttis *et al.*, 2010). GNShells and gold nanorods (GNRs) (with suitable aspect ratios) can absorb and scatter light strongly in the NIR region (650−900 nm), therefore, they have been successfully employed to detect and image cancer cells *in vitro* (Taruttis *et al.*, 2010; Loo *et al.*, 2004; 2005a; 2005b; Sokolov *et al.*, 2003; Zhou *et al.*, 2010; Li *et al.*, 2008; Manfait *et al.*, 1991). As an example, El-sayed and co-workers diagnosed two oral squamous carcinoma cell lines, HSC 313 and HOC 3 by using GNRs conjugated to anti-epidermal growth factor receptor (anti-EGFR) monoclonal antibodies. Accumulation of anti-EGFR gold nanorods to the surface of the carcinoma cell lines results in observation of intense resonance scattering from GNRs in the dark field, using a laboratory microscope (Figure 1.6 and Figure 1.7) (El-Sayed *et al.*, 2005).
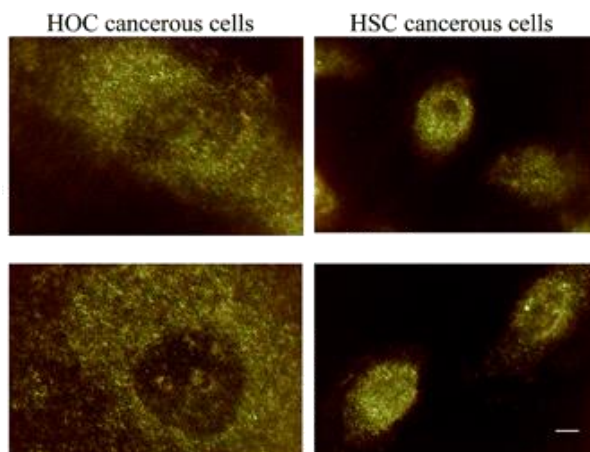
Figure 1.6. Light scattering images of HOC cancerous cells (left column), and HSC cancerous cells (right column) without gold nanoparticles. The dim greenish light represents the autofluorescence and scattered light from the cell organelles (El-Sayed *et al.*, 2005)**.**
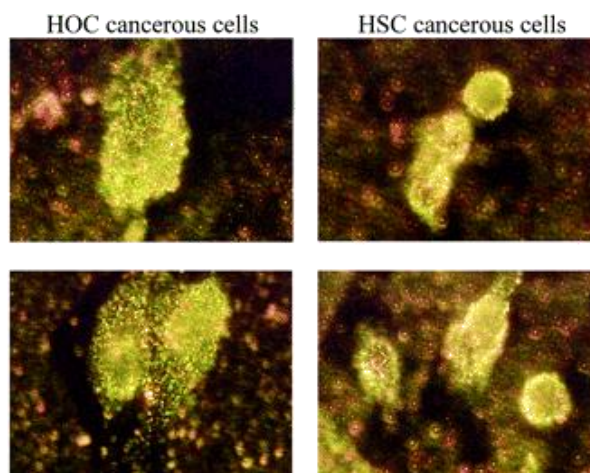
Figure 1.7. HOC cancerous cells (left column), and HSC cancerous cells (right column) after incubation with anti-EGFR antibody conjugated GNPs. The colored image of nanoparticles on a dark background results from the intense surface-plasmon-enhanced scattering of GNRs under white light excitation (El-Sayed *et al.*, 2005).

Loo *et al.* also used anti-HER2-conjugated GNShells to detect and image HER2-positive SKBr3 breast adenocarcinoma cells using dark-field microscopy *in vitro.* Bound NShells on the membrane of cancer cells, strongly scattered signals that enable the detection of abnormal cancer cells in contrast to weak auto-scattering from normal tissue (Figure 1.8) (Loo *et al.*, 2005a).
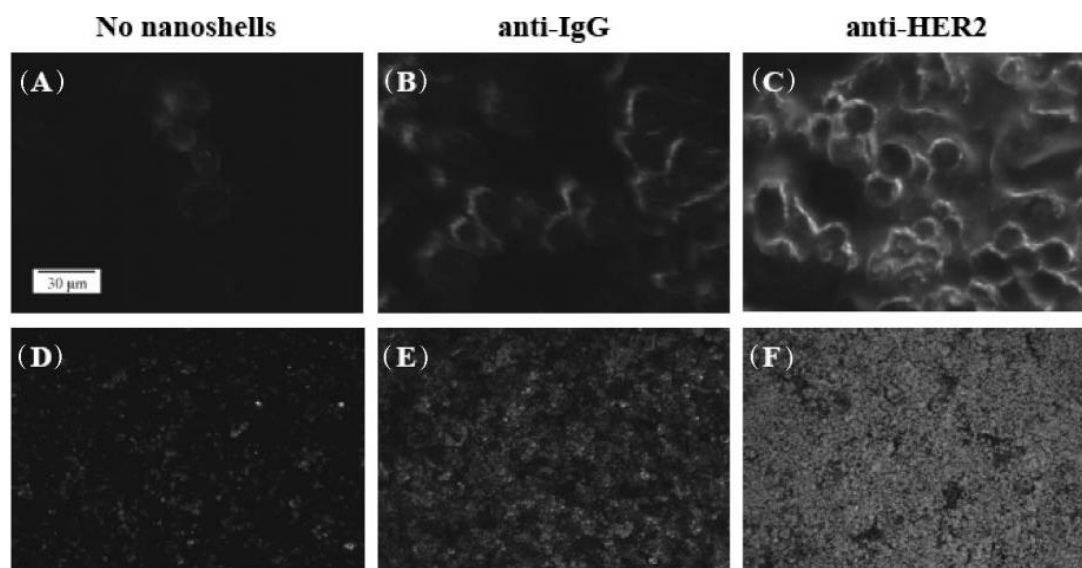
Figure 1.8. The anti-HER2 (specific) or anti-immunoglobulin G (anti-IgG) (non-specific) antibodies were attached to a polyethyleneglycol (PEG) linker through a hydroxysuccinimide group (NHS). The antibody–PEG linker complex was then attached to GNShells surfaces through Au–S bonds. According to the reported darkfield microscopy images, optical contrast is greatly enhanced by anti-HER2-labeled nanoshells attached to the surface of HER2-positive cancer cells (A-D) compared with SKBr3 cells targeted by either anti- IgG-labeled nanoshells (B-E) or cells not exposed to nanoshell conjugates (C-F). Images (A-C) are cross-sectional slices of cells taken at the mid-focal plane at 40X magnification and images (D-F) taken at a lower magnification 10X (Loo *et al.*, 2005a).

1.6.2 Spectroscopic cancer detection

In addition to the elastic Rayleigh scattering of light, GNPs can enhance the inelastic Raman scattering (by up to 10^5-10^6 times) from the adsorbed molecules on their surface, that is, surface-enhanced Raman scattering (SERS) (Schatz, 1984; Jackson and Halas, 2004). Highly enhanced local electric field on GNPs surface generates, owing to the resonance between strong confinements of the photon oscillation with the surface plasmon

oscillations upon exposure of GNPs to an appropriate frequency of electromagnetic light. This intense local optical frequency field along with the electronic coupling between absorbed molecules and GNPs surface enhance the Raman signals. Electronic coupling occurs as a result of molecular polarisation change via metal-molecule charge-transfer interaction (Schatz, 1984; Nikoobakht and El-Sayed, 2003; Jackson and Halas, 2004; Huang *et al.*, 2007; Boisselier and Astruc, 2009). A number of research groups have applied SERS by highly polarisable GNPs such as GNShells to detect cancer cells (Nabiev *et al.*, 1991; Manfait *et al.*, 1992; 1993; Kneipp *et al.*, 2002; Nikoobakht and El-Sayed, 2003; Bishnoi *et al.*, 2006; Tang *et al.*, 2007). As an example, in 2006, Halas and co-workers designed a SERS sensor based GNShells with a plasmon band in the NIR region and provided SERS enhancement, using a NIR laser source (785 nm). They successfully detected the acidic cancer environment by conjugating a pH sensitive SERS responding molecule (para-mercaptobenzoic acid) to the surface of GNShells. Protonation of the pH sensitive adsorbate in acidic media caused monitoring changes in the Raman spectrum at 1393 cm^{-1} that represents the carboxyl group (COO^-) band (Figure 1.9) (Bishnoi *et al.*, 2006).
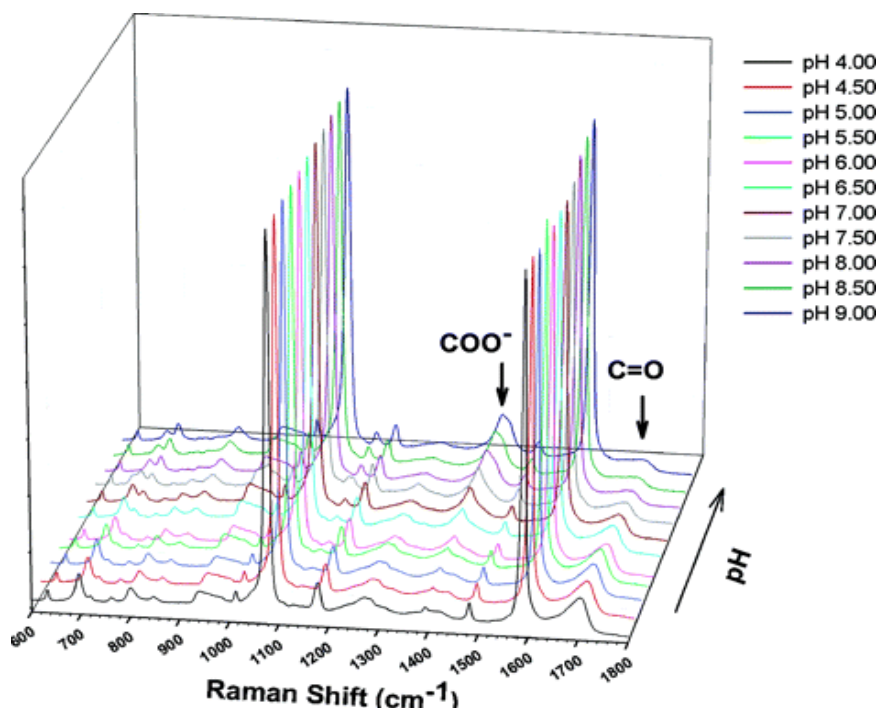
Figure 1.9. SERS spectra of para-mercaptobenzoic acid (pMBA) on nanoshells at various pH values ranging from pH 4.0 to pH 9.0 in steps of 0.50 pH units (Bishnoi *et al.*, 2006).

In 2007, Huang *et al.* utilised the difference in the SERS of anti-EGFR conjugated GNRs to distinguish EGFR overexpressed HSC oral cancer cells from HaCat normal cells. The molecules on the surface plasmon field of GNRs comprised CTAB capping molecules, PSS bridge molecules, anti-EGFR anti-bodies, and EGFR receptors which along with the other molecules on the cellular surface of cancer cells were found to give highly enhanced, sharp and polarised SERS, whereas, normal cells showed weak or no SERS because they did not specifically bind to the anti-EGFR conjugated GNRs (Figure 1.10) (Huang *et al.,* 2007).
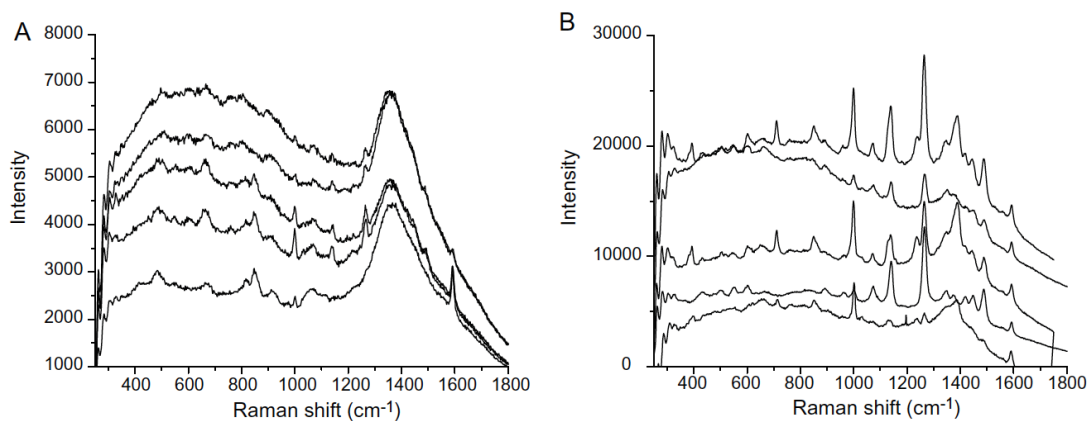
Figure 1.10. Molecular diagnosis of cancer cells using Raman spectra of anti-EGFR conjugated gold nanorods incubated with the (A) HaCat normal cells and (B) HSC oral cancer cells. Assembly of anti-EGFR conjugated GNRs on the surface of HSC cancer cells and surface plasmon-molecule coupling resulted in stronger, sharper and well-resolved Raman spectra compared to that of HaCat normal cells (Huang *et al.*, 2007).

1.7 Tuning SPR to NIR region

Light can penetrate through the turbid tissue media and attenuate due to the effect of absorption and scattering by biomolecules, such as hemoglobin, lipids, water or the intracellular matrix. Reduction of the extinction coefficient of the electromagnetic spectrum at the NIR region allows deep optical tissue penetration with minimal absorption and auto-fluorescence through high scattering tissue media. At the visible region of the spectrum (400-650 nm), light is almost completely absorbed by oxy- and deoxy-hemoglobin whereas, at the first NIR optical tissue window with wavelengths from 650 to 950 nm, light is readily absorbed by any living tissue. At wavelengths longer than 950 nm, major light absorption occurs by water and lipids. Practically, the depth of NIR light penetration is about two centimeters and is partly related to the strength of the light source and also depends on the tissue type. NIR lasers are used as a non-invasive optical tool for imaging and light mediated cancer therapy since they exert deeper penetration compared to visible lasers (Figure 1.11) (Whitesides, 2003; Joshi and Wang, 2010; Weissleder, 2011; Mitsunaga *et al.*, 2011; Lim *et al.*, 2013; Sordillo *et al.*, 2014).
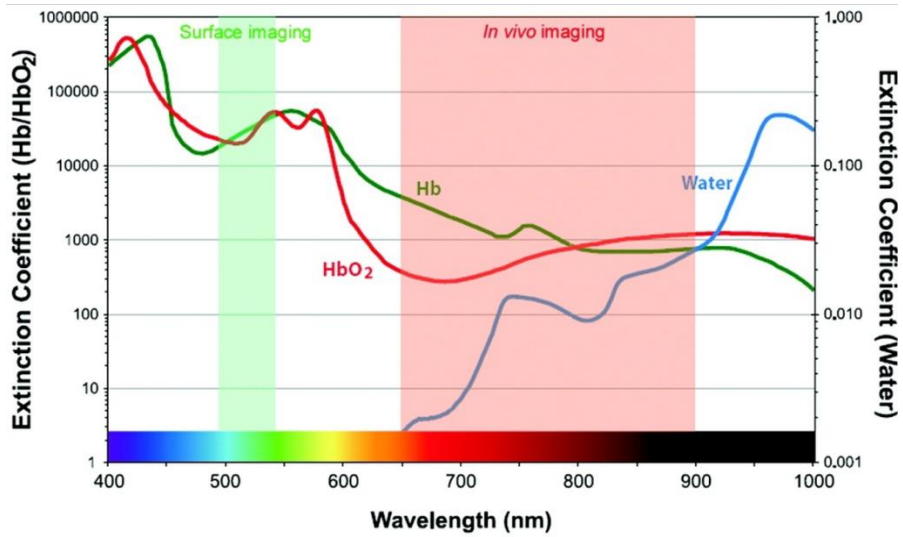
Figure 1.11. Scheme of the *in vivo* NIR window and the extinction coefficient values of water (>900 nm), oxy- and deoxy-hemoglobin (<650 nm) are plotted ranging from visible to NIR wavelengths (Joshi and Wang, 2010).

1.8 Non-radiative properties

In addition to enhanced and tunable radiative properties, plasmonic GNPs can convert the absorbed light into heat via a series of non-radiative processes to form a hot metallic lattice. The GNP plasmon non-radiative decay mechanism has been extensively studied by the El-Sayed group (Link and El-Sayed, 1999; 2000; 2003; El-Sayed, 2001; Link *et al.*, 1999; 2000a; 2000b; 2001; 2002; 2003).

After photon absorption and SPR excitation, coherently excited electrons are damped non-radiatively through the creation of hot electrons via electron-electron relaxation. This rapid quantum mechanical process occurs on a timescale ranging from one to hundred femtoseconds. Plasmonic hot electrons with several thousands Kelvin degrees redistribute their energy to the phonon by reaching thermal equilibrium with the lattice via electron-phonon relaxation on the order of hundred femtosecond to several picoseconds. Upon electron-phonon relaxation process, the lattice temperature is elevated by few tens of degrees even with laser excitation powers as low as hundred nanojoules. Finally, phonon-phonon relaxation results in dissipation of the initially absorbed photon energy (lattice cooling). Thermal energy transfers from the lattice to the surrounding medium occurs on a timescale ranging from hundred picoseconds to one nanosecond depending on the material, particle size and the thermal conduction properties of the immediate environment of the nanoparticles. Such a rapid energy conversion and dissipation can be used for photothermal cancer therapy. Heat dissipation may result in GNPs melting or reshaping within about thirty picoseconds, or it can cause nanoparticle ablation in hundreds of femtoseconds but in order to cure cancer, lattice cooling via phonon-phonon relaxation at the lower rate (hundred picoseconds to one nanosecond) must be the dominant process (Figure 1.12) (Link and El-Sayed, 1999; 2000; 2003; El-Sayed, 2001; Link *et al.*, 1999; 2000a; 2000b; 2001; 2002; 2003; Clavero, 2014, Brongersma *et al.*, 2015; Kim *et al.*, 2016).
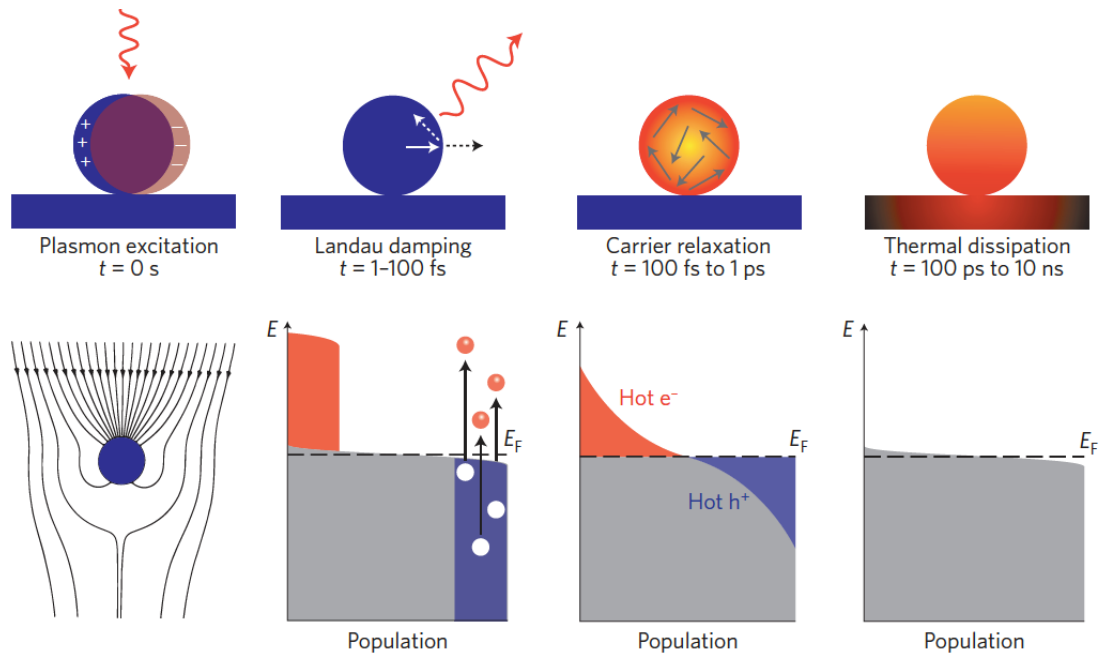
Figure 1.12. Schematic diagram of non-radiative decay of SPR through Landau damping following illumination of metal nanoparticles with a laser. Redistribution of electron charge density, enhancement of the electric filed and consequently SPR upon interaction between electromagnetic wave and conduction electrons of metal nanoparticles result in the generation of highly energetic hot carriers [electron-hole pair (e⁻-h⁺)] via Landau damping (1-100 fs) which is a pure quantum mechanical process where single electron-hole pair excitation is created through plasmon relaxation. The hot carriers decay very fast and transfer their accumulated energy into the metallic nano-lattice upon electron-phonon relaxation (100 fs - 1 ps) in order to achieve equilibrium and subsequent lattice temperature elevation. Dissipation of thermal energy takes place via phonon-phonon relaxation at a comparatively slower rate (100 ps-few ns) (Brongersma *et al.*, 2015).

1.9 Hyperthermia in cancer therapy

Surgical resection, radiotherapy and chemotherapy are the current available conventional treatments of solid-organ malignancies. Surgery is highly effective for eradication of non-hematological primary tumors located within non-vital tissue regions but it is limited to metastases, and tumors that are embedded within vital regions and hence cannot eliminate cancer cells completely (Leung *et al.*, 2012). Chemotherapy is the most non-invasive approach that uses one or more anti-cancer (anti-neoplastic) drugs to slow or stop the growth of cells that are dividing rapidly, especially cancer cells. Systematically administered chemotherapeutic agents circulate in the body

and effect cancer cells via interfering with their cell division in various possible ways. Depending on the type of drugs, the amount and the length of cancer treatment, chemotherapy suffers from dramatic side effects due to drug toxicity to normal cells that have a high replacement rate (e.g. hair follicles, bone marrow, intestinal lining, etc.) and development of drug resistance by malignant cancer cells (Jaracz *et al.*, 2005). Radiation (also called radiotherapy) comprises invisible high-energy rays (X-rays, gamma rays) or beams of subatomic particles (electrons) to kill or shrink tumor cells. Radiotherapy is usually applied with other treatments, for instance it may be used both before and after surgery to reduce the size of the tumor or destroy any remaining cancer cells, respectively. This aggressive therapy damages healthy cells by causing inflammation of tissues and organs in and around the treatment site (Botchway *et al.*, 2015). Other common secondary effects of chemo and radiotherapy are pain, nausea and vomiting, diarrhea or constipation, tiredness, fertility loss, hair loss, anaemia and depression (Jaracz *et al.*, 2005; Botchway *et al.*, 2015).

In the past few decades, hyperthermia (also called thermal therapy or thermotherapy) is considered as an adjuvant technique for current established treatment modalities and artificial way to elevate the body tissue temperature. In oncology, the term 'mild or moderate hyperthermia' refers to various techniques used to raise the temperature to about 41°C - 42°C, through the application of external sources of energy for a certain period of time in order to increase the susceptibility of cancer cells to chemotherapy and radiotherapy (Wust *et al.*, 2002). Based on the fact that tumor cells are more sensitive to temperature increment than normal tissue cells, hyperthermia utilises heat energy to induce thermal-based effects that suppress the growth of solid neoplasms (Chicheł *et al.*, 2007). Generation of heat can be achieved by several methods, but recently electromagnetic radiation (EM) dominated the field of cancer therapy. Thermal techniques using EM energy include, radiofrequency therapy, microwave thermotherapy, high intensity focused ultrasound thermotherapy, magnetic thermal ablation and laser-induced photothermal therapy (Chicheł *et al.*, 2007). All these therapeutic techniques are relatively simple to perform and therefore have the potential to improve

recovery times and reduce the complication rates and hospital stays. However, despite their benefits, they are non-specific and suffer from some limitations such as inability to distinguish malignant cells from surrounding normal tissue, which cause undesired tissue injury, unwanted burn and pain (Hauck *et al.*, 2008; Wust *et al.*, 2002).

Over the last decade, the implementation of nanomedicine-based cancer therapy holds the promise to overcome the limitations associated with conventional cancer treatments (Day *et al.*, 2009). Laser-induced phototherapy (laser-induced hyperthermia) is a highly specific, minimally invasive therapeutic strategy that employs photothermal agents (e.g. organic dyes and metal nanoplatforms) to generate heat sufficient for causing irreversible damage to cancer cells upon laser irradiation (most often in NIR region) while not affecting the surrounding healthy tissue (Cherukuri and Curley, 2010). This strategy induces localised heating, has a precise spatiotemporal selectivity, has a great capacity to treat tumors entrenched in vital regions and may also be combined with current available treatments such as chemotherapy (Huang and El-Sayed, 2011; Zou *et al.*, 2016; Bao *et al.*, 2016).

Gold nanoparticles (GNPs) have been investigated as a promising candidate in nanometal-assisted photothermal cancer therapy. Taking advantage of their optical attributes, GNPs are exploited for the eradication of malignant cells by efficiently absorbing light, tuned to their SPR frequency (Huang and El-Sayed, 2010).

1.10 Gold nanoparticle-mediated hyperthermia in cancer therapy

As mentioned before, the photophysical origin of the enhanced plasmonic photothermal therapy efficacy of the metallic GNPs is the collective and coherent oscillations of free and mobile conduction band electrons at the nanoparticles surface coupled to an incident resonant light, termed as surface plasmon resonance (SPR) (Mie, 1908; Link and El-Sayed, 1999). Illumination of GNPs and SPR formation at certain resonance frequency generates

considerable local optical field enhancement due to strong scattering and absorption of incident photons (Shibua *et al.*, 2013). The photon energy absorbed by GNPs is transduced to thermal energy, which travels through the nano-gold by lattice vibration and subsequently dissipated into the surrounding environment. The photothermal heating elevates the temperature only in the area around the GNPs without over-heating the surrounding healthy tissue, thereby minimising collateral damage and scarring. The selective localised photothermal heating of targeted malignant cells as the result of non-radiative relaxation of photoexcited nanoparticles corroborates the role of gold nanostructure as an exceptional photosensitiser in photothermal cancer therapy (Day *et al.*, 2009; Huang and El-Sayed, 2011; Iancu, 2013). In contrast to conventional organic dyes (e.g. indocyanine green, naphthalocyanine and porphyrin) that have potential performance drawbacks such as poor photostability (photo-bleaching and permanent degradation), low absorption coefficient requiring high irradiation energy /or need of energy-absorbing molecules in high quantities (that can be toxic), GNPs are emerging as promising agents for photothermolysis of cancer cells due to the following characteristics:

- They are chemically stable and non-toxic in the biological environment.
- They show less susceptibility to chemical and thermal denaturation due to their rigid metallic structure.
- They have a strong absorption cross-section (several orders-of-magnitude greater when compared to organic dyes) requiring only minimal irradiation energy.
- They have high photothermal conversion efficiency.
- Furthermore, geometry and dimensions of GNPs can be controlled and their SPR can be systematically tuned to desired resonant frequency, therefore, they have the potential to exploit the enhanced permeability and retention effect for tumor targeting.

However, it should be noted that appropriate temperature increment, intratumoral homogenous distribution of GNPs, gold nanostructure's concentration, laser power density, duration of laser exposure, optimisation of extinction cross section of nano-golds, penetration depth of laser radiation in tumor region, laser type, as well as, types of tissue and thermoregulation ability of living organism are the major considerations of utilising plasmonic gold nanoparticle-based photothermal cancer therapy in the laboratory and the clinical setting (Prashant *et al.*, 2008; Huang and El-Sayed, 2010; 2011; Chatterjee *et al.*, 2011; Bao *et al.*, 2016).

The photothermal therapy of lymphocytes *in vitro* using GNPs coupled with a nanosecond visible pulsed laser was first reported, in 2003, by Pitsillides *et al.* Human T lymphocyte cells labeled with 30 nm spherical gold nanoparticles (GNPs) by first incubating with anti-CD8 mouse IgG and then with GNPs conjugated to anti-mouse IgG antibody. The illumination of labeled T cells with nanosecond laser pulses (Q-Switched Nd:YAG laser, 565 nm, 20 ns duration) induced cellular death at 100 laser pulses at a fluence of 5 J cm^{-2} which is above the threshold for laser-induced cavitation bubble formation. The cellular lethality was not observed in unlabeled cells treated under the same laser conditions (Pitsillides *et al.*, 2003).

Following the first work on application of GNPs in plasmonic photothermal therapy, the number of scientific reports focusing on the idea of using gold as a potential photothermal agent have been significantly increased (Figure 1.13). The GNPs that have been studied extensively for this purpose are mostly nanorods, nanoshells and nanocages.
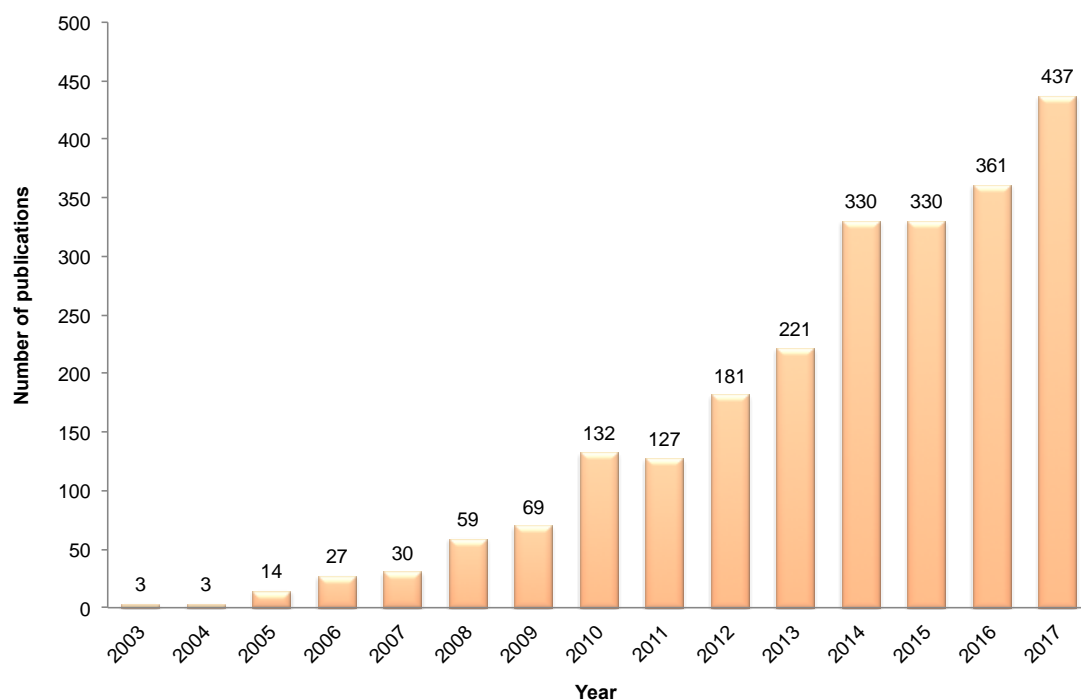
Figure 1.13. Number of SciFinder Scholar references per year after the first publication on gold naoparticle-mediated photothermal therapy in 2003 containing the search terms, gold*, photothermal*, and cancer* as of December 2017.

As mentioned above, visible or NIR light can locally excite GNPs of various shapes and sizes. The tissue-depth penetration of visible light is weak; absorption of visible light by primary absorbers in tissue (water, hemoglobin, oxyhemoglobin, and melanin) causes complexity in distinguishing between abnormal and normal cells that may lead to photothermal tissue damage (Day *et al.*, 2009). In contrast, NIR radiation (approximately between 650 and 900 nm) is capable of large penetration depth even at low laser intensities (depending on tissue types) with minimal optical attenuation by biological tissue (Joshi and Wang, 2010). Therefore, for conducting *in vivo* photothermal treatments, NIR-absorbing nano-scaled gold was pioneered by Halas and co-workers (silica-gold core-shell nanoparticels) (Hirsch *et al.,* 2006), Zasadzinski's group (hollow gold nanoshells) (Prevo *et al.,* 2008), Murphy's group (research in rod-shaped GNPs) (Jana *et al.*, 2001), El-Sayed groups (research in rod-shaped GNPs) (Nikoobakht and El-Sayed, 2003) and Xia's research group (research in gold nanocages) (Chen *et al.*, 2005). Due to their strong NIR absorption efficiency (extinction coefficient is about $10^{-9}\,M^{-1}\,cm^{-1}$), once NIR-laser-activated GNPs bind to or accumulate at the tumor site, laser

illumination with the corresponding resonance triggers photothermal destruction of the cells without unwanted damage and death of the intervening healthy tissues (Yao *et al.*, 2016).

In 2003, West, Halas and co-workers reported the first studies on NIR photothermal therapy of cancer both *in vitro* and *in vivo* using GNShells (Hirsch *et al.*, 2003). The silica core GNShells synthesised with SPR peak tuned to the NIR region and stabilised with thiolated poly(ethylene glycol). Human breast epithelial carcinoma SK-BR-3 cells incubated with PEGylated GNShells for 1 h and then exposed to NIR light (diode laser, 820 nm, 35 W cm^{-2}) for 7 min. The results showed that GNShells-treated SK-BR-3 cells underwent localised, irreversible photothermal ablation within the laser spot as determined by calcein AM viability staining; exposing the cells to either GNShells or NIR laser individually did not compromise the cellular viability (Figure 1.14).
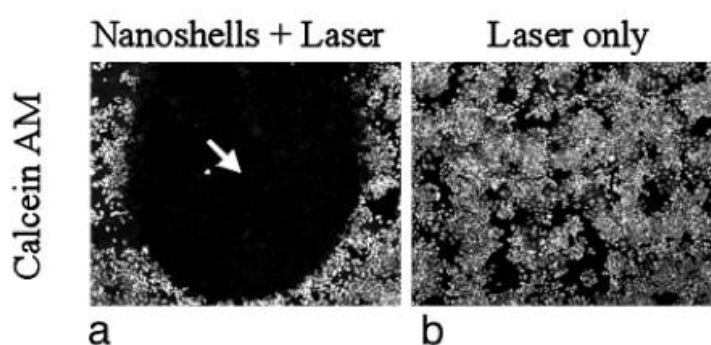
Figure 1.14. *In vitro* NIR photothermal cancer therapy using GNShells. Human breast epithelial carcinoma SK-BR-3 cells underwent phothermal induced morbidity following exposure to continuous-wave NIR light (diode laser, 820 nm, 35 W cm^{-2}, 7 min), as indicated by the loss of Calcein AM staining (a) while cells treated with laser only remained intact (b) (Hirsch *et al.*, 2003).

To demonstrate the potential of the therapy *in vivo*, PEGylated GNShells were injected interstitially into the tumor volume that was inoculated subcutaneously into the hind legs of female nonobese diabetic CB17-Prkd c SCID/J mice. About 30 min after injection, breast cancer xenografted tumours were exposed to similar laser at intensity of 4 Wcm^{-2} for 4 min. *In vivo*

magnetic resonance temperature imaging (MRTI) analysis revealed an average temperature rise of 44.6 ± 60 °C in irradiated GNShell-treated tumor compared to 9.1 ± 2.5 °C in GNShell-free control tumor (Table 1.1) (Hirsch *et al.*, 2003). The GNPs-mediated photothermal therapy increased temperatures well above the damage threshold necessary to induce irreversible tissue damage and did so by using laser dosage 10 to 25 times less than the dose required for Indocyanine green dye (Chen *et al.*, 1996).

| Mouse | $\Delta T \pm SD$ | |
	Control	Nanoshell
1	4.7 ± 0.7	39.7 ± 4.7
2	8.4 ± 1.6	60.4 ± 3.4
3	9.1 ± 2.5	44.6 ± 6.0
4	5.9 ± 1.2	32.8 ± 1.2
5	8.7 ± 0.9	28.1 ± 1.0
6	7.6 ± 1.6	32.5 ± 0.7

Table 1.1. The average temperature elevation in GNShell-treated and GNShell-free control tumors upon NIR laser therapy (diode laser, 820 nm, 4 W cm^{-2}, 4 min). Variation in the average temperature elevation obtained from each study could be due to heterogeneous distribution of the nanoshells within the tumor (particularly, distant from skin surface), the angle of incidence, and source-to-skin distance of the laser fiber, as well as the placement of the MR plane for observation (Hirsch *et al.*, 2003).

In subsequent studies reported by the same research group (O'Neal *et al.*, 2004), PEG-passivated NIR-absorbing GNShells were intravenously injected into the blood stream of BALB/cAnNHsd mice and allowed to circulate for 6 h. The CT26.WT murine colon tumour was then illuminated with a diode laser (808 nm, 4 W cm^{-2}, 3 min). The GNShells-treated tumors exhibited complete tumor eradication by day 10 without regrowth for over 90 days. Conversely, all GNShell-free control tumors continued to grow rapidly and all control mice euthanised by day 19.

The GNR-mediated photothermal cancer therapy was first developed by El-Sayed and co-workers (Huang *et al.*, 2006). GNRs were synthesised with an aspect ratio of 3.9 and the longitudinal plasmon band tuned to the incident

laser wavelength (800 nm) and functionalised with anti-epidermal growth factor receptor (anti-EGFR) monoclonal antibodies that facilitated binding of the GNRs to the cancer cells. The EGFR-positive human oral malignant cells (HSC-3 and HOC-313) and non-malignant cells (HaCat) were incubated with the same concentration of anti-EGFR antibody-conjugated GNRs for 30 min and subsequently irradiated with Ti:Sapphire continuous-wave laser at different energies (40 mW-160 mW) for 4 min. Cell viability was detected by trypan blue staining. Interestingly, the threshold energy for photothermal destruction of human oral malignant cells was found to be 10 W cm^{-2}, which was about half the energy required for killing the non-malignant cells (20 W cm^{-2}). Hence, rod-shaped nanoparticles were introduced as efficient photothermal sensitisers for cancer therapy (Figure 1.15).
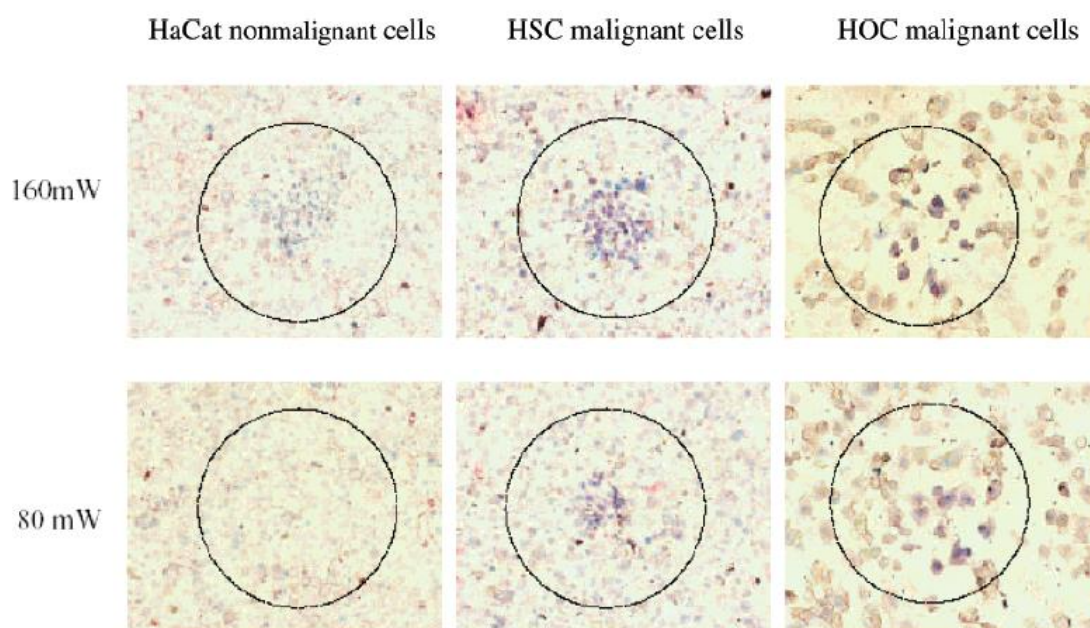
Figure 1.15. Selective *in vitro* NIR photothermal cancer therapy using GNRs. The cancer cells required half the energy to be photothermally damaged as compared with normal cells. Exposure to the NIR laser at 800 nm (80 mW=10 W cm^{-2}, 4 min.) caused irreversible photodestruction of the human oral malignant cells (HSC and HOC) while normal cells (HaCat) remained unaffected and only underwent photothermal injury at higher laser energy (160 mW = 20 W cm^{-2}) (Huang *et al.*, 2006).

Two years later, the same researchers published on the regression of xenograft tumors from squamous cell carcinoma in female *nu/nu* mice by NIR photothermal therapy (Dickerson *et al.*, 2008). The GNRs were conjugated to

a thiolated poly(ethylene glycol) (mPEG-SH, 5000 M_W) and injected into mice either by direct administration within the tumor interstitium (15 µL, $OD_{\lambda800}$ = 40) or by intravenous delivery and accumulation at the tumor site through passive targeting (100 µL, $OD_{\lambda800}$ = 120). After exposure to a continuous-wave NIR diode laser with intensity of 1-2 W cm^{-2} for 10 min, dramatic decrease in tumor growth was reported for both administration routes, with minimal damage inflicted in surrounding tissue which indicated the specificity of the hyperthermic effect on tumor growth due to the ability of GNRs to efficiently absorb and convert NIR light into heat through a non-radiative mechanism. Thermal transition measurements revealed that temperature increased by over 20°C (Figure 1.16).
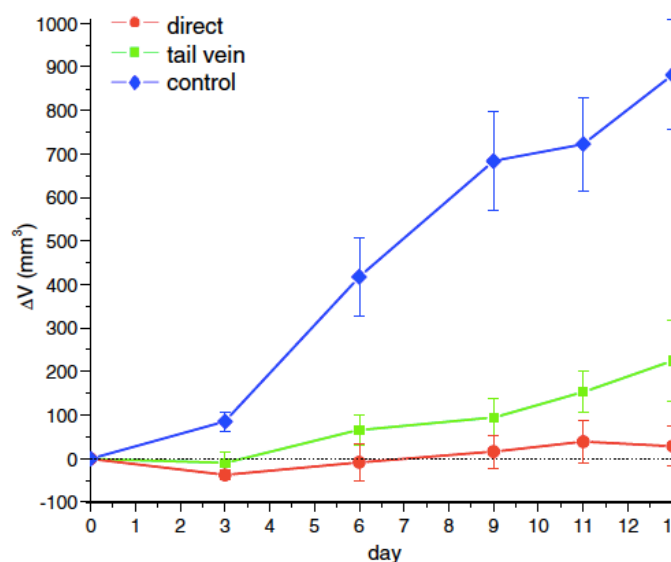
Figure 1.16. *In vivo* NIR photothermal cancer therapy using GNRs. NIR illumination of the GNR-treated tumours (diode laser, 1-2 W cm^{-2}, 10 min) resulted in the significant inhibition of average tumour growth over a period of 13 days, with resorption of >57% of the intratumorally injected tumors and 25% of the intravenously treated tumors (Dickerson *et al.*, 2008).

Synergistic administration of photothermal therapy and chemotherapy to cancer cells is now considered as a new and exciting possibility for nanomedicinal applications. NIR laser-induced photothermal therapy with GNPs can promote chemotherapy by enhanced drug delivery and controlled

drug release through temperature increase in the tumor regions that consequently accelerates the endocytic internalisation of GNPs into the tumor cells and mediates NIR light-triggered drug release. Growing evidence supports the efficacy of NIR-induced chemo-photothermal therapy as a potent anti-tumor strategy (Issels, 2008).
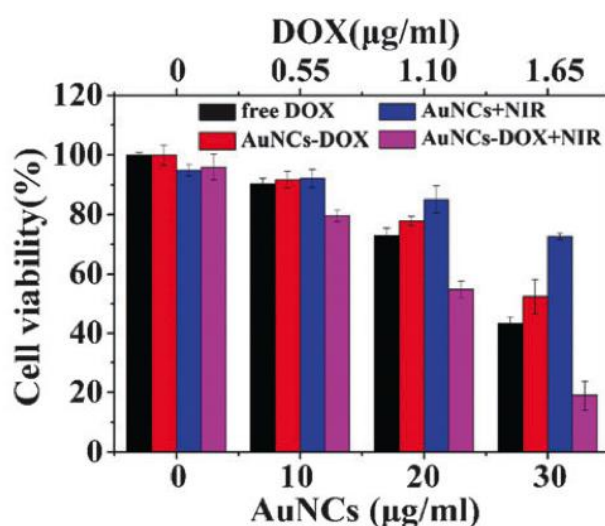
Figure 1.17. 24 hrs viability of human breast cancer cells (MCF-7) treated with different concentration of free DOX, Fe_3O_4@CaP capped GNCs with or without 5 min NIR irradiation (1 W cm^{-2}, 808 nm) and GNCs–DOX with or without 5 min NIR irradiation (1 W cm^{-2}, 808 nm). The cytotoxicity of GNCs–DOX under NIR irradiation was even higher than the sum of chemotherapy by AuNCs–DOX and photothermal therapy by DOX-free AuNCs. (Shi *et al.*, 2012).

As an example, in 2012, Shi *et al.* encapsulated the chemotherapeutic agent doxorubicin (DOX) into carboxylate-functionalised gold nanocages (GNCs) followed by capping the GNCs porous walls with pH responsive calcium phosphate-coated iron oxide nanoparticles (Fe_3O_4@CaP). The DOX release was triggered as the result of dissolution of the calcium phosphate cap in acidic endocytic compartments. The surge release of DOX (up to 48%) after irradiation of Fe_3O_4@CaP capped DOX-loaded AuNCs with NIR laser (808 nm, 1 W cm^{-2}, 5 min) illustrated the augmenting effect of laser irradiation on drug release (Figure 1.17) (Shi *et al.*, 2012).

Hauck *et al.* investigated the synergism between chemotherapeutics and moderate hyperthermia against human myeloid leukemia cells OCI/AML3. The synthesised GNRs were coated with a layer of negatively charged PSS (poly(4-styrenesulfonic acid)) followed by a layer of positively charged poly(diallyldimethylammonium chloride) (PDADMAC). OCI/AML3 cells were incubated with PDADMAC-coated GNRs for 12 h. To probe the synergistic cytotoxicity in combination with hyperthermia, cisplatin was added to the culture immediately prior to irradiation. Cells were illuminated with a fiber-coupled 810 nm laser at constant power density of 1 W cm^{-2} for 30 min, which represented a mean equilibrium temperature of $\approx$ 42 °C. Flow cytometry results indicated that the fraction of surviving OCI/AML3 cells after combinational treatment was significantly lower compared to the projected additive value derived by the multiplication of the surviving fraction of cancer cells from each independent treatments (Figure 1.18). The combined chemo-photothermal therapy lowered the effective cisplatin dose and consequently alleviated the dose-dependent renal side effects of cisplatin (Hauck *et al.*, 2008).
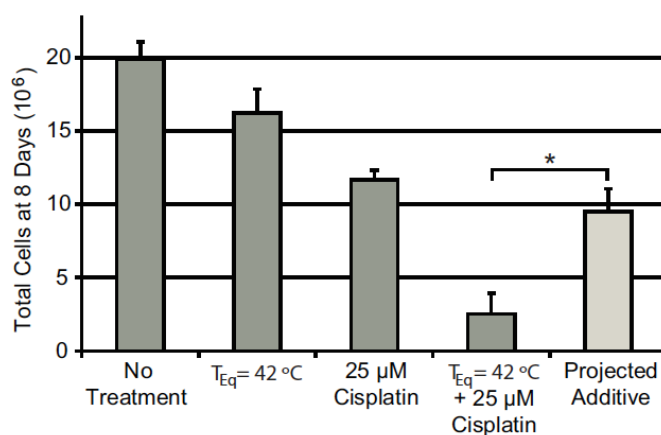
Figure 1.18. The synergistic effect of cisplatin with moderate hyperthermia against human myeloid leukemia cells (OCI/AML3). The surviving fraction of combinational therapy-treated OCI/AML3 cells was 78% lower than chemotherapy treatment alone, 84% lower than hyperthermia alone, and 73% lower than the projected additive model (Hauck *et al.*, 2008).

Lee *et al.* studied the NIR laser–induced photothermal therapy using DOX-loaded gold nanoshells (DOX@PEG-GNShells). The release of Dox from DOX@PEG-GNShells and the intratumoral temperature alteration during photothermal heating were monitored by fluorescence optical imaging and photoacoustic imaging, respectively. *In vitro* studies showed the maximum fluorescence intensity of DOX after irradiation of DOX@PEG-GNShells for 3 min (0.15 W mm^{-2}). In subsequent *in vivo* experiments, both intratumoral and intravenous administration of DOX@PEG-GNShells followed by NIR laser treatment (0.15 W mm^{-2}, 1 min) performed on 4T1 breast tumour–bearing nude mice. The fluorescence optical imaging showed stronger fluorescence signals in laser–treated tumors 24 hr after treatment compared to the untreated tumors (Figure 1.19). The photoacoustic imaging (acquisition wavelength = 800 nm) computed the temperature-induced changes during photothermal therapy by monitoring the elevated intratumoral temperature up to 50°C. Hence, the *in vitro* and *in vivo* experimental evidence confirmed the efficacy of GNShell-mediated laser-induced thermal therapy (Lee *et al.*, 2013).
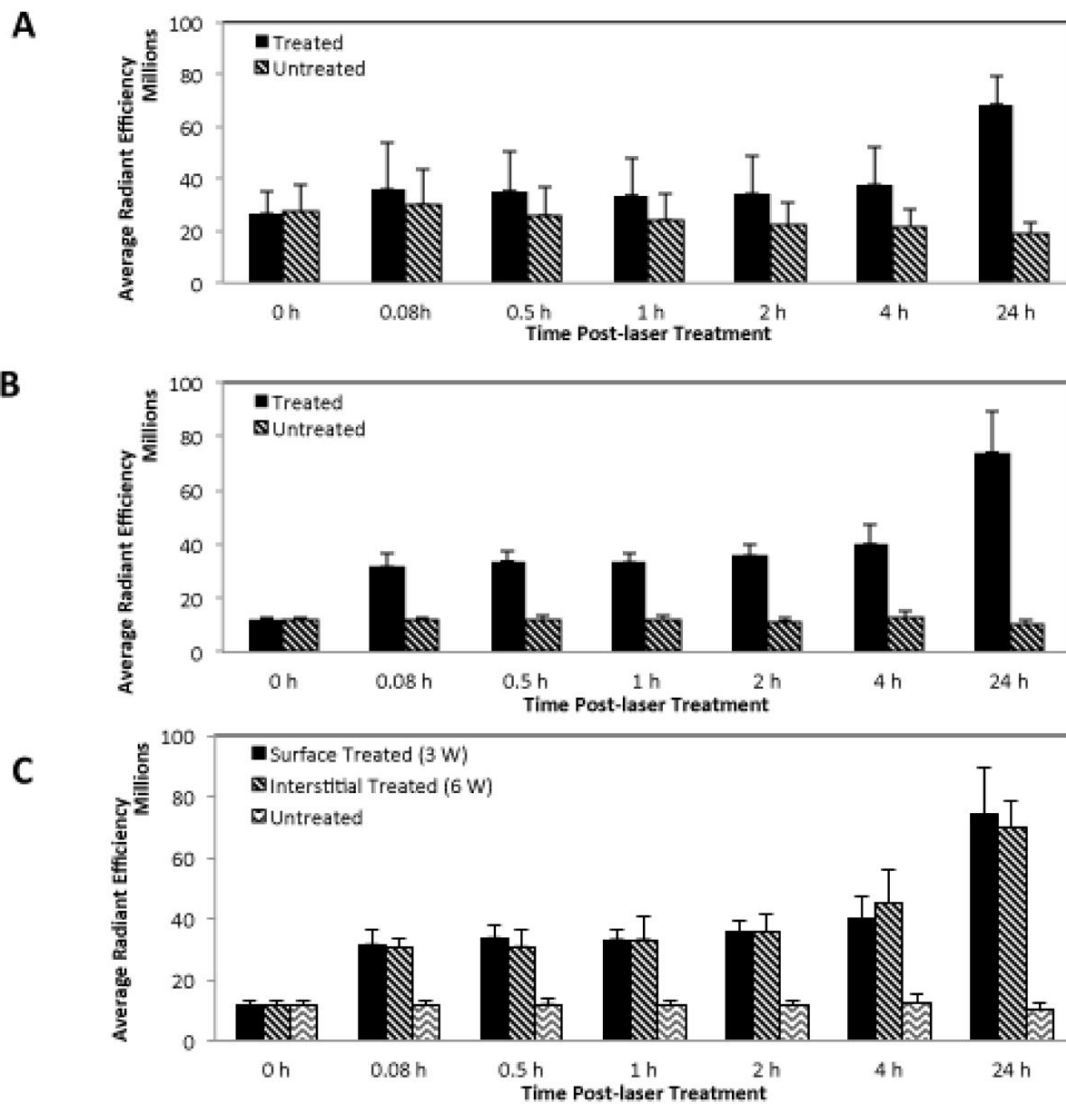
Figure 1.19. The Fluorescence intensity of released DOX from DOX@PEG-GNShells under different injection and laser treatment conditions using a fluorescence optical imaging system. (A) *In vivo* intratumoral injection of DOX@PEG-HAuNS (1.32 ×10^{12} particles mL^{-1}) followed by DOX release and treatment with 3 W (0.15 W mm^{-2}) surface laser for 1 min. (B) *In vivo* DOX release following intravenous injection of DOX@PEG-GNShells (3.3×10^{12} particles mL^{-1}) and treatment with 6 W (1.9 W mm^{-2}) surface laser for 1 min. (C) Comparison of *in vivo* DOX release after intravenous injection of DOX@PEG-GNShells (3.3×10^{12} particles mL^{-1}) and treatment with a 3 W (0.15 W mm^{-2}) surface laser probe or with a 6W (0.12 W mm^{-2}) interstitial laser probe. The NIR laser irradiation of the 4T1 breast tumor promoted the drug release from DOX@PEG-GNShells as the laser–treated tumors showed stronger fluorescence signals than the untreated controls (Lee *et al.*, 2013).

Numerous *in vitro* and *in vivo* studies conducted using different platforms of GNPs in photothermal cancer treatment among which, GNRs and GNShells are exploited the most due to their attractive optical properties of their plasmon resonance band at the visible or NIR regime.

Bhatia and co-workers showed that NIR-absorbing GNRs exhibited longer circulation half-life *in vivo* ($t_{1/2}$, ~17 hours) compared to gold nanoshells ($t_{1/2}$, ~4 h) with the plasmon band adjusted at the same wavelength (Von Maltzahn *et al.*, 2009). It was also found that, due to higher absorption coefficients, GNRs are able to elicit photothermal effect by employing three times lower laser intensity in comparison to GNShells (Jain *et al.*, 2006).

Despite the aforementioned advantages, GNRs bear some drawbacks such as:

1. The cytotoxicity of GNRs is related to the surfactant used in their synthesis; hexadecyltrimethylammonium bromide (CTAB) is highly toxic and is adsorbed strongly on the surface of GNPs. Replacing it with other ligands is quite challenging and can lead to particle aggregation. This cationic surfactant is also known to disrupt biomembranes and denature proteins (Niidome *et al.*, 2006; Day *et al.*, 2009).

2. Upon illumination of GNRs by NIR laser, the tunable longitudinal band is blue shifted largely to the visible region. Therefore, they gradually lose their strong NIR radiation absorbing properties (Bao *et al.*, 2016).

3. A relatively low specific surface area results in GNRs low-payload-carrying capabilities. This is attributed to the aggregation of the NRs in the cell culture media (Bao *et al.*, 2016). In contrast, hollow GNshells have high drug loading capacity because of their high surface area-to-volume ratio. In addition, they have been proven to be safe for biological applications (Hirsch *et al.*, 2003).

1.11. Enhanced Permeability and Retention (EPR) effect

In contrast to normal vessels that are aligned by a tightly sealed endothelium supported by a basement membrane and pericytes, the vasculature of solid tumors is leaky and typically comprises chaotic networks of tortuous endothelium with defective pericytes and fragmented basement membrane, which result in the formation of endothelial fenestrations (400-800 nm). Furthermore, the extracellular fluid is constantly drained to the lymphatic vessels at a mean flow velocity of around 0.1-2 $\mu m\ s^{-1}$ in normal tissues, whereas in tumors, the absence or non-functional performance of lymphatic vessels contributes to insufficient drainage of extravasated solutes and colloids from the interstitial fluid (Danhier *et al.* 2010; Bertrand *et al.*, 2014; Hare *et al.*, 2017). Based on the anatomical and pathophysiological differences between normal tissues and solid tumors (Figure 1.20), macromolecules/nanoparticles penetrate through the fenestrated endothelium and accumulate in the tumors interstitial space due to ill-defined vasculature and suppressed lymphatic filtration that block their clearance from the tumor; conversely, they will not be distributed extensively in normal tissue since interendothelial junctions (with a size range of 6-7 nm) in normal vessels provides resistance to the delivery of nanocarries. This passive phenomenon referred to as "Enhanced Permeability and Retention (EPR) effect" was first reported by Matsumura and Maeda in 1986 (Matsumura and Maeda, 1986) and was described in more detail by Maeda *et al.* (Maeda, 2001; Maeda *et al.*, 2006; 2009) as EPR based chemotherapy and has emerged as an important strategy to improve the delivery of therapeutic agents to tumors. It has been demonstrated that active targeting can only occur after passive accumulation in tumors (Bae, 2009). Passive accumulation within the leaky tumor vasculature occurs when the size of the nano-scale drugs exceeds the limit of renal excretion threshold i.e. if they are not small enough (<5.5 nm) to be excreted by the kidney or not large enough (>500 nm) to be rapidly recognised and trapped by the reticuloendothelial system (RES). Such nanosized agents tend to circulate for longer times, and after intravenous administration they penetrate preferentially into the tumors interstitium through the leaky tumor vasculature and then accumulate within tumors due to the

EPR effect. The concentration of nanoparticles drugs in the tumor region is in the magnitude of 7-10-fold higher compared to equivalent doses of the same drugs in the low molecular weight form (due to their instability and short half-life) (Maeda, 2001; Fang *et al.*, 2011).

It is important to note that the surface of long-circulating nanocarriers can be engineered with biocompatible polymeric layers, which will be discussed in more detail in the forthcoming chapters.
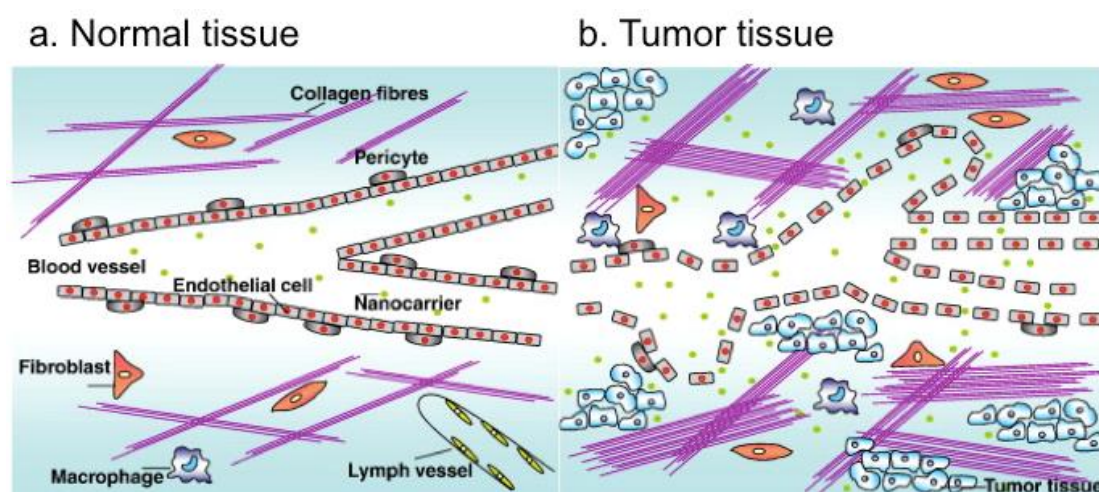
Figure 1.20. Representative comparison between normal and malignant tissues. a) Normal tissue comprises linear blood vessels with closely aligned epithelium that are covered by basement membrane and pericytes. Lymph vessels are also present. Collagen fibres, fibroblasts and macrophages are in the extracellular matrix. b) Tumor tissues lack functional lymphangiogenesis and contain irregular blood vessels that are composed of discontinuous epithelium and bigger fenestration pores than normal vasculature. Also, The extracellular matrix in tumor tissue contains more collagen fibres, fibroblasts and macrophages than in normal tissue. (Danhier *et al.*, 2010)**.**

Although the EPR effect is the basis of nanotechnology platforms to deliver nano-sized therapeutic agents to tumors, thereby enhancing their anti-cancer effects, other factors such as the type, size, shape, charge, surface characteristics and overall biocompatibility influence the therapeutic potency; in addition, anatomical characteristics that affect the therapeutic outcome include:

⇒ Tumor: type, size, proliferation rate, necrosis, intra-tumoural volume,

and anatomical location.

⇒ <u>Vasculature:</u> density, volume, permeability, distribution relative to stromal and tumour cells, and blood flow.

⇒ <u>Stroma:</u> architecture, density, composition, and matrix rigidity.

⇒ <u>Macrophages:</u> number and function.

⇒ <u>Lymphatics:</u> density, function, and location within and around the tumour.

⇒ <u>Interstitial fluid pressure:</u> local effects and cross-tumour pressure gradients. (Hare *et al.,* 2017).

⇒ <u>Patient's characteristics</u> including gender, age, and body compositions. (Natfji *et al.,* 2017)

Natfiji and coworkers systematically analysed clinical data to identify the key parameters affecting the extent of the EPR effect. They collected data from 24 studies in order to investigate the impact of tumor type on the magnitude of the EPR effect (either quantitative or qualitative). It was shown that pancreatic, colon, breast, and stomach cancers have the highest levels of accumulation of nanomedicines, respectively (Figure 1.21).

Furthermore, Natfiji and coworkers analysed the influence of tumor perfusion (according to type, size, stage, and location) on the magnitudes of EPR by making reference to two relevant clinical studies for pancreatic cancer (d'Assignies *et al.,* 2009; Komar *et al.,* 2009). The results revealed that blood perfusion in most of the cases were higher in pancreatic tumors compared to normal tissue (Table 1.2).
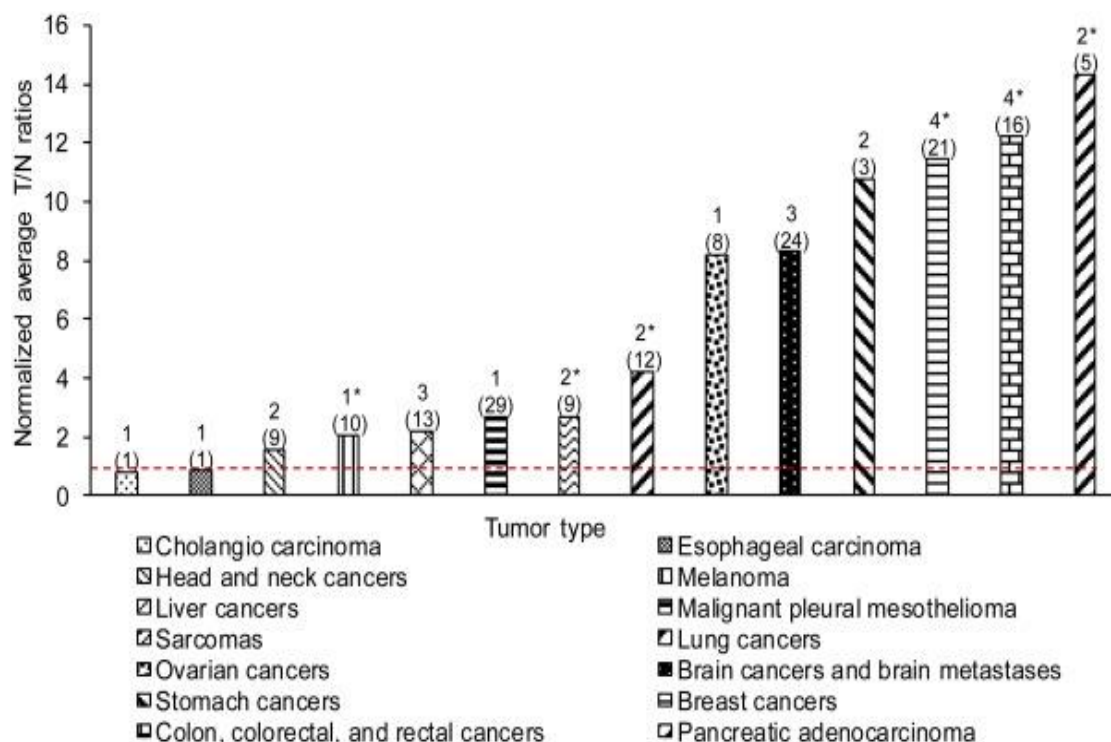
Figure 1.21. Nanomedicines accumulation in different tumors demonstrated as normalised average tumor/normal (T/N) tissue content ratios. The number in parentheses indicates the total number of patients included in the study, and the number above parentheses represents the number of clinical studies of an individual tumor. * Indicates that in one study, the nanomedicine was not detected because the concentration was lower than the limit of detection. In those studies, the presence of nanomedicine in normal tissues was arbitrarily set at the limit of detection (i.e. the lowest concentration of nanomedicine that could be detected). The red line denotes T/N ratio of 1 (i.e., columns above the red lines had a degree of preferential accumulation in the tumor). Six tumor types displayed the highest levels of normalised T/N ratios of nanomedicine accumulation in comparison with other tumors. These were (i) pancreatic adenocarcinoma, (ii) colon, colorectal, and rectal cancers, (iii) breast cancers, (iv) stomach cancer, (v) brain cancer and brain metastases, and (vi) ovarian cancer. Adapted from (Natfji *et al.*, 2017).

Table 1.2. Available clinical data about the variations of tumor perfusion according to tumor type, size, stage, and location.

Tumor Type	Tumor Stage, Size, or Location	Blood Flow in Tumor Tissue	Blood Flow in Normal Tissue
Pancreatic cancers	Tumor classification: WHO 1	284 mL/100 g/min	130.4 mL/100 g/min
	Tumor classification: WHO 2	229.1 mL/100 g/min	130.4 mL/100 g/min
	Tumor classification: WHO 3	153.5 mL/100 g/min	130.4 mL/100 g/min
	Tumor diameter <2 cm	292 mL/100 g/min	130.4 mL/100 g/min
	Tumor diameter ≥2 cm	159.8 mL/100 g/min	130.4 mL/100 g/min
	Tumors with lymph node metastases	141.6 mL/100 g/min	130.4 mL/100 g/min
	Tumors without lymph node metastases	264 mL/100 g/min	130.4 mL/100 g/min
	Tumors with liver metastases	122.8 mL/100 g/min	130.4 mL/100 g/min
	Tumors without liver metastases	236.5 mL/100 g/min	130.4 mL/100 g/min
	All tumors (stages ≥ IIB)	45.7 ± 18.2 mL/min/dL[a]	113.8 ± 48.2 mL/min/dL[a]
	Medium-size tumors[d]	51 ± 3.9 mL/min/dL[a]	113.8 ± 48.2 mL/min/dL[a]
	Large-size tumors[d]	21.1 ± 7.9 mL/min/dL[a]	113.8 ± 48.2 mL/min/dL[a]
	Very large–size tumors[d]	45.1 ± 7.4 mL/min/dL[a]	113.8 ± 48.2 mL/min/dL[a]

a Data presented as mean ± SD.
d Data calculated for tumors with identified stage. The size of tumors was considered as medium if tumors were on stage IIB or with low-grade neuroendocrine tumor, as large if tumors were on stage III, and as very large if tumors were on stage IV or with high-grade neuroendocrine tumor. Adapted from (Natfji *et al.*, 2017).

65

Summary

Pancreatic cancer is one of the most deadly types of cancer, with a yearly incident that equals its mortality. Radical resection is still the only curative option, but only less that 10% of all pancreatic cancer patients can undergo curative resection and the high incidence of life threatening complications such as damage of the liver is imminent. Since this aggressive human malignance usually develops without any symptoms, about 80% of pancreatic cancers are diagnosed at locally advanced and/or metastatic stage (the stage where radical resection is not possible) thus, chemotherapy remains the main treatment for most pancreatic cancer patients (Affram *et al.*, 2015; Dia *et al.,* 2017). Gem is currently the first-line chemotherapeutic drug used to treat pancreatic cancer.

Chemically, Gem (2',2'-difluoro-2'- deoxycytidine) is a pyrimidine analog of deoxycytidine, from which it differs by two fluorine atoms in position 2 of the deoxyribose. Gem prodrug is required cellular uptake and intracellular phosphorylation and converted to the mainly active metabolite gemcitabine triphosphate (dFdCTP) after energy dependent uptake of the parent compound into cells *via* nucleoside transporters since it is too hydrophilic to passively cross the plasma membrane. The active metabolite, dFdCTP, is incorporated into DNA as a false nucleoside, eventually leading to inhibition of DNA polymerases, and induces cells to undergo apoptosis. Although the molecular events mentioned above eventually contribute to the effectiveness of Gem in fighting tumor cells, however the drug possesses certain demerits. The major deficiencies of Gem therapy are: poor cell membrane permeability, short plasma half-life and toxic side effects. Following intravenous administration, Gem is quickly metabolised into the inactive and more soluble metabolites, 2', 2'-difluorodeoxyuridine (dFdU) *via* deoxycytidine deaminase and is then cleared by the kidneys. Rapidly excretion of dFdU out of the body causing a very short biological half-life (7-18 min) that subsequently results in necessity of administration of high doses of Gem (1000 mg/ m^2) in order to assure an adequate pharmacological effect, leading to undesirable side effects such as hepatotoxicity, nephrotoxicity, myelosuppression, mild and

transient neutropenia, thrombocytopenia, anemia and toxicities in well-perfused organs including liver, long and kidney, which prohibit more frequent administration of Gem than once-weekly dosing in cancer patients. Moreover, drug resistance associated with deficiencies in the expression of nucleoside transporters (e.g. hENT1) confers lower Gem toxicity in tumor cells by blocking the cellular transport of Gem (Celano *et al.*, 2004; Gabizon *et al.*, 2006; Lanz *et al.*, 2007; Dasanu, 2008; Toyama *et al.*, 2013; Wang *et al.*, 2014; Affram *et al.*, 2015; Dai *et al.*, 2017).

Effective drug delivery in pancreatic cancer treatment remains a major challenge due to the growth of dense, collagen-rich, extracellular matrix and stroma with high interstitial pressure around pancreatic tumors, known as the desmoplastic reaction, which accentuates hindrance of drug delivery by creating a unique microenvironment that paradoxically promotes both tumor growth and metastatic spreading and at the same time forms a barrier to chemotherapy penetration (Koay *et al.*, 2014).

In order to and improve the pharmacokinetic characteristics and overcome the obstacles for effective drug delivery, a nanoparticles-mediated drug delivery system can be utilised. Nano-sized carriers (1) prolong the circulation of Gem molecules in the blood stream by protecting them from metabolic inactivation and accumulating them at the site of action *via* the EPR effect; (2) penetrate the cell membrane in a transporter-independent pathway; (3) decrease severity of toxic side effects by avoiding accumulation of drug in healthy tissues due to size limitation; and (4) they are non-toxic and release their payload in a controllable and sustained manner (Wang *et al.*, 2014; Dai *et al.*, 2017).

GNPs have been investigated as carriers for drug delivery. This is due to their distinctive shape, size and surface-dependent properties. Furthermore, their intriguing radiative and non-radiative properties, chemical stability, biocompatibility, non-toxicity and high delivery efficiency render GNPs as promising candidates for various biological applications including drug delivery.

Besides their drug delivery application potential, GNPs also exhibit a prominent phothothermal therapeutic effect by inducing cancer cell damage and even death with minimal damage of the surrounding normal cells, through the conversion of optical energy to cytotoxic thermal energy upon laser irradiation. Photo-chemothermal thaerapy based on drug-loaded GNPs has been shown to be an effective cancer treatment option since the localised heating effect can increase the vascular permeability and in turn elevate the levels of nanoformulation accumulation and eventually the drug release inside solid tumor, and therefore improve the therapeutic outcome and potentially decrease toxic effects (Huang and El-Sayed, 2010; 2011; Liu *et al*., 2017).

In the present work, multifunctional GNPs-based nanoformulations are developed for the treatment of pancreatic cancer cells *via* a combination of chemotherapy and photothermal ablation.

Aim

In order to appropriately assess the kinetics of Gem uptake, the complicating factor of its rapid intracellular metabolism needs to be controlled. GNP-based drug delivery system holds great potential to overcome some of the barriers to efficient targeting of cells in cancer treatment. The drug-loaded GNP formulations transport to the nucleus resulting in the release higher doses of drug for prolonged period of time and expression of certain genes that control cell proliferation. Also, the therapeutic effects produce by laser-induced phototehrmal therapy mediated by GNPs as one of the most effective heat conversion agents give the benefits of combining GNP-mediated phototehrmal therapy with other treatment strategies for multimodal cancer treatment to improved patient outcomes.

This research is focused on the development of a nanomedicine-mediated drug delivery strategy by designing a system for combined chemo- and photothermal therapy. It includes:

a) The synthesis of well-defined thiol-terminated poly (ethylene glycol) methacrylate homopolymers *via* Reversible Addition-Fragmentation Chain Transfer (RAFT) polymerisation in order to coat the surface of GNPs to reduce protein adsorption and provide biocompatibility.

b) Synthesis and characterisation of thiol-functionalised gold nanoshells as nano-carriers for Gem delivery to increase cytotoxic activity and drug delivery efficiency of Gem.

c) Develop a combinational chemo- phototherapeutic protocol to treat pancreatic cancer cells and explore the possible synergism effects of drug cytotoxicity and photothermal treatment by laser irradiation.

Chapter 2

Reversible Addition-Fragmentation Chain Transfer (RAFT) polymerisation of poly (ethylene glycol) methyl ether methacrylate(M_n = 300 g mol^{-1}, PEGMA) monomer

The well-defined hydrophilic polymers with anti-fouling properties were synthesised and used as a hydrophilic coating of the nanoformulations in order to diminish their non-specific association with proteins, cells or microorganisms in physiological fluids and tissues and also to enhance their colloidal stability. Among all the hydrophilic synthetic polymers designed for the aforementioned application, poly(ethylene glycol)(PEG) appears to be the best candidate as it is non-toxic, non-immunogenetic, non-antigenetic, biocompatible and FDA approved for biomedical applications (Jokerst *et al.*, 2011). Indeed, PEG can be present on the side chain of a methacrylate backbone (PEGylated methacrylate) to yield a more sophisticated and processable material. Herein, poly (ethylene glycol) methyl ether methacrylate (M_n = 300 g mol^{-1}, PEGMA) used as the monomer for the synthesis of well-defined thiol-terminated homopolymer chains *via* RAFT polymerisation.

2.1. Introduction

2.1.1. Reversible Addition-Fragmentation Chain Transfer (RAFT) polymerisation

Free radical polymerisation is the most common synthetic method for the commercial production of high-molecular weight polymers due to:

- Its high tolerance against a wide range of monomers and functional groups.
- Its compatibility with a variety of reaction conditions and,
- Its simplicity.

However, occurrence of bimolecular termination reactions, viz. recombination

and disproportionation of free radicals limits the control that can be asserted over molecular-weight distribution, co-polymer composition, and macromolecular architecture (Moad *et al.*, 2008a; 2008b; 2013).

In comparison, living / controlled radical polymerisation (CRP) techniques allow for the synthesis of polymers with well-defined structure, precise molecular weight and low polydispersity since the side reactions such as irreversible chain transfer and chain termination are virtually eliminated; "living" polymer chains continue their growth at the same rate by the provision of additional monomers to the system.

CRP permits reversible termination of propagating free radicals based on the establishment of a rapid dynamic equilibration between a minor amount of active propagating chains and a large majority of dormant chains. CRP is suitable for synthesising polymers with exquisitely controlled molecular weight and chain length distribution compared to that of free radical polymerisation. Three of the most investigated CRP techniques are:

- Nitroxide Mediated Living Free Radical Polymerisations (NMP),
- Atom Transfer Radical Polymerisations (ATRP), and
- Reversible Addition-Fragmentation Chain Transfer (RAFT) polymerisation.

The NMP was developed at the Commonwealth Scientific and Industrial Research Organisation (CSIRO) of Australia in the early 1980s and has been exploited extensively for the synthesis of styrenic and acrylic polymers. However, NMP is only applicable to a restricted range of monomers (Hawker *et al.*, 2001; Studer and Schulte, 2005; Nesvadba, 2006). ATRP is substantially more versatile and proved to be applicable to much broader range of monomers than NMP. Nevertheless, it requires high concentration of transition-metal catalyst (e.g. copper I/II), which is retained in the final product and has to be removed from the polymer (Kamigaito *et al.*, 2001; Matyjaszewski and Xia, 2001; Jakubowski *et al.*, 2006).

The RAFT polymerisation process is certainly the most robust and versatile method of the controlled radical systems. The radical addition-fragmentation process using thiocarbonylthio compounds was first demonstrated at CSIRO in 1998 by Moad and co-workers (Chiefari *et al.*, 1998). The most significant advantage of RAFT process is the compatibility of this technique with a wide range of monomers, such as (meth-)acrylates, (meth-)acrylamides, acrylonitrile, styrene and its derivatives, butadiene, vinyl acetate and N-vinylpyrrolidone. In addition, suitability for a broad range of functional groups and reaction conditions, and high tolerance to various organic and aqueous solvents enable RAFT to be used for the synthesis of various types of highly controlled polymers with predetermined molecular weight, narrow polydispersity and novel architectures (Moad *et al.,* 2008a).

In principle, RAFT polymerisation is a degenerative chain transfer process that is mediated by thiocarbonylthio compounds, which are also, referred to as RAFT agents or more generally, chain transfer agents (CTA) (e.g. dithioesters, trithiocarbonates, dithiocarbamates and xanthates).

An efficient RAFT process depends on the appropriate choice of CTA for the specific monomer and reaction conditions. The RAFT agents are unsaturated organic compounds that possess thiocarbonylthio moiety (S=C−S), R-group and Z-group (Figure 2.1) (Moad *et al.,* 2005), where,

- The C=S double bond is reactive towards radical addition and imparts the living behaviour of free radical polymerisation.
- Z-group is the activating agent that controls the reactivity of the double bond towards radical addition and fragmentation and modifies the stability of the intermediate radicals.
- R-group is the free radical homolytic leaving group which is responsible for re-initiating the polymerisation.
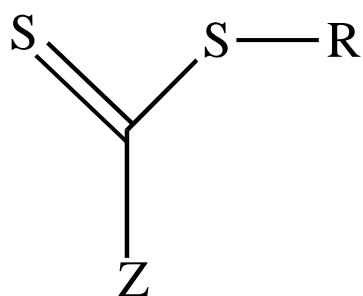
Z = aryl or alkyl (dithioester), NR$_2$ (dithiocarbamate), OR (xanthate), SR (trithiocarbonate). **R** = alkyl or H.

Figure 2.1. The general structure of the RAFT agent.

The mechanism of RAFT polymerisation consists of: initiation (I), pre-equilibrium (II), reinitiation (III), addition–fragmentation equilibrium (main equilibrium) (IV), and bimolecular termination reactions (V) (Figure 2.2).

The reaction is initiated by the thermal decomposition of RAFT initiators such as azobis(isobutyronitrile) (AIBN) and 4,4'-azobis(4-cyanovaleric acid) (ACVA). The free radical initiators react with the monomer molecules and generate active propagating chains (I). The addition of the propagating radical (P$_n$•) to the RAFT chain transfer agent (RSC(Z)=S) and fragmentation of the intermediate radical produces a polymeric RAFT agent (P$_n$SC(Z)=S) and a new radical (R•) (II). The homolytic leaving group radical (R•) reacts with another monomer species and reinitiates the polymerisation by forming a new propagating radical (P$_m$•) (III).

The highly active propagating radicals can chain transfer to dormant dicarbonylthio compounds that are stable and unable to propagate or terminate. This constant interchange between a small population of propagating radicals with much larger population of the dormant species should be fast relative to propagation rate.

73

In the main equilibrium of the RAFT process, rapid central addition-fragmentation equilibrium between propagating radical polymer chains ($P_n\bullet$, $P_m\bullet$) and the corresponding dormant thiocarbonylthio-bound chains provides uniform chain growth, resulting in polymers with narrow molecular weight distribution (IV).

Ideally, the equilibrium should be shifted towards the dormant products in order to keep the radical concentration extremely low, thereby suppressing the irreversible termination reactions, such as combination or disproportionation (V) (Moad *et al.*, 2008a; 2008b; 2013).
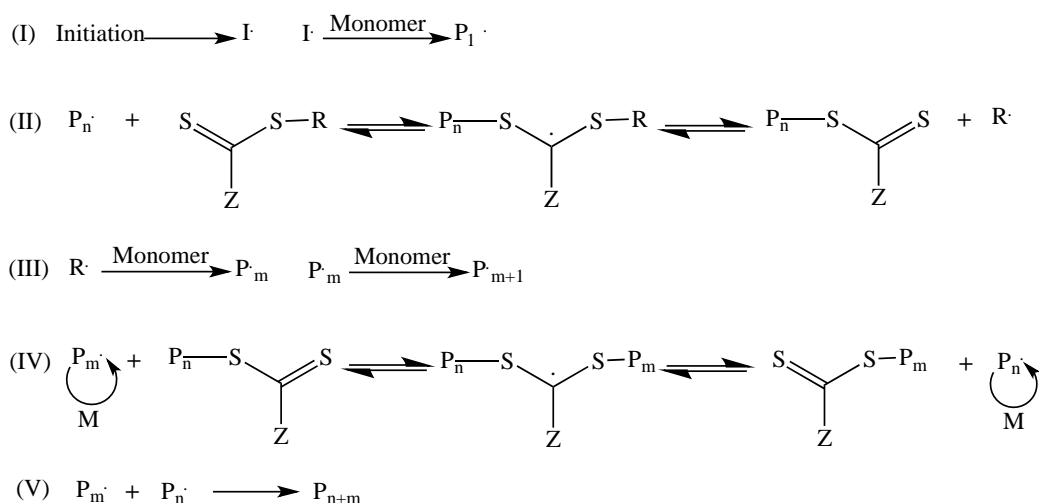
Figure 2.2. Mechanism of Reversible Addition-Fragmentation Chain Transfer (RAFT) process.

Furthermore, polymeric products may be colored depending on the absorption spectrum of the particular thiocarbonylthio chromophore. The removal or transformation of the thiocarbonyl end group from RAFT polymers therefore can mitigate or eliminate these disadvantages and enhance the stability and functionality of the polymer (Chong *et al.*, 2007). Various methods for the end group removal or transformation are: reaction with nucleophiles (aminolysis) (Shen *et al.*, 2010), thermal elimination (thermolysis) (Chong *et al.,* 2006), radical-induced reactions (reduction or elimination) (Chong and Thang, 2007) and hydrolysis (Aqil *et al.*, 2008) (Figure 2.3).
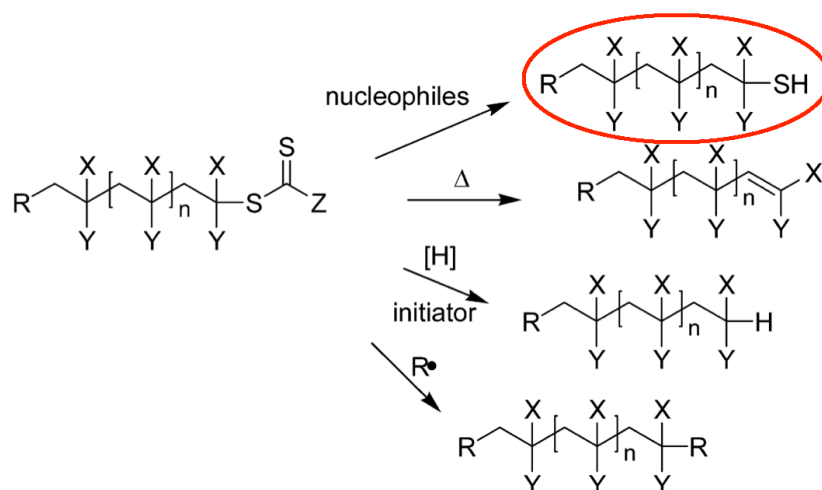
Figure 2.3. Processes for end group removal/transformation ([H] = H Atom Donor). Among all, the nucleophilic aminolysis is an efficient method for the production of thiolated polymers (Chong *et al*, 2007).

The nucleophilic aminolysis of thiocarbonylthio-terminated RAFT polymers, which results in the production of highly reactive polymer thiols, is one of the most effective approaches among all the above-mentioned methods of RAFT polymer end group modification. Shen *et al*. demonstrated a fast and effective conversion of CTA end-capped polymers to thiol end-capped polymers via the nucleophilic aminolysis method using hydrazine (Shen *et al.,* 2010) (Figure 2.4). Hydrazine is a strong nucleophile with a small steric hindrance compared to common primary amines (e.g. butylamine and hexylamine) used for nucleophilic aminolysis (Minegishi and Mayr, 2003). It consists of two equivalent amine groups, which enhance the collision chances with CTAs during aminolysis. In addition, it is capable of cleaving disulfides (Maiti *et al.,* 1988).
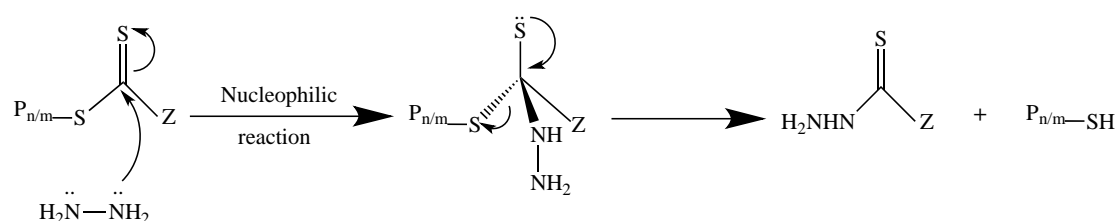
Figure 2.4. The nucleophilic aminolysis of thiocarbonylthio-terminated RAFT polymer with hydrazine for the generation of thio-terminated polymer (Wu *et al.*, 2014).

2.2. Materials

2,2′-azobis (2-methylpropionitrile) (AIBN), 4-cyano-4-[(dodecylsulfanyl thiocarbonyl) sulfanyl] pentanoic acid (CTA/RAFT agent), 1,4-dioxacyclohexane, dimethylformamide (DMF), hexane, and methanol, poly (ethylene glycol) methyl ether methacrylate (M_n = 300 g mol^{-1}) (PEGMA), sodium tetrafluoroborate. All the chemicals and solvents were purchased from Sigma-Aldrich and used without further purification. Distilled water (dH$_2$O) was used for all of the experiments.

2.3. Methods

This section of the research report describes the experimental details on the synthesis and characterisation of thiol-terminated poly (ethylene glycol) methyl ether methacrylate polymers. The targeted degrees of polymerisation were 10, 50 and 100.

2.3.1. Synthesis of poly (ethylene glycol) methacrylate polymer by RAFT polymerisation

Typically, poly(ethylene glycol) methyl ether methacrylate (M_n = 300 g mol^{-1}) (PEGMA) monomer (1 g, 3.333 mmol), 4-Cyano-4-[(dodecylsulfanylthiocarbonyl)sulfanyl]pentanoic acid (CTA/RAFT agent, M_w = 403.67 g mol^{-1}), 2,2′-Azobis(2-methylpropionitrile) (AIBN) (initiator, M_w = 164.21 g mol^{-1}) and dioxane solvent (10 mL) were introduced into a single-neck round-bottom flask (25 mL). The reaction mixture was sealed with a rubber septum and purged with argon for 30 min and then placed in a preheated oil bath at 70 °C for 17 h under magnetic stirring. The reaction was stopped by exposure to air at room temperarture and the polymer was precipitated in excess hexane (100 mL) in order to dissolve the unreacted monomers. Then, the precipitated polymer was dissolved in acetone, dried under reduced pressure and collected as a yellowish viscous liquid.

The three different degrees of polymerisation (DP = 10, 50 and 100) of a PEGMA homopolymer were determined using equation 2.1. and 2.2 :

Equation 2.1.

$$Degree\ of\ polymerisation\ (DP) =\ moles\ of\ monomer\ /moles\ of\ CTA$$

Equation 2.2.

$$Number\ of\ moles =\ Mass/Molar\ mass$$

The degree of polymerisation (DP) is defined as the average number of monomer molecules per polymer chain (Moad *et al.*, 2007).

2.3.2. Aminolysis of RAFT-synthesised polymer

The removal of the thiocarbonyl end group from the P(PEGMA) was conducted under ambient temperature, following the protocol described by Shen *et al.* (Shen *et al.*, 2010).

The P(PEGMA) was dissolved in methanol at a concentration of 0.004 M in a single-neck round-bottom flask (25 mL). Hydrazine (M_w = 50.06 g mol^{-1}) was added to the solution and the reaction mixture was allowed to stir at room temperature until the appearance of clear solution. The resulted mixture was dialysed for two days against distilled water using dialysis tubing with MWCO of 1 kDa. The thiolated polymer was dried using rotary evaporator (Buchi) and collected as a colorless viscous liquid.

2.3.3. Polymer characterisation

The physical-chemical properties of the synthesised polymers were evaluated by performing the following characterisation techniques:

- Nuclear Magnetic Resonance spectroscopy (NMR)
- Gel permeation chromatography (GPC)
- Ultraviolet–visible spectroscopy (UV-Vis)

2.3.4.1. Nuclear Magnetic Resonance (NMR)

Nuclear Magnetic Resonance (NMR) is a nuclei specific spectroscopy method, which uses intense magnetic fields to perform analytical experiments on the nuclei of atoms and elucidates the chemical structure of an analyte. The NMR technique is based on the resonance of the electromagnetic radiation in the radio frequency region (4-900 MHz) by the nuclei of the atoms. Upon strong external magnetic field (B_0) application, atomic nuclei (^{1}H, ^{13}C, ^{31}P, ^{15}N, ^{19}F, etc.) undergo spin state energy separations, and populate the nuclear spin states with either lower energy level (aligned with B_0) or higher energy level (aligned against B_0). As the nuclei magnetic moments relax back to equilibrium with the applied magnetic field, the transition frequencies (resonance frequencies) are recorded and monitored by NMR spectroscopy. The NMR spectrum is a plot of signal intensity *versus* resonance frequency (also known as chemical shift, δ) with unit of parts per million (ppm) in reference to a standard molecule tetramethylsilane (TMS) having the chemical formula $Si(CH_3)_4$. The chemical shift of TMS singlet is assigned as *δ* 0, and all other chemical shifts are determined relative to the standard (Becker, 1999). ^{1}H NMR spectra were recorded on a Bruker NMR spectrometer (Ultrashield 400 MHz). ^{1}H NMR was performed to characterise the chemical composition of the synthesised polymers. The ^{1}H NMR samples were prepared by dissolving 5 mg of the synthesised polymer in 0.6 mL of dimethyl sulfoxide-d6 (DMSO-d_6).

2.3.4.2. Gel permeation chromatography (GPC)

The average molecular weights (M_n) and weight-average molecular weights (M_w), and dispersity $Đ_M$ of the synthesised polymers were measured by using a Viscotek Gel Permeation Chromatography (GPC) system equipped with a solvent pump (Viscotek VE 1121), a degasser (Viscotek VE 7510), two Styragel columns (MGH$_{HR}$-M E0057 and MGH$_{HR}$-M E0058) and a refractive index detector (Viscotek VE 3580). Dimethylformamide (DMF) containing sodium tetrafluoroborate (5 mM) was used as the mobile phase at 70 °C at a flow rate of 1 mL min^{-1}. Linear poly(methyl methacrylate) polymers with narrow molecular weight distributions were used as standards to calibrate the apparatus (conventional calibration). The GPC aliquots were prepared by dissolving 5 mg of the synthesised polymer in 1 mL of DMF.

Similar to other types of the liquid chromatography, gel permeation chromatography (GPC), also referred to as size exclusion chromatography (SEC), comprises solid stationary and liquid mobile phase. The prepared GPC sample is injected into the mobile phase and pumped through the GPC column. The separation mechanism in the stationary phase of a column is based on the hydrodynamic size of each polymer molecule with the larger molecules eluting first. The column gels contain porous beads with controlled porosity and particle size that are tightly packed together. The small analytes spend more time permeating across the porous matrix of the column; therefore their retention time increases. Conversely, larger molecules have shorter retention time, as they are unable to permeate through all of the pores. Detectors (i.e. refractive index, UV-Vis, light scattering and viscometer) monitor and record the separation process. The GPC software collects and collates the data and calculates the relative molecular weight values of the analytes by reference to their retention time using the method of conventional calibration (Moore, 1964; Skoog, 2006).

2.3.4.3. Ultraviolet–visible spectroscopy

UV-Visible spectroscopy was conducted to confirm the disappearance of the thiocarbonyl end group absorption band after aminolysis of the synthesised polymers. The absorption spectra were obtained in a plastic cuvette at 25 °C by an Agilent Cary series UV-Vis spectrophotometer in the wavelength range between 400-800 nm. The samples were prepared by dissolving 5 mg of the synthesised polymer in 1 mL of methanol.

In UV-Vis spectroscopy, the amount of the light with different wavelength passing through the sample, so called as transmittance (T), is calculated using equation 2.3:

Equation 2.3

$$T = I/I_0$$

Where, I_0 and I are the incident and transmitted light intensities, respectively.

The absorbance of the sample (A) is measured from the determined percentage transmittance (T% = T × 100) (Equation 2.4):

Equation 2.4

$$A = log_{10} \, T\%^{-1}$$

The Beer-Lambert law suggests that the amount of radiation absorbed at a specific wavelength is directly proportional to the concentration of the solution (Equation 2.5) (Ricci *et al.* 1994):

Equation 2.5.

$$A = log_{10} (I_0/I) = \varepsilon CL$$

Where,   A is the absorbance (optical density) in arbitrary unit

ε is the molar absorptivity or the molar extinction coefficient (constant for each type of molecule at each wavelength), L mol^{-1} cm^{-1}

C is the concentration of nanoparticles, mol L^{-1}

L is the path length, cm

An absorption spectrum is the plot of the absorbance versus the wavelength of the incident light.

2.4. Results and Discussion

Results of this chapter were obtained after series of laboratory experiments and data analysis. Each individual section corresponds to the sections given in materials and methods.

Anti-fouling water soluble homopolymers of poly(ethylene glycol) methyl ether methacrylate (P(PEGMA)) with three different target degree of polymerisation (DP) of 10, 50 and 100 were synthesised *via* RAFT polymerisation. The reaction conditions are summarised in Table 2.1 and the synthetic route of the polymer is given in Figure 2.5.

Table 2.1. Reaction conditions for the RAFT polymerisation of PEGMA.

Monomer		Degree of polymerisation (DP)	CTA		AIBN		Organic solvent
mmol	mg		$\times 10^{-3}$ mmol	mg	$\times 10^{-3}$ mmol	mg	mL
		10	333.00	134.42	33.30	5.50	
3.33	1000	50	66.60	26.88	6.66	1.10	10
		100	33.00	13.32	3.33	0.55	

Note: The amount of CTA and AIBN were calculated using Equation 2.1 and 2.2.
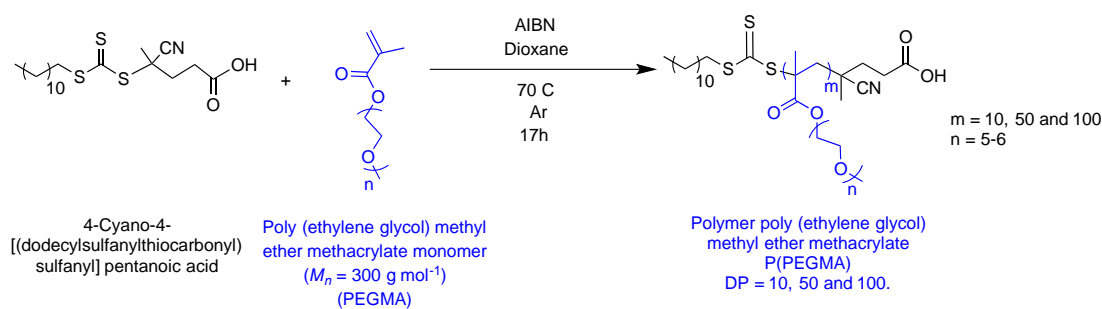
Figure 2.5. Schematic for the synthesis of P(PEGMA) RAFT polymerisation.

The reactions were quenched after 17 h and the synthesised P(PEGMA) were purified in hexane and dried under reduced pressure. The products obtained (Figure 2.6) were transparent viscous liquids with different hues of yellow due to the presence of the RAFT agent end-capping; the respective targeted degree of polymerisation (DP) of 10, 50 and 100 are referred to as P(PEGMA)10, P(PEGMA)50, and P(PEGMA)100.
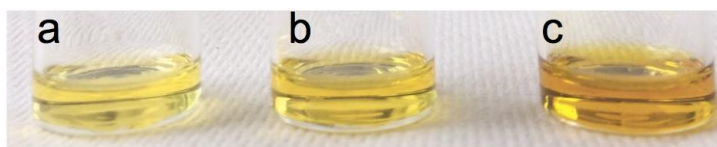
Figure 2.6. Digital photographs of samples of P(PEGMA)100 (a), P(PEGMA)50 (b) and P(PEGMA)10 (c).

The percent yield of the RAFT polymerisation reaction is the ratio between the actual mass of the products and mass of the reactants expressed in percentage rates. The percent yield was determined using equation 2.6:

Equation 2.6.

$$Percent\ Yield = \frac{Mass\ of\ the\ synthesised\ P(PEGMA)}{Mass\ of\ the\ reactant\ (monomer + RAFT\ agent)} \times 100$$

83

The percent yields were calculated for P(PEGMA)10 , P(PEGMA)50 and P(PEGMA)100 using equation 2.6.

P(PEGMA300)10 → [(930.5 mg) / (1000 mg + 134.42 mg)] x 100 = % 82

P(PEGMA300)50 → [(921.5 mg) / (1000 mg + 26.76 mg)] x 100 = % 90

P(PEGMA300)100→ [(835.5 mg) / (1000 mg + 13.42 mg)] x 100 = % 82

The products were obtained with good yield that was calculated to be 82%, 90%, and 82% for P(PEGMA)10 , P(PEGMA)50 and P(PEGMA)100, respectively.
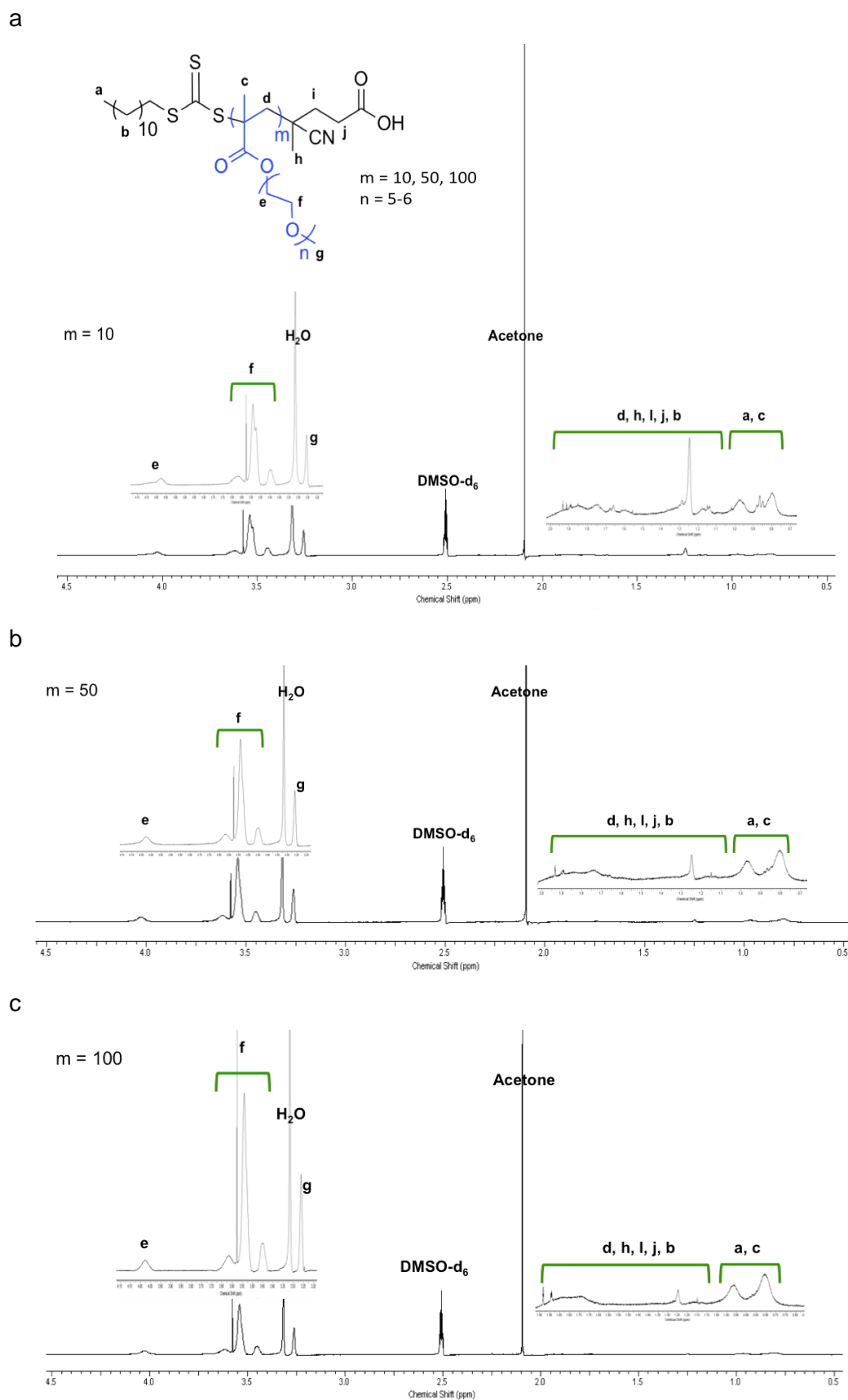
Figure 2.7. ^{1}H NMR (400 MHz, d₆-DMSO) spectrums of P(PEGMA)10 (a), P(PEGMA)50 (b) and P(PEGMA)100 (c).

^{1}H NMR spectra of P(PEGMA)10 , P(PEGMA)50 and P(PEGMA)100 are presented in Figure 2.7.

The broad ^{1}H NMR resonance signals in upfield at approximately δ = 0.75 ppm and δ = 1.10 ppm (c) are attributed to the methyl protons (-CH$_3$) of the polymer backbone. The appearance of a broader signal with low intensity (d) at about δ = 1.11 ppm to 1.95 ppm is ascribed to the methylene group (-CH$_2$) of the polymer backbone. The chemical shifts at approximately δ = 3.40 ppm to 3.65 ppm (f) and δ = 4 ppm (e) correspond to methylene groups in the polymer chains. The methyl groups of each pendant PEGMA chain (g) had chemical shift at 3.25 ppm. Due to bonding to the electronegative oxygen atom, the assigned methylene (e and f) and methyl (g) groups are deshielded to the higher resonance frequency (downfield shift). The ^{1}H NMR spectrum of the resultant polymer did not clearly show the proton resonance signals corresponding to the RAFT agent since the RAFT end groups of the polymer backbone ^{1}H-NMR signals (a, b, h, j and i) overlapped with peaks assigned to the methyl and methylene protons of the polymer backbone at approximately δ = 0.75 - 1.95 ppm.

The monomer conversion (%) calculated by comparing the integral area of the remaining unreacted monomers at δ = 5.7 ppm and δ = 6.1 ppm to the terminal methyl of the polymer at δ = 3.25 ppm after 17 h of polymerisation, using the equation 2.7:

Equation 2.7.

$$^{1}HNMR \; monomer \; conversion = \frac{1H_p}{1H_p \; + \; 1H_m} \times 100$$

Where, $1H_p$ and $1H_m$ represents the integral per proton values of the obtained polymer and the unreacted monomers, respectively.

Figure 2.8 is shown the decrease in intensity of the vinylic =CH$_2$ proton resonance signal in the range of δ = 5.5 ppm - 6.3 ppm after polymerisation (before purification), which is verified the monomer conversion for P(PEGMA)100.
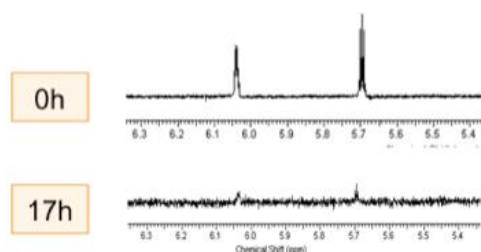
Figure 2.8. Disappearance of chemical shift of the vinylic protons (two distinct resonance peak due to spin-spin splitting) at δ = 5.7 ppm and 6.1 ppm is confirmed the monomer consumption after RAFT polymerisation of P(PEGMA)100.

^{1}HNMR monomer conversion (%) was calculated to be 92%, 87% and 94% for P(PEGMA)10 , P(PEGMA)50 and P(PEGMA)100, respectively

The number-average molecular weight (M_n), weight-average molecular weight (M_w) and molar mass dispersity (M_w/ M_n, represented as $Ð_M$) of the polymers were analysed by gel permeation chromatography (GPC) using the conventional calibration method with poly(methyl methacrylate) (PMMA) standards. The GPC traces of the polymers P(PEGMA)10, P(PEGMA)50 and P(PEGMA)100 are shown in Figure 2.9. The GPC chromatogram displayed uni-modal and symmetric peaks with a clear shift to lower elution volumes as a function of the DP.

The M_n of the P(PEGMA) was found to be 5 200 g mol^{-1} , 15 300 g mol^{-1} and 29 300 g mol^{-1} for P(PEGMA)10, P(PEGMA)50 and P(PEGMA)100, respectively. The M_n values obtained by GPC were in good agreement with the theoritical M_n calculated from ^{1}HNMR monomer conversion (Table 2.2). Theoritical M_n calculation from ^{1}HNMR monomer conversion is presented in Appendix 1.

In all cases, the $Ð_M$ values were equal or lower than 1.30, indicating a narrow molecular weight distribution and well-controlled polymerisation (Table 2.2).

The underlying principle of separation on the basis of polymer hydrodynamic volume, utilising polymer standards (PMMA) with the same molecular weight but different hydrodynamic volumes from that of resultants was making the method susceptible to errors.
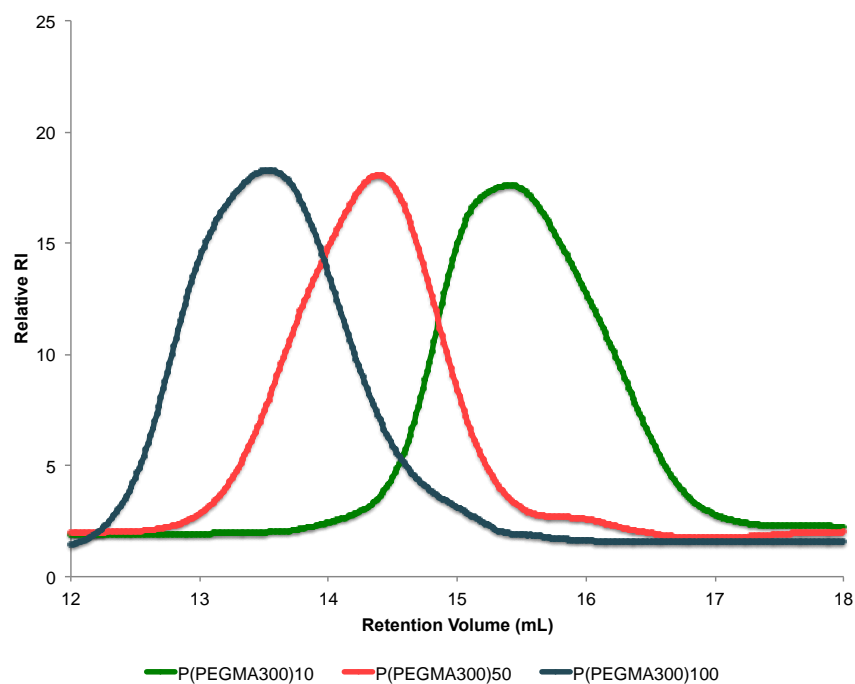
Figure 2.9. RI traces as recorded by GPC showing molecular weight distribution of the P(PEGMA)10 (green), P(PEGMA)50 (red) and P(PEGMA)100 (blue).

Table 2.2. Theoretical M_n, and M_n and $Đ_M$ of P(PEGMA)10, P(PEGMA)50 and P(PEGMA)100 determined by GPC analysis.

DP	Theoritical M_n (g mol^{-1})	M_n (g mol^{-1})	$Đ_M$
10	3 200	5 200	1.30
50	13 600	15 300	1.30
100	28 600	29 300	1.20

Then, the polymers underwent aminolysis reaction with hydrazine in methanol (Table 2.3) in order to produce thiol-termini for subsequent attachment with GNPs (Shen *et al.*, 2010) (Figure 2.10). The details of the nucleophilic aminolysis of the thiocarbonylthio-terminated RAFT polymers have been described in section 2.1.

Table 2.3. Reaction conditions for the aminolysis of P(PEGMA).

Synthesised polymer		Hydrazine		Methanol (mL)
polymers	mg	$\times 10^{-5}$ mmol	μL	
P(PEGMA)10	500	100	47	25.00
P(PEGMA)50	500	33	16	8.25
P(PEGMA)100	500	17	8.3	4.25

Poly (ethylene glycol) methyl
ether methacrylate polymer
P(PEGMA)

Thiol-terminated poly
(ethylene glycol) methyl ether
methacrylate polymer
SH-P(PEGMA)
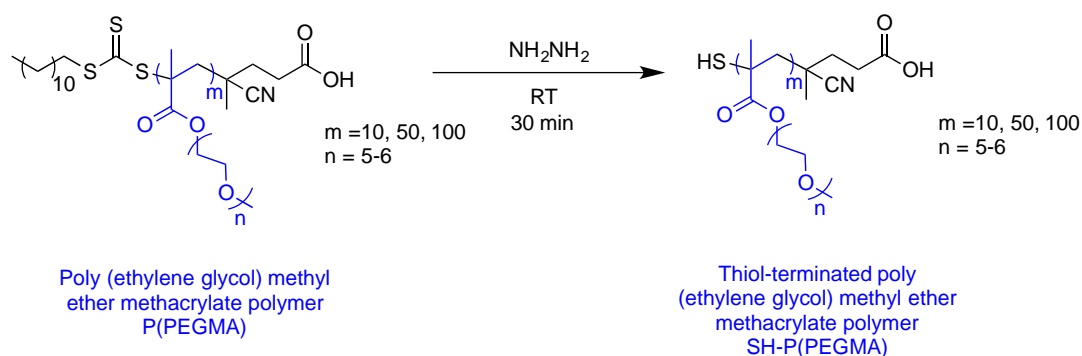
Figure 2.10. The nucleophilic aminolysis of thiocarbonylthio-terminated P(PEGMA) with hadrazine to generate of thio-terminated polymers (SH-P(PEGMA)).

The resulted mixture was dialysed for two days against dH₂O using dialysis tubing with MWCO of 1 kDa. The polymers were dried under reduced pressure and collected as a transparent viscous liquid (Figure 2.11). The yield percent was calculated to be 90%, 85%, and 72% for SH-P(PEGMA)10 , SH-P(PEGMA)50 and SH-P(PEGMA)100), respectively.
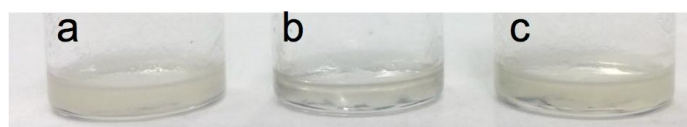
Figure 2.11. Digital photographs of SH-P(PEGMA)10 (a), SH-P(PEGMA)50 (b) and SH-P(PEGMA)100 (c).

Figure 2.12 displays the UV-Vis spectra of P(PEGMA)10, P(PEGMA)50 and P(PEGMA)100 before and after aminolysis. The P(PEGMA) showed an absorption band at 440 nm, which is indicated the presence of trithiocarbonate end groups (Shen *et al.,* 2010). The complete disappearance of the absorption band after aminolysis is indicated the quantitative cleavage of the RAFT end groups and the formation of the thiol-terminated polymers (SH-P(PEGMA)10 , SH-P(PEGMA)50 and SH-P(PEGMA)100).
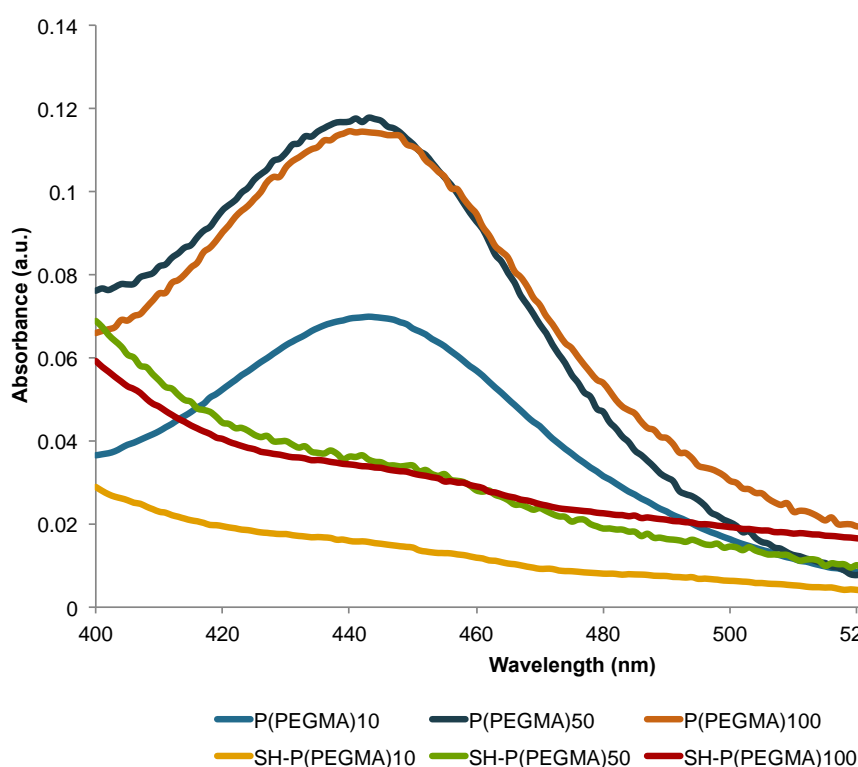
Figure 2.12. Comparison of the absorption spectrum of P(PEGMA)10, P(PEGMA)50 and P(PEGMA)100 before and after aminolysis.

The ^{1}H-NMR spectrum of the resultant thiol-terminated polymer showed no significant chemical shift or peak area change related to the cleavage of thiocarbonylthio group due to the overlap of peaks in the ^{1}H-NMR signals assigned to the cleaved thiocarbonylthio group and methyl and methylene protons of the polymer backbone (Figure 2.13).

a

m = 10

m = 50

m = 100
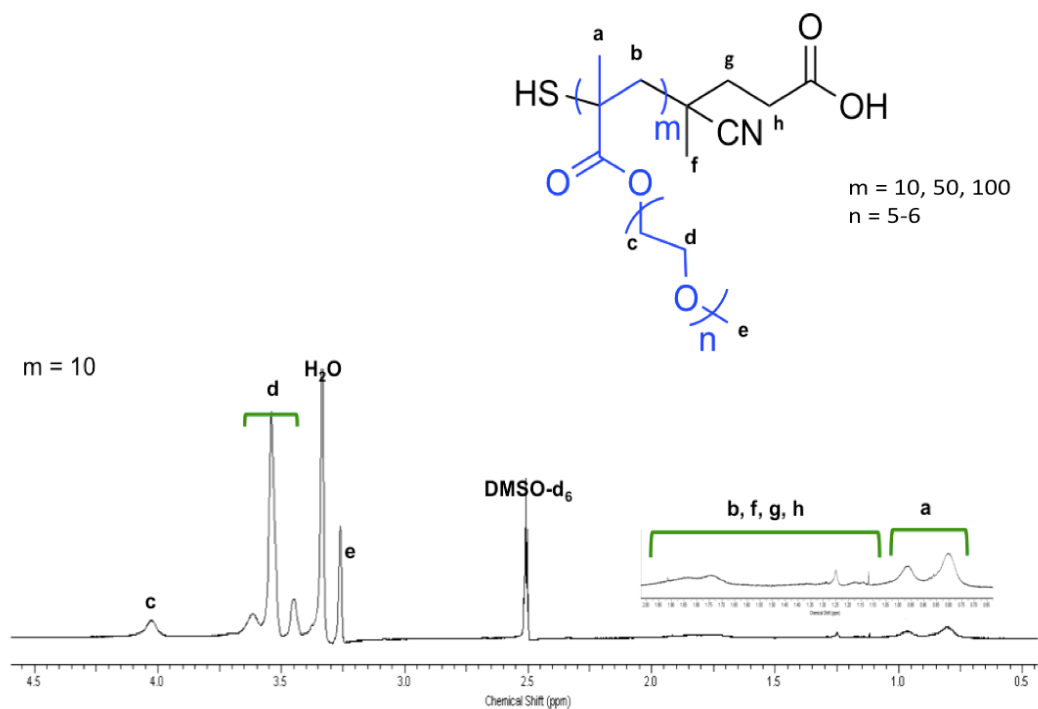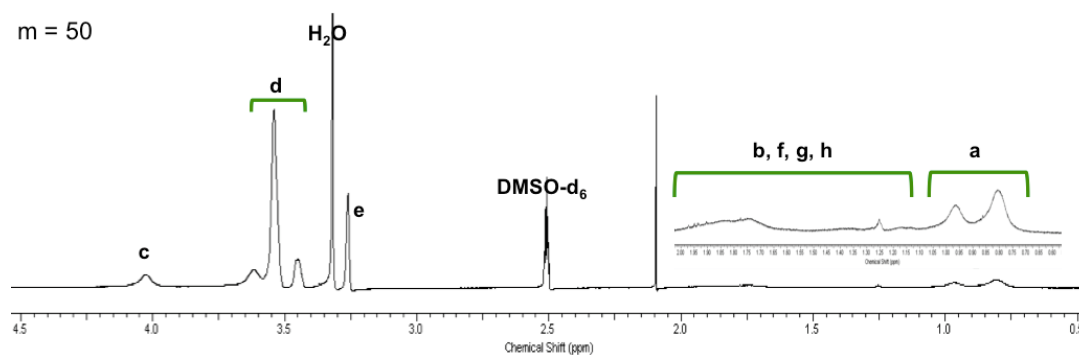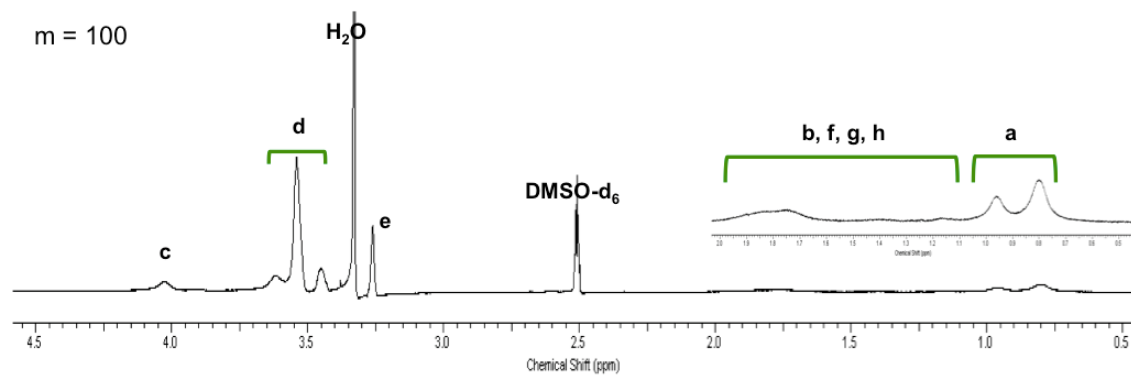
Figure 2.13. ^{1}H NMR (400 MHz, d_6-DMSO) spectrum of SH-P(PEGMA)10 (a), SH-P(PEGMA)50 (b) and SH-P(PEGMA)100 (c).

Compared to the originally synthesised P(PEGMA), the GPC traces of SH-P(PEGMA) displayed a clear shift towards higher retention times with symmetric distribution, implying a reduction of the molecular weight of the polymer P(PEGMA) due to the partial loss of the CTA. The M_n of the SH-P(PEGMA) was found to be 4 200 g mol^{-1} , 14 900 g mol^{-1} and 28 300 g mol^{-1} for SH-P(PEGMA)10, SH-P(PEGMA)50 and SH-P(PEGMA)100, respectively. The M_n values obtained by GPC were in good agreement with the theoritical M_n calculated from ^{1}HNMR monomer conversion (Table 2.4).

Table 2.4. Theoretical M_n, and M_n and $Đ_M$ of SH-P(PEGMA)10, SH-P(PEGMA)50 and SH-P(PEGMA)100 determined by GPC analysis.

DP	Theoritical M_n (g mol^{-1})	M_n (g mol^{-1})	$Đ_M$
10	3 000	4 200	1.30
50	13 400	14 900	1.20
100	28 000	28 300	1.30

Furthermore, the unimodal (one peak) symmetric distribution showed that the use of hydrazine prevented the formation of a disulphide bridge between two chains under the experimental conditions (Figure 2.14).
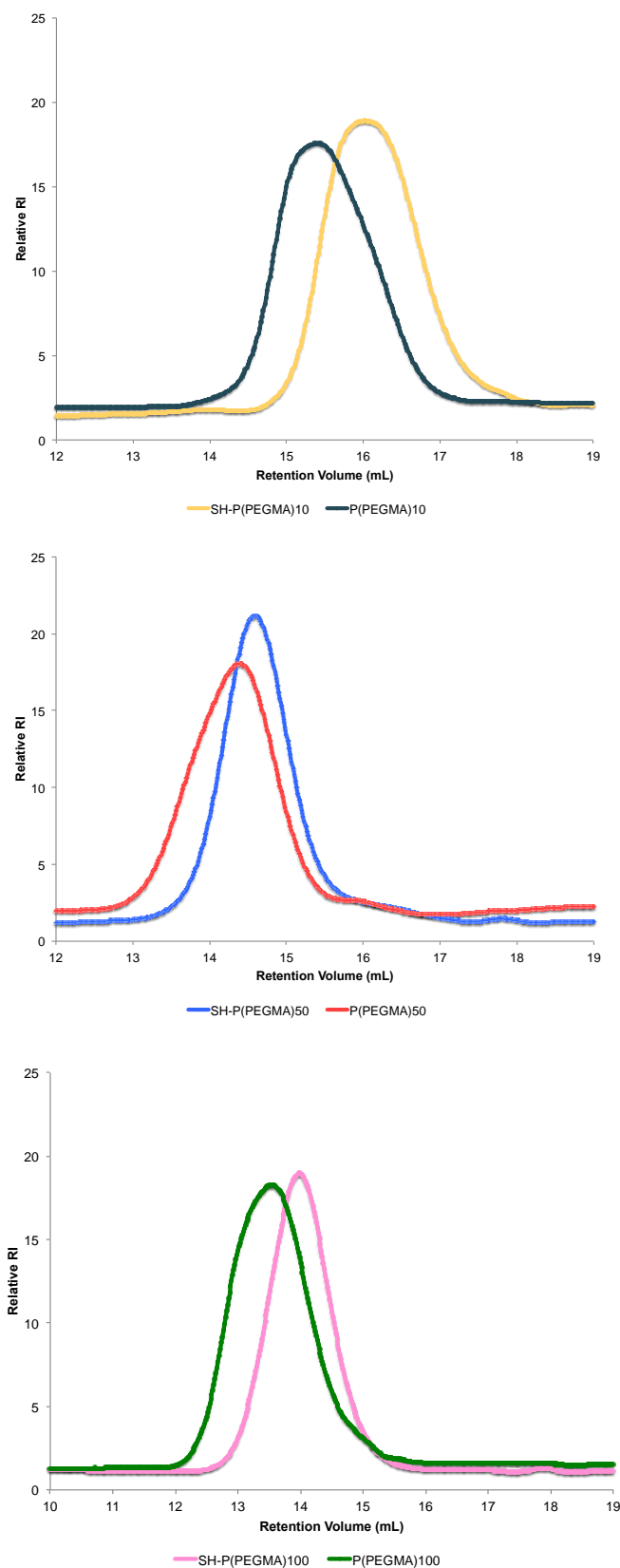
Figure 2.14. GPC traces of P(PEGMA)10, P(PEGMA)50 and P(PEGMA)100 and their corresponding thiol-capped functionalised polymers SH-P(PEGMA)10, SH-P(PEGMA)50 and SH-P(PEGMA)100.

2.5. Conclusion

The results support the successful synthesis of the P(PEGMA) polymer with the targeted degree of polymerisation of 10 (P(PEGMA)10), 50 (P(PEGMA)50) and 100 (P(PEGMA)100) by RAFT polymerisation. The synthesised polymers were further aminolysed to form thiol-capped polymers for binding to GNPs with high affinity by forming covalent Au-S bonds. The chemical composition of the polymers was successfully characterised by ^{1}H NMR and it was confirmed that the polymer products had well defined structure and predictable molecular weights according to the results obtained by GPC. Finally, characterisation of the thiol-capped products by GPC, and UV/Vis confirmed the successful synthesis of the thiol-rich polymers for further conjugation to GNPs.

The formulation properties of the as synthesised thiol-end P(PEGMA) with GNPs were compared with commercially available thiol-terminated methoxypoly (ethylene glycol) (PEG, M_n = 6000 g mol^{-1}, SH-PEG6000) in the following chapter.

Chapter 3

Formulation and characterisation of Gem-loaded GNShells for treatment of the pancreatic cancer

Drug toxicities can be mitigated through NP formulation, while simultaneously increasing tumor accumulation through the EPR effect. GNShells are spherical nanoparticles consisting of an ultrathin metallic layer and possess highly favourable optical and chemical properties for biomedical and therapeutic applications. Herein, GNShells (λ_{max} = 640 nm) were synthesised by a galvanic replacement reaction and coated with commercially available thiol-terminated methoxy poly (ethylene glycol) (PEG, M_n = 6000 g mol^{-1}, PEG6000) or RAFT synthesised thiol-terminated polymers of poly(ethylene glycol) methyl ether methacrylate with targeted degree of polymerisation of 10 (SH-P(PEGMA)10), 50 (SH-P(PEGMA)50) and 100 (SH-P(PEGMA)100) to reduce protein binding (opsonisation), increase hydrophilicity and stability, and extend the circulation half-life of the formulation. Further, drug loading was conventionally performed to protect Gem against rapid plasmatic metabolisation and also maintain the drug cytotoxicity at lower doses. Characteristics, such as size, shape, surface properties and drug loading, can affect therapeutic efficacy, biodistribution, pharmacokinetics and toxicity of the nano-formulations and hence full characterisation of the proposed system was performed. The successful surface functionalisation of the GNShells was investigated by means of ultraviolet-visible (UV-vis) spectroscopy, Raman spectroscopy, transmission electron microscopy (TEM), X-ray photoelectron spectroscopy (XPS), thermogravimetric analysis (TGA), as well as dynamic light scattering (DLS), and zeta (ξ) potential measurements. The effect of polymer chain length and surface density on drug loading efficacy, drug release and cytotoxicity of nanoformulation was also investigated via High-performance liquid chromatography (HPLC) and cell viability assay.

3.1. Introduction

3.1.1. GNShells mediated photothermal cancer therapy

Ultrathin hollow GNShells belong to a novel class of GNPs with distinctive optical properties (You *et al.*, 2010). They possess an adjustable plasmon absorption band that can be tuned to the red/NIR region where light has a negligible interaction with physiological media (water, blood and tissue) (Joshi and Wang, 2010). With such plasmonic properties, GNShells display efficient conversion of light into thermal energy upon exposure to moderately low laser-generated light thus they can be utilised as an intense laser light-absorber for photothermal cancer treatment (Chicheł *et al.,* 2007).

Following the first report on using GNShells for laser-induced thermal therapy by the Halas research group (Hirsch *et al.,* 2003), GNShells have attracted the attention of researchers as evidenced by the increasing number of publications (Figure 3.1).
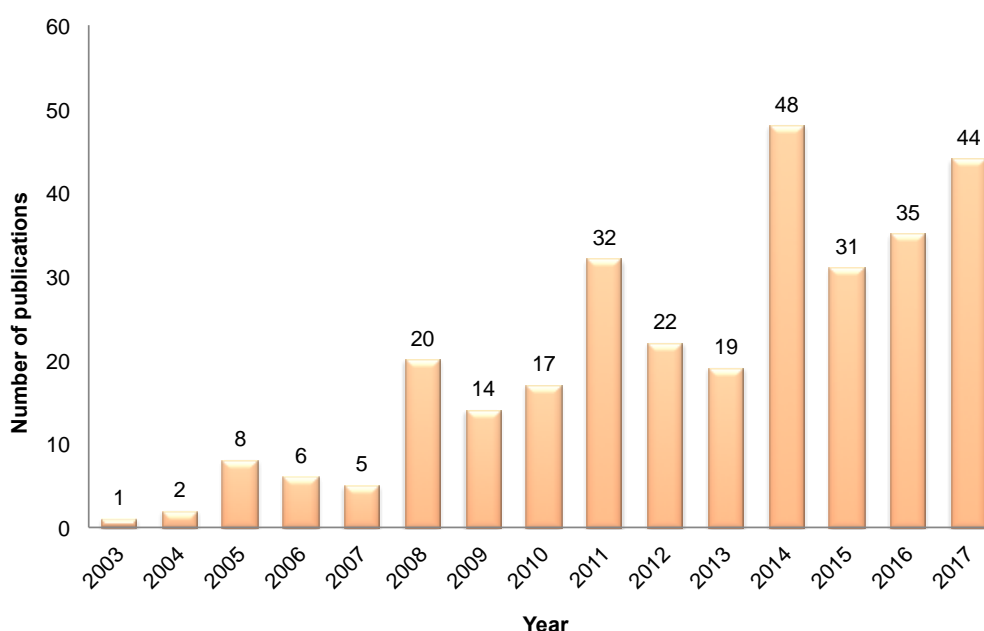
Figure 3.1.　Number of SciFinder Scholar references per year after the first publication on GNShells-mediated photothermal therapy in 2003 containing the search terms, gold nanoshell*, photothermal*, and cancer* as of December 2017.

In contrast to Indocyanine green which has an absorption cross section of $\approx$ 1.66×10^{-20} m^2, GNShells exploited favorably high optical absorption cross section of 3.8×10^{-14} m^2, which is over 10^6 times greater than that of the conventional dye (Hirsch *et al.*, 2003). Like the other types of GNPs, the rigid metallic structure of GNShells protects them against photobleaching, which is a major disadvantage of organic dyes. In addition, the pure and biologically inert gold composition of hollow GNShells facilitates their surface functionalisation with a wide variety of polymers, anti-cancer agents and biomolecules, which GNShells can deliver their diagnostic /or therapeutic payloads to targeted sites (Hirsch *et al.*, 2003; O'Neal *et al.*, 2004). Furthermore, there is no available evidence on the long-term (in years) cytotoxicity profile of GNShells (without conjugated drugs or laser radiation). However, growing evidence from numerous experimental animal studies indicates that GNShells are non-toxic and safe since no clinical sign of systemic toxicity or incidence of side effects have been reported months after treatments (Hirsch *et al.*, 2003; O'Neal *et al.*, 2004; Stern *et al.*, 2008). To date, among all GNPs, only nanoshell-mediated photothermal therapy has progressed from laboratory into clinic. In 2008, Nanospectra Bioscience commenced the first human clinical trial to test the GNShells photothermal therapy, commercially named as AuroLase® Therapy. The company, exclusively licensed from Rice University, works on NIR-resonant GNShells for the thermal destruction of solid tumors. Nanospectra has conducted pilot study under open Investigational Device Exemption (IDE) approved by the U.S. Food and Drug Administration (FDA) for the treatment of refractory head and neck as well as lung cancer (Table 3.1). There are scientific publications regarding AuroLase® Therapy for photothermal ablation, imaging and other commercial applications (Hirsch *et al.*, 2003; O'Neal *et al.*, 2004; Stern *et al.*, 2008; Schwartz *et al.*, 2009; Day *et al.*, 2010).

Table 3.1. Clinical study details as provided by Nanospectra Biosciences, Inc. (Clinicaltrials.gov. NCT00848042; NCT01679470; NCT02680535).

Clinical trials	Intervention	Brief summary	Resutls of clinical trials
Pilot study of AuroLase® Therapy in refractory and/or recurrent tumors of the head and neck. (NanospectraBiosciences, Inc., NCT00848042)	▪ Device: AuroLase® Therapy ▪ Enrollment: 11 ▪ Study start date: April 2008 Study completion date: August 2014	This pilot study was an open-label, multi-center, single-dose AuroLase™ Therapy for three treatment groups of five patients with refractory and/or recurrent head and neck tumors, who observed for six (6) months following treatment. The single dose of AuroShell™ particles infused into the blood stream of the patients followed by one or more interstitial illuminations with an 808 nm laser.	Primary end-point was not met.

A pilot study of AuroLase® Therapy in subjects with primary and/or metastatic lung tumors. (NanospectraBiosciences, Inc., NCT01679470)	▪ Device: AuroLase® Therapy ▪ Enrollment: 1 ▪ Study start date: October 2012 Study completion date: June 2014	This was an open-label, single-center, single-dose efficacy pilot study of AuroLase® Therapy in the treatment of primary and/or metastatic lung tumors. In this study patients were given a systemic IV infusion of AuroShell™ particles followed by escalating dose of laser radiation delivered by optical fiber via bronchoscopy.	Results have not yet been published
A study of MRI/US fusion imaging and biopsy in combination with nanoparticle directed focal therapy for ablation of prostate tissue. (NanospectraBiosciences, Inc., NCT02680535)	▪ Device: AuroLase® Therapy ▪ Enrollment: 45 ▪ Study start date: February 2016 Estimated study completion date: December 2018	This pilot study is an open-label, multi-center, single-dose AuroLase® Therapy for the focal ablation of neoplastic prostate tissue via nanoparticle directed irradiation. The AuroShell™ particles are infused intravenously 12 to 36 h prior to ultrasound-guided laser illumination using a FDA cleared laser and an interstitial optical fiber.	Results have not yet been published

3.1.2. Synthesis of GNShells

In 2002, Xia and co-workers developed the template galvanic replacement reaction to produce hollow metallic nanostructures with tunable size and absorbance profiles (Sun *et al.*, 2002).

The method proposed by Xia *et al.* is superior to the method of fabrication of silica core/gold shell nanoparticles (Hirsch *et al.,* 2003) and also to the methods that comprise the use of galvanic replacement reaction (e.g. sacrificial galvanic replacement of cobalt nanoparticles by Schwartzberg *et al.*). Xia's method is safer, simpler, highly reproducible, stable and produces small particles (≈ 20-60 nm) and is a true one-pot synthesis method. However, it does not produce extremely monodisperse hollow nanoparticles.
The synthesis of silica–gold core-shell nanoparticles pioneered by Halas research group (Hirsch *et al.*, 2003) is a time consuming and laborious process and the synthesised nanoshells are large in size (at least 100 nm). Besides, there are concerns about the biological effects of silica or its degradation products (Hirsch *et al.,* 2006).

In addition, the toxicity of cobalt and the air-sensitivity of the reaction are the two main drawbacks of the Schwartzberg technique (Schwartzberg *et al.*, 2006).

The galvanic replacement of the silver core with gold using small silver nanoparticles as sacrificial templates and gold ions as the galvanic replacement reagent is discussed in the following paragraphs.

3.1.3. Sacrificial silver sol

The monodisperse solid silver nanospheres can be synthesised via the Turkevich's seed-mediated growth mechanism. This method takes place in two stages: seed formation and growth (Kimling *et al.*, 2006; Wuithschick *et al.*, 2015).

At the seed stage, spherical seed nanoparticles are synthesised by reducing the silver salts ($Ag^+NO_3^-$) with sodium citrate along with the addition of sodium borohydride ($NaBH_4$), which is a strong reducing agent and accelerates the chemical reaction (Figure 3.2). Sodium citrate functions as both stabilising and mild reducing agent. The silver seed that is formed via this process at room temperature serves as a template for the growth mechanism (Kimling *et al.*, 2006; Wuithschick *et al.*, 2015).

Silver nitrate   Trisodium citrate   Sodium borohydride   Silver nanoparticle seed
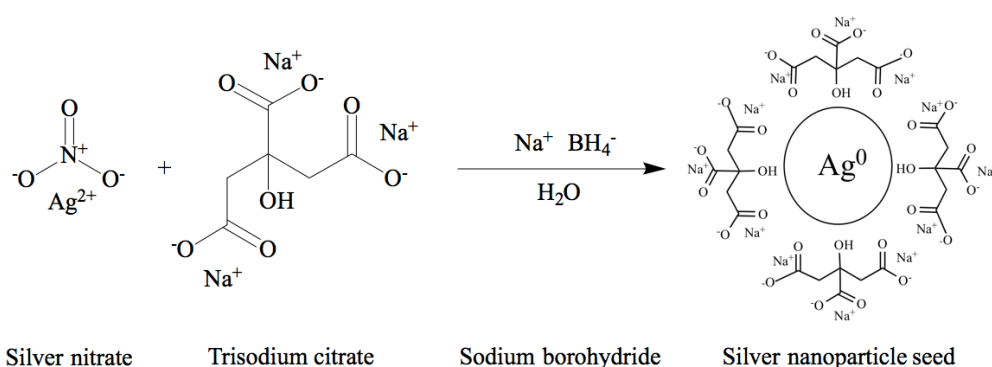
Figure 3.2. Synthesis of silver seed nanoparticles by the chemical reduction method involves the reduction of silver nitarte with sodium citrate and a strong reducing agent such as sodium borohydride.

The growth mechanism takes place via further reduction of silver nitrate with hydroxylamine hydrochloride ($NH_2OH.HCl$) in the presence of the existing silver seed (the nuclei). In contrast to the nucleation agent ($NaBH_4$), $NH_2OH.HCl$ is a gentle reducing agent that causes diffusion of silver ions on the nanoseed's surface without inducing the secondary nucleation of new silver nanoparticles (Figure 3.3) (Jana *et al.*, 2001; Cao *et al.*, 2006).

| Silver nanoparticle seed | Silver nitrate | Hydroxylamine hydrochloride | Silver nanoparticle |
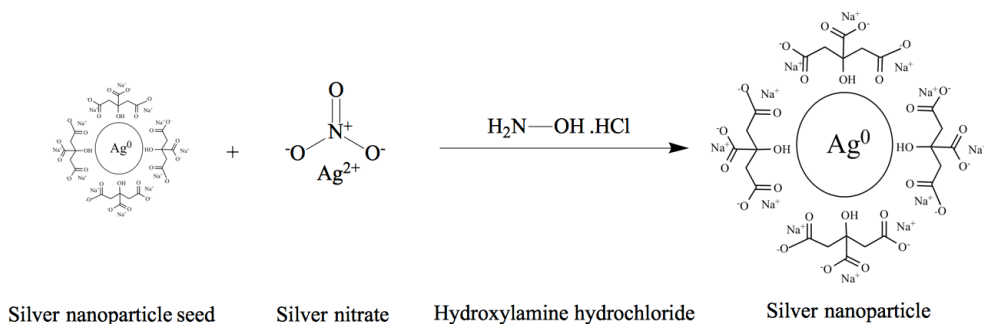
Figure 3.3. The growth mechanism of silver nanoparticles. The reducution of silver ions by hydroxylamine hydrochloride onto the present silver nuclei leads to the production of uniform silver nanoparticles. Hydroxylamine hydrochloride acts as a growth agent that accelerates the rate of silver ion reduction on the surface of the nano-seeds.

3.1.4. Galvanic replacement reaction

The galvanic replacement reaction is an electrochemical process in which, the oxidation or corrosion of one metal (referred to as the sacrificial template) in solution phase is accompanied by the reduction of another metal ion. The difference in reduction potentials of the two metal species is the driving force behind the galvanic replacement reactions, whereby the reduction potential of the sacrificial template is lower than the deposited outer shell metal (Cobley and Xia, 2010; Xia *et al.,* 2013).

Since the standard reduction potential of the $AuCl_4^-$/Au redox pair (0.99 V vs. the standard hydrogen electrode (SHE)) is higher than that of the Ag^+/Ag redox pair (0.80 V vs. SHE), the galvanic replacement initiates immediately after addition of $HAuCl_4$ solution into the suspension of Ag nanoparticles (Sun *et al.*, 2003).

The nanosilver templates (3 Ag^0) are oxidised and act as electron suppliers (3 Ag^0+ 3 e^-), reducing the ionic gold ($AuCl_4^-$) into the pure nanogold (Au^0). The gold atoms nucleate and grow into small clusters and are deposited epitaxially on the surface of a silver nanoparticle (on the facets with the highest surface energy) (Prevo *et al.,* 2008). This eventually results in the formation of hollow gold-silver alloyed nanoshells, as a homogeneous silver-gold alloy is

thermodynamically more stable than a mixture of segregated pure gold and silver. Further oxidisation and subsequent dissolution of the silver core upon further addition of gold salt solution (AuCl⁻$_4$) causes galvanostatic dealloying of the bimetallic nanostructures and formation of thin crystalline GNShells (Sun and Xia, 2003).

Since the elemental gold should be mainly confined to the vicinity of the template surface, the morphology of the GNShells are similar to that of silver templates (Figure 3.4) (Sun *et al.*, 2003).

$$3Ag_{(s)} \ + \ AuCl^-_{4\,(aq)} \longrightarrow Au_{(s)} \ + \ 3Ag^+_{(aq)} \ + \ 4Cl^-_{(aq)}$$
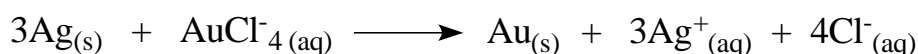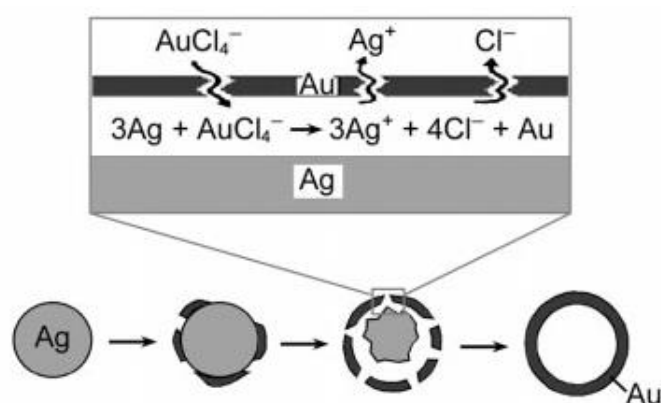
Figure 3.4. Schematic illustration of galvanic replacement reaction between gold solution and silver template. The hollow gold nanostructure is generated due to the dissolution of the oxidised silver atoms in the solution phase and deposition of the reduced gold salts on the surface of the sacrificial silver nanoparticles during the galvanic replacement reaction (Sun *et al.*, 2003).

The galvanic replacement reaction between silver and gold occurs at around 100 °C because the generated silver chloride (Ag⁺ Cl⁻) loses its solubility and forms a white solid precipitation in cold water ($\approx$ 20 °C). The silver chloride solubility increases by $\approx$ 6700 times at higher temperature (60 °C) when the concentration of silver nanoparticles (in terms of pure silver, Ag^0) is controlled below 1.1×10^{-3} M (Sun *et al.*, 2002; 2003).

According to Mie theory, the optical properties of GNShells depend strongly on their size and shell thickness. The surface plasmon resonance absorbance maximum of GNShells can be tuned across the red/NIR region by changing the ratio of the core diameter and the shell thickness. This can be controlled by adding sufficient amount of gold salt solution ($AuCl^-_4$) during the galvanic replacement reaction and/or by adding sufficient quantities of silver nitrate during the preparation of the silver sol (Prevo *et al.,* 2008).

3.1.5. Surface functionalisation of gold nanoparticles

When bare nanoparticles are introduced into the body and exposed to the biological media, with a broad range of pH and ionic strength, they immediately undergo non-specific interaction with plasma proteins (opsonisation). The adsorption of proteins on the surface of the nanoparticles, which is positively correlated with particles size and charge (independent of whether it is negative or positive), enhances the susceptibility of the protein-coated nanomaterials for uptake by phagocytic cells (such as monocytes, dendritic cells and macrophages) thus accelerate their clearance from the blood stream (Cedervall *et al.*, 2007; Lynch and Dawson, 2008; Aggarwal *et al.*, 2009).

The clearance of nanoparticles by the mononuclear phagocytic system (MPS) is a size dependent phenomenon. For instance, particles smaller than 20 nm are rapidly cleared by the renal excretion, while colloids of sizes 200-400 nm undergo rapid hepatic clearance (Moghimi *et al.*, 2001; Moghimi, 2003). Sonovane *et al.* showed the bioaccumulation of citrate-capped GNPs (15-200 nm) in the liver, spleen, lung and kidney (Sonavane *et al.*, 2008).

In order to shield the nanoparticles from opsonisation, avoid phagocytosis and rapid clearance and consequently increase the blood circulation half-life, surface modification of nanoparticles with poly(ethylene glycol) (PEG) has been widely used in industrial and medical applications. Due to the inertness, non-toxicity, hydrophilicity and chemical stability of PEG, PEGylation of

nanomaterials (PEG coating) diminishes their immunogenicity and enhances their stability, biocompatibility, biodistribution and surface hydrophilicity both *in vitro* and *in vivo*. PEG-modification of nanoparticles provides a steric barrier against aggregation (steric repulsion between the PEG chains) since the PEGylated nanoparticles are electrostatically neutral and cannot penetrate into the hydrated PEG layer of surrounding molecules (Figure 3.5) (Sperling and Parak, 2010; Adabi *et al.,* 2016).

Gold nanoparticles designed for biomedical applications are often passivated with thiol-terminated polymers such as PEG and its derivatives (e.g. PEGMA). PEG based polymers or any other ligand molecules (e.g. polymers, drugs, peptides, etc.) can be covalently grafted to the surface of GNPs if they contain free thiol (-S), amine ($-NH_2$) or carboxylate functional group (-COOH) (Liu *et al.*, 2015; Radenkovic *et al.,* 2017).
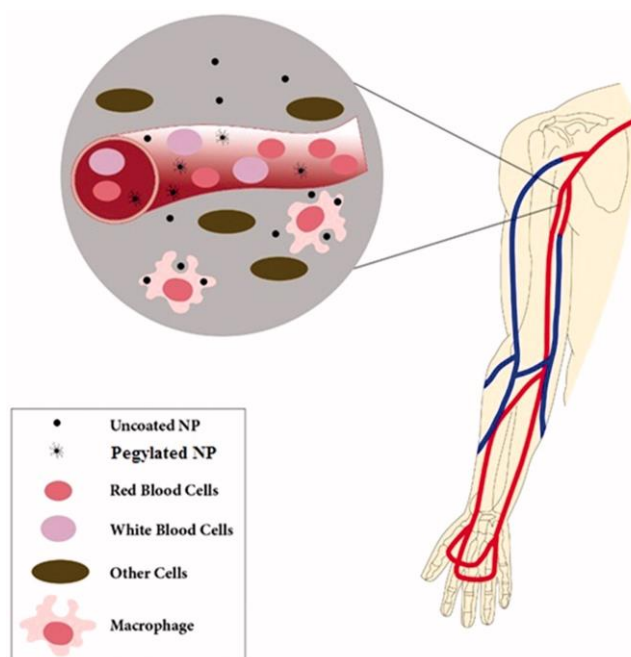
Figure 3.5. PEGylation of nanoparticles. The unmodified NPs are rapidly tagged with proteins corona, and are thereby cleared from the blood stream by the MPS (also known as RES) and bioaccumulate in organs such as the liver, spleen, etc. Functionalisation of nanoparticles with PEG polymer (PEGylation) increases their circulation time by resisting opsonisation and rapid blood clearance (Adabi *et al.*, 2016).

However, surface functionalisation of the GNPs with thiol-functionalised ligands is the dominant strategy due to the strong Au-S bond between the soft Au acid and the weak thiolated base with a much higher bond dissociation energy compared to that of Au-N and Au-O bond (Figure 3.6) (Iancu, 2013). The strong binding of the ligand molecules to the nanoparticles surface enhances the particles stability in biological systems.

$$Au - S \quad > \quad Au - N \quad > \quad Au - O$$

$$\approx 40 \ Kcal \ mol^{-1} \qquad \approx 8 \ Kcal \ mol^{-1} \qquad \approx 2 \ Kcal \ mol^{-1}$$

⟵

Bond dissociation energy
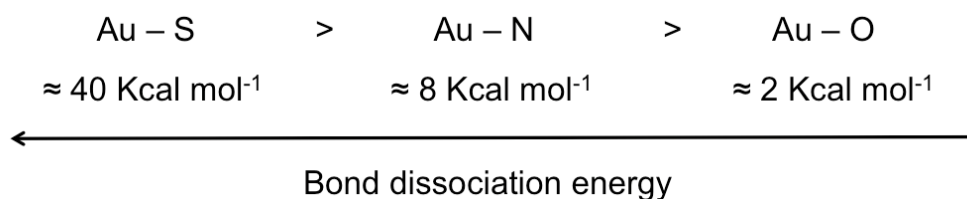
Figure 3.6. . Bond dissociation energies for Au-S, Au-N and Au-O in Kcal mol^{-1} (Iancu, 2013).

In this research, Au-S and Au-N interaction were employed to conjugate the thiolated PEG or P(PEGMA) and Gem to the GNShells surface, respectively. The SH-PEGMA was synthesised by RAFT polymerisation and the CTA-end group was cleaved via aminolysis, as described in chapter 2.

3.2. Materials

Ammonium acetate (≥99.0%), dimethyl sulfoxide (DMSO), dulbecco's modified eagle's medium - high glucose (DMEM), dulbecco's phosphate buffered saline (DPBS), fetal bovine serum (FBS), glacial acetic acid, gold (III) chloride trihydrate (≥99.0%), hydroxylamine hydrochloride (≥98%), L-glutamine, methanol, phosphate buffered saline (pH 7.4), poly(ethylene glycol) methyl ether thiol (average M_n = 6000, SH-PEG6000), phosphate buffered saline (PBS) tablets, penicillin-streptomycin, silver nitrate (≥99.0%), sodium borohydride (99.99%), sodium-1-octane-sulphonate (≥99.0%), sodium acetate buffer solution (pH 5.2±0.1), thiazolyl blue tetrazolium bromide (98%), trisodium citrate dehydrate were all purchased from Sigma-Aldrich and used without further purification. Gemcitabine.HCl (Gem.HCl) was purchased from Sequoia Research Products Ltd. All solvents were of high-performance liquid chromatography grade and used without further purification. Distilled water (dH$_2$O) was used for all of the experiments. Silicon wafer (single side polished), <100>, P-type, with boron as dopant, diam. × thickness 3 in. × 0.5 mm was purchased from Aldrich. The human epithelia MiaPaCa-2 cell line was purchased from the American Type Culture Collection (ATCC).

3.3. Methods

3.3.1. Synthesis of hollow GNShells by galvanic replacement reaction

Hollow spherical GNShells were synthesised through the sacrificial oxidation of nanosilver templates by gold salt solution, following the protocol described by Prevo *et al.* (Prevo *et al.*, 2008) with several modifications to prepare the nanoparticles in a larger scale. For the silver sols synthesis, 100 mL millipore water was added to a 250 mL round bottom flask. To this water, 0.2 mM silver nitrate and 0.5 mM sodium citrate were added while stirring. After about 5 minutes, 0.6 mL of freshly prepared ice-cold solution of 100 mM sodium borohydride was injected quickly into the above mixture with vigorous stirring. The resulting silver colloids (yellow colour) were allowed to stir for a minimum

of 2 h. The prepared silver seed particles were then grown to larger diameters by adding 1 mL of 200 mM hydroxylamine hydrochloride solution. The colloidal suspension was subsequently stirred for 5 min. After further addition of 1.5 mL of 16.6 mM silver nitrate, the silver nanocolloids were allowed to age overnight under magnetic stirring. The slightly turbid greenish-brown colored silver template was subjected to a galvanic replacement reaction with 0.25 mM tetrachloroauric acid at 60 °C. Dropwise addition of 0.25 mM gold solution (1 mL) into the hot colloids of silver nanoparticles (60 °C) resulted in the complete disappearance of the silver plasmon band at 400 nm and appearance of broad absorption maximum at about 640 nm. The colour of the synthesised GNShells was dark blue.

3.3.2. Surface functionalisation of GNShells

The resulting GNShell suspension (1 mL) was centrifuged (Sigma 3-16 KL) at 8000 rpm for 20 min. The GNShell pellet was resuspended in 1 mL of dH_2O and saturated with excess thiolated polymers (1 mL) as shown in Table 3.2.

Table 3.2. The thiolated PEG/PEGMA polymers used for PEGylation of GNShells.

Polymers	M_n (g mol^{-1})	mg mL^{-1}
SH-PEG6000	6000	1
SH-P(PEGMA)10	4 200	0.65
SH-P(PEGMA)50	14 900	0.2
SH-P(PEGMA)100	28 300	0.1

The GNShells (1 mL) were mixed with each thiolated polymer (1:1 v/v) under magnetic stirring for 4 h at room temperature followed by centrifuging the PEGylated samples (8000 rpm, 20 min) using centrifugal Filter (Amicon Ultra-4 mL – with a membrane NMWL of 30 kDa) in order to remove the unbound polymers. Subsequently, the PEGylated GNShell pellets were re-suspended

in 1 mL of Gem solution (0.1 mg mL^{-1}) to prepare Gem-loaded GNShells and the mixture was allowed to stir at room temperature for 1 h. The purification of each sample was carried out by performing another centrifugation cycle (8000 rpm, 20 min) using centrifugal filter (Thermo Scientific™ Pierce concentrators (PES), 3k MWCO, 0.5 mL). The resulting pellets were resuspended in dH$_2$O (0.5 mL) for characterisation and/or in PBS buffer (0.5 mL) for conducting *in vitro* cytotoxicity assays.

After synthesis and surface functionalisation of the GNShells, their physical-chemical properties and cytotoxicity behavior were evaluated by performing the following characterisation techniques:

- Ultraviolet–Visible spectroscopy (UV-Vis)
- Transmission electron microscopy (TEM)
- Dynamic light scattering (DLS)
- Zeta (ζ) potential
- Thermogravimetric analysis (TGA)
- Raman spectroscopy
- High performance liquid chromatography (HPLC)
- X-ray photoelectron spectroscopy (XPS)
- *In vitro* cytotoxicity assay (MTT assay)

3.3.3. Ultraviolet–visible spectroscopy

UV-Visible spectroscopy was conducted to monitor the formation of the silver nanoparticles, the galvanic reaction, the alloying process (silver-gold nanoparticles) and the formation of GNShells. The optical absorption measurements of PEGylated GNShells and Gem-loaded GNShells were also assessed with UV-Visible spectroscopy. The absorption spectra were obtained in plastic cuvettes at 25 °C by an Agilent Cary series UV-Vis spectrophotometer in the wavelength range between 400-800 nm. The samples were diluted in dH$_2$O (1:1 v/v).

3.3.4. Transmission electron microscopy (TEM)

The size and morphology of the GNShells were characterised by TEM on a FEI/PHILIPS CM120 BioTwin operating at 120 KV. After one cycle of centrifugation of GNShells, an aliquot of concentrated nanoparticle suspension was placed on a carbon coated copper grid. The excess of sample was drained gently by filter paper and allowed to dry out in open air for a few minutes. The grid was transferred to the sample holder and placed in the middle of the main microscope vacuum chamber to be introduced into the electron beam.

In TEM, the incident electrons are scattered by GNPs due to their high electron density (significantly higher than the amorphous carbon). However, the transmitted electron beams are refocused and magnified by a series of magnetic lenses and hit the fluorescent plate at the base of the instrument. The enlarged image is displayed on screen in varied darkness according to the GNPs thickness (spherical GNPs are distinctly darker than hollow spherical GNShells) (Williams and Carter, 2009). The size distribution of GNShells was measured quantitatively from TEM images using Image J software version 1.51 (available at https://imagej.nih.gov/ij/).

3.3.5. Dynamic light scattering (DLS) and Zeta Potential

DLS is a technique used for determining the hydrodynamic size of nanoparticles in liquid phase. Interaction of a monochromatic laser beam with nanoparticles in colloidal solutions gives rise to a Doppler shift in the frequency of the scattered photons due to particles erratic Brownian motion. The method of DLS is based on a time-resolved measurement of the scattered light intensity fluctuation, which is subsequently converted into an effective diffusion coefficient, D, using autocorrelation function.

The hydrodynamic radius (D_h), that is inversely proportional to the diffusion coefficient, is calculated by the Stokes-Einstein equation (Equation 3.1) (Berne and Pecora, 2000):

Equation 3.1.

$$D_h = KT/(6\Pi\eta D)$$

Where, K = Boltzmann's constant, T = Kelvin temperature, and η = the solvent viscosity.

DLS measurements were carried using a Zetasizer Nano ZS, Malvern Instruments Ltd., UK. equipped with a HeNe 633 nm laser. The scattered laser beams were measured at the angle of 175° and the data were recorded by Malvern Zetasizer software 7.11. The samples were diluted in dH_2O (1:1 v/v) and the measurements were conducted in plastic cuvettes at 25° C.

The nanoparticles surface charge (also called zeta potential) was obtained using a Zetasizer Nano ZS, Malvern Instruments Ltd., UK. The samples were diluted in dH_2O (1:1 v/v) and the measurements were conducted in disposable folded capillary zeta cells (Malvern) and performed 3 times, with 100 runs each time.

Zeta (ζ) potential, also known as electrokinetic potential, is measured in millivolts (mV) and defined as the electrical potential difference between the shear plane and the dispersion medium and can be calculated via experimental data from the electrophoretic mobility of the particles in an electrical field, using the Smulochowski equation (Equation 3.2) (Smoluchowski, 1903).

Equation 3.2.

$$\mu = \zeta\varepsilon/\eta$$

Where, μ is the electrophoretic mobility, ε is the electric permittivity of the liquid, η is the viscosity and ζ is the zeta potential.

3.3.6. Thermogravimetric analysis (TGA)

TGA (TA instruments) was used to perform thermogravimetric analysis under nitrogen gas. The concentrated colloids of the PEGylated GNShells were prepared by centrifuging 8 mL of PEGylated samples (8000 rpm, 20 min) using centrifugal filter (Amicon Ultra-4 mL – with a membrane NMWL of 30 kDa). The obtained concentrated PEGylated GNShells were placed in a platinum crucible and dried at room temperature prior to analysis. The temperature of sample was raised from 40 °C to 700 °C at a heating rate of 10 °C min^{-1} under an inert atmosphere of nitrogen (25 mL min^{-1}). The amount of the polymer attachment to the surface of gold nanoparticles was found from the percentage mass loss over the temperature range of 300 °C – 450 °C, which was attributed to the decomposition of surface-bound polymer.

Thermogravimetric analysis or thermal gravimetric analysis is an analytical technique in which the mass of a substance is recorded as a function of temperature or time as the sample specimen is subjected to a controlled temperature program in a controlled atmosphere. It is used to perform compositional analysis of multi-component materials, or to determine thermal stabilities, decomposition kinetics, moisture and volatiles content of the examined materials. The thermogravimetric curve is recorded using a programmed precision balance called thermobalance. A typical thermobalance consists of a sample holder, a purge gas system, a microbalance, a furnace, a temperature programmer and a recorder. The thermogravimetric curve or thermogram represents the results by a plot of weight change against temperature or time with the mass change in percentage (weight%) on the y-axis and temperature (T) or time (t) on the x-axis (Figure 3.7).
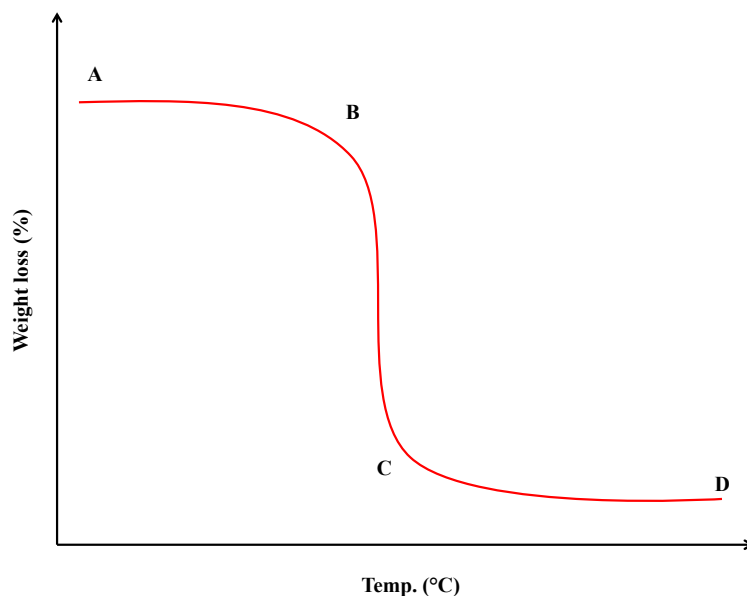
Figure 3.7. A typical thermogravimetric curve.

The plateau parts of the thermogram (A-B and C-D) are the regions of no mass change. The procedural decomposition temperature (B) represents the lowest temperature at which the onset of weight change occurs and the final temperature (C) shows the temperature at which the mass change reaches the maximum. The B-C portion of the TG curve indicates the mass change. Instrumental factors (i.e. the furnace atmosphere and heating rate) and sample characteristics (samples weight, particle size and compactness) are the two main factors that may affect the TG curve (Hatakeyama and Quinn, 1999).

3.3.7. Grafting density calculation

The grafting density (σ) in terms of polymer chains per square nanometer of the surface of the nanoparticles (chain nm^{-2}) was calculated from TGA analysis using Equation 3.3:

Equation 3.3.

$$\sigma = \frac{\left[\dfrac{W_{40-800}}{100 - W_{40-800}}\right] \times 100 - W_{gold}}{M \times S \times 100} \times 10^6 \ (\mu mol \ m^{-2})$$

Where, W_{40-800} Weight loss (%) of polymer on GNPs after grafting

W_{gold} Weight loss (%) for GNPs before grafting

M   Number-average molecular weight of the polymer

S   Specific surface area of a GNP

The radius of the GNShells required for the calculation of the surface area was obtained from the TEM images (Babu and Dhamodharan, 2009). The synthesised GNShells were nearly monodispersed and had a spherical shape (as confirmed by TEM), therefore, specific surface area of the GNShells was determined from the geometrical relationship between the surface area and mass using the Brunauer–Emmette– Teller (BET) equation (Equation 3.4):

Equation 3.4.

$$D_{BET} = 6000/(\rho \times S_{BET})$$

Where, D_{BET} is the average diameter of a GNShell, ρ is the theoretical density of gold (19.28 g cm^{-3}) and S_{BET} is the specific surface area of a GNShells (Farhadi *et al.*, 2013; Ahmad *et al.*, 2014; Xu *et al.*, 2014).

The determined σ was expressed as number of moles of the grafted polymer molecules per square meter of gold surface. By multiplying the obtained grafting density (μmol m^{-2}) by Avogadro's number (6.02 x 10^{23} chain mol^{-2})

and converting the meters to nanometers, the number of polymer chains per square nanometer of the nanoparticle surface (chain nm^{-2}) could be calculated.

The number of polymer chains per a nanoparticle was obtained by multiplying the grafting density (chain nm^{-2}) with the GNShells surface area ($4\pi r^2$).

3.3.8. Estimation of the conformation of thiol-end polymers on the surface of GNShells

The conformation of the grafted polymer chains can be divided into two regimes: 'brush' and 'mushroom' (Unsworth *et al.,* 2005). This can be estimated based on the Flory dimensions (R_F) of the grafted polymer and the distance between grafting points (D) (Rahme *et al.*, 2013).

The Flory radius for the different PEG used in this study is calculated using equation 3.5:

Equation 3.5.

$$R_F = \alpha n^{3/5}$$

Where, α is the length of one monomer in Angstroms (α = 3.5 A° for PEG) and n is the number of monomer units in the polymer.

By assuming that polymers are homogenously and randomly distributed around the whole surface of GNShells, the value of D (effective distance between two grafting point) was estimated according to the distance of the empty space on the GNPs between two grafted sites (Equation 3.6). Since the thiol-end polymers are attached to the GNShells through thiol-gold linkage, D can be obtained by calculating the square root of the nanoparticle surface area divided by the number of polymer ligands (Rahme *et al.*, 2013; Zan *et al.*, 2015).

Equation 3.6.

$$D = \sqrt{\frac{Nanoparticle\ surface\ area}{Number\ of\ grafted\ polymer\ chains}}$$

When $D > R_F$, the grafted polymer chains adopt a 'mushroom' conformation which normally occurs to low grafting density. In contrast, for increased grafting densities ($D < R_F$), the polymers acquire a 'brush' type conformation.

3.3.9. Raman Spectroscopy

Raman spectroscopy is a non-destructive means of probing molecular vibrations optically through inelastic scattering (Figure 3.8). The Raman scattering involves in the interaction between photon and molecular vibration, and since each molecule has unique vibrational energy states, Raman-scattered photons can be exploited for specific molecules/or molecular bond detection.

The surface-enhanced Raman spectroscopy (SERS) is an efficient technique used to enhance the Raman scattering intensity by employing rough transition metal surfaces (e.g. GNPs). Irradiation of GNPs on their surface resonance band causes electromagnetic field enhancement near the GNPs surface that in turn increases the intensity of the Raman-shifted photon frequency (scattered light from the analyte that is chemically bonded to the SERS-active GNPs) (Li *et al.*, 2014).

The Raman spectrum of the PEGylated GNShells was obtained to determine the binding interaction between thiol-end polymers and the nanoparticles (Au-S bond). The PEGylated GNShell colloids were dried onto glass substrates and the films were characterised in a microRaman spectrometer (inVia Raman Microscope, Renishaw). For vibrational excitation, a diode laser (785 nm, Renishaw) with a maximum laser power of 300 mW was applied. Raman spectra in the range $150 - 950\ cm^{-1}$ were collected using acquisition time of 60 s and 100% laser power per sample. The Raman spectrometer consists of

a Renishaw spectrograph system based on the use of Kayser™ notch filters with a sensitive CCD detector coupled to a microscope for point-by-point analyses. Generally, the Raman spectrum is generated by plotting the intensity of the scattered light (y-axis) *versus* the Raman shift, which is the frequency shift of the Raman signals relative to the excitation source. Raman shift is expressed in wavenumber (cm^{-1}).
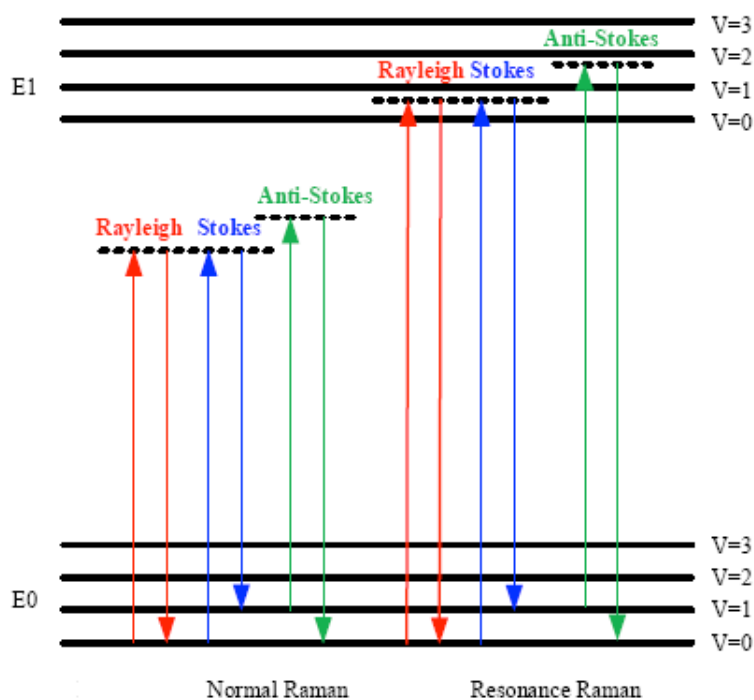
Figure 3.8. Energy level diagram related to elastic (Reyleigh) and inelastic (Raman scattering) scattering of light. In Reyleigh scattering, photons are scattered with the same frequency as the incident radiation whereas in Raman scattering, scattered photons have frequency above (anti-Stokes) or below (Stokes) that of the incident photons. This energy difference is equal to the molecular vibrational energy of the scattering molecule. SERS enhances the Raman scattering intensity by employing transition metal substrates such as GNPs (Li *et al.*, 2014).

3.3.10. X-ray photoelectron spectroscopy

X-ray photoelectron spectroscopy (XPS) was conducted in order to determine the presence (or absence) of covalent bonding of the Gem nitrogen to nano-gold. XPS, also known as electron spectroscopy for chemical analysis

(ESCA), is a sensitive quantitative spectroscopic technique for analysing the surface chemistry of a material. X-ray spectra are generated by irradiating a solid surface with a beam of X-rays such as typical Al-Kα or Mg Kα sources, while simultaneously measuring the kinetic energy and number of electrons that are emitted from atoms on the surface of the material. The kinetic energy (KE) of the emitted electrons depends upon the photon energy (hv) and the binding energy (BE) of the electron (i.e. the energy required to remove the electron from the surface). The binding energy (determined from the measured kinetic energy recorded, KE = hv − BE) and the intensities of the photoelectron peaks enable the identification and quantification of elements that are near a material's surface (Korin *et al.*, 2017).

X-ray photoelectron spectra (XPS) were collected on a Thermo K-alpha instrument utilising a 72 W monochromated Al-Kα X-ray source (with photon energy of 1486.6 eV). The depth profiles were completed using an Ar+ ion gun at 3000 kV. Samples were prepared by drop coating of nanoformulations on a clean silicon wafer, and the drops were allowed to air dry. The nano-formulations coated silicon wafers mounted onto the XPS specimen holder with vacuum compatible, double-sided adhesive carbon tape before the measurement (Figure 3.9). Clean gloves and tweezers were used to avoid contaminating the wafer. Binding energies were referenced against the Au 4*f* 7/2 at 83.58 eV and the spectra were analysed using CasaXPS version 2.3.16.

Figure 3.9. Sample preparation for XPS. The silicon wafer was cut to the desired size and used as substrate for drop-casting the colloids.

3.3.11. High performance liquid chromatography (HPLC) analysis for the quantification of the drug loading efficiency

HPLC is a technique used to separate, identify and quantify each component of an analyte. The basic components of an HPLC system include: mobile phase reservoir, pump, injector, column and detector. The pump pressurises the mobile phase (comprising organic solvents and their mixtures) through the column and regulates the flow rate. The injector introduces sample into the continuously flowing mobile phase stream and conveys the sample into the column filled with silica gel. Based on the degree of the molecular polarity, each component of the sample interacts differently with silica at different lengths of the separation column as flows through it and exhibits different retention time. The UV detector measures the absorbance of the components at predetermined wavelength and monitors the chromatogram on a computer screen (Lough and Wainer, 1995).

The HPLC method for the quantification of Gem was developed using an Agilent Technologies 1200 Series HPLC system. The data was acquired and analysed using ChemStation for LC software, also by Agilent Technologies,

UK. The chromatographic separation was achieved using a Phenomenex Synergi™ 4 µm Polar-RP 80 Å, LC Column 250 x 4.6 mm.

The surface-functionalised GNShells (GNShells + thiol-end polymer + Gem) were centrifuged at 8000 rpm for 20 min at 25 °C using a centrifugal concentrator (Thermo Scientific™ Pierce concentrators (PES), 3k MWCO, 0.5 mL). The obtained 500 µL supernatant was diluted up to 800 µL with HPLC grade water followed by addition of 200 µL methanol to adjust the total volume at 1 mL.

The prepared HPLC samples were isocratically eluted with a mobile phase of buffer and acetonitrile (95:5 v/v). The aqueous buffer was prepared by dissolving 3.86 g of ammonium acetate (0.05 M) and 1 g of sodium-1-octane-sulphate in 1 L of HPLC grade water and adjusted to pH 4 with glacial acetic acid.

The mobile phase was pumped through the column at a flow rate of 1 mL min^{-1}. The UV detector was set at 270 nm and the injection volume was 20 µL.

The Gem standard solutions used for quantification were prepared by suitably diluting 75 µg mL^{-1} working standard of the drug in a mixture of 80:20 water:methanol. The duration of each run was 20 min and the Gem peak appeared at around 8.5 min. The measurements were performed in triplicate and the Gem loading efficiency (LE) was obtained using Equation 3.7 (Feng *et al.*, 2014):

Equation 3.7.

$$LE \ (\%) = \frac{Gem_{Original} \ - \ Gem_{Supernatant}}{Gem_{Origianl}}$$

3.3.12. HPLC Method validation

The HPLC method was validated for: linearity, limit of detection (LOD), limit of quantitation (LOQ), intermediate precision, and percent recovery (Contreras-Sanz *et al.*, 2012; Singh *et al.*, 2015).

Determination of the linear range is one of the main concerns in validation of HPLC analysis methods. The linearity was assessed by calibration of nine-point standard curves in HPLC grade water, sodium acetate buffer solution (pH 5.2±0.1), phosphate buffered saline (pH 7.4) and cell culture medium for Gem, from 75 µg mL^{-1} down to 1 µg mL^{-1} (regression analysis).

LOD and LOQ are calculated based on the standard deviation of the response (σ) and the slope of the calibration curve (S), using Equations 3.8 and 3.9:

Equation 3.8.

$$Limit\ of\ Detection\ (LOD) = \ 3.3\ (\sigma/S)$$

Equation 3.9.

$$Limit\ of\ Quantitation\ (LOQ) = \ 10\ (\sigma/S)$$

The standard deviation of the response (σ) is a measure of the amount of error in the prediction of y-value for an individual x in the regression and it can be determined by using STEYX function in Microsoft Excel. [STEYX(known_y's, known_x's)].

Intermediate precision was assessed by determining the relative standard deviation (RSD) of the triplicate analytes, using Equation 3.10:

Equation 3.10.

$$RSD\ (\%) = \frac{Standard\ deviation\ of\ triplicate\ analyte\ values}{Means\ of\ triplicate\ analyte\ values} \times 100$$

The percent recovery is the ratio of the actual drug concentration in the formulation (C) to the theoretical concentration (C_{theory}), expressed as a percentage, using Equation 3.11:

Equation 3.11.

$$Percent\ Recovery = \left(C/C_{theory}\right) \times 100$$

3.3.13. *In vitro* release study

In vitro release testing is an important analytical tool that is used to investigate the amount of drug release from the nanoformulation at physiological conditions. 10 mL of each Gem-loaded GNShells samples (GNShells + thiol-end polymer + Gem) were centrifuged (8000 rpm, 20 min) using centrifugal filter (Amicon Ultra-15 mL – with a membrane NMWL of 3 kDa). The obtained concentrated nanoformulation was resuspended in 10 mL release medium at different physiological pH level: sodium acetate buffer solution (pH 5.2±0.1), phosphate buffered saline (pH 7.4). The temperature and stirring of the system were maintained at 37 °C and at 100 rpm, respectively. 500 µL of sample was withdrawn at predetermined time points for 48 h ($n = 3$) After each sample collection, the same amount of fresh media was added back to the release medium. The collected samples were centrifuged; using centrifugal filter (Thermo Scientific™ Pierce concentrators (PES), 3k MWCO, 0.5 mL) for 20 min at 8000 rpm and then, the samples supernatant were subjected to HPLC analysis. The results were presented in terms of cumulative release as a function of time (mean ± SD). The cumulative percentage drug released versus time was calculated using Equation 3.12:

Equation 3.12.

$$Cumulative\ drug\ release\ (\%) = \frac{C_t}{C_\infty} \times 100$$

Where, C_t is the mass of drug released at time t and C_∞ refers to the initial loaded mass.

3.3.14. *In vitro* drug delivery study

The 3-(4,5-dimethylthiazol-2-yl)-2,5-diphenyltetrazoliumbromide (MTT) assay is a rapid colorimetric assay that is widely used for measuring the cytotoxic potential of drugs (Mosmann, 1983). It is based on the reduction of the yellow tetrazolium salts to the purple formazan in viable cells due to their mitochondrial activity. The net positive charge on MTT dyes facilitates their cellular uptake via the plasma membrane potential, enable them to readily enter cells and reduce to insoluble formazan crystals by NAD(P)H-dependent cellular oxidoreductase enzymes. Thus, there is a linear relationship between cell viability, mitochondrial activity and reduction of salt to formazan (Mosmann, 1983; Berridge, *et al.* 2005; Van Meerloo, *et al.* 2011).

The human epithelia cell line MiaPaCa-2 was used in *in vitro* experiment. The MiaPaCa-2 cell line (American Type Culture Collection) is a human Caucasian pancreatic carcinoma cell line. The cells are large with abundant cytoplasm, exhibit a high degree of aneuploidy, have a tendency to grow on the top of other cells, eventually growing free in suspension (ATCC). The cells were incubated in DMEM supplemented with 10% fetal bovine serum, 1% penicillin-streptomycin and 1% L-glutamine. MiaPaCa-2 cells were seeded in a 96-well plate at a density of 1×10^4 cells per well and incubated in humidified atmosphere with 5% CO_2 for 24 h before the assay. The culture medium containing different concentrations of drug ranging from 0.001 to 100 µmol L^{-1} was added to the adherent cells while control cells remained untreated (Figure 3.10).
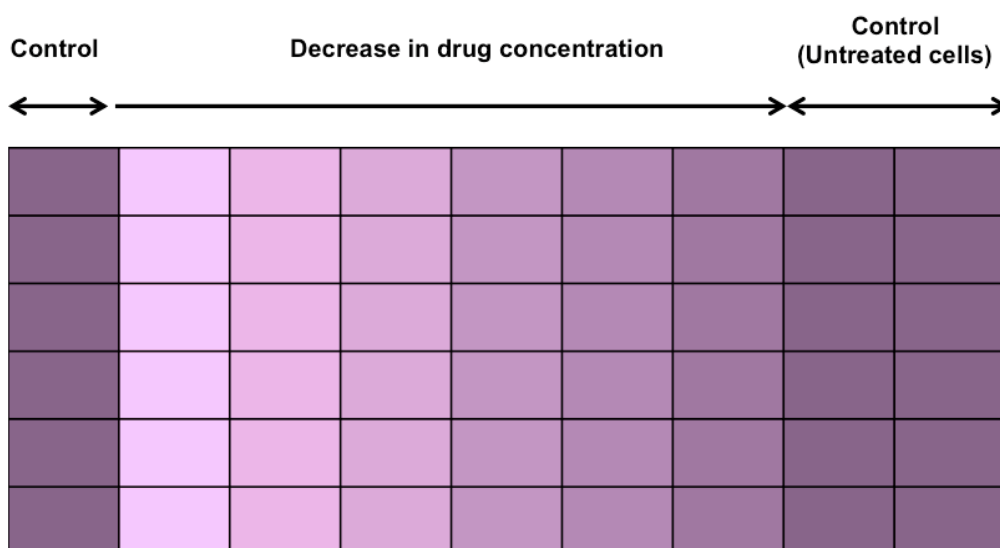
Figure 3.10. MTT assay plate setup.

After incubation for 48 and 72 h with different concentrations of drug, the medium was replaced by 100 µL of fresh medium and 25 µL of MTT stock solution (5 mg mL^{-1} in PBS) and incubated for an additional 4 h. Subsequently, the medium was gently removed and the water insoluble formazan crystals were dissolved in 200 µL of DMSO. The plates were shaken for 2 min at room temperature before measuring the optical density (OD) at 570 nm on a SpectraMax® M2/M2e Multimode Microplate Reader, with SoftMax® Pro Software. The obtained data was analysed with the help of Prism software to acquire half maximal effective concentration (EC$_{50}$) value. The same procedure was repeated for treating the cells with formulation (GNShells + thiol-end polymer + Gem) at concentration of 0.001-100 µmol L^{-1} Gem equivalent doses. All the MTT experiments were performed in triplicate and the variation in the readings were shown as error bars (± SD).

3.4. Results and discussion

Results of this chapter were obtained after series of laboratory experiments and data analysis. Each individual section corresponds to the sections given in materials and methods.

The hollow spherical GNShells were synthesised based on the galvanic replacement reaction method with gold ions as precursors and silver nanoparticles as sacrificial templates. The SPR of the GNShells was tuned to red/NIR wavelengths by controlling the dimension of interior cavity and shell thickness. Figure 3.11 showed the extinction spectra of the GNShells with surface plasmon resonance maximum value at 640 nm, which is situated in the red/NIR optical window where photons penetrate deeper into living tissue. The disappearance of the absorption peak at about 400 nm confirmed the oxidation of silver atoms during the transmetallation reaction and deposition of the gold in the form of a shell around the silver core. The details of nanoshells preparation have been described in section 3.2.
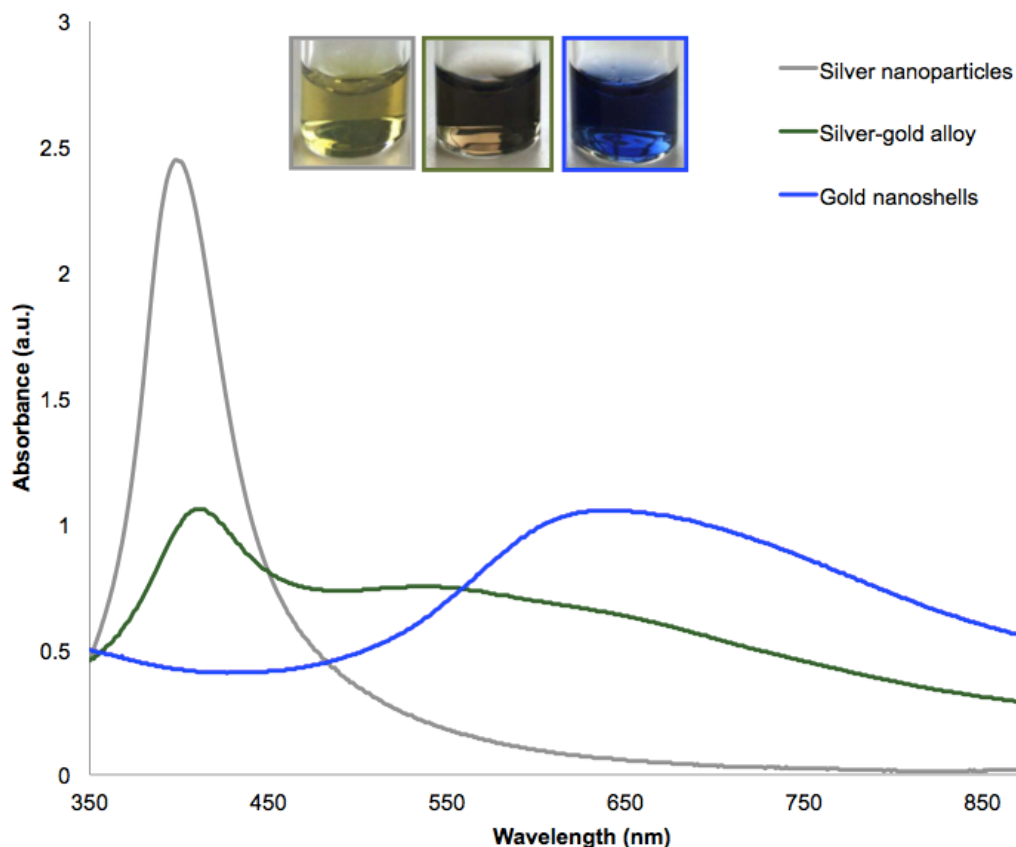
Figure 3.11. The absorbance spectrums of the silver colloids (gray) and the silver-gold alloy bimetallic nanoparticles (dark green) and the originally synthesised gold nanoshells (blue).

The morphology of the synthesised GNShells was evaluated by TEM as shown in Figure 3.12. The obtained image showed that hollow nanoparticles were mostly spherical and fairly uniform in size. The size distribution of 100 GNShells was measured by image J software and the plotted histogram of diameter range distribution is presented in Figure 3.13. The frequency distribution curve of the GNShells showed Gaussian size distribution. The most frequent GNShells size (mode) that appeared in the data set was 54 nm and the average effective diameter was measured to be 53.5 ± 1.72 nm.

The hydrodynamic diameter (D_h) of crude GNShells was measured by DLS and the mean D_h was found to be 60.44 ± 2.16 nm (polydispersity index, PDI 0.204 ± 0.01) as shown in Figure 3.14.

Since DLS measures the D_h indirectly based on determination of frequency of particles movement, the DLS result showed the larger z-average for colloidal GNShells compared to TEM result.

The D_h of the GNShells includes not just the particle itself, but the ionic and solvent layers associated with it in colloids under the particular measurement conditions. In addition, DLS is a dynamic measurement, extremely sensitive to the dispersion/aggregation behaviour of the particles in solution. In contrast, in TEM measurements of GNShells, without staining, almost all of the signal will come from the metallic core of the NPs, ignoring any organic capping layer (Eton *et al.*, 2017).
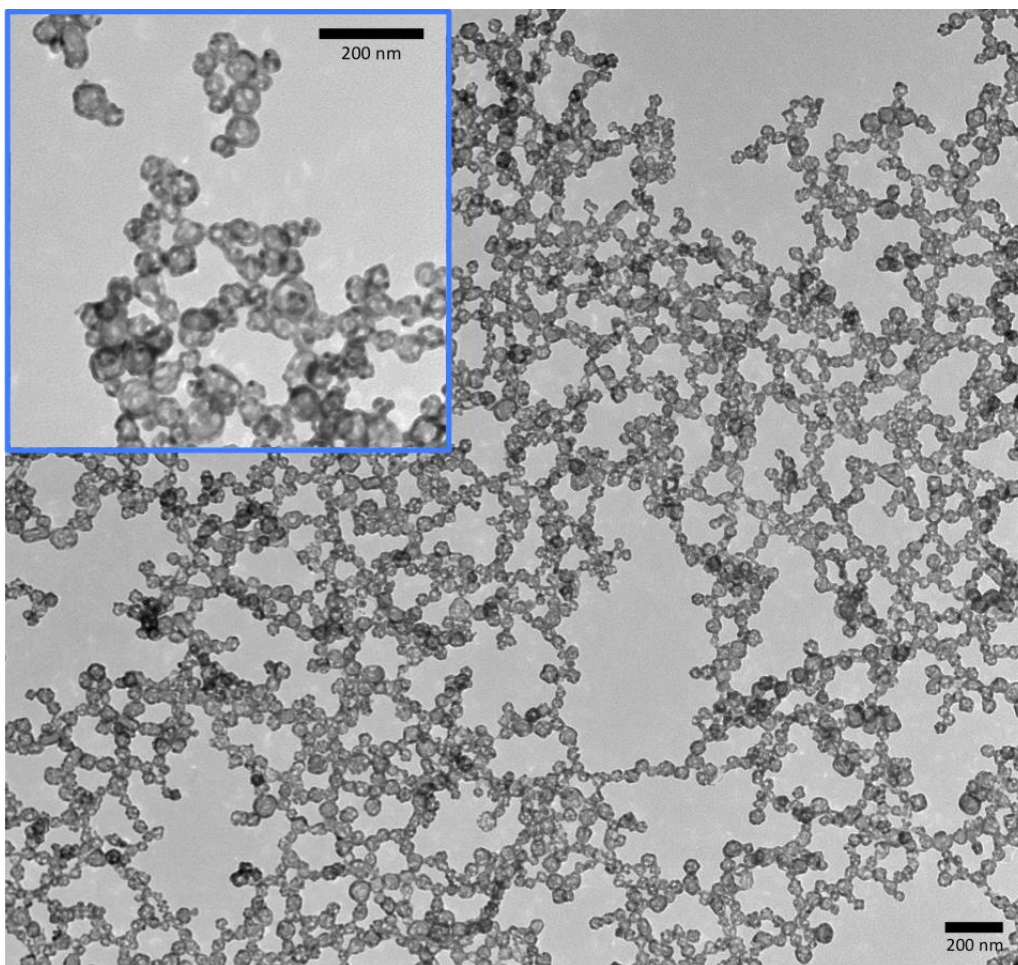
Figure 3.12. TEM image of representative batch of GNShells produced by the galvanic replacement reaction.
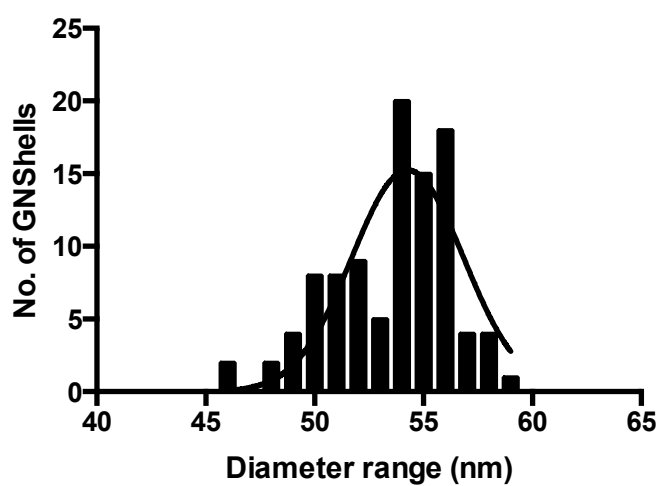
Figure 3.13. The particle size distribution histogram derived from TEM images of the synthesised GNShells.
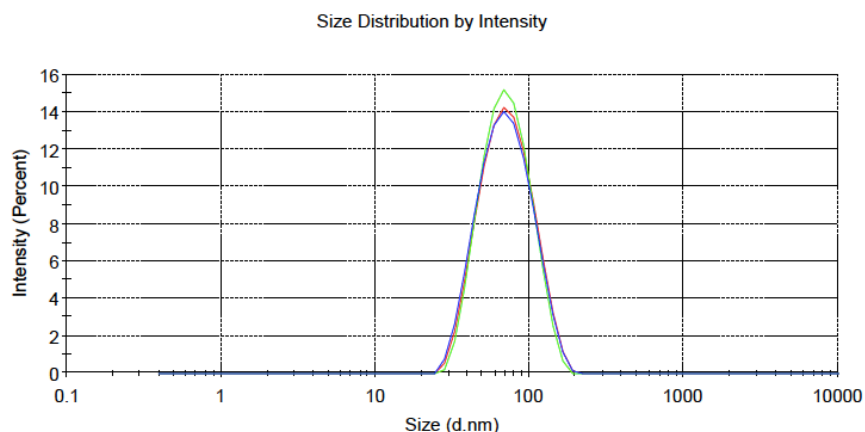
Figure 3.14. DLS spectra on hydrodynamic size distribution of representative batch of GNShells reports hydrodynamic radius as an intensity distribution.

The surface charge as well as electrostatic stability of the synthesised GNShells was measured through zeta (ζ) potential analysis. ζ-potential can affect the stability of dosage forms and their release rate in the blood stream and also can influence their absorption into the body membranes. A negative ζ-potential generally results in rather low phagocytosis activity (Honary and Zahir, 2013). The ζ-potential value of the crude GNShells was determined to be -37.5 mV due to the presence of sodium citrate on the surface of GNShells.

The non-specific adsorption of biomolecules on the surface of the originally synthesised GNPs significantly increases their uptake by the MPS immediately after intravenous administration. The functionalisation of nanoparticles with PEG and its derivatives, often referred to as PEGylation, increases the particles stability and circulation half-life. PEGylation also provides a hydrated steric barrier on the nanoparticles surface that reduces protein opsonisation and subsequent phagocytosis (Cedervall *et al.*, 2007; Sperling and Parak, 2010). Since brush-type polymers based on PEGMA are highly water-soluble, biocompatible and anti-fouling, they have been widely used in surface-modification of nanoparticles, polymer–biomolecule conjugation, drug delivery and bioimaging (Mantovani *et al.*, 2005;

Magnusson *et al.*, 2008; Zhang *et al.*, 2014; Yang *et al.* 2015; Lega *et al.*, 2015).

In this research, the hollow spherical GNShells were functionalised with thiol-end polymers. PEGylation of GNShells was performed by following the procedure in section 3.3.2. Briefly, surface of bare GNShells were covered with thiol-end polymers (SH-P(PEGMA)) with the DP of 10, 50 and 100 and number-average molecular weight (M_n) of 4 200 g mol^{-1}, 14 900 g mol^{-1} and 28 300 g mol^{-1}, respectively. Therefore, the PEGylated products were referred to as GNShells+SH-P(PEGMA)10, GNShells+SH-P(PEGMA)50 and GNShells+SH-P(PEGMA)100, respectively. The performance of thiol-end polymer grafted GNShells were compared with commercially available SH-PEG6000 coated samples, which are referred to as GNShells+SH-PEG6000.

Gold (I) with its [Xe] $4f^{14}5d^{10}$ electronic configuration is a soft metal ion and therefore according to Pearson acid base concept (HSAB concept) has a preference for soft donor ligands such as sulfur. The thiol group is the most commonly selected anchor group for adsorption onto the surface of the gold nanoparticles because of the strong chemical bond, with high bond enthalpy of 418 KJ mol^{-1}, between gold and sulfur that makes this interaction desirable as a robust attachment mechanism (Damge *et al.*, 2008).

As explained in section 1.6.2 GNPs are important materials for their surface-enhanced Raman scattering/spectroscopy (SERS) effect. The intensified Raman scattering signals from the grafted thiol-end polymers are due to the strong electromagnetic near-field enhancement of GNPs stimulated with laser light illumination that allows gold nanoparticles to act as metallic substrates for SERS.
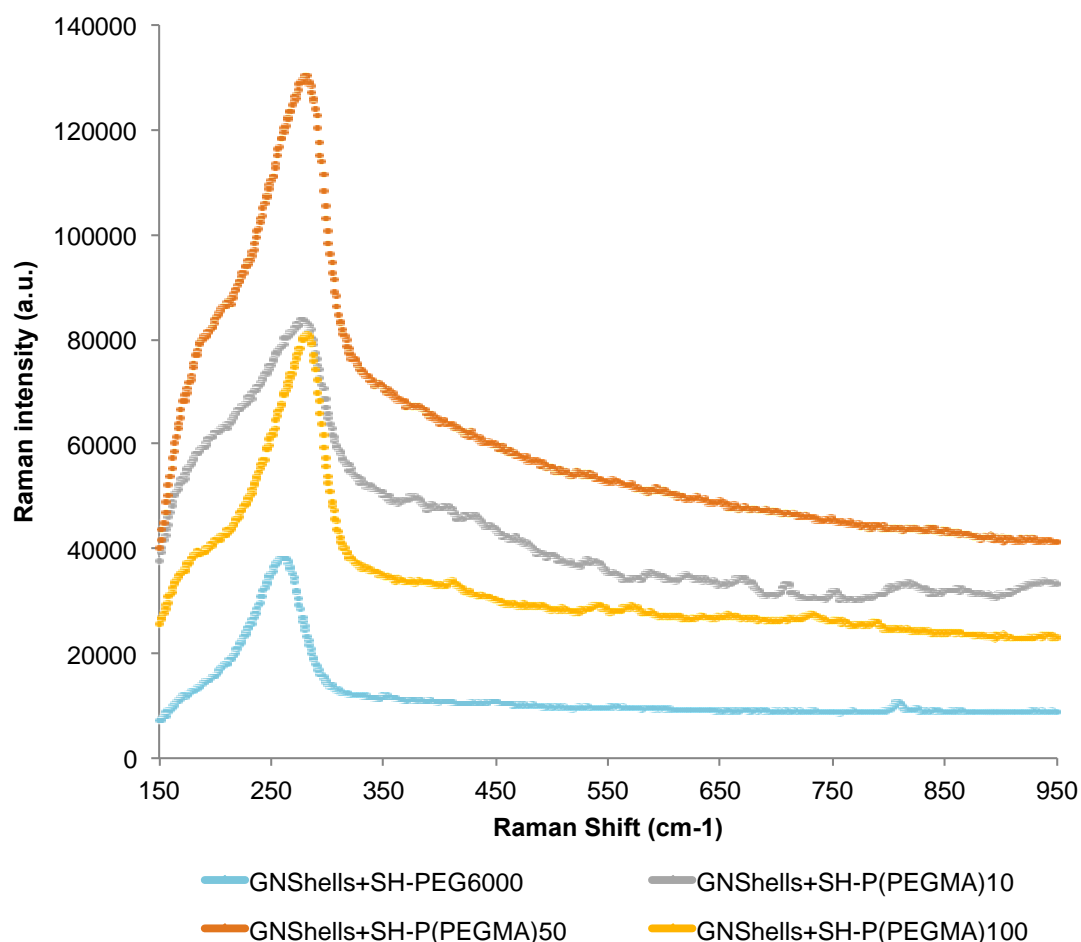
Figure 3.15. Raman spectrum of GNShells+SH-P(PEGMA)10 (gray), GNShells+SH-P(PEGMA)50 (orange) and GNShells+SH-P(PEGMA)100) (yellow) and GNShells+SH-PEG6000 (blue).

Figure 3.15 shows the Raman peaks between 267–285 cm^{-1} that correspond to the vibrational modes of SH-PEG/PEGMA molecules adsorbed on the GNShells surface. The results confirmed the covalent attachment of the SH-PEG/PEGMA molecules to the GNShells core after replacing the citrate as the stabiliser because of the strong binding affinity of the sulfur atom.

The stretching modes of Au-S are typically reported to be between 200 – 240 cm^{-1}. However, this mode may shift towards higher wavenumber (300 – 310 cm^{-1}) when the sulfur atom attach to the longer polymer chains (Liao and Hafner, 2005; Zhang and Lin, 2014; Liu *et al.*, 2015).

All Raman spectra of the PEGylated GNShells were taken from the coffee ring area, where PEGylayed GNShells were closely packed, to ensure the precise SERS detection of the grafted PEG polymers. The intensity of Raman-active vibrations contributing to each thiol-end polymer-grafted GNShells depends on the local concentration of the components responsible for that vibrational mode.

Note: The coffee-ring phenomenon occurred when GNShells in the droplets of colloidal suspension transferred to the rim and left a ring-shaped image after evaporation on glass slide.

Monitoring the changes in the surface plasmon absorption bands after PEGylation of GNShells with SH-P(PEGMA)10, SH-P(PEGMA)50, SH-P(PEGMA)100 and SH-PEG6000 along with their photographic images displays in Figures 3.16 and 3.17, respectively.
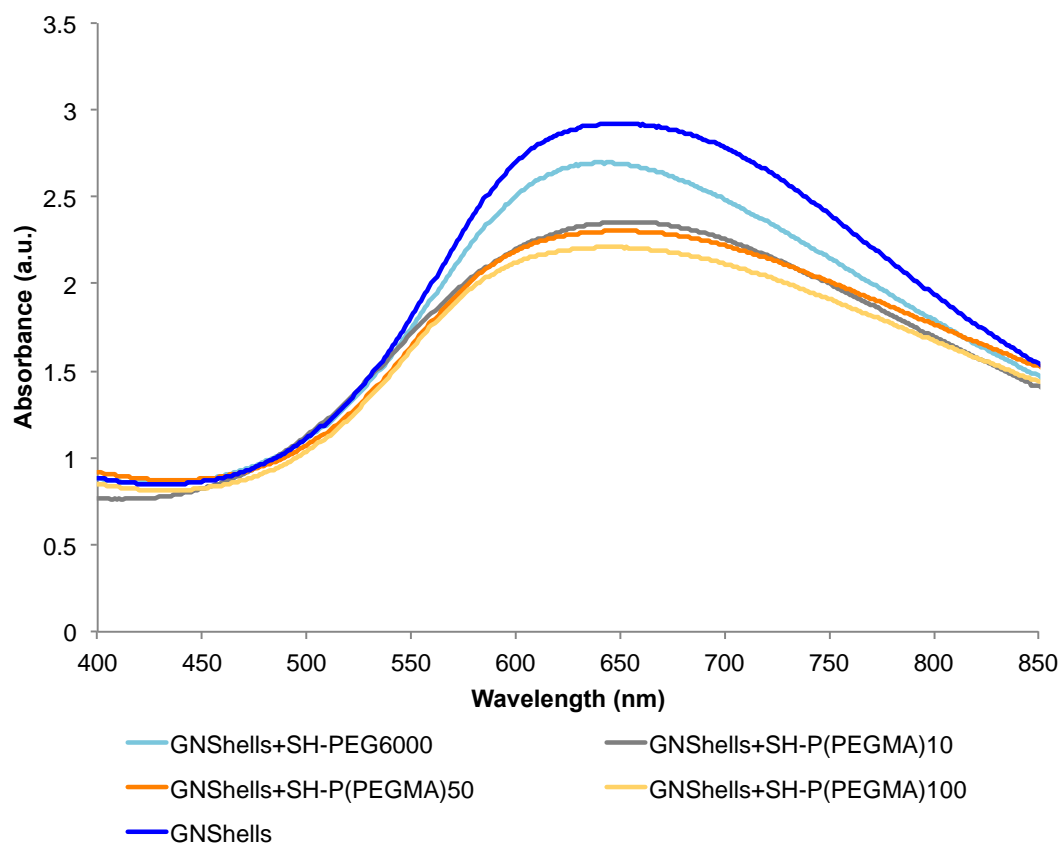
Figure 3.16. Optical absorption spectra of crude GNShells (Dark blue), GNShells+SH-PEG6000 (light blue), GNShells+SH-P(PEGMA)10 (gray), GNShells+SH-P(PEGMA)50 (orange) and GNShells+SH-P(PEGMA)100) (yellow).

Figure 3.17. GNShells+SH-PEG6000 (light blue), GNShells+SH-P(PEGMA)10 (gray), GNShells+SH-P(PEGMA)50 (orange) and GNShells+SH-P(PEGMA)100) (yellow) and crude GNShells (Dark blue).

The colloidal dispersion of the surface functionalised GNShells showed absorption bands in the red/NIR spectral range. The slight red-shifting accompanied by peak broadening and a decrease in the intensity was observed in the absorption peak of all four batches of thiol-polymer grafted GNShells.

As discussed in section 1.5, the SPR band wavelength and intensity depends on the factors affecting the local density of electronic states on the GNPs surface such as particle size, shape, structure and dielectric constant of the surrounding medium. El-Sayed and co-workers studied the dependency of the ratio of the scattering to absorption cross-section to the diameter of gold nanoparticles using full Mie theory (Mie, 1908). They confirmed that the relative contribution of SPR absorption and scattering could be tuned by changing the particle size and the ratio of the photon scattering to absorption linearly increase with size particles enlargement (Lee and El-Sayed, 2005; Jain *et al.*, 2006). Therefore, the obtained data implies that PEGylation, reduced the inter-particle distance between the neighboring particles and induce particle aggregate assemblies which in turn shift the SPR band to lower energies, corresponding to longer wavelengths of spectrum for the larger gold core. These red-shifting and SPR damping are the consequence of increase of the relative contribution of surface plasmon scattering to the total light extinction for larger size particles and is in good agreement with Mie theory. The band broadening is due to coupling of the plasmon resonance from multiple GNShells and contribution of higher order electron oscillation (Huang and El-Sayed, 2010). Changing of the local refractive index around the GNShells as the result of PEGylation could be another reason of the SPR spectral extinction peak shift (Huang and El-Sayed, 2010).

TGA was perfomed to evaluate the amount of grafted polymers required to reach surface saturation of the gold site (molecules nm^{-2}). Figure 3.18 shows the collected TGA data for the as-synthesised GNShells, GNShells+SH-P(PEGMA)10, GNShells+SH-P(PEGMA)50, GNShells+SH-P(PEGMA)100) and GNShells+SH-PEG6000. As expected, no weight loss step was observed in the TGA trace of the originally synthesised hollow spherical GNShells indicative of their purity and absence of organic material.

For all PEGylated samples, about 2 % weight loss around 100 °C was due to the loss of adsorbed water. Up to 5% weight loss before 300 °C could be assigned to the presence of grafted polymers minor impurities. The major weight reduction occurring between 300 °C and 450 °C was attributed to the thermal degradation of SH-PEG/SH-PEGMA polymers.

The mass loss (%) from the TGA thermograms was found to be 80% for SH-PEG6000, and 65.50%, 43.70% and 36.70% for the SH-P(PEGMA)10, SH-P(PEGMA)50 and SH-P(PEGMA)100, respectively.

The grafting density (chain nm^{-2}) was calculated from the weight loss (%) derived from TGA analysis along with the corresponding M_n data obtained from GPC measurements (Table 3.3). A maximum density of 68.80, 46.70, 5.37 and 2.10 chain nm^{-2} were reported for SH-PEG6000, SH-P(PEGMA)10, SH-P(PEGMA)50 and SH-P(PEGMA)100, respectively. The calculated grafting densities (chain nm^{-2}) correspond to 619 200 SH-PEG6000, 420 300 SH-P(PEGMA)10, 48 330 SH-P(PEGMA)50 and 18 900 P(PEGMA)100 molecules per nanoparticle.
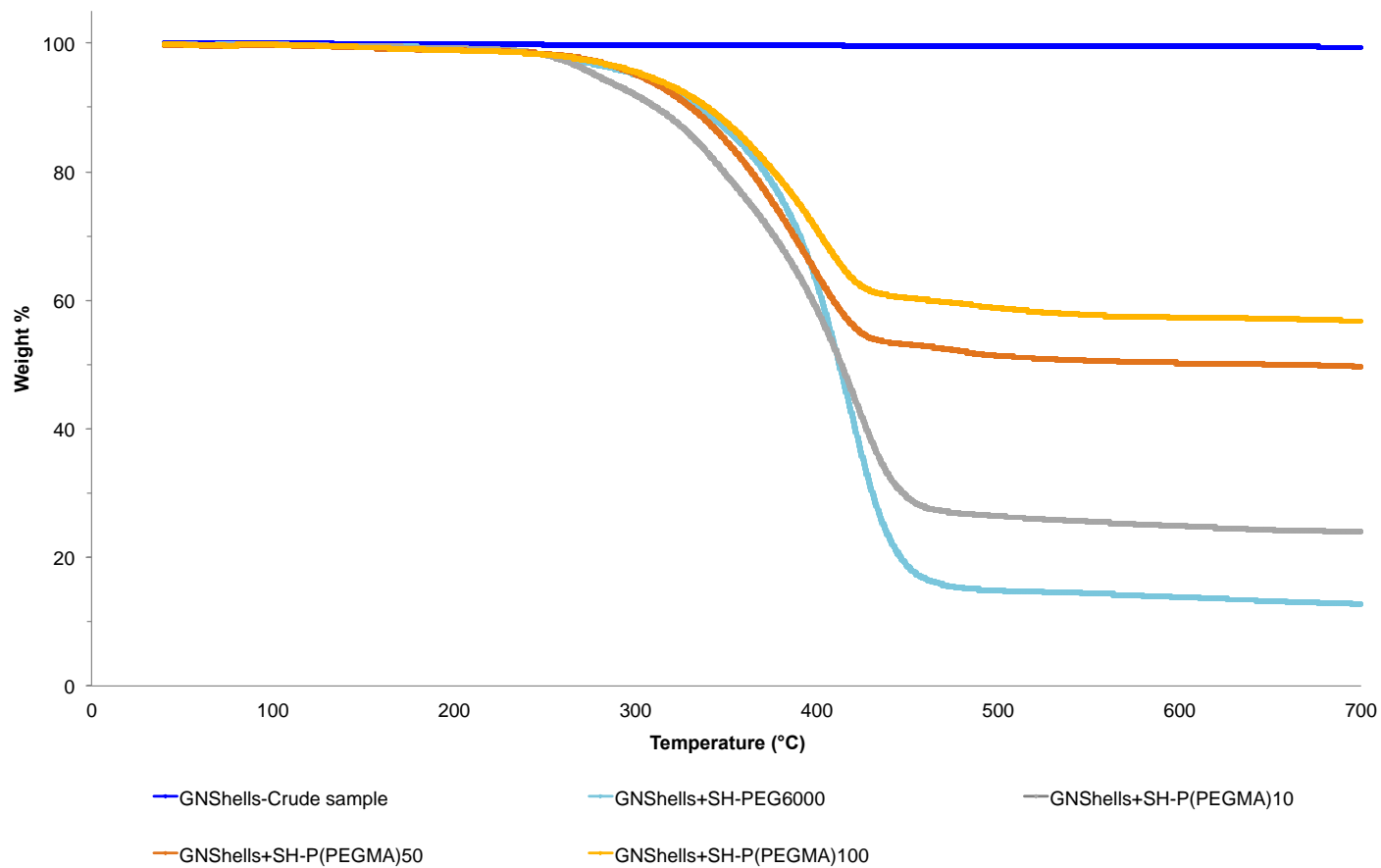
Figure 3.18. Thermogravimetric analysis of crude GNShells (dark blue), GNShells+SH-P(PEGMA)100) (yellow), GNShells+SH-P(PEGMA)50 (orange), GNShells+SH-P(PEGMA)10 (gray) and GNShells+SH-PEG6000 (light blue).

Table 3.3. Calculated specific surface area (m^2 g^{-1}), grafting density (µmol m^{-2}, chain nm^{-2}) and number of polymer chain per GNShell.

Gold nanoparticles	Calculated specific surface area (m^2 g^{-1})	Weight loss (%)	Grafting density (µmol m^{-2})	Grafting density (chain nm^{-2})	Number of polymer chains per each nanoparticle
GNShell		0.00	0.00	0.00	0.00
GNShell+SH-PEG6000		80.00	114.30	68.80	619 200
GNShell+SH-P(PEGMA)10	5.83	65.50	77.55	46.70	420 300
GNShell+SH-P(PEGMA)50		43.70	8.93	5.37	48 330
GNShell+SH-P(PEGMA)100		36.70	3.5	2.10	18 900

The obtained grafting density as a function of polymer M_n revealed a correlation between grafting density and M_n of the SH-PEG/SH-PEGMA polymers, which is in good agreement with previous studies presented in Table 3.4 (Xia *et al.*, 2011; Benoit *et al.*, 2012).

Table 3.4. The influence of surface-grafted polymer molecular weight on grafting density.

Surface-grafted polymer	M_w (gmol^{-1})	Grafting density	References
Thiol-functionalised methyl-poly(ethylene glycol) (mPEG-SH)	2 000	2.3 Chain/nm^2	Benoit *et al.*, 2012
	20 000	0.8 Chain/nm^2	
Thiol-PEG-Amine (HS-PEG-NH2)	3 000	8 860 chain/GNPs	Xia *et al.*, 2011
	5 000	4 760 chain/GNPs	
	20 000	1 010 chain/GNPs	

The grafting density (chain nm^{-2}) decreased with increasing molecular weight for SH-PEG6000 and PEGMA-based polymers (Figure 3.19). Therefore, denser packing (619 200 molecules/nanoparticle) was achieved for SH-PEG6000 compared to SH-P(PEGMA)100 (18 900 molecules/nanoparticle).

Figure 3.19. The grafting density (chain/nm^2) decreases with increasing molecular weight/chain length of the corresponding polymer (Benoit *et al.*, 2012).

Depending on the surface density and molecular mass of the SH-PEG/PEGMA grafted onto the GNShells surface, there are two possible regimes that SH-PEG/PEGMA chains can acquire, "mushroom" and "brush". The controlling factor is the distance between two polymer chains on the GNShells surface (D) relative to their Flory dimensions (R_f). The Flory radius (R_f) described as $R_f = \alpha n^{3/5}$ where n is the number of monomers per polymer chain and α is the length of one monomer in Angstroms (α = 3.5 A° for PEG). The effective distance between two grafting points (D) can be simply obtained by calculating the square root of the NP surface area divided by the number of PEG/PEGMA ligands (D= √NP surface area/number of polymers).

If the distance between the attached points of polymer to a surface is larger than its Flory dimensions, the mushroom conformation is acquired indicative of low density polymer coverage, and therefore the polymer chains are not fully extending away from nanoparticle surface, resulting in a thin coverage layer. In contrast, brush conformation is known to occur for high surface densities; when D decreases compared to R_f, the polymer chains are arranged in a brush conformation, with the long and thin chains of SH-PEG/PEGMA polymers extending from the nanoparticle surface, resulting in a thick layer (Figure 3.20) (Jokerst *et al.*, 2011).
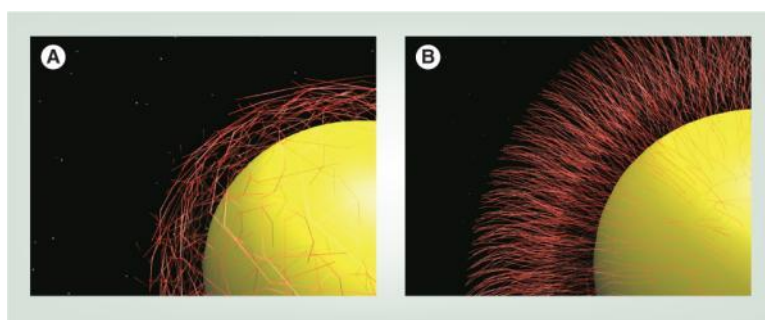
Figure 3.20. Gold spherical nanoparticle with two types of PEG modifications. PEG orientations on the nanoparticle surface include (A) low-density mushroom configurations and (B) high-density brush-type arrangements (Jokerst *et al.*, 2011).

The values of R_f and D were estimated in Table 3.5. The Flory radius of the grafted polymers increased as a function of the number of monomers (n) and

the distance between grafted sites, D, also increased at lower grafting density (chain nm^{-2}). In this study, none of the D values was found to be greater than R_f, therefore upon the basis of R_f and D, all four thio-end polymers were in brush conformation (Figure 3.21).

Table 3.5. Calculated values of the distance between two polymer chains (D) and their Flory dimensions (R_f) for estimating the molecular conformation of the grafted thiol-end polymers.

Gold nanoparticle	Distance between the two grafted polymer chains (D)	Flory radius (R_f)	Conformation
GNShells+SH-PEG6000	0.120	6.67	
GNShells+SH-P(PEGMA)10	0.146	8.52	
GNShells+SH-P(PEGMA)50	0.431	18.30	Brush (R_f>D)
GNShells+SH-P(PEGMA)100	0.690	26.72	
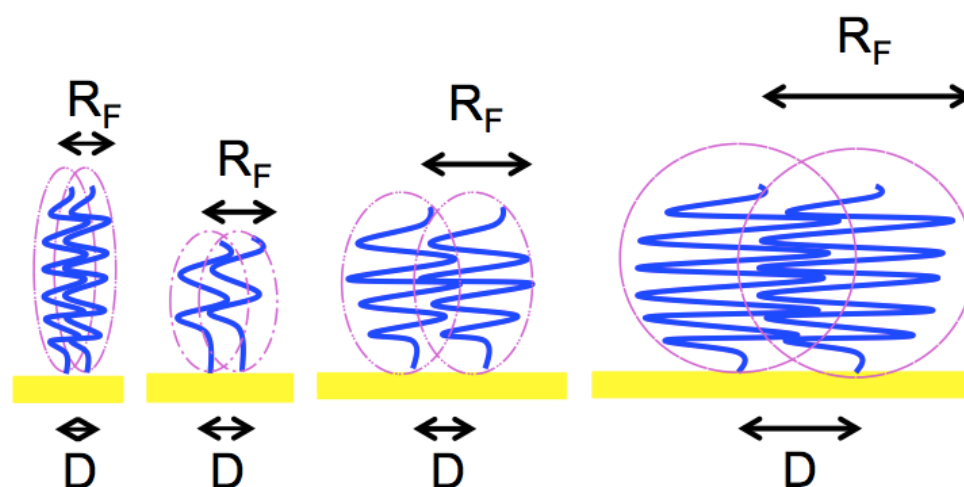
Figure 3.21. Schematic of the grafted thiol-end polymers (from left to right); SH-PEG600, SH-P(PEGMA)10, SH-P(PEGMA)50 and SH-P(PEGMA)100 in brush conformation. Despite the variation in length of the polymers and their grafting densities, the Flory dimensions (R_f) were obtained to be larger than the distance between grafting points (D) for all the four batch of the polymer chains on the GNShells surface (R_f>D).

It is important to mention the well understood fact that stretching-entropy and excluded-volume interactions influence the chain density in the brush regime,

in both cases as a result of the lateral confinement. Thus by varying the chain density, chain conformations ranging from unperturbed random coils to fully extended forms can, in principle, be obtained (see figure 3.21) (Unsworth *et al.,* 2005). Overall, the data suggests that the grafting protocol was very efficient for coating the GNSsells with high fidelity for all the polymers tested.

The DLS experiment was used to determine the hydrodynamic diameter (D_h) of the GNShells after PEGylation. The obtained data is shown in Table 3.6.

Table 3.6. Hydrodynamic size (D_h) of the GNShells after PEGylation with thiol-terminated polymers.

D_h (nm)			
GNShells+SH-PEG6000	**GNShells+SH-P(PEGMA)10**	**GNShells+SH-P(PEGMA)50**	**GNShells+SH-P(PEGMA)100**
70.63 ± 1.91	64.94 ± 2.42	67.87 ± 2.20	70.58 ± 1.46

The increase in hydrodynamic size (D_h) of the PEGylated shells could be related to the formation of larger particles (due to surface coating) that affect the Brownian motion and light scattering over time (Lee and El-Sayed, 2005).

The reported hydrodynamic sizes for originally synthesised GNShells was 60.44 ± 2.16 nm and linearly increased from 64.94±2.42 nm for SH-P(PEGMA)10 to 67.87 ± 2.20 nm and 70.58 ± 1.46 nm for SH-P(PEGMA)50 and SH-P(PEGMA)100 grafted GNShells evidencing that PEGMA polymer with the higher molecular weight/longer chain length provides a thicker brush shell around the nanoparticles. However, the hydrodynamic sizes of PEG6000-grafted GNShells was reported to be 70.63±1.91 nm, which is about the same value as that of GNShells+SH-P(PEGMA)100.

The thickness of the grafted polymer layers on the GNShells surface correlates with their reported grafting densities (chain nm^{-2}) and conformation i.e. the grafted polymers adopt the extended chain conformation as a function

of grafting densities (chain nm^{-2}). In the case of the SH-P(PEGMA)10 and PEG6000 polymers, low molecular weight and high grafting density indicated the adaptation of extended chain structures and dense brush regimes, whereas, the polymers SH-P(PEGMA)50 and SH-P(PEGMA)100 with higher molecular weights and lower grafting density values adopted a close-packed layers of unperturbed coils that are referred to as 'dilute brush regime' (see Figure 3.22).
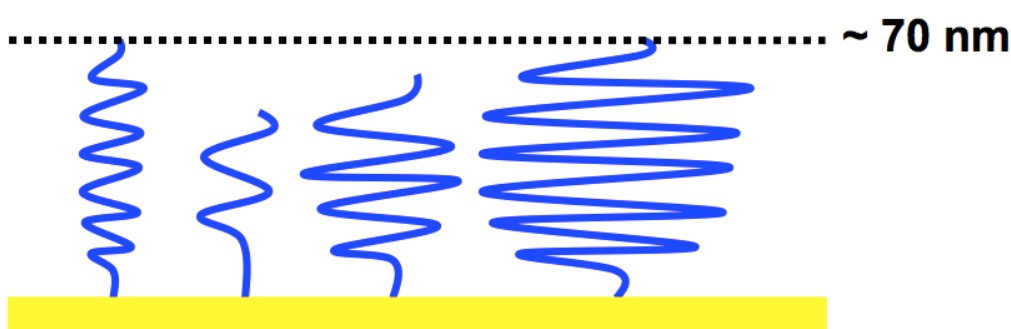
Figure 3.22. Illustration of a polymeric solid in stretched and relaxed states. From left to right: SH-PEG6000, SH-P(PEGMA)10, SH-P(PEGMA)50 and SH-P(PEGMA)100 in brush conformation. Increased conformational entropy of the PEGMA molecules with polymer chain length leads to an increase of their footprint at the GNShells surface.

The aforementioned comparison showed the influence of the polymer conformation on the hydrodynamic size of the nanoparticles, and also confirmed the well-controlled GNShells PEGylation as the saturation of anchoring sites on the gold surface and the coverage steric hindrance between the tethered chains prevented further chemisorption. Potentially, a low surface concentration of the grafted polymers could cause the collapsed PEG/PEGMA conformation, which in turn could result in the formation of large aggregates.

The colloidal stability of the PEGyalted GNShells in aqueous dispersion over time was investigated by monitoring the D_h of the nanoformulation after PEGylation for 14 days (Figure 3.23 and 3.24). Data are presented as the mean ± standard deviation of three separate samples.
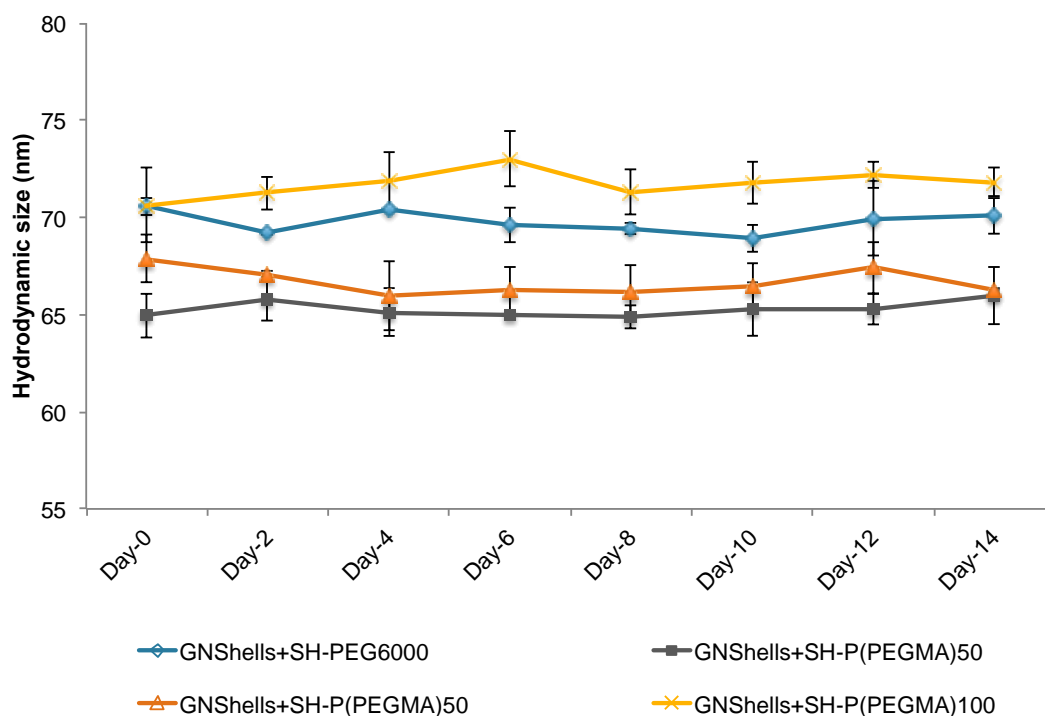
Figure 3.23. Colloidal stability of the PEGyalted GNShells throughout 14 days by monitoring the hydrodynamic size. The data represented as the mean of three experiments and the variations in the readings were shown as error bars (±SD).
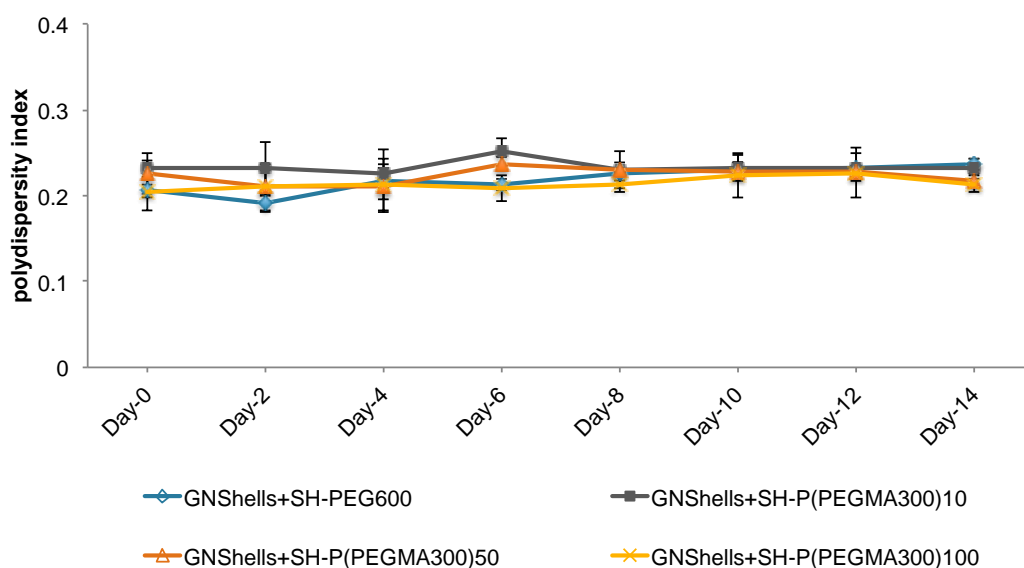
Figure 3.24. PDI of the PEGyalted GNShells throughout 14 days that further confirms their colloidal stability in time. The data represented as the mean of three experiments and the variations in the readings were shown as error bars (±SD).

No significant changes in D_h and PDI was observed by DLS over two weeks of storage at 4 °C, indicating the PEGylated GNShells remain well dispersed in water and maintain a narrow size distribution. Tables of numerical data and size distribution graphs are also presented in Appendix 2, 3 and 4.

The ζ-potential values represent the charge state at the slipping plane around moving particles. The ζ-potential value for the uncoated citrate stabilised GNShells was -37.5 mV and increased to -21.6 mV, -34 mV, -30.5 mV and -26.3 mV for SH-PEG6000, SH-P(PEGMA)10, SH-P(PEGMA)50 and SH-P(PEGMA)100 grafted GNShells, respectively.

The batch of GNShells coated with mPEG6000-SH had lower ζ value compared to that of synthesised thiolated PEGMA polymers with a carboxylic acid functional group on each polymer chain end. Higher molecular weight polymers yielded higher levels of neutralisation. Although the electrostatic repulsion between charged nanoparticles decreases as a function of neutralisation degree, PEGylated nanoparticles maintain their colloidal stability due to steric repulsion that increases along with increasing the PEG chain length (Jokerst *et al.,* 2011). Furthermore, with the longer PEG polymer chain grafted to their surface, GNPs have a higher capacity to resist the adsorption of plasma proteins (Dobrovolskaia *et al.,* 2014). Monitoring the zeta potential values of the nanoparticles after PEGylation provided further evidence of colloidal stability of polymer-coated GNShells (Figure 3.25). Tables with numerical data are included in Appendix 5.
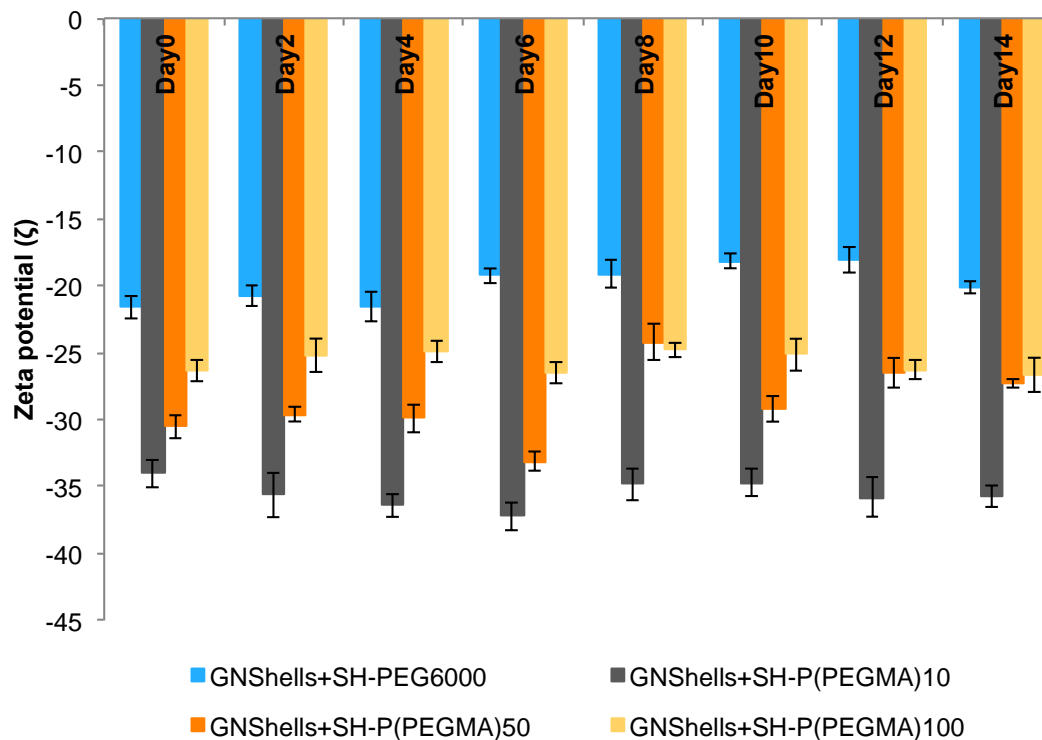
Figure 3.25. ζ-potential values (mV) of GNShells coated with thiol-terminated SH-PEG6000 (blue), SH-P(PEGMA)10 (gray), SH-P(PEGMA)50 (orange) and SH-P(PEGMA)100 (yellow) over the period of 14 days. The data represented as the mean of three experiments and the variations in the readings were shown as error bars (±SD).

As mentioned previously Gem exhibits anti-proliferative activity against adenocarcinomas of the pancreas. However, once introduced to the blood stream, Gem undergoes deamination by cytidine deaminase and is converted to an inactive uracil derivative with very short plasma half-life (8-17 min.) (Brusa *et al.,* 2007). The conjugation of Gem molecules to the gold nanoparticles surface *via* covalent bonding (Au-N), protects Gem's metabolite 4-(N)-amine group against enzymatic degradation and improves its metabolic stability and consequently the cytotoxic activity (Cavalcante and Monteiro, 2014). The cellular metabolism of Gem has been explained in detail in section 1.2.

Gem has an exocyclic amino group located at the 4th position, with the ability to establish high affinity interaction with gold *via* chemisorption. In terms of the Hard Soft Acid Base (HSAB) theory, GNPs do not effectively coordinate to a donor nitrogen atom. However, the nature of bonding interaction between gold and Gem can be attributed to the electron delocalisation from the lone pair on the nitrogen atom to the empty orbitals of the gold atom, which promote this binding reaction (Koo *et al.*, 2015; Radenkovic *et al.,* 2017)

XPS studies confirmed the attachment of Gem molecules on the metallic surface (Table 3.7). XPS involves the energy analysis of photoelectrons emitted from a surface due to the impact of characteristic X-rays, under vacuum conditions.

The nitrogen 1s peak with binding energy at ~ 399.5 eV represented as un-ionised, non-protonated nitrogen, which demonstrates that the nitrogen atom was successfully incorporated into the GNPs surface *via* covalent bonding.

The typical Au 4f core-level XPS spectrum with the spin-orbital coupling observed at ~ 83.6 eV (Au 4*f* 7/2) and ~ 87.4 eV (Au 4*f* 5/2) corresponds to metallic Au (0). There was no sign of oxidised Au (III) peak, which is usually appears at a binding energy of around 92 eV, indicating that all of the gold salts used in GNShells synthesis are reduced and are in the form of metallic gold.

The obtained results were in agreement with previous studies on adsorption of proteins/amino acids or nucleotides on gold surfaces (Demers *et al.,* 2002; Bhattacharya *et al.,* 2004; Patra *et al.,* 2008; Ashwell *et al.,* 2011; Xin *et al.*, 2013; Koo *et al.*, 2015; Vilian *et al.*, 2015; Won *et al.,* 2016; Radenkovic *et al.,* 2017).

Table 3.7. X-ray photoelectron spectra of gold (a) and nitrogen (b) obtained from GNShells-Gem conjugates.

	a	b
GNShells+ SH-PEG6000 +Gem		
GNShells+ SH- P(PEGMA)10 +Gem		
GNShells+ SH- P(PEGMA)50 +Gem		
GNShells+ SH- P(PEGMA)100 +Gem		
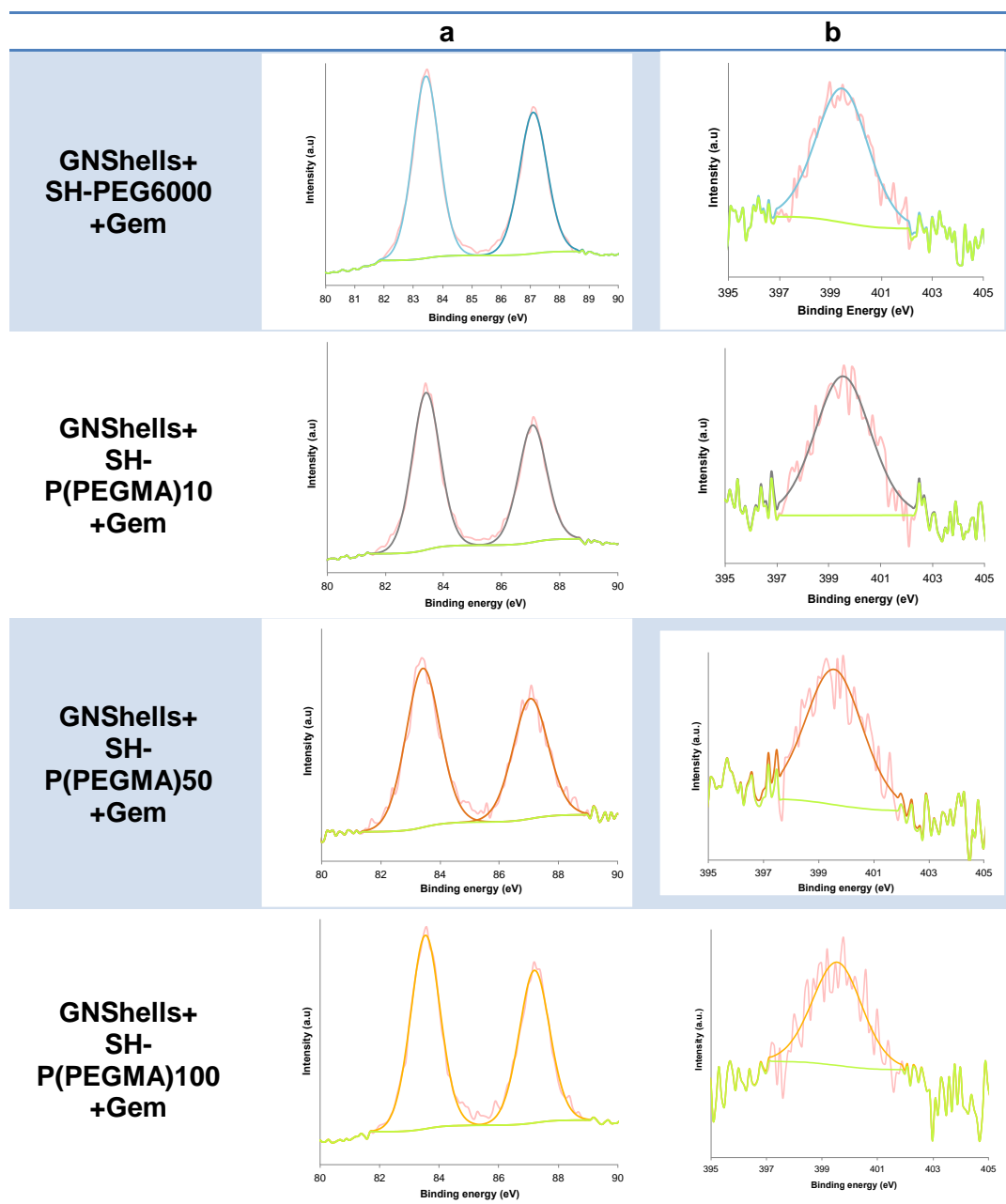
XPS composition-depth profile measurements shown in Table 3.8 were carried out to examine the atomic distribution of nitrogen on the NPs surface after loading of Gem on PEGylated GNShells. The results showed the decrease in N and increase in Au atomic percent profile upon etching closer to the surface of GNShells (14 etch cycles and each etch level was 5 s). This implies that although Gem travels along the polymer boundaries to the GNShells surface to form a covalent bond but larger amount of Gem molecules trapped within the polymer coating or interact with the coated-polymer electrostatically.

Table 3.8. XPS composition-depth profiles (atomic percent against etch time (s)) of GNShells+SH-PEG6000+Gem (a), GNShells+SH-P(PEGMA)10+Gem (b), GNShells+SH-P(PEGMA)50+Gem (c), GNShells+SH-P(PEGMA)100+Gem (d).
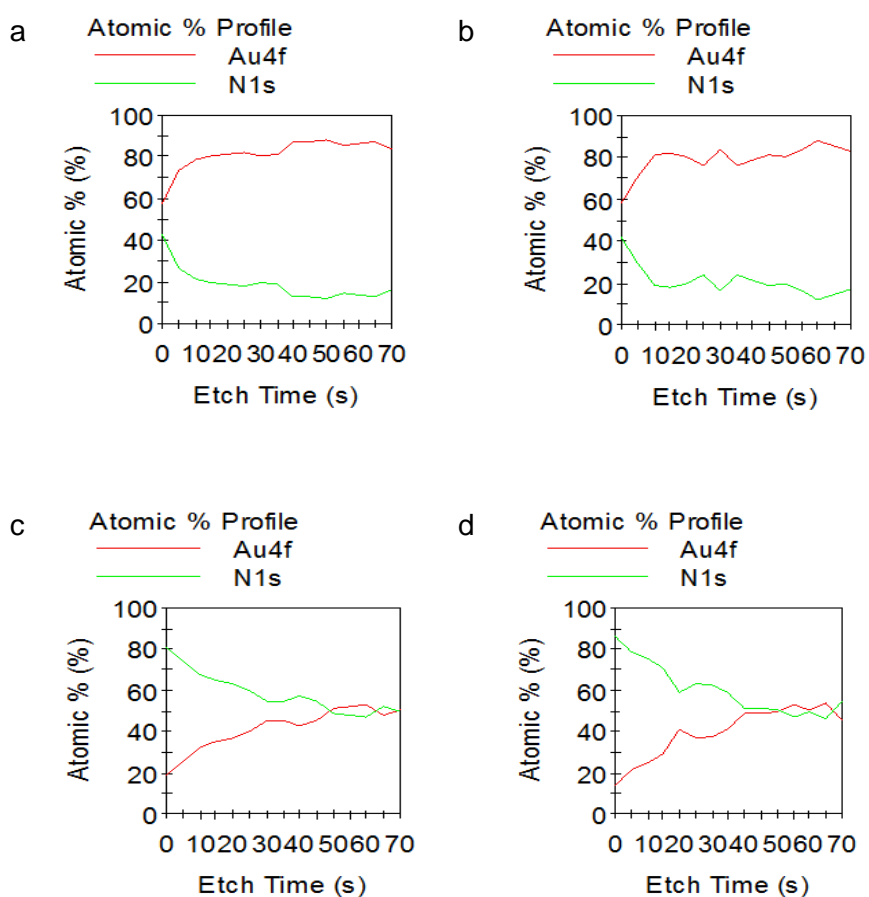
The extinction spectra of each of the Gem-loaded GNShells samples were collected and the surface plasmon resonance (SPR) band position and width were reported (Figure 3.26). The peak positions did not change significantly, indicating there is little or no agglomeration of nanoparticles after drug loading (Figure 3.27). However, a decrease in intensity of the SPR bands implied the loss of nanoparticles possibly due to sticking to the filter after centrifugation. Moreover, Gem loading did not alter the hydrodynamic size of the nanoparticles (Appendix 6, 7 and 8). However, there was an increase in average ζ-potential from -21.6 mV, -34.0 mV, -30.5 mV and -26.3 mV to -15.8 mV, -29.6 mV, -26.3 mV and -20.3 mV for SH-PEG6000, SH-P(PEGMA)10, SH-P(PEGMA)50 and SH-P(PEGMA)100 grafted GNShells after Gem loading that could be attributed to the cationic nature (amino groups) of the Gem molecules that were present on the surface of the functionalised GNShells (Appendix 9).
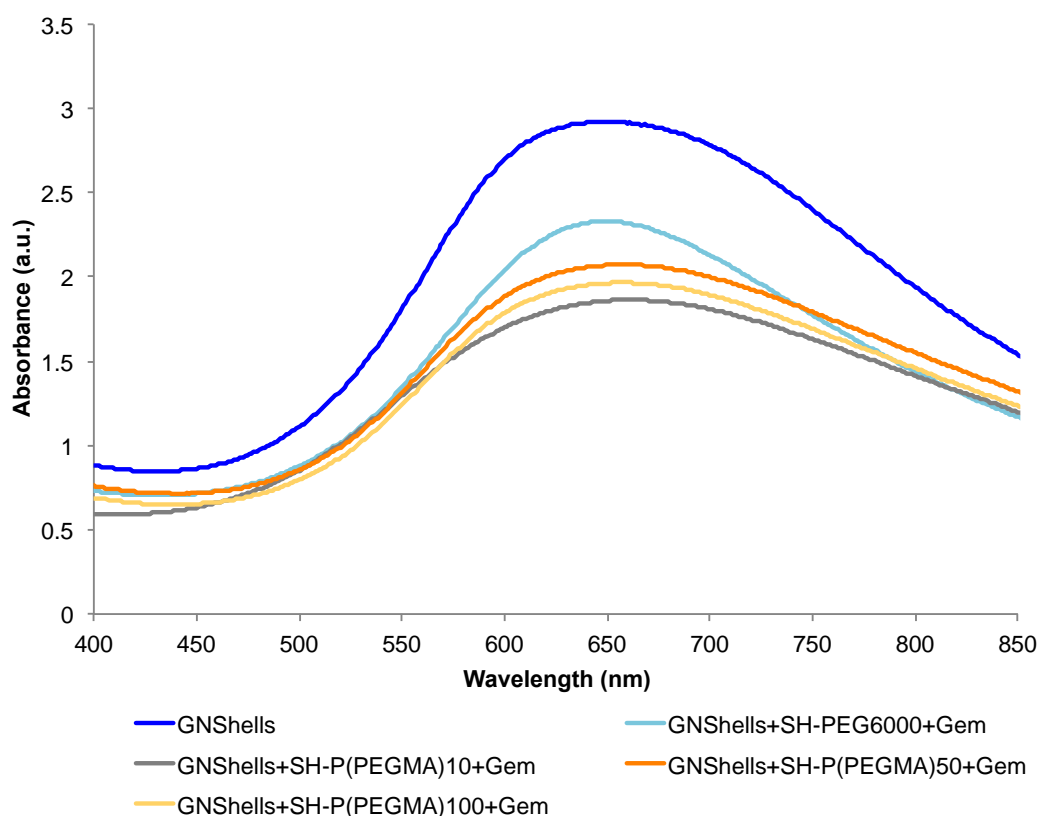
Figure 3.26. Optical absorption spectra of crude GNShells (Dark blue), GNShells+SH-P(PEGMA)10+Gem (gray), GNShells+SH-P(PEGMA)50+Gem (orange), GNShells+SH-P(PEGMA)100+Gem (yellow) and GNShells+SH-PEG6000+Gem (light blue).
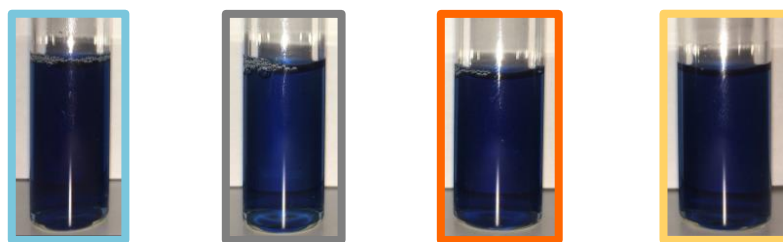
Figure 3.27. GNShells+SH-PEG6000+Gem (light blue). GNShells+SH-P(PEGMA)10+Gem (gray), GNShells+SH-P(PEGMA)50+Gem (orange) and GNShells+SH-P(PEGMA)100+Gem (yellow).

The data obtained from measuring the changes of D_h, PDI and ζ-potential of the nano-formulations over two weeks after drug addition, indicated the colloidal stability of the functionalised GNShells in aqueous dispersion over time (Figure 3.28, 3.29 and 3.30) (Appendix 6-9).
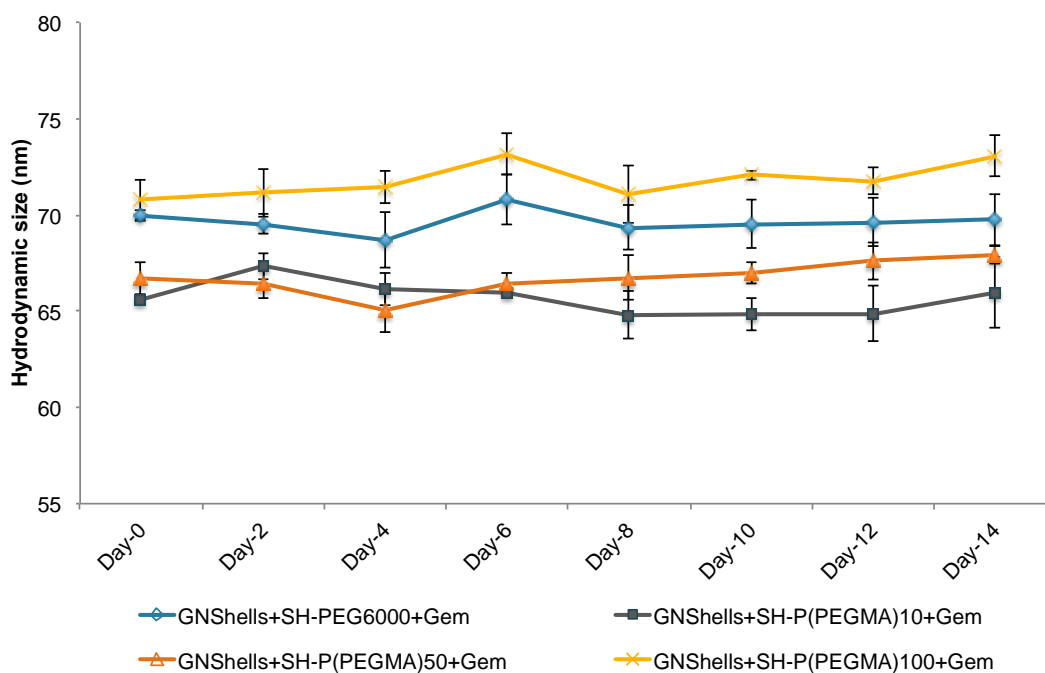
Figure 3.28. Colloidal stability of the Gem-loaded GNShells throughout 14 days by monitoring the hydrodynamic size of the nanoformulations. The data represented as the mean of three experiments and the variations in the readings were shown as error bars (±SD).
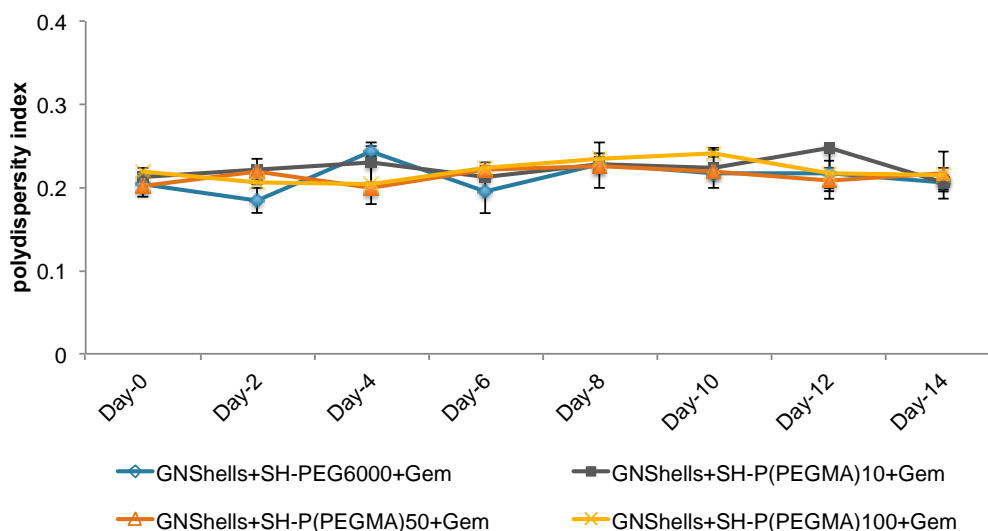
Figure 3.29. PDI of the Gem-loaded GNShells throughout 14 days indicating the stability of the overall distribution. The data represented as the mean of three experiments and the variations in the readings were shown as error bars (±SD).
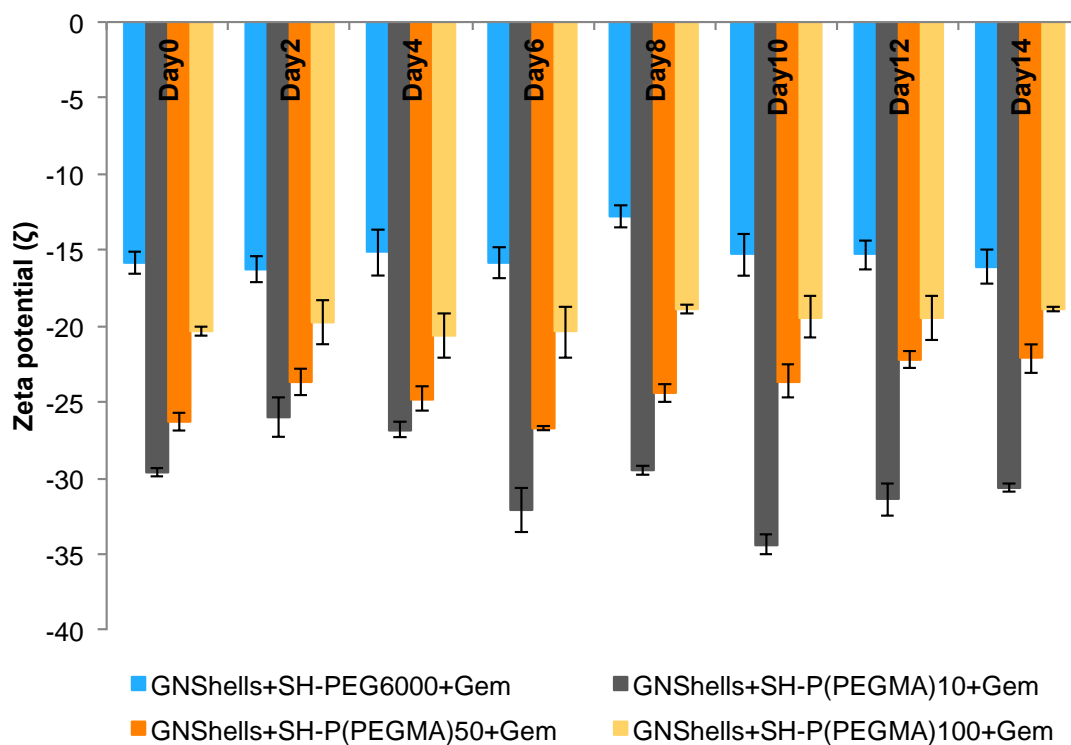
Figure 3.30. ζ-potential (mV) values of GNShells+SH-PEG6000+Gem (blue), GNShells+SH-P(PEGMA)10+Gem (gray), GNShells+SH-P(PEGMA)50+Gem (orange) and GNShells+SH-P(PEGMA)100+Gem (yellow) over 14 days. The data represented as the mean of three experiments and the variations in the readings were shown as error bars (±SD).

The percentage amount of free Gem in the supernatant solution after ultracentrifugation of Gem-conjugated GNShells (SH-PEG/SH-PEGMA+GNShells+Gem) was measured by the developed HPLC method.

A simple, fast, reliable, and reproducible method for quantifying Gem.HCl was developed by performing reversed-phase HPLC. In this study, a buffer containing alkylsulfonate (sodium-1-octane-sulphate) was used in order to properly retain the analytes. The polar embedded C18 with TMS endcapping was used as a stationary phase (phenomenex Synergi™ 4 µm Polar-RP 80 Å, LC Column 250 x 4.6 mm).

The concentration of Gem was determined by using UV detection at 270 nm. The total analysis time was 20 min per sample. Figure 3.31 displays the ideal HPLC chromatogram of Gem with a sharp symmetrical shape on a flat baseline.
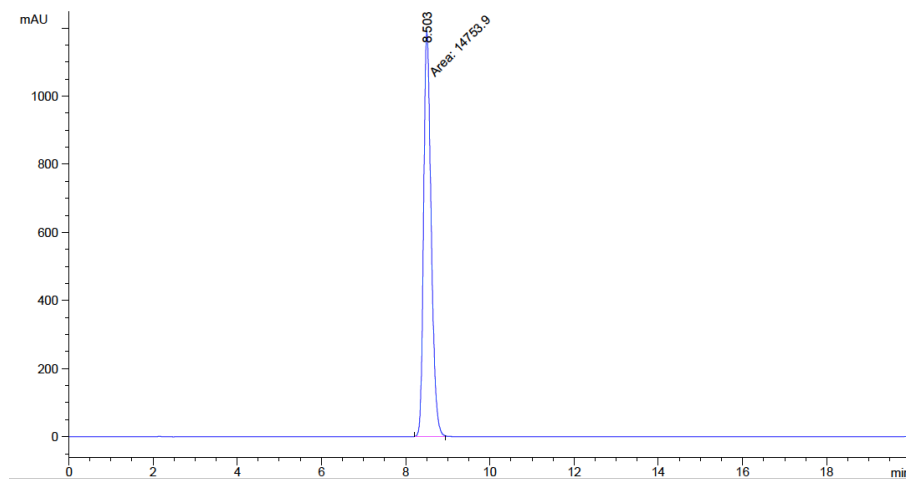
Figure 3.31. HPLC chromatogram of Gem.

Calibration curves were obtained by using linear regression analysis of nine-point concentration curves (Appendix 10). The regression parameters including slope, intercept, and correlation coefficient (R^2) are shown in Table 3.9. Excellent correlation coefficients were found ($R^2 > 0.9989$ in all cases) and linearity was checked for the range of concentrations from 75 µg mL^{-1} down to LOD and LOQ of the respective analytes. The relative standard deviation (%RSD) and recovery (%) was found to be satisfactory. Selective chromatograms of Gem in different media are presented in Appendix 11.

Table 3.9. Analytical data for Gem detection. Data are the mean of three separate experiments (n=3).

Analyte	Retention time (min)	Regression parameters (y=$slope$x+$intercept$)	R^2	Limit of Detection (LOD) (µM)	Limit of Quantitation (LOQ) (µM)	Relative standard deviation (% RSD)	Recovery (%)
Gem in H$_2$O		y = 40.3x - 21.68	0.99894	3.00	9.11	0.11 - 1.49	96 - 105
Gem in PBS		y = 39.116x - 7.78	0.99947	2.13	6.48	0.07 – 2.33	97 - 106
Gem in Na.Ac. buffer	8.5	y = 42.053x + 11.64	0.99973	1.52	4.62	0.15 – 0.73	97 - 102
Gem in Medium		y = 39.854x + 10.31	0.9996	1.85	5.61	0.08 – 1.63	98 - 103

Table 3.10 shows the percentage amount of Gem attached to the GNShells surface calculated from HPLC data analysis. The results show 59% of Gem loading efficiency (%) for PEG6000-grafted GNShells, which was about 5-6% lower than that of SH-P(PEGMA) coated GNShells i.e. 65% drug loading (%) for GNShell+SH-P(PEGMA)10+Gem, 64% and 65% for GNShell+SH-P(PEGMA)50+Gem and GNShell+SH-P(PEGMA)100+Gem, respectively. As the prepared nano-shells were homogeneous in size, this small loading efficiency (%) variation could be related to the structural difference between the commercial PEG and synthesised PEGMA-based polymers. Although the bulky and relatively rigid structure of the thiol-terminated PEGMA polymer chains can reduce the drug access to the binding sites i.e. limits the conjugation of Gem molecules to GNShells surface by utilising Au-N bonding affinity, the Gem molecules can be trapped in inter-polymer complexes which are formed by the grafted PEGMA brushes. This is in accordance with the reported XPS composition-depth profiles (atomic percent against etch time (s)) of Gem-loaded GNShells.

Table 3.10. The percentage amount of Gem bound to the GNShells surface as calculated from HPLC data analysis.

Gold nanoparticle	Initial amount of drug in 1 ml of GNShells solution (µg/ml)	Loading efficiency (%)
GNShell+SH-PEG6000+GEM		59
GNShell+SH-P(PEGMA)10+Gem		65
GNShell+SH-P(PEGMA)50+Gem	100	64
GNShell+SH-P(PEGMA)100+Gem		65
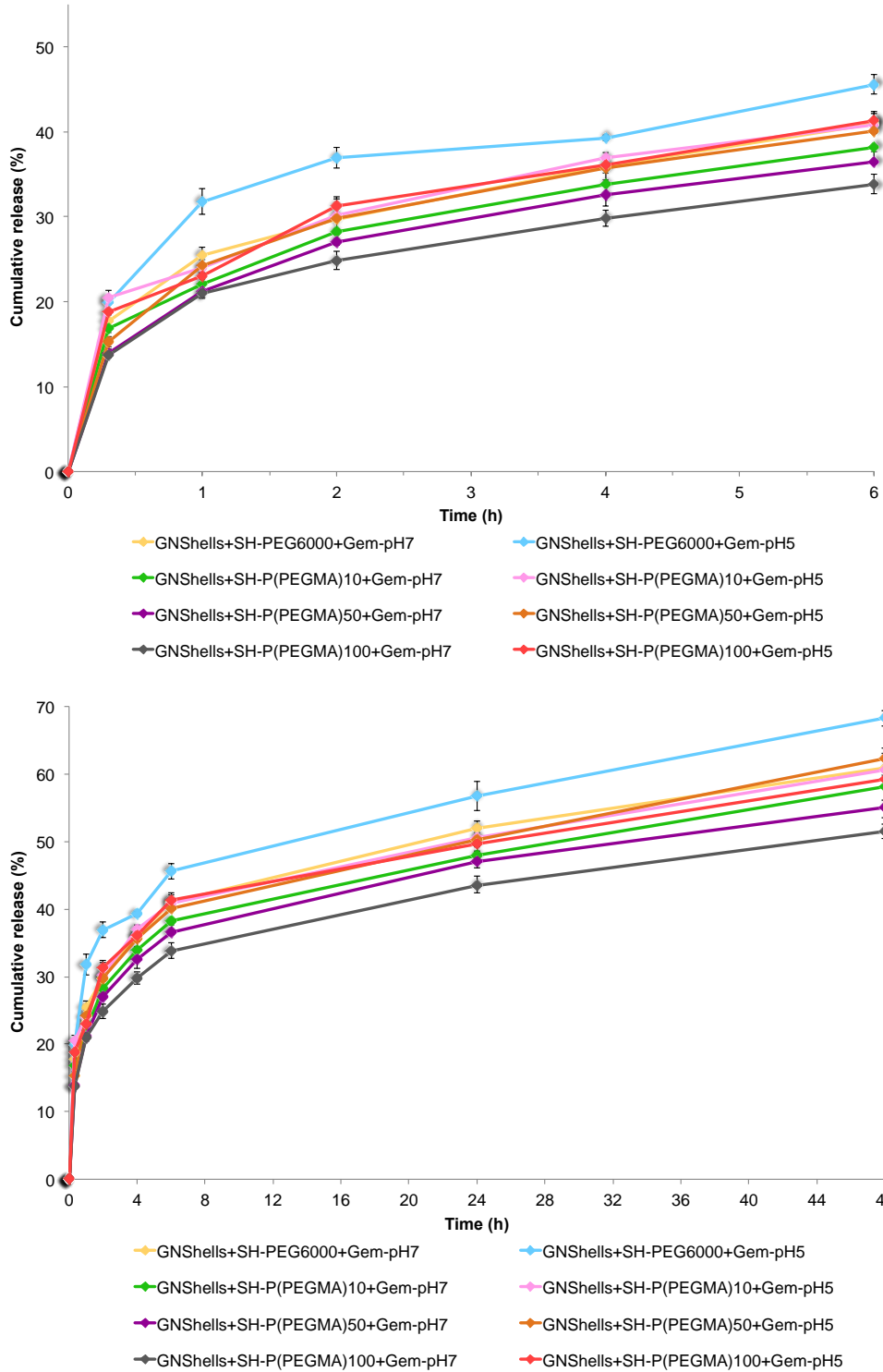
Figure 3.32. *In vitro* cumulative drug release profiles of Gem-loaded nanoshells dispered in PBS (pH 7.4) and acetate buffer (pH 5.2) over the first 6 h (top) and 48 h (bottom). The data represented as the mean of three experiments and the variations in the readings were shown as error bars (±SD).

It is worth mentioning that increasing the initial drug/GNShells ratio did not improve the loading efficiency (%), which indicates some sort of saturation binding that was reached for the concentrations studied. Therefore, with the obtained optimal loading efficiency, further characterisation was performed.

The drug release behavior of Gem-loaded nanoshells at 37°C was investigated in phosphate buffer saline (pH 7.4) to mimic the physiological environment and also performed in acetate buffer saline (pH 5.2) to mimic the acidic late endosome intracellularly. Cumulative percent Gem release was plotted against time (Figure 3.32).

The drug release profile of GNShell+SH-PEG/SH-PEGMA+Gem under each pH conditions showed two stages: a relatively rapid release of Gem within 6 h followed by a constant release of lower rate. The initial rapid release, known as "burst effect", occurs probably due to the physically adsorbed drug on the outer shell of the polymer layer (Hervault *et al.,* 2016).

The slower drug release after 6 h could be due to the diffusion barrier created by the PEG/PEGMA coating. The PEG chains interact with one another so that a complex could form amongst the grafted chains. As the polymer chain length increases and the more inter-polymer complexes are formed, the release rate of the drug is decreased and that is the reason why Gem molecules showed slower release from GNshells coated with SH-P(PEGMA) polymers than from the SH-PEG coated ones. Furthermore, the complexation effects of the grafted polymer conformations provided an additional diffusion barrier for a more tortuous path for drug release (Lee *et al.,* 2015). GNShell+ SH-P(PEGMA)100+Gem showed the slower release rate compared to all other nanoformulations.

The percentage of cumulative release in PBS at pH 7.4 was found to be 41% at 6 h and 61% at 48 h from GNShell+SH-PEG6000+Gem. Moreover, in PBS (pH 7.4) at 6 h, 38%, 36% and 33% of Gem was released from GNShell+SH-P(PEGMA)10+Gem, GNShell+SH-P(PEGMA)50+Gem and GNShell+ SH-P(PEGMA)100+Gem, respectively. While the release at 48 h was reported to

be 58% for GNShell+SH-P(PEGMA)10+Gem, 55% for GNShell+SH-P(PEGMA)50+Gem and 51% for GNShell+SH-P(PEGMA)100+Gem.

At 6 h, 45%, 41%, 40% and 41% Gem was released in acetate buffer saline (pH 5.2) from GNShell+SH-PEG6000+Gem, GNShell+ SH-P(PEGMA)10+Gem, GNShell+ SH-P(PEGMA)50+Gem and GNShell+ SH-P(PEGMA)100+Gem, respectively. While at 48 h the measured percentage of cumulative release values were 68% for GNShell+SH-PEG6000+Gem, 60% for GNShell+SH-P(PEGMA)10+Gem, 62% for GNShell+SH-P(PEGMA)50+Gem and 59% for GNShell+SH-P(PEGMA)100+Gem.

In acidic media (pH 5.2), more Gem release was obtained compared with physiological pH (pH 7.4) but the reported differences were not statistically significant. Nevertheless, the slightly enhanced release (4%-8%) could be due to the protonation of the Gem under acidic condition, which improves its water solubility (Dai *et al.,* 2017).

The behavior of Gem-conjugated GNPs and its drug delivery efficacy *in vitro* were examined by performing MTT assay, which was compared with plain Gem. The MTT assay is designed to monitor the MiaPaCa-2 cells viability (metabolic activity) based on the conversion of tetrazolium salt into formazan crystal by mitochondrial activity of viable cells (Meerloo *et al.,* 2011). Any change in the number of viable cells that is linearly related to their mitochondrial activity was obtained by measuring the absorbance of the formazan product using spectrophotometer. EC_{50} (the half-maximal effective concentration of drug) was determined from the dose-response curves obtained by the MTT assay after treatment of MiaPaCa-2 cell with different concentration of Gem alone and Gem-loaded PEGylated GNShells at different time points (48 h and 72 h). The results are presented in Table 3.11 with their corresponding charts and graphs in Figure 3.33 and Appendix 12, respectively.

The results showed excellent viability of MiaPaCa-2 cells even after 72 h of incubation with PEGylated GNShells, which demonstrated that nano-shells were not toxic, and hence confirmed their suitability and safety for biological applications (data not shown). The obtained results showed that free Gem and all four samples of Gem-loaded PEGylated GNShells did not inhibit above 50% of cell growth (EC_{50} wasn't achieved) after 48 h of post-treatment. However, free Gem and all the PEG/PEGMA-coated nanoshells+Gem showed cytotoxic effect on MiaPaCa-2 cells after 72 h incubation with detected EC_{50} of 0.72 µM, 9.20 µM, 4.20 µM, 3.36 µM and 1.76 µM for free Gem, GNShells+SH-PEG6000+Gem, GNShells+SH-P(PEGMA)10+Gem, GNShells+ SH-P(PEGMA)50+Gem and GNShells+ SH-P(PEGMA)100+Gem, respectively.

Table 3.11. The cytotoxicity of anti-cancer drug Gem and the cytotoxicity of Gem-loaded PEGylated GNShells against MiaPaCa-2 pancreatic cell line. All the MTT experiments were performed in triplicate and the variation in EC_{50} are shown as mean±SD.

Cell line	Treated with	Incubation time (h)	EC_{50} (µM)
	Gem		0.72±0.18
	GNShells+SH-PEG6000+Gem		9.20±0.27
MiaPaCa-2 (1x10^4 cells/well)	GNShells+SH-P(PEGMA)10+Gem	72	4.20±1.40
	GNShells+SH-P(PEGMA)50+Gem		3.36±0.68
	GNShells+SH-P(PEGMA)100+Gem		1.76±0.31

As shown in table 3.11, SH-P(PEGMA)-coated GNShells exhibited higher cytotoxic activity than the GNShells coated with SH-PEG6000.

Enhanced cellular uptake and efficient penetration of nanocarriers inside tumor cells is paramount to successful anti-cancer therapy. The cellular uptake kinetics can be regulated by controlling the surface chemistry of NPs (Massignani *et al.,* 2009) and is highly depending on the coated-polymer

architecture (Deshpande *et al.,* 2004). The lower cytotoxic efficiency of GNShells+SH-PEG600+Gem might be possibly because of the long SH-PEG6000 chains (136 PEG units) with high grafting density (68.80 chain nm^{-2}), which might cause decrease in PEG chain hydration and mobility and hence affect NPs interactive potential with the cell membrane (Massignani *et al.,* 2009; Salatin and Yari Khosroushahi, 2017).

Since the synthesised GNShells were uniform in size and there was no significant difference between Gem-loading efficiency (%) of PEGylated GNShells (GNShells-SH-P(PEGMA)n, n= 10, 50, 100), higher cytotoxic activity of SH-P(PEGMA)100-coated GNShells among PEGMA-based nanoformulations could be related to the lower grafting density (2.10 chain nm^{-2}), higher R_f and dilute brush conformation of SH-P(PEGMA)100 that improved cellular internalisation and efficiency of GNShells+ SH-P(PEGMA)100+Gem.

The Fundamental understanding of the role played by grafted PEGMA polymers in cellular uptake of NPs is beyond the scope of this research and need to be further quantified.

Although the EC_{50} values of the Gem-loaded GNShells were found to be higher than that of the free Gem but due to the fact that the non-restricted cytotoxicity of chemotherapeutics limits the full use of their therapeutic potential, Gem-loaded GNShells extend the systemic circulation half-life of conjugated Gem, which in turn increase the concentration of drug at the site of action and provides strategies for more specific therapy.

As radiative and non-radiative properties of GNPs endow these nanocomposites with photothermal effects, combinational photo-chemotherapy could potentially augoment the cytotoxicity of cancer chemotherapeutic agents such as Gem, at elevated temperatures since GNPs can deliver both drug and heat simultaneously to the tumorigenic region in a highly confined manner.

a

b
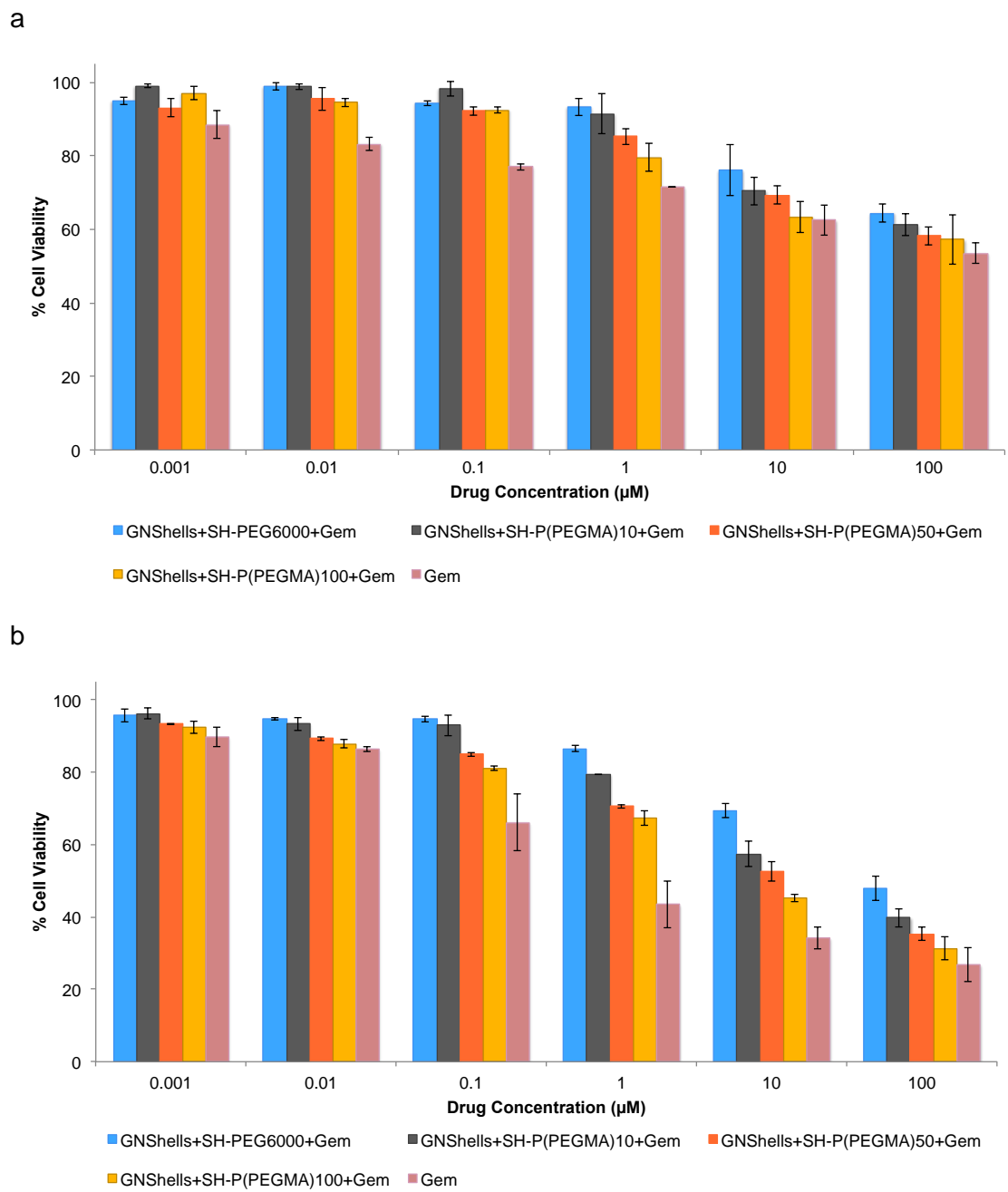
Figure 3.33. The bar charts represents cell viability (MTT assay) of MiaPaCa-2 cell line (1×10^4 cells/well) after 48 h (a) and 72 h (b) incubation with Gem alone and Gem-loaded PEGylated GNShells. The data represented as the mean of three experiments and the variations in the readings were shown as error bars (±SD).

3.5. Conclusion

Hollow spherical GNShells were synthesised using the galvanic replacement reaction. The GNShells were successfully functionalised with commercially available thiol-PEG (6,000 g mol^{-1}), and RAFT synthesised thiol-terminated PEGMA polymers with different M_n and were subsequently loaded with Gem. The covalent attachment of the SH-PEG/PEGMA and Gem molecules on the GNShells surface was confirmed by Raman and XPS, respectively. The data obtained from TEM/DLS and ζ-potential of the nanoformulations indicated the colloidal stability of the bi-functionalised GNShells in aqueous dispersions over two weeks. The number of grafted polymers per each nanoparticle and their brush conformation along with the amount of the conjugated Gem (µM ml^{-1}) was successfully determined by TGA and HPLC, respectively. The drug release experiments found no statistically significant difference ($p < 0.05$) between the Gem release in pH 7.4 and pH 5.2 at the end of 48 h. The *In vitro* cytotoxicity assay showed that, compared with the commercial SH-PEG6000, prepared gold nano-carriers enhanced cytotoxicity of Gem upon PEGylating with synthesised thiol-end RAFT-polymers, among which, SH-P(PEGMA)100 polymers, showed better cellular uptake efficiency and improved drug delivery, attributing to their lower grafting density and dilute brush conformation.

The next chapter describes the *in vitro* experimental results from combined photo- chemical treatment of cancer cells to improve the therapeutic efficiency of Gem.

Chapter 4

Increasing the cytotoxic potency of Gem with laser-induced hyperthermia mediated by GNShells+SH-P(PEGMA)100+Gem

This chapter is focused on the combination of chemo- and phototherapy in order to enhance the therapeutic outcome of the designed nanoformulation by augmenting the accumulation of Gem into tumor cells along and to simultaneously lower the effective dose that could potentially alleviate the side effects of Gem (Figure 4.1). In this chapter, Gem-loaded PEGylated GNShells (GNShells+SH-P(PEGMA)100+Gem) were used for multimodal cancer therapy due to its ability of delivering the cytotoxic drug and inducing heat simultaneously in a spatiotemporally confined manner. The effect of photothermal therapy on the drug release profile and the cellular uptake of functionalised GNShells was investigated. *In vitro* synergistic chemothermal therapy effects of the designed nanoformulation at different concentrations and laser power densities were also studied.
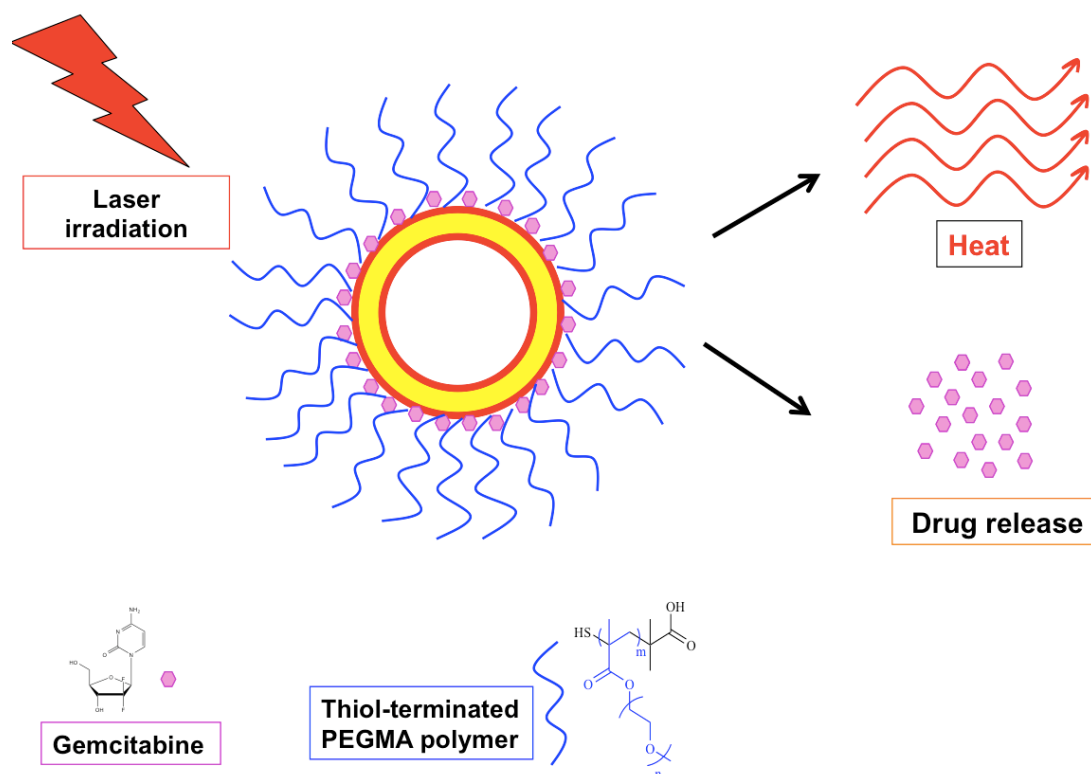
Figure 4.1. The colloidally stable GNShells+SH-P(PEGMA)100+Gem have been developed in order to enhance the therapeutic efficacy of Gem in combination with phototherapy, resulting in synergism of the two modalities.

A more detailed analysis regarding the effects of hyperthermia and its contribution to to the efficacy of chemotherapy, as well as its effects on cellular structures and physiology alteration, and the mechanisms of cell killing (apoptosis/necrosis) are described.

4.1. Introduction

4.1.1. Hyperthermia in combination with chemotherapy

There is no inherent difference among tumor cells, tumor vascular endothelial cells and normal cells regarding to their susceptibility to heat-induced cytotoxicity *in vitro*. However, tumor cells show thermo-sensitivity against mild hyperthermia (40 °C – 42 °C) *in vivo* (Hildebrandt *et al.,* 2002; Indran *et al.,* 2011). The susceptibility of cancer cells in response to heat is due to the inimical conditions of the tumor microenvironment. The chaotic vasculature causes insufficient blood flow across the solid tumor, which consequently stresses cancer cells by hypoxia, acidotic and nutrient-deprived milieu and renders them more "thermo-sensitive" compared to normal cells (Figure 4.2) (Chicheł *et al.,* 2007).
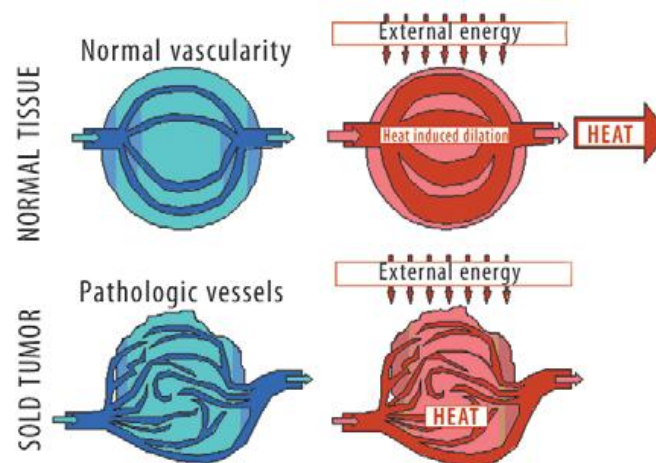
Figure 4.2. Heating the normal tissue results in intrinsic heat dissipation due to augmented blood flow. In contrast, intratumoral temperature increases over heating due to lack of organised vasculature structure (Chicheł *et al.*, 2007).

At temperatures above 42 °C, heat has a direct cytotoxic effect on tumor cells together with morphological changes such as endothelial swelling, shifting of the plasma fluid into the interstitium, micro-thrombosis due to activation of hemostasis, and change of the blood viscosity. All of these hyperthermia-induced changes can promote reduction of intratumoral blood flow and acidosis and cause irreversible damage to cancer cells (Hildebrandt *et al.,*

165

2002). Intense heating (>45 °C) termed as 'thermo-ablation' gives rise to sudden cellular death through necrotic mediated coagulation of cellular proteins. In contrast, moderate hyperthermia (≤42 °C) is used to optimise the temperature homogeneity in the tumor region, which is challenging due to the physical and physiological characteristics such as the electric tissue boundaries, the local perfusion variation and perfusion regulation (Wust *et al.,* 2002; Elsherbini *et al.,* 2011). Moderate hyperthermia improves tumor blood flow and therefore oxygen and nutrient contents in the target area and hence it constitutes an effective therapy in combination with other conventional modalities, especially chemotherapy (Wust *et al.,* 2002; Chicheł *et al.* 2007; Elsherbini *et al.,* 2011). Improvement of blood flow, fluid flux balance or pH adjustment and vascular permeability through moderate hyperthermia, enhances the cytotoxicity of many antineoplastic agents (chemo-sensitisation) (Indran *et al.,* 2011, DeWitt *et al.,* 2014). The type and concentration of drug, time interval between drug and heat application can affect the degree of chemo-sensitisation (Indran *et al.,* 2011). For instance, the drug-heat interaction of most alkylating agents (e.g. cyclophosphamide and ifosfamide), platinum and nitrosoureas compoundsenhances linearly their potency by elevating the temperature from 37 °C to 40 °C whereas, doxorubicin or bleomycin have a temperature threshold for synergistic interaction with heat at or near 42.5 °C. Conversely, most anti-metabolites (e.g. 5-fluorodeoxyuridin and methotrexate) as well as vinca alkaloids and taxanes show independent contribution to hyperthermia. Also, there are thermo-sensitisers that exert their cytotoxic action only at elevated temperatures (e.g. the local anesthetic drug lidocaine) (Bull, 1984; Engelhardt, 1987; Dahl, 1988). It has been recognised that the mechanisms of the thermal enhancement are generally supported by increased rate constants of alkylation, increases in intracellular drug uptake and inhibition of repair drug-induced lethal or sublethal damage (Zhao *et al.,* 2011). Research in drug-heat sequence demonstrated that thermal chemo-sensitisation is maximised by synchronous drug-heat application and is diminished at longer intervals (Rudin and Thompson, 1997). For example, ifosfamide should be applied several hours before hyperthermia because it undergoes extensive hepatic metabolism, however, in combination with regional hyperthermia, promising results have been achieved within shorter

intervals (Issels *et al.,* 1990; Wiedemann *et al.,* 1993; Urano *et al.,* 1999). In an exceptional case like the anti-metabolite Gem, a time interval of ~ 24 h between drug-heat application is necessary to achieve a synergistic effect *in vitro* and *in vivo* (Haveman *et al.*, 1995; Van Bree *et al.*, 1999).

It is worthwhile to note that the thermal energy dose required for the induction of cell death depends on the type of cancer cells, cell cycle phases, the amount of energy required for cellular protein denaturation (140 Kcal mol^{-1}), the duration of heating and the tumor microenvironment (Nikfarjam *et al.*, 2005). In the case of combination with chemotherapy, the thermal dose also depends on the type of the anti-cancer drugs (Hildebrandt *et al.*, 2002; Indran *et al.,* 2011).

When mammalian cells are exposed to heat shock above a threshold temperature with an interval shorter than 48 - 72 h, they develop 'thermotolerance' that is partially due to the expression of heat shock proteins (HSPs) and other post transitional adaptation processes (e.g. cell cycle arrest in the G2-phase and change in cell metabolism). Therefore, most fractionated hyperthermia regimens allow at least 72 h between sessions in order to minimise the clinical impact of thermotolerance (Overgaard, J. and Horsman, 1997; Sneed *et al.*, 2004; Jones *et al.*, 2004).

In general, hyperthermia with milder temperatures in combination with cytotoxic agents increases malignant cell destruction by enhancing the pharmacokinetics of the drugs while minimising the side effects in healthy tissue.

4.1.2. Cellular effect of hyperthermia

Hyperthermia (HT) induces non-lethal (in the temperature range between 39 °C – 42 °C) or lethal (>42 °C) changes in tissue physiology (Kanwal and Zaidi, 2013). The fundamental molecular event initiated by hyperthermia is protein

damage (cytosolic, nucleosolic and membrane proteins) (Spiro *et al.*, 1982; Michels *et al.,* 1997). Protein denaturation and aggregation cause structural and functional alterations of cellular components which results in protein synthesis inactivation, metabolic changes, membrane permeability modification, DNA synthesis impairment, DNA repair inhibition and modification of gene expression and signal transduction (Sonna *et al.,* 2002; Richter *et al.*, 2010).

Mild heat stress affects the cellular membrane fluidity and stability by obstructing the function of transmembrane transport proteins and cell surface receptors, and changes in the ratio of membrane protein to membrane lipids (Hildebrandt *et al.*, 2002; Richter *et al.*, 2010). Heat causes morphological changes of the membrane by transforming the tightly packed gel phase of the lipid bilayer into the less stiff liquid-crystalline phase (Kanwal and Zaidi, 2013) which leads to a decrease in viscosity and increase in permeability of the plasma membrane.

Enhanced membrane permeability can alter the membrane potential, change the ion homeostasis by elevating the activity of the intracellular ATP-dependent sodium-potassium pump (Ruifork *et al.,* 1987), activate the calcium ion dependent apoptotic pathway by over expressing the receptor inositol triphosphate that regulates the release of Ca^{2+} (Mikkelsen *et al.*, 1991; Cividalli *et al.*, 1999) and improve drug delivery by increasing the size of the endothelial gap in capillary vasculature (Gerner *et al.*, 1980; Lecavalier and Mackillop, 1985; Bates and Mackillop, 1986).

Mild HT has been demonstrated to induce disassembly of the cytoskeleton by converting the actin filaments into stress fibers, which can affect the correct localisation of the cellular organelles and disturb the intracellular transport process (Richter *et al.*, 2010).

Heat stress can also be the source of the fragmentation of the endoplasmic reticulum (ER) and the reduction of the number of mitochondria that results in excessive accumulation of misfolded proteins and dramatic reduction of ATP

levels, respectively (Ahmed *et al.*, 2008). In addition, aggregation and accumulation of ribosomal proteins, non-translating mRNA, initial components and other proteins involved in the process of translation, form large RNA-protein structures called stress granules in cytosol (Richter *et al.*, 2010).

Despite the fact that HT induces protein damage in virtually all cellular compartments, the nuclear environment shows even more sensitivity towards the heat shock (Roti Roti and Laszlo, 1988; Kampinga *et al.,* 1989; Lepock *et al.*, 1993; 2001; Michels *et al.*, 1995; 1997; Lepock, 2004). DNA fragmentation and formation of double-strand breaks, inhibition of transcription and DNA replication, and prevention of DNA repair mechanism (by denaturation of DNA polymerases or alteration of the chromatin structure) induce by HT and result in enhancement of the nuclear protein concentration, which leads to loss of cellular clonogenic or proliferative capacity via cell cycle arrest (permanent G1 arrest) or via apoptosis and/or necrosis (depending on the cell type, temperature and duration of the heat exposure) (Samali *et al.*, 1999; Sugahara *et al.*, 2008; Bettaieb and Averill-Bates, 2008).

As an example, upon exposure to 41 °C, CHO (chinese hamster ovary) cells undergo G1-arrest and become thermotolerant whilst, HeLa cells undergo M phase death after completion of DNA-synthesis (S phase) (Mackey *et al.* 1992; Mackey and Roti Roti, 1992; Higashikubo *et al.*, 1993; Kampinga, 1993; Roti Roti *et al.*, 1998). Several studies reported that cells are more sensitive to heat during mitosis (Yuguchi *et al.* 2002) and especially during the S phase of the cell cycle as the significant proportion of oncogenic transformation of cell occurs in the S phase (Kampinga and Dikomey, 2001; Hunt *et al.,* 2004; 2007).

As mentioned previously, environmental stress such as HT affects protein biosynthesis, folding, translocation and assembly into the native conformation (stable state), hence HT can disturb protein homeostasis by fluxing non-native proteins, which if left unprotected, are going through misfolding and aggregation. One of the known cytoprotective mechanisms in response to heat is the proliferation of heat shock proteins (HSPs). Immediately after HT,

tumor cells sense the stress and upregulate the transcription of genes that encode a class of stress-inducible proteins called heat shock proteins (HSP). Expression of HSPs is induced by transient activation of stress-responsive transcription factors known as heat shock factors-1 (HSF-1). HSF-1 binds to the promoter regions of various heat shock genes and provokes the synthesis of HSPs. The HSPs belong to the super family of proteins called molecular chaperones; under thermal condition they bind with high affinity to the non-native or (partially) unfolded proteins unselectively and prevent irreversible intracellular aggregation and repair protein damage (refolding proteins to their native structure) in order to re-establish protein homeostasis (Hildebrandt *et al.*, 2002; Kampinga, 2006; Richter *et al.*, 2010). The HSPs are divided into subgroups with different molecular mass and partially varying biological functions (e.g. HSP 27, HSP 60, HSP 70, HSP90, HSP100, etc.) (Parsell and Lindquist, 1993; Favatier *et al.*, 1997; Krebs and Feder, 1997). The chaperone activity of HSPs is transiently elevated during HT but is gradually depleted again after removal of heat. However, upon prolonged heating, HSPs increase cellular resistance to a subsequent stress by the development of thermotolerance (Landry *et al.*, 1982a ; 1982b; Hildebrandt *et al.,* 2002). Thermotolerance may occur upon continuous exposure (e.g. 3 to 24 h) of cultured cancer cells to non-lethal fever range temperature (39 °C – 41.5 °C) (Przybytkowski *et al.*, 1986; Ostberg *et al.*, 2002), which results from the accumulation of HSPs 27, 32, 60, 70, 90 and 110 (Przybytkowski *et al.*, 1986; Bettaieb and Averill-Bates, 2008). Increase in expression of HSPs 70 and 110 in mouse tissue have been reported as the result of exposing the MALB/c mice to the fever range whole body HT (39.5 °C – 40 °C) for 6 h (Ostberg *et al.*, 2002). On the contrary, lethal temperature (42 °C – 45 °C) can generate thermotolerance in cancer cells after about 10 to 30 min of heat exposure (Landry *et al.*, 1982a; 1982b; Subjeck *et al.*, 1982; Samali and Cotter, 1996).
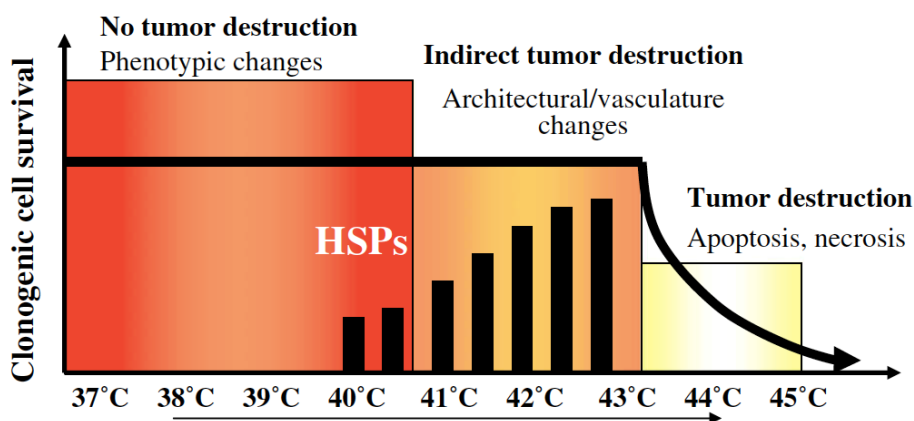
Figure 4.3. HT elevates the temperature in tumor site about 3 – 7 °C more than that of adjutant normal cells due to the great thermo-sensitivity of malignant cells. Mild HT improves blood flow, which in turn increases tissue oxygenation and makes cancer cells more chemo-sensitive. However, intense or prolonged thermal stress is thought to induce cell death (apoptosis or necrosis) by causing intracellular damages. Therefore, it is important to adjust an ideal temperature for the purpose of using HT in combination with chemotherapy (Issels, 2008).

Its important to note that HSPs promote the thermo-sensitive cells' recovery by development of thermotolerance in a time- and temperature-dependent manner via inhibiting mitochondrial or death receptor-mediated apoptosis pathways but over prolonged heating or high temperature application, cell death (apoptosis/necrosis) can not be prevented by HSPs-expression (Figure 4.3) (Issels, 2008).

4.1.3. Hyperthermia induced apoptosis

Apoptosis (also known as programmed cell death) is a highly regulated, energy dependent ordered cascade of enzymatic events and plays a crucial role in many biological processes such as embryonic development, regulation of cell numbers and tissue homeostasis (Kwak, 2013). The ability of cancer cells to avoid apoptosis and continue to proliferate is one of the hallmarks of cancer and the major focus of cancer therapy development (Hanahan and Weinberg, 2000). Many types of cancer treatments cause damage to cancer cells that result in apoptotic cell death. Stimulation of apoptosis in malignant

cells can therefore promote the susceptibility to anti-cancer treatments such as hyperthermia (Landry *et al.*, 1986; Kanwal and Zaidi, 2013). Two distinct molecular cascades known as intrinsic and extrinsic cellular pathways support the implementation of the apoptosis pathway (Figure 4.4).
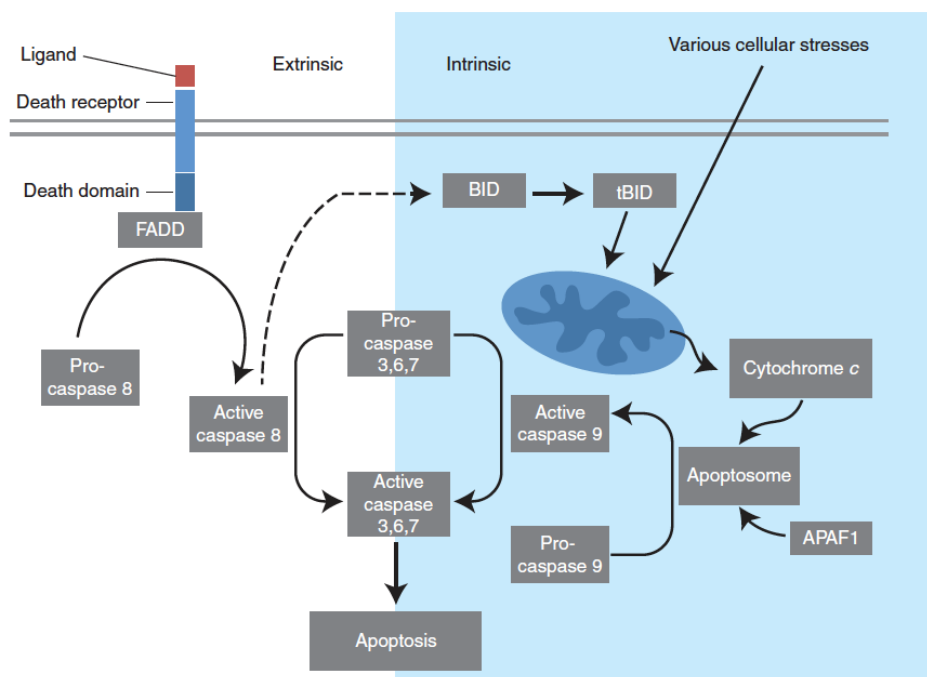
Figure 4.4. Extrinsic and intrinsic pathways of apoptosis. The intrinsic apoptotic pathway (also called as mitochondria-mediated apoptotic cascade) is activated in response to a variety of cellular stresses. The overexpression of pro-apoptotic proteins causes outer mitochondrial membrane permeabilisation and cytochrome c release. The cytosolic cytochrome c binds to the apoptotic caspase activating factor (Apaf1) and recruits procaspase-9 to form the apoptosome. Active caspase-9 then initiates apoptosis by cleaving and thereby activating executioner caspases (-3, -6, -7). The extrinsic apoptosis pathway is initiated by the binding of a ligand to a death receptor, which in turn leads to recruitment, dimerisation, and activation of caspase-8 with the help of the adapter proteins (FADD/TRADD). Once caspase-8 is activated, the execution phase of apoptosis is triggered either directly by cleaving and thereby activating executioner caspases (-3, -6, -7), or indirectly by activating the mitochondria-mediated apoptotic cascade through cleavage of BID (McIlwain *et al.*, 2013).

Although it has been shown that HT enhances the susceptibility of cancer cells towards apoptosis, molecular pathways that meditate HT-induced apoptosis are still a matter of controversy (Rong and Mack, 2000; Falk and Issels, 2001). HT alone or in combination with chemotherapy provokes elevated expression of tumor suppressor genes (e.g. P53), pro-apoptotic

factors (e.g. cytochrome c, ROS, Ca^{+2}) and heat shock proteins (HSPs), thereby, overcomes the suppression of apoptosis during carcinogenesis.

The HSPs encompass an anti-apoptotic role by the development of thermotolerance, however, if the thermal stress is sever, they are associated with the occurrence of programmed cell death in order to inhibit perpetuation of mutated DNA (Khan and Brown, 2002). For instance, it has been reported that HSP70 interferes with caspase activation by inhibiting the production and action of pro-apoptotic proteins such as Bax, cytochrome c release and direct blocking of apoptosome formation. However, under excessive stress, overexpression of HSP70, induces apoptotic cell death (Filippovich *et al.*, 1994; Liossis *et al.*, 1994).

Oxygen-free radicals, also known as reactive oxygen species (ROS) are highly reactive chemical species that are generated as by-products during aerobic respiration (Trachootham *et al.*, 2009). The excessive formation of ROS or perturbation of the antioxidant defense mechanism can disrupt redox homeostasis, leading to oxidative stress that plays a pivotal role in apoptosis (Kannan and Jain, 2000; Li *et al.*, 2003; Turrens, 2003; Valko *et al.*, 2006; Trachootham *et al.*, 2009). Increased level of endogenous ROS is prevalent in malignant cells due to oncogenic signaling, aberrant metabolism, mutant P53 and malfunction of mitochondria (Irani *et al.*, 1997; Brandon *et al.*, 2006; Horn and Vousden, 2007; Rodrigues *et al.*, 2008). Further exogenous ROS insults such as HT can induce further oxidative stress that promote the vulnerability of cancer cells to ROS damage, leading to apoptosis (depends on the magnitude and duration of thermal stress) (Lu *et al.*, 2008; Trachootham *et al.*, 2009). As an example, synergistic effects of mild HT (41 °C for 20 min) and a non-toxic dose of diketone macrosphelide (MS5) can activate a ROS-dependent apoptotic program in U937 cells (Ahmed *et al.*, 2007).

It has also been reported that, heat-shock- induced oxidative stress upregulates the activation of stress-activated protein kinases, JNK (c-Jun N-terminal kinase). JNK phosphorylates and regulates the activity of transcription factors such as c-Jun and P53, and non-transcription factors,

such as members of the Bcl-2 family Bim. Pro-apoptotic activity of Bim facilitates MOMP and promotes mitochondria- and caspase-dependent apoptosis (Hirano *et al.*, 2005).

HT can induce endoplasmic reticulum (ER)-triggered apoptosis in numerous malignant cells by augmentation of calcium levels in mitochondria, depletion of mitochondrial membrane potential ($\Delta\psi$m), overproduction of ROS and activation of intrinsic pro-apoptotic signals that can trigger apoptosis (Hou *et al.*, 2014). ER is involved in lipid and protein synthesis, protein post-translational modification and protein folding (Foufelle and Fromenty, 2016). When cancer cells are subjected to apoptotic stimuli such as HT, accumulation of unfolded or misfolded proteins in ER impact ER homeostasis and induce ER stress (Tsai *et al.*, 2013). ER stress elicits an elaborate signaling network called the 'unfolded protein response' (UPR), which is a protective and adaptive response with the aim to alleviate ER stress and maintain proper ER homeostasis. However, under severe/or prolonged stress conditions, the ER promotes apoptotic signaling cascades (Toltl *et al.*, 2011; Shellman *et al.*, 2008).

Furthermore, mild HT is also reported to trigger the extrinsic apoptotic pathway by activating the cell surface death receptors, which are overexpressed on the surface of the cancer cells (Gonzalvez and Ashkenazi, 2010). Death receptors transmit apoptotic signals that initiate by specific ligands such as Fas ligand, TNF alpha and TRAIL to the downstream caspases and induce apoptosis either directly through the activation of caspase-8 or indirectly via activation of BH3 only protein Bid (Tran *et al.*, 2003).

Apart from the classic extrinsic and intrinsic pathways, HT can induce programmed cell death through ER-mediated apoptosis. It has been determined that accumulation of Ca^{2+} in ER as a result of HT-induced ER stress in melanoma and non-melanoma skin cancer cells, triggers the proteolytic activity of Ca^{2+}-sensitive caspase-12 (located on the cytoplasmic side of the ER) that eventually activates caspase 3/7 and causes apoptotic

DNA fragmentation (Shellman *et al.*, 2008). Mechanism of apoptosis induced by hyperthermia (HT) is shown in Figure 4.5.
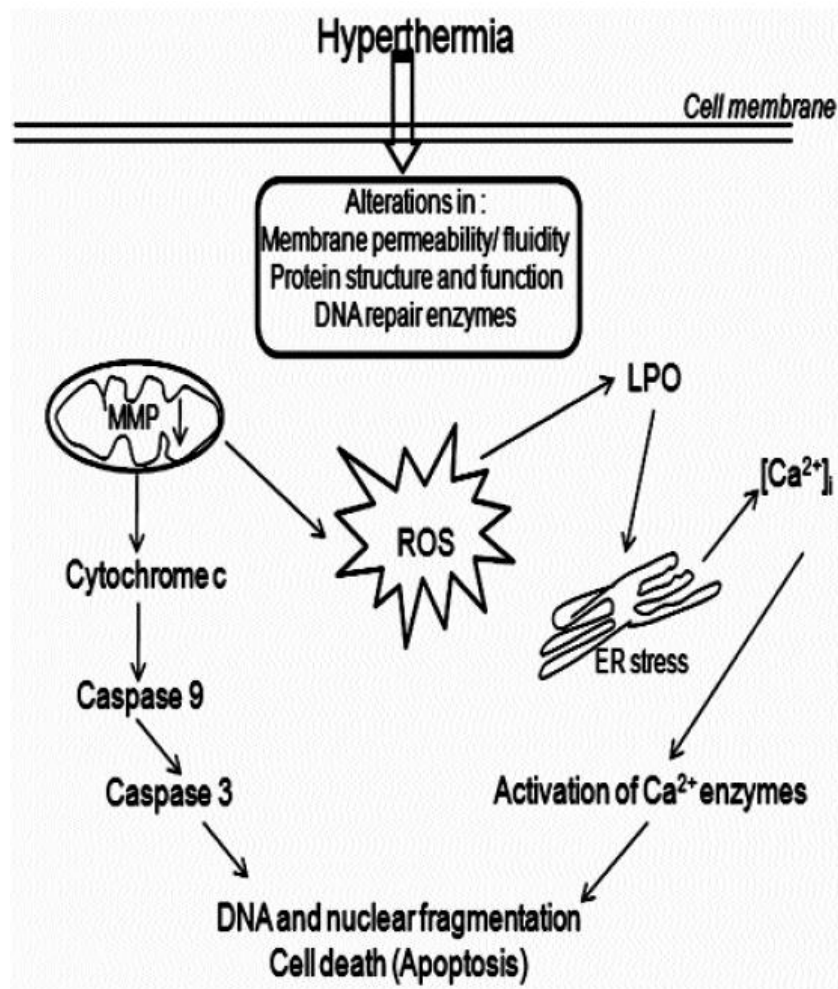
Figure 4.5. Mechanism of apoptosis induced by hyperthermia (HT). HT provokes membrane potential modification, protein unfolding and aggregation, mitochondrial malfunction, ROS production, lipid peroxidation (LPO) and ER stress regulation. Each of these cellular responses to heat can act as a mediator of apoptosis (Kanwal, A. and Zaidi, 2013).

HT induces both apoptosis and necrosis mediated cell death in cancer cells in a time and temperature dependent manner. Non-inflammatory and inflammatory outcomes of these two distinct pathways, which will be explained in more detail, raise interest in designing strategies for cellular protection against necrosis.

During apoptosis, cells undergo controlled suicide program where dismantling

intracellular components, elude the immune response and damage the surrounding tissue (Indran *et al.*, 2011).

The morphological characteristics of this tidy method of cell elimination include: cell shrinkage, increase in cellular density, chromatin condensation (by shifting to the margin of the nucleus), DNA fragmentation (by endonuclease activity) followed by nucleus fragmentation, maintenance of organelle integrity, plasma membrane blebbing, and formation of vacuoles containing cytoplasm and intact organelles called apoptotic bodies, followed by modification of plasma membrane phospholipid content (e.g. loss of asymmetric distribution of phosphatidylserines in the plasma membrane), to mark apoptotic bodies for engulfing and ingestion by phagocytes without causing an inflammatory reaction (Figure 4.6). (Vermes and Haanen, 1994; Tait and Green, 2010; Indran *et al.*, 2011; McIlwain *et al.*, 2013).

In contrast to the programmed cell death, pathological necrosis is an unexpected, accidental and energy independent mode of cell death in response to toxic insult or extreme trauma. Necrotic cells are characterised by the cell swelling, formation of cytoplasmic vacuoles, distended endoplasmic reticulum, formation of cytoplasmic blebs, condensed, swollen or ruptured mitochondria, disaggregation and detachment of ribosomes, disrupted organelle membranes, swollen and ruptured lysosomes, and eventually loss of cell membrane integrity (Elmore, 2007). Disruption of the plasma membrane results in releasing the cytoplasmic contents and pro-inflammatory molecules (e.g. cytokines) into the interstitial environment, which can cause inflammatory reactions and stress (Figure 4.6) (Edinger and Thompson, 2004).

A broad range of cytokines support tumor growth and dissemination, attenuate apoptosis and facilitate invasion and metastasis (Negus and Balkwill, 1996; Dranoff, 2004; O'Hayre *et al.*, 2008). These polypeptide immunomodulating agents are involved in autocrine, paracrine and endocrine signaling, and include interleukins, tumor necrosis factors, interferons, colony stimulating factors, peptide growth factors and chemokines.
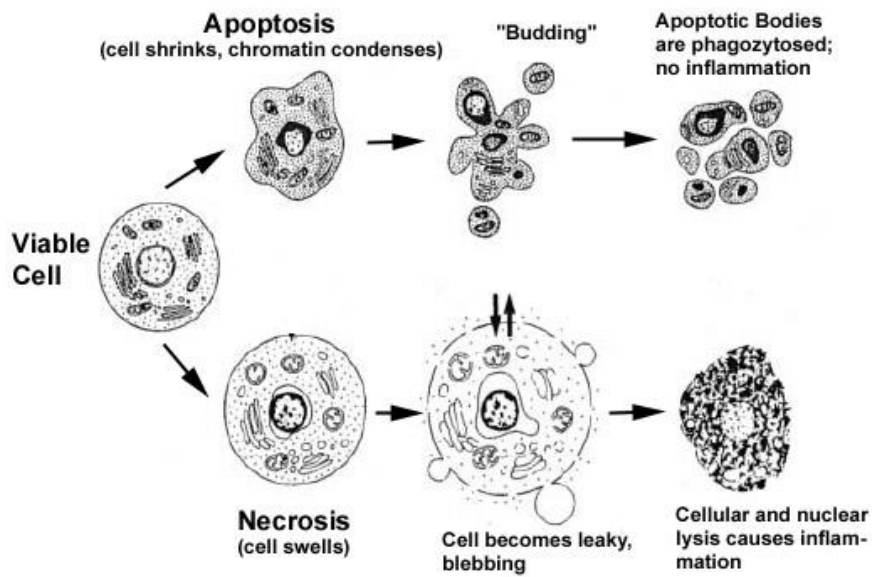
Figure 4.6. Morphological changes of a cell during apoptosis and necrosis (Andreas Gewies, 2003).

Increase in the release of pro-inflammatory proteins (chemokines in particular) triggers angiogenesis and tumor progression. Cytokines may also cause chemo-attraction of host immune cells (e.g. leukocytes), activation of other pro-tumorigenic enzymes and cytokines, foster proliferation and survival of cancer cells by activating ERK and PI3K pathways; they also influence the migration of cancer cells by regulating the production of extracellular matrix-degrading proteinases that facilitates migration of tumor cells from their primary site to metastasis sites (Negus and Balkwill, 1996; Dranoff, 2004; O'Hayre *et al.* 2008).

All the degradative processes that occur after necrosis mark it as an inappropriate mechanism and a passive uncontrolled type of cell death in cancer therapy compared to apoptosis with essentially no inflammatory reaction (Elmore, 2007).

The following sections represent the methods, results and discussion of the combination of photho- and chemotherapy of GNShells+SH-P(PEGMA)100+Gem at different concentrations and irradiation times (640 nm, 0.9 W cm^{-2}) in comparison with either therapies alone.

4.2. Materials

Glutaraldehyde solution - grade I, 50% in H_2O, specially purified for use as an electron microscopy fixative, osmium tetroxide solution (2% in water), poly-L-lysine solution bioreagent (0.01%), paraformaldehyde powder (95%) and sodium cacodylate trihydrate BioXtra were purchased from Sigma-Aldrich. Apoptosis and necrosis quantitation kit plus was purcheased from Biotium. Laser photothermal treatment was carried out with a continuous-wave red laser coupled with an optical fiber (640 nm, MRL-MD-640-1W).

4.3. Methods

All the experiments were performed in triplicate and the variation in the readings were shown as error bars (±SD). The data were analysed by performing a t-test in Microsoft Excel. $P < 0.05$ was considered statistically significant ($*p < 0.01$-0.05, $**p < 0.001$-0.01, $***p < 0.0001$-0.001).

4.3.1. Photothermal effects of GNShells

The laser-induced temperature elevation of GNShells, GNShells+SH-P(PEGMA)100 and GNShells+SH-P(PEGMA)100+Gem was investigated by irradiating 1 mL of each colloidal suspension (OD = 1) in quartz cells (surface area = 1 cm^2) with a continuous-wave fiber coupled diode laser with a center wavelength of 640 nm and output power of 0.9 W cm^{-2} (540J 600s cm^{-2}) for 10 min. Water, PBS (pH 7.4), sodium acetate buffer solution (pH 5.2) and cell culture medium were used as control groups. The temperature was monitored every 1 min over 20 min, including 10 min cooling time period, by a digital thermometer (digitron-TM-22) with a thermocouple probe submerged in the colloidal suspensions in the quartz cuvettes.

4.3.2. Evaluation of photothermal conversion efficiency (η) of GNShells+SH-P(PEGMA)100+Gem

The photothermal conversion efficiency (η) of GNShells+SH-P(PEGMA)100+Gem from incident laser energy to thermal energy was determined according to Equation 4.1:

Equation 4.1.

$$\eta = \frac{hs\,(T_{max} - T_{amb}) -\ Q_0}{I\,(1 - 10^{-A640})}$$

Where, h is the heat transfer coefficient, s is the surface area of the quartz cuvette, T_{max} is the maximum steady temperature, T_{amb} is ambient temperature of the surroundings, Q_0 expresses the heat dissipation from the light absorbed by the quartz sample cell- that was determined independently by using a quartz cuvette filled with 1 mL of dH_2O- I is the incident laser power (0.9 W cm^{-2}), and A_{640} is the absorbance of the GNShells+SH-P(PEGMA)100+Gem at 640 nm.

The value of *hs* is derived according to Equation 4.2:

Equation 4.2.

$$hs = \frac{m_D C_D}{\tau_s}$$

Where, τ_s is the sample system time constant, m_D (g) and C_D (J g^{-1}) are the mass and heat capacity of the deionised water used as a solvent, respectively.

The value of τ_s was determined during the cooling stage using equation 4.3:

Equation 4.3.

$$t = -\tau_s \ln(\theta)$$

Therefore, time constant for heat transfer from the system is determined by applying the linear time data from the cooling period *vs.* negative natural logarithm of driving force temperature. A dimensionless driving force temperature, θ, is introduced using the maximum system temperature (T_{max}), as:

Equation 4.4.

$$\theta = \frac{T - T_{amb}}{T_{max} - T_{amb}}$$

4.3.3. Investigation of photothermal effect on drug release profiles

Pellets obtained from centrifugation of 10 mL GNShells+SH-P(PEGMA)100+Gem, were resuspended in 10 mL of release medium at different physiological pH levels: sodium acetate buffer solution (pH 5.2±0.1), and PBS (pH 7.4). All the release studies were carried out at 37 °C and stirring of was maintained at 100 rpm. The *in vitro* release behavior of Gem from GNShells+SH-P(PEGMA)100+Gem with and without laser irradiation was monitored. One hour after starting the procedure, stirring samples (10 mL) in glass vials (surface area = 4 cm^{-2}) were irradiated with red laser (640 nm, 0.9 W cm^{-2}) for 20 min. 0.5 mL of each sample was withdrawn at fixed time intervals and the same amount of fresh media was added back to the release medium. The collected samples were centrifuged using centrifugal filter (Thermo Scientific™ Pierce concentrators (PES), 3k MWCO, 0.5 mL) for 20 min at 8000 rpm and then, the samples supernantant were collected. By comparing to the concentration of the pure Gem (0 h, equivalent to 100% Gem release) in each buffer, the concentration of released Gem (from the collected supernatants) was quantified by HPLCanalysis. The results were

presented in terms of cumulative release as a function of time. The cumulative percentage drug released versus time was calculated using Equation 4.5:

Equation 4.5.

$$cumulative\ drug\ release\ (\%) = \frac{Ct}{C\infty}$$

Where, C_t is the mass of drug released at time t and C_∞ refers to the initial loaded mass.

4.3.4. Cell viability evaluation of *in vitro* chemotherapy, phothothermal, and chemothermal treatments

MiaPaCa-2 cells were incubated in Dulbecco's modified eagle's medium-high glucose supplemented with 10% fetal bovine serum, 1% penicillin-streptomycin and 1% L-glutamine. The cells were then seeded in a 96-well plate at a density of 1×10^4 cells per well and incubated at 37°C in humidified atmosphere with 5% CO_2 for 24 h before addition of free Gem, GNShells+SH-P(PEGMA)100 and GNShells+SH-P(PEGMA)100+Gem. Three batches of culture medium containing free Gem and GNShells+SH-P(PEGMA)100 and GNShells+SH-P(PEGMA)100+Gem at different concentrations (or equivalent concentrations) of Gem, ranging from 0.001 to 100 µmol L^{-1} were added to the adherent cells while control cells remained untreated. After incubation for 24 hours, treated/untreated cells were irradiated with red laser (640 nm, 0.9 W cm^{-2}) at various exposure times (1, 5 and 10 min). For chemotherapy treatment alone, the cells were not exposed to laser light (Table 4.1).

Table 4.1. Experimental design of *in vitro* chemotherapy, phothothermal, and chemothermal treatments.

Drug/nanoformulations	Dose of drug/ nanoformulations	Laser exposure time
Free Gem.		
GNShells+SH-P(PEGMA)100+Gem.	ranging from 0.001 to 100 µmol L^{-1}	1 min. 5 min. 10 min.
GNShells+SH-P(PEGMA)100	GNShells+SH-P(PEGMA)100+Gem equivalent doses	

Note: For irradiating cell culture experiments, the treated cells in 96-well plates exposed to red laser (640 nm, 0.9 W cm^{-2}) for 1 min (54J 60s cm^{-2}), 5 min (270J 300s cm^{-2}) and 10 min (540J 600s cm^{-2}).

After laser exposure, the cells were maintained at 37° C under 5% CO_2 for additional 24 h and 48 h. Finally, the MTT assay was utilised to study the cytotoxicity of drug/nanoformulation after predetermined times (Figure 4.7). The obtained data was analysed with the help of Prism software to acquire the half maximal effective concentration (EC_{50}) value.
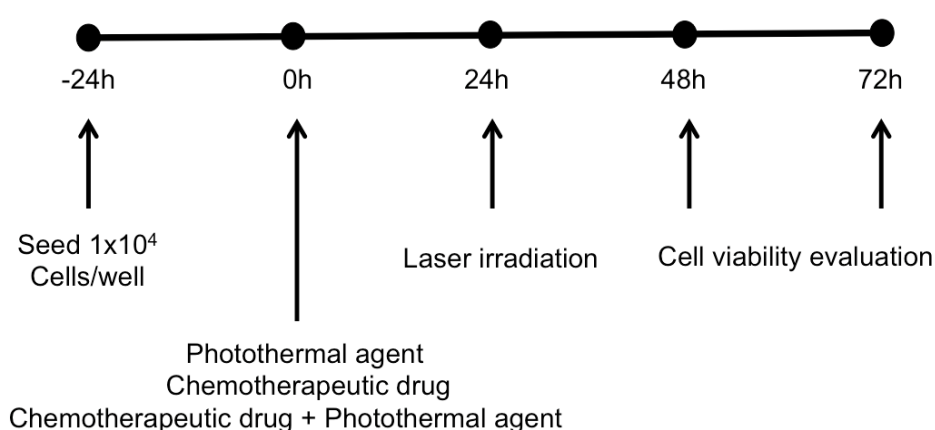
Figure 4.7. Experimental design. Illustration of the experimental design, with each treatment replicated in triplicate independent experiments.

4.3.5. Investigation of the behavior of MiaPaca-2 cells after chemothermal combinational therapy to determine the prevalence of synergistic, antagonistic, or additive interactions.

MiaPaCa-2 cells were seeded onto 6-well plates (surface area of each well = 9.5 cm^{-2}) at a density of $1x10^6$ cells per well and incubated at 37°C in humidified atmosphere with 5% CO_2. On the next day, the medium was replaced with fresh medium containing 100 µmol L^{-1} of free Gem, GNShells+SH-P(PEGMA)100+Gem (Gem equivalent dose) and GNShells+SH-P(PEGMA)100 (GNShells+SH-P(PEGMA)100+Gem equivalent dose). After 24 h of incubation, the cells were irradiated with red laser (640 nm) at a power level of 0.9 W cm^{-2} for 60 min (3240J 3600s cm^{-2}). After further 48 h of incubation, the cells were harvested with trypsin and the populations of survived cells after each treatment were counted. The population of cells after treatment with GNShells+SH-P(PEGMA)100+Gem +laser was compared with the number of cells after an additive interaction (P $_{Additive}$) in order to determine the type of interaction between the applied nanoformulation and the photothermal treatment (synergistic, antagonistic, or additive).

P $_{Additive}$ was calculated using Equation 4.6 (Hauck *et al.*, 2008):

Equation 4.6.

$$P_{Additive} = \left(f_{chemotherapy} \times f_{phototherapy} \right) P_0$$

Where, *P $_{additive}$* represents the number of cells after an additive interaction, $f_{chemotherapy}$ is the fraction of survived cells after treatment with Gem + laser exposure, $f_{phototherapy}$ is the fraction of survived cells after treatment with GNShells+SH-P(PEGMA)100+ laser exposure, and P_0 represents the starting population of cells.

4.3.6. Evaluation of cellular uptake of GNShells+SH-P(PEGMA)100.

MiaPaca-2 cells were seeded in 6-well plates at a density of 1×10^5 cells per well (surface area of each well = 9.5 cm^{-2}) and incubated at 37°C in humidified atmosphere with 5% CO_2 until they reached 70–80% confluency. The medium was replaced with fresh medium containing 100 µL of GNShells+SH-P(PEGMA)100 (~1×10^9 particles per mL) followed by irradiating the cells with red laser (640 nm) at a power level of 0.9 W cm^{-2} for 60 min (3240J 3600s cm^{-2}). while control cells remained untreated (without phothothermal treatment). After 18 h of incubation, the cells were rinsed three times with PBS and the cell pellets were collected by trypsinisation and centrifugation. The cell pellets were fixed in 0.1 M cacodylate buffer (pH 7.3) containing 2.5% glutaraldehyde for 2 h at 4°C, and post-fixed with 1% osmium tetroxide in 0.1 M cacodylate buffer (pH 7.3) for 1 h at 4°C. The cells were then dehydrated in a graded series of ethanol solutions (30% for 15 min, 50% for 15 min, 70% for 15 min, 90% for 15 min, and 100% for 15 min twice) and embedded in Epon resin. Ultrathin sections of embedded cells were cut and transferred on to copper grid, stained with lead citrate, and observed in a Philips BioTwin CM120 (FEI) transmission electron microscope, operating at 120 kV.

4.3.7. Clonogenic cell survival assay

The clonogenic cell survival assay enables an assessment of the differences in the capacity of cells to produce progeny (i.e. a single cell to form a colony of 50 or more cells) between control untreated cells and cells that have undergone various treatment such as exposure to cytotoxic agents, laser light irradiation, etc. Therefore, the clonogenic assay investigates the survival of treated cells by monitoring the effect of anti-cancer therapeutics on the colony forming ability in different cell line. 1×10^5 MiaPaCa-2 cells were seeded in 6-well plates (using 2 mL of culture medium). Once the cells reached 70–80% confluency, each well (surface area of each well = 9.5 cm^{-2}) was treated with the different concentration of Gem (ranging from 0.001 to 100 µmol L^{-1}), GNShells+SH-P(PEGMA)100+Gem (Gem equivalent doses) and GNShells+SH-P(PEGMA)100 (GNShells+SH-P(PEGMA)100+Gem equivalent

doses). One well was remained untreated as a control. After 24 h, the treated and untreated wells were irradiated with red laser (640 nm) at a power level of 0.9 W cm^{-2} for 60 min (3240J 3600s cm^{-2}). For chemotherapy alone, the cells were not exposed to laser light. The cells were harvested by trypsinisation, counted and subsequently specific number of cells (100 cells) from each well was seeded in a new 6-well plate (using 2 mL of culture medium) in triplicate. After 14 days, the colonies were washed with PBS and then fixed using methanol and acetic acid in ratio 3:1. The colonies were stained with 0.5% crystal violet solution (diluted with methanol) for 5 min. The stained plates were rinsed in the tray full of distilled water and left in the fume hood overnight to dry. Colonies appeared as clusters of violet stained cells and could be visualised with naked eye. The number of air-dried colonies for the average of three colony counts for each plate was recorded. A cluster of 50 or more cells were counted as one colony. After counting colonies, plating efficiency (PE) was calculated by dividing the number of colonies counted by the number of cells plated and then multiplying by 100 (Equation 4.7):

Equation 4.7.

$$Plating\ efficiency\ (PE) = \frac{No.\ of\ colonies\ counted}{No.\ of\ cells\ plated} \times 100$$

PE was determined to investigate the percentage of the single cells seeded in the plates that form a colony. PE of the control was considered as 100%. By determining PE, Survival fraction of the single cells seeded in the plates also calculated by dividing the PE of the treated cells by the PE of the control and then multiplying by 100 (Equation 4.8):

Equation 4.8.

$$Survival\ fractions\ (SF) = \frac{PE\ of\ the\ treated\ cells}{PE\ of\ the\ control} \times 100$$

The survival fraction was calculated to determine the fraction of surviving cells after the exposure to the different concentration of drug and laser exposure (Munshi *et al.*, 2005).

4.4. Results and discussion

Results of this chapter were obtained after series of laboratory experiments and data analysis. Each individual section corresponds to the sections given in materials and methods.

Photothermal therapy (PTT) has been increasingly recognised in the area of cancer therapy owing to its specific spatiotemporal selectivity, precise delivery of energy and minimal invasiveness. The high photothermal conversion efficiency of gold-based nanostructures makes them suitable candidates for PTT. When colloidal GNP suspensions are irradiated at the resonance frequency, the oscillating electrons transfer their kinetic energy into the particle lattice through electron-phonon interactions, followed by phonon-phonon interactions with the surrounding medium. Phonon-phonon coupling dissipates heat across a particle-medium interface at a rate dependent on the medium, the particle size, and the laser source as the nanoparticle returns to its initial temperature (Roper *et al.*, 2007; Jiang *et al.*, 2013).

The sufficient amount of heat generated locally by the laser-irradiated GNPs can increase the cell membrane permeability or induce destruction of cancer cells via apoptosis, necroptosis and/or necrosis. Drug-loaded GNPs can be used as photothermally activated drug-delivery vehicles in order to combine their drug delivery and PTT properties via a photo-chemotherapy approach (Rau *et al.*, 2016).

Currently, only PEGylated GNShells are used in clinical trials as photothermal agents (Clinicaltrials.gov. NCT00848042; NCT01679470; NCT02680535). Clinical studies with Auroshell particles (table 3.1) have shown some promise in photothermal ablation of solid tumors.

In this study, photothermally activated therapeutic nanoparticle formulation was prepared with the synthesis of polymer coated GNShells through the use of a galvanic replacement reaction followed by the installation of thiol capped polymers and loading with Gem.

Although the surface plasmon resonance absorption peak of GNPs is size and geometry dependent, the clinical parameter for the efficiency of GNPs-mediated laser-activated hyperthermia is the amount of energy delivered by the laser per time and area. The heat generated by plasmonic GNPs is influenced by the concentration of nano-scale gold, wavelength of the laser and the type of the laser.

In general, a pulsed lasers deliver more energy then a continuous wave laser in a very short time (Rau *et al.,* 2016). However, in this study, a continuous wave (CW) red laser (640 nm, MRL-MD-640-1W) was employed. Since GNShells+SH-P(PEGMA)100+Gem showed an absorption peak at 640 nm, their photothermal conversion properties was investigated by red laser illumination at 640 nm with a power density of 0.9 W cm^{-2}.

CW irradiation of colloidal gold nanoformulation at low power (0.9 W cm^{-2}) allows even heating with reproducible efficiencies at temperatures within physiological limits, whereas high-power nano-, pico-, and femtosecond pulses produce large particle to matrix temperature gradients that cause vaporisation and concomitant cavitation and nanoparticle fragmentation, which are incompatible with biological or steady-state application (Roper *et al.*, 2007).

The energy conversion efficiency (η) represents an intrinsic property of GNPs and it is proportional to the absorption/extinction ratio of colloidal nano-sized gold (Jiang *et al.*, 2013). Unfortunately, there is no consensus on the gold-based materials (e.g., particles concentration, temperature elevation profile, etc.) or laser parameter (e.g., laser energy, intensity, duration, etc.) to optimise the efficiency of laser-induced phothothermal effects of GNPs to initiate cell death. However, some generalisation can be extracted from the available data in the literature. Table 4.2 represents the photothermal efficiency of GNShells as reported in the literature.

Table 4.2. Photothermal conversion efficiency, η, of GNShells reported in the literature.

Nano-material	Irradiation λ (nm)	Incident power (W)	η (%)	Reference
GNShells	800	2	13	Hessel *et al.*, 2011
	808	2	25	Pattani *et al.*, 2012
	808	1	18	Huang *et al.*, 2013
	810	2	39	Ayala-Orozco *et al.*, 2014

Under red laser illumination (λ = 640 nm, 0.9 W cm^{-2}, 10 min), colloidal suspensions of GNShells, GNShells+SH-P(PEGMA)100 and GNShells+SH-P(PEGMA)100+Gem (all the nanoparticles were dispersed in 1 mL of dH$_2$O) were heated up to about 21 °C, 22 °C and 20 °C, respectively (Figure 4.8). These data indicated that surface functionalisation of GNShells did not impair their phothothermal performance. The temperature increase of control groups (dH$_2$O, PBS, sodium acetate buffer and cell culture medium) was significantly lower, about 10 °C to 11 °C.
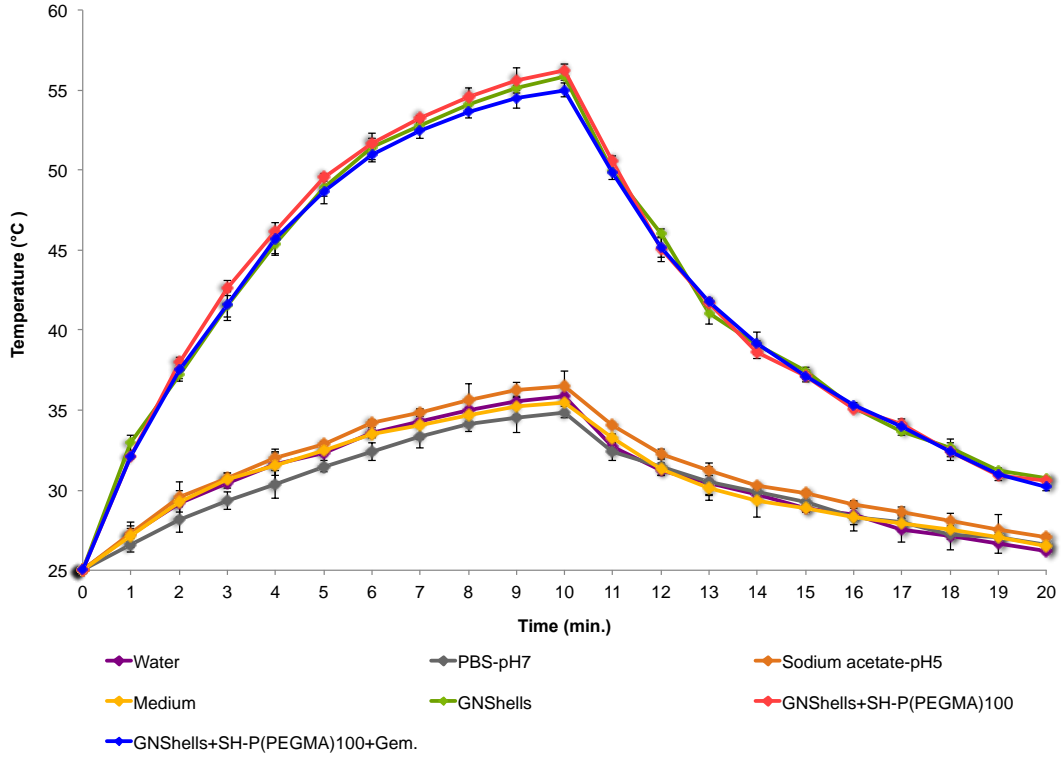
Figure 4.8. Temperature elevation of dH_2O, PBS, sodium acetate buffer, cell culture medium, GNShells, GNShells+SH-P(PEGMA)100 and GNShells+SH-P(PEGMA)100+Gem induced by CW red laser irradiation (0.9 W cm^{-2}, 640 nm, 10 min) followed by monitoring the cooling effect after the laser was turned off (n = 3).

The phothothermal conversion (η) performance of GNShells+SH-P(PEGMA)100+Gem (~1.8 × 10^{11}) was calculated using the equation proposed by Roper (Roper *et al.,* 2007) as following (Equation 4.1):

$$\eta = \frac{hs\,(T_{max} - T_{amb}) - Q_0}{I\,(1 - 10^{-A640})}$$

Where T_{max} is the maximum steady-state temperature (T_{max}) of GNShells+SH-P(PEGMA)100+Gem colloids and T_{amb} is the ambient temperature (25 °C). The temperature change (T_{max} - T_{amb}) of the colloidal suspension was 20 °C (Figure 84). The laser power (*I*) was 0.9 W. The absorbance of GNShells+SH-P(PEGMA)100+Gem at 640 nm (*A640)* is 1.25. Q_0 is the heat associated with light absorption by the quartz sample cell containing pure water without the nanoparticles and it was measured independently to be 70 mW. The time constant (τ_s) for heat transfer from the system is determined to be τ_s = 350 s

by applying the linear time data from the cooling period *vs* negative natural logarithm of the dimensionless driving force temperature, $\theta = (T - T_{amb}) / (T_{max} - T_{amb})$. The slope of regression line is represented in the sample system time constant (τ_s) (Figure 4.9). In addition, the m_D is 1 g and the C_D is 4.2 J g^{-1}. Therefore, *hs* is deduced to be 0.012 W/°C ($hS = m_D C_D / \tau_s$).

a

b
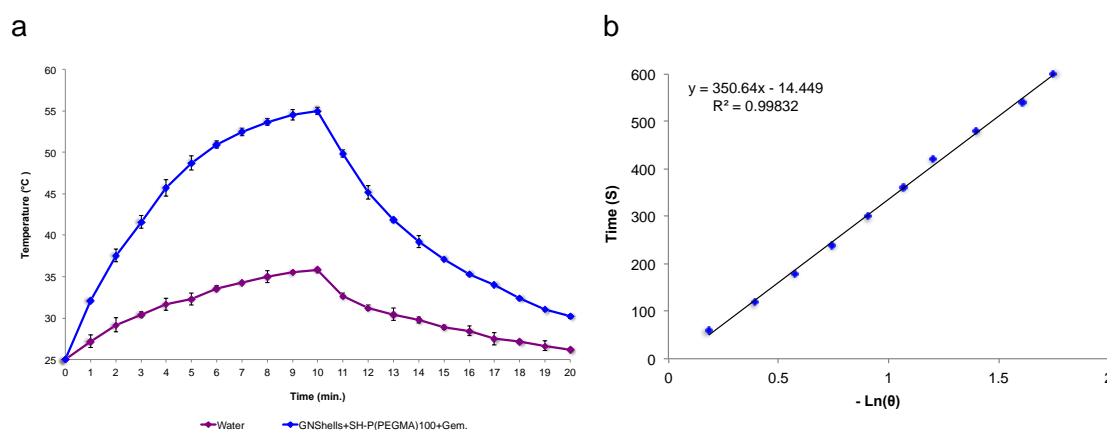
Figure 4.9. The temperature profile (n = 3) generated by dH$_2$O and GNShells+SH-P(PEGMA)100+Gem being excited at 640 nm with a CW red laser with a power density of 0.9 W cm^{-2} (a). Plot of the negative natural logarithm of driving force temperature (θ) as a function of time after the laser was turned off (b).

By substituting all the values in Roper's equation, the 640 nm laser η of GNShells+SH-P(PEGMA)100+Gem can be calculated to be 20 %. The η *value* is in accordance with the finding from literature (Huang *et al.*, 2013).

The *in vitro* drug release behavior of GNShells+SH-P(PEGMA)100+Gem with and without laser irradiation (CW red laser, 640 nm, 0.9 W cm^{-2}, 20 min) was studied in buffers at different pH at 37 °C using a zero order kinetic model (cumulative % drug release *vs* time). The schematic diagram of Gem release from GNShells+SH-P(PEGMA)100+Gem with and without laser irradiation is shown in Figure 4.10. In the absence of laser irradiation at 37 °C, the Gem release from the nanocarriers was 51.52% at pH 7.4 and 59.23% at pH 5.2 after 48 h. The small difference in the release amounts between different pH, was attributed to the increased hydrophilicity and higher solubility of Gem at lower pH due to protonation of -NH$_2$ groups on Gem and COO$^-$ groups on the surface of GNShells, which reduced the electrostatic interactions between

Gem and GNShells. 1 h After laser irradiation of GNShells+SH-P(PEGMA)100+Gem (begun after 1 h of the release experiment) at 0.9 W cm^{-2} output power for 20 min, the amount of Gem released was 39.43% at pH 7.4 and 46.61% at pH 5.2. The total release of Gem from the irradiated nanoformulation was 65.96% at pH 7.4 and 74.28% at pH 5.2 after 48 h. Therefore, upon one-time irradiation (for 20 minutes), the cumulative release amount of Gem over the whole experiment was observed to be significantly higher (15 %) than that without laser irradiation for any pH because the local temperature elevation (laser-converted heat) via absorption of red light by GNShells+SH-P(PEGMA)100+Gem promoted the dissociative interactions between Gem and nano-gold (Au-N covalent bond and COO$^-$ N$^+$ electrostatic attraction) and accelerated the rate of release.

The maximal release of Gem was observed when the nano-carriers were exposed to both acidic pH and temperature stimuli. Therefore, these data suggested that; 1) the photothermal effect of GNShells can be utilised to partially trigger Gem release from GNShells+SH-P(PEGMA)100+Gem and 2) Gem is expected to be released more in acidic environment.

a

GNShells+SH-P(PEGMA)100+Gem-pH7   GNShells+SH-P(PEGMA)100+Gem-pH5
GNShells+SH-P(PEGMA)100+Gem-laser-pH7   GNShells+SH-P(PEGMA)100+Gem+laser-pH7

b

GNShells+SH-P(PEGMA)100+Gem-pH7   GNShells+SH-P(PEGMA)100+Gem-pH5
GNShells+SH-P(PEGMA)100+Gem+Laser-pH7   GNShells+SH-P(PEGMA)100+Gem+Laser-pH5
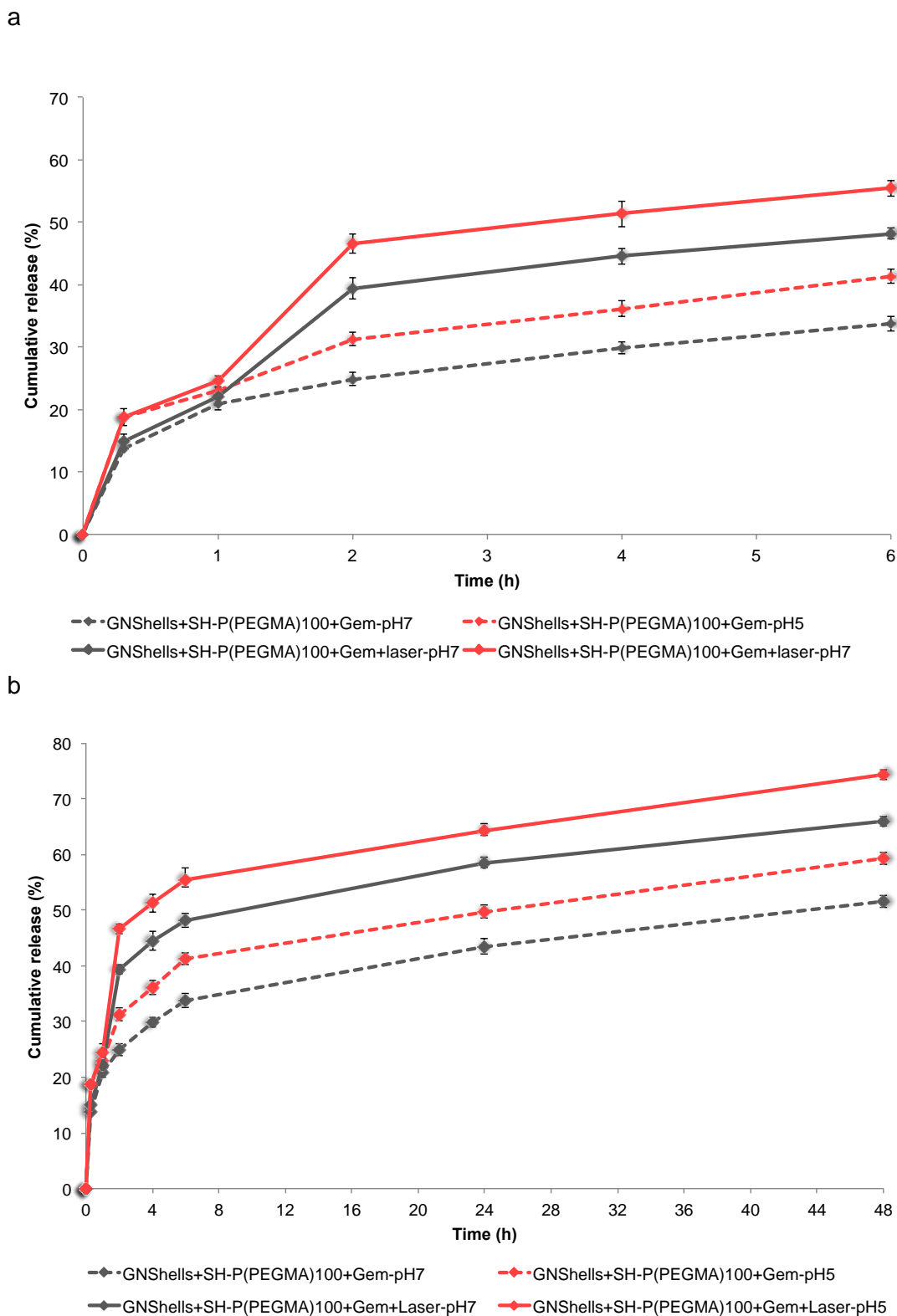
Figure 4.10. *In vitro* cumulative drug release profiles of GNShells+SH-P(PEGMA)100+Gem dispered in PBS (pH 7.4) and sodium acetate buffer (pH 5.2) over 6 h (a) and 48 h (b). The data represented as the mean of three experiments and the variations in the readings were shown as error bars (±SD).

Studies showed that hyperthermia could augment Gem-induced apoptosis, and the effectiveness of combined hyperthermia and Gem is schedule-dependent (Haveman *et al.*, 1995; Van Bree *et al.*, 1999; Vertrees *et al.*, 2005; Adachi *et al.*, 2009; Raoof *et al.* 2014; Asayesh *et al.*, 2016). Gem is a chemotherapeutic drug that is known to have synergy with heat. The optimal timing for cytotoxicity enhancement of Gem was observed when hyperthermia was applied after an interval of 24 h following exposure to Gem (Asayesh *et al.,* 2016). However, further studies are required regarding optimal scheduling. Several mechanisms of interaction have been proposed for hyperthermia enhanced cytotoxicity of chemotherapeutic agents: hyperthermia is thought to inhibit the repair of drug induced DNA damage, to increase drug-induced DNA damage, to induce primary protein damage and to beneficially influence the pharmacokinetics of drugs (Dahl 1994; Van Bree *et al.*, 1999). In this study MiaPaCa-2 cells were treated with Gem and Gem loaded nanoformulations for 24 h and then exposed to laser irradiation.
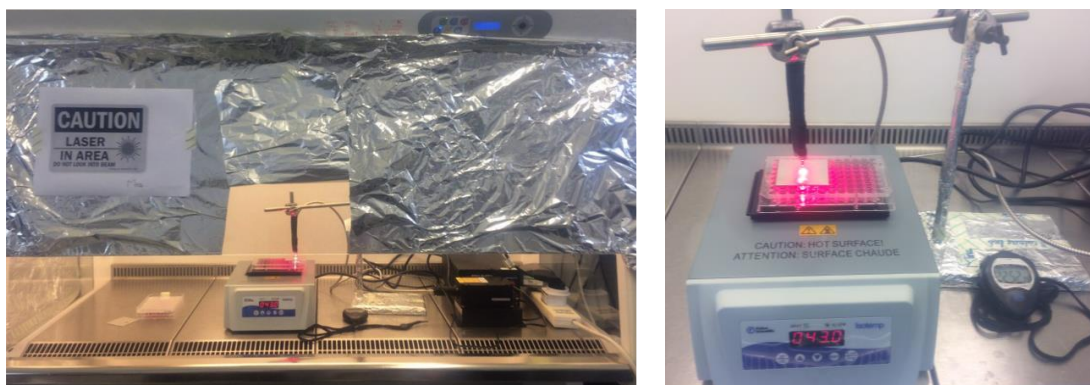
Figure 4.11. The red laser system setup (640 nm, MRL-MD-640-1W) for laser-induced hyperthermia in vitro.

The laser system was assembled in order to deliver hyperthermia to cells 24 h after incubation of MiaPaCa-2 cells with free Gem / GNShells+SH-P(PEGMA)100 / GNShells+SH-P(PEGMA)100+Gem (Figure 4.11). The system comprised a laser (640 nm, MRL-MD-640-1W), a fiber holder and 96 well plate/microplate heater (isotemp™-Fisher scientific). During the experiment the laser fiber was fixed to a holder so that the laser beam was directed perpendicularly to the 6/96-well plates, which was placed on the

heated stage. The heated stage was positioned directly below the laser and the temperature was adjusted at 37 °C prior to laser application.

The yields of photothermal transformation by GNPs are related to the amount of taken up by cells and laser intensity. Although the optical-thermal effect is more prominent with higher energy laser irradiation, but can lead to increase non-specific cell death. Since most cells can uptake nono-sized particles through non-specific endocytosis, therefore GNPs-induced phothothermal effect should also induce unavoidable cell damage in surrounding tissues when used for laser-activated hyperthermia in cancer treatment. (Rau *et al.*, 2016). 1 W cm^{-2} is the threshold at which cellular damage begins (Hauck *et al.,* 2008), and since a significant population of live cells still exist at this power density, it was decided to combine irradiation at 0.9 W cm^{-2} with Gem treatment in search for synergism between chemotherapy and phototherapy. The mechanism of the synergistic effect is supposed to be reflected as an enhanced cytotoxicity of GNShells+SH-P(PEGMA)100+Gem at elevated temperature and increasing heat sensitivity of cells exposed to this nanoformulation.

The solo photo-chemotherapeutic cytotoxicity of Gem (ranging from 0.001 to 100 µmol L^{-1}) and the solo photo-hyperthermic cytotoxicity of GNShells+SH-P(PEGMA)100 (Gem equivalent doses) were evaluated by performing traditional MTT tetrazolium assay for cell viability. The possibility of utilising GNShells+SH-P(PEGMA)100+Gem (Gem equivalent doses) for photo-chemothermal synergistic therapy was also assessed (Figures 4.12, 4.13, 4.14).

a

b
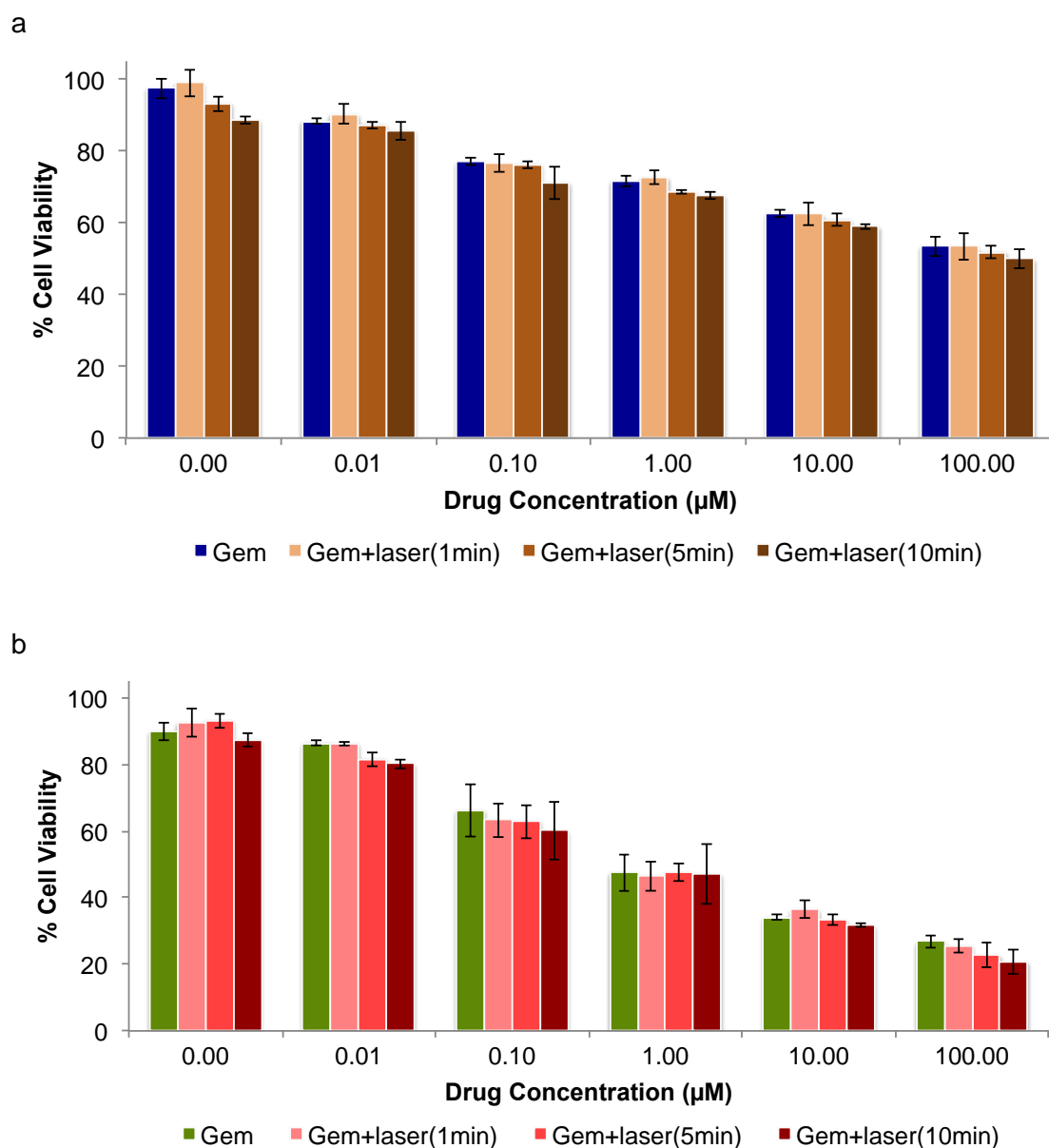
Figure 4.12. Cell viability of Gem and Gem plus laser (λ = 640 nm, 0.9 W cm^{-2}, 1-5-10 min) for MiaPaCa-2 cells as a function of Gem concentration after 48 h (a) and 72 h (b) incubation, respectively. The data represented as the mean of three experiments and the variations in the readings were shown as error bars (±SD).

The free Gem exhibited concentration-dependent cytotoxicity to MiaPaCa-2 cells after 48 h and 72 h incubation (Figure 4.12) (Appendix 13). However, there was no significant difference in cell viability between the free Gem group and Gem under red laser irradiation groups (λ = 640 nm, 0.9 W cm^{-2}, 1-5-10 min) at equal Gem concentration (Table 4.3). The obtained results indicated that the laser had no cytotoxicity to MiaPaCa-2 cells nor could it enhance the effectiveness of chemotherapy treatment alone.

Table 4.3. The EC$_{50}$ (μM) of Gem against MiaPaCa-2 cells before and after irradiation (λ = 640 nm, 0.9 W cm^{-2}, 1-5-10 min). All the MTT experiments were performed in triplicate and the variation in EC$_{50}$ are shown as mean$\pm$SD.

Cell line	Treated with	Incubation time (h)	EC$_{50}$ (μM)
Miapaca-2 (1x10^4 cells/well)	Gem. (No irradiation)	72	0.72$\pm$0.04
	Gem (1 min irradiation)		0.66$\pm$0.05
	Gem (5 min irradiation)		0.68$\pm$0.01
	Gem (10 min irradiation)		0.74$\pm$0.14

The photothermal effect of GNShells+SH-P(PEGMA)100 (Gem equivalent doses) on MiaPaCa-2 cells upon laser irradiation (λ = 640 nm, 0.9 W cm^{-2}, 1-5-10 min) was evaluated at 48 h and 72 h of incubation (Figure 4.13) (Appendix 13).

The data showed that with or without laser, PEGylated GNShells exhibited no obvious effect on cell viability as tested with a series of equivalent concentrations of Gem ranging from 0.001 μM to 1 μM after 48 h and 72 h incubation.

Similarly, the viability of cells incubated with GNShells+SH-P(PEGMA)100 for 48 h and 72 h at higher concentrations (10 µmol L^{-1} and 100 µmol L^{-1} Gem equivalent doses) were more than 85% even after exposure to red laser for 1 min, which indicated that the PEGyalted GNShells had negligible toxicity and superior safety. However, since the increase in the temperature of the cell culture medium is proportional to the GNPs concentration, the amounts of absorbed fraction of incident light energy and the duration of energy absorption, hence by increasing laser exposure time, the GNShells+SH-P(PEGMA)100 sample exhibited a concentration-dependent decrease in cell viability.

These results showed that when GNShells+SH-P(PEGMA)100 were irradiated withthe laser up to 10 min, they could produce cytotoxic heat at higher gold concentrations (10 µmol L^{-1} and 100 µmol L^{-1} Gem equivalent doses).

a

b
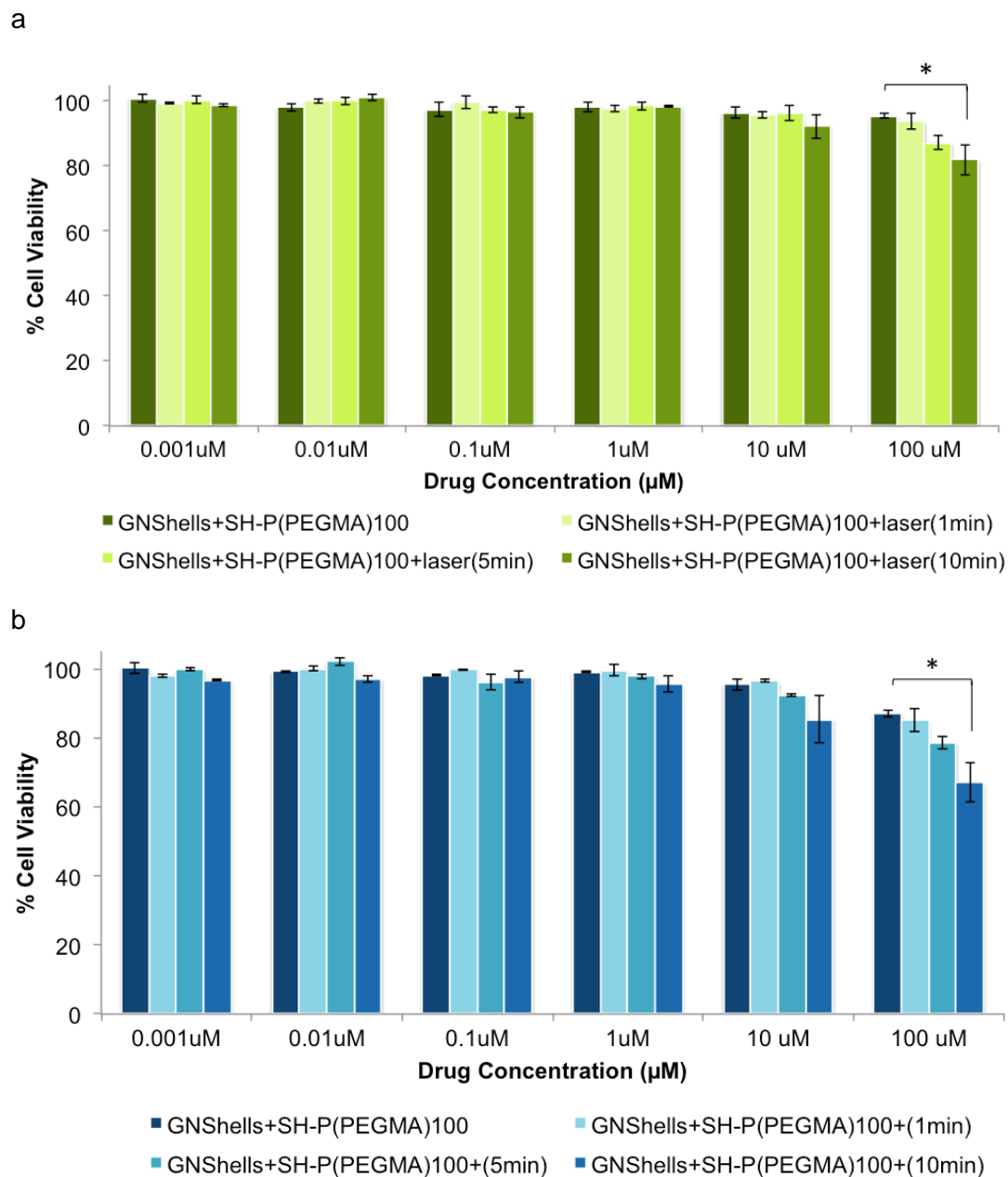
Figure 4.13. Cell viability of GNShells+SH-P(PEGMA)100 and GNShells+SH-P(PEGMA)100 plus laser irradiation (λ = 640 nm, 0.9 W cm^{-2}, 1-5-10 min) for MiaPaCa- 2 cells as a function of Gem concentration after 48h (a) and 72 h (b) incubation, respectively. Error bars were based on standard deviations of three samples at each data point. Asterisks denoted statistical significance from control (*p<0.01-0.05).

The elevated temperature between 41 °C to 45 °C induces sublethal effects, such as expression of apoptosis genes, caspase activation, mitochondrial damage, etc. while temperature above 50 °C induces irreversible tissue damage (Shibu *et al.,* 2013). Moreover, it has been demonstrated that hyperthermia-induced cellular toxicity occurs after maintenance at a temperature over 50 °C for 6 min (Habash *et al.,* 2006) and within 1 h at 42 °C (Dewey and Diederich, 2009).

In this study, when MiaPaCa-2 cells were exposed to laser light 24 h post treatment with GNShells+SH-P(PEGMA)100, the concentration-dependent temperature elevation from ~ 42 °C to ~ 54 °C was reported in 10 min. Although the focus temperature of laser irradiation exceeded the damage threshold (>50 °C) after 10 min at highest concentration of GNShells+SH-P(PEGMA)100 and induced thermal cytotocity (*p<0.01-0.05), still the therapeutic efficacy of photothermal therapy alone was not sufficient to induce irreversible cellular injury to a higher extent. Encouraged by the *in vitro* photothermal conversion performance of GNShells+SH-P(PEGMA)100 and since hyperthermia can enhance the chemotherapeutic efficacy of chemotherapy, multi-functional photo-chemothermal therapeutic effects of GNShells+SH-P(PEGMA)100+Gem was further studied.

The cytotoxic activity of GNShells+SH-P(PEGMA)100+Gem by determining the cell viability using the MTT assay, was reported in chapter 3. The GNShells+SH-P(PEGMA)100+Gem showed lower cytotoxicity against MiaPaCa-2 cells in comparison with free Gem at 72 h of incubation. The EC_{50} value of GNShells+SH-P(PEGMA)100+Gem was reported to be 1.76 µM which was higher than that of free Gem ($EC50$ = 0.72 µM).

After investigating the potential of chemo-phototherapy combination using laser irradiation, the results showed that GNShells+SH-P(PEGMA)100+Gem under laser irradiation achieved impressive antitumor effect against MiaPaCa-2 cells compared with the experiments with single chemotherapy treatment.

As shown in Figure 4.14, with and without laser irradiation, the viability of MiaPaCa-2 cells decreased with the increasing GNShells+SH-P(PEGMA)100+Gem concentration. Significant decrease in cell viability at 72 h post chemotherapy treatment (compared to 48 h of incubation) showed the optimum Gem effect and confirmed that the activity of Gem was not adversely influenced during the formulation step; also, the cytotoxicity of the main active component from GNShells+SH-P(PEGMA)100+Gem was Gem.

According to the data presented in Figure 4.14 (b) when the laser irradiation time was prolonged from 1 to 5 to 10 min, the cell viability decreased significantly compared to the control group at all tested concentrations. Therefore, the curative effect of the photothermal therapy was related with the duration of laser irradiation. After 10 min irradiation with red laser, the cell killing efficacy of GNShells+SH-P(PEGMA)100+Gem was statistically improved for 0.001 µmol L^{-1} and 100 µmol L^{-1} Gem equivalent concentrations. In addition, the EC$_{50}$ value of GNShells+SH-P(PEGMA)100+Gem decreased from 1.76 µM without laser irradiation to 0.54 µM with 10 min laser irradiation, which is significantly lower than that of irradiated free Gem group (EC$_{50}$ = 0.74 µM). The results are presented in Table 4.4 with their corresponding graphs in Appendix 13.

Based on the fact that laser irradiation did not cause any acute damage to GNShells+SH-P(PEGMA)100 incubated cells, these results showed that laser-induced hyperthermia mediated by GNShells increased the potency of GNShells+SH-P(PEGMA)100+Gem against MiaPaCa-2 cells and also increased the heat sensitivity of MiaPaCa-2 cells exposed to the nanoformulation. However, for 10 µmol L^{-1} and 100 µmol L^{-1} Gem equivalent doses, the combined effect of heat-induced ablation of cancer cells also enhanced the therapeutic effect of GNShells+SH-P(PEGMA)100+Gem in addition to the synergistic effect of photo-chemothermal therapy at elevated temperatures.
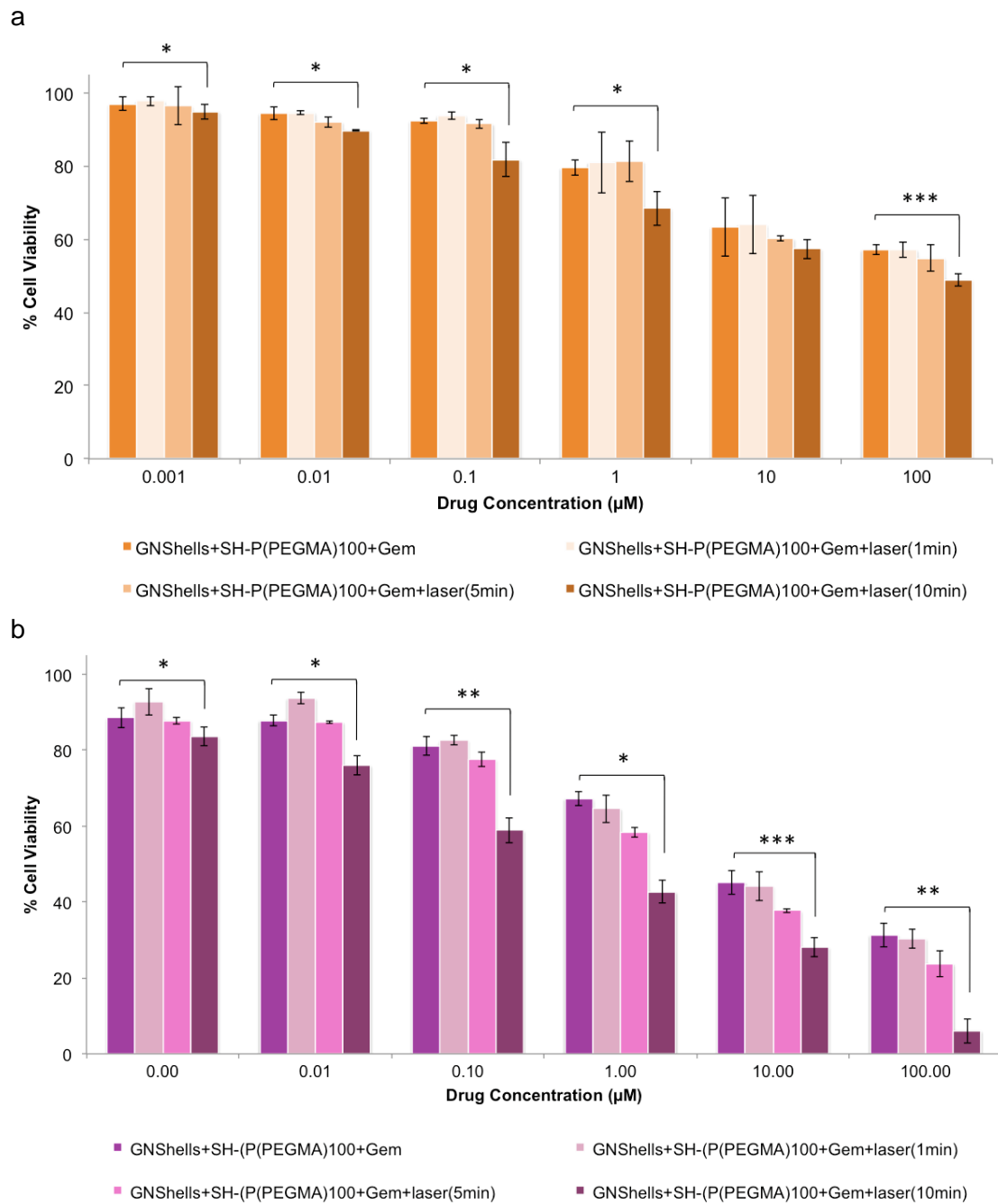
Figure 4.14. Cell viability of GNShells+SH-P(PEGMA)100+Gem and GNShells+SH-P(PEGMA)100+Gem plus laser irradiation (λ = 640 nm, 0.9 W cm^{-2}, 1-5-10 min) for MiaPaCa-2 cells as a function of Gem concentration after 48h (a) and 72 h (b) incubation, respectively. Error bars were based on standard deviations of three parallel samples at each data point. Asterisks denoted statistical significance from control (*p<0.01-0.05, **p<0.001-0.01, ***p<0.0001-0.001).

Table 4.4. The EC_{50} (μM) of GNShells+SH-P(PEGMA)100+Gem against MiaPaCa-2 cells before and after irradiation (λ = 640 nm, 0.9 W cm^{-2}, 1-5-10 min). All the MTT experiments were performed in triplicate and the variation in EC_{50} are shown as mean±SD.

Cell line	Treated with	Incubation time (h)	EC50 (μM)
Miapaca-2 (1x10⁴ cells/well)	Free Gem (10 min. irradiation)		0.74±0.14
	GNShells+SH-P(PEGMA)100+Gem (No irradiation)	72	1.76±0.31
	GNShells+SH-P(PEGMA)100+Gem (1 min. irradiation)		1.63±0.21
	GNShells+SH-P(PEGMA)100+Gem (5 min. irradiation)		1.20±0.27
	GNShells+SH-P(PEGMA)100+Gem (10 min. irradiation)		0.54±0.17

The synergistic effect of photo-chemothermal therapy was calculated according to the additive therapeutic interaction of independent treatments (chemotherapy and phototherapy) as an evaluation index. The final population of MiaPaCa- 2 cells after additive interaction (so called as projected additive, $P_{additive}$) was calculated by multiplying the fractions of surviving cells after each independent treatment (f), that is, $P_{additive} = (f_{chemotherapy} \times f_{phototherapy}) \times P_0$, where P_0 is the starting population.

The effect of either chemotherapy or phototherapy treatments was determined by counting the number of cells after laser exposure (λ = 640 nm, 0.9 W cm^{-2}, 60 min). Figure 4.15 shows the cell viability of three different treatment groups: Gem (100 μmol L^{-1}) + laser, GNShells+SH-P(PEGMA)100+Gem (Gem equivalent dose) + laser and GNShells+SH-P(PEGMA)100 (GNShells+SH-P(PEGMA)100+Gem equivalent dose) + laser. $P_{additive}$ is the cell viability expected if there was no interplay between chemotherapy and phototherapy and was found to be significantly higher compared with the surviving cells exposed to the combinational photo-chemothermal therapy

(*p<0.01-0.05). The results confirmed that GNShells+SH-P(PEGMA)100+Gem possessed a marked synergistic effect for the combined photo-chomothermal therapy and thus achieved a high therapeutic efficacy.
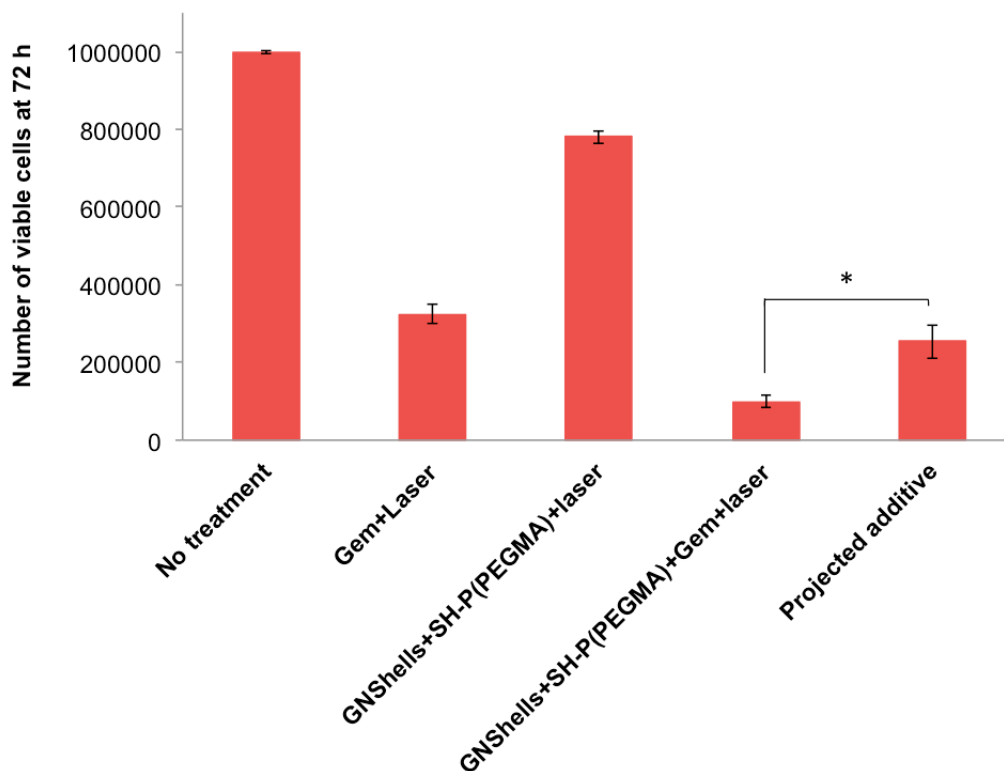
Figure 4.15. Cell count at 72 h incubation of MiaPaCa-2 cells with free Gem plus laser, GNShells+SH-P(PEGMA)100 plus laser, GNShells+SH-P(PEGMA)100+Gem plus laser (λ = 640 nm, 0.9 W cm^{-2}, 60 min) as a function of Gem concentration (100 µmol L^{-1}). The calculated projected additive was used as an evaluation index. Error bars were based on standard deviations of three samples at each data point. Asterisks denoted statistical significance level (*p<0.01-0.05).

It is important to mention that it has not reported to the literature that the enhancement of the therapeutic efficacy of a designed nanoformulation is either due to the synergy of action between chemotherapeutic and photothermal agents or the enhancement of the cellular damage produced by each agent alone. Also, the extent that heat-related changes can alter or interact with the damage from the chemotherapeutic agents?

Despite the popularity of the subject, it has not been well understood and more research is required in order to fully elucidate the mechanism of action in full detail.

However, the mechanism of interaction of hyperthermia and chemotherapy agents is primarily a function of the agents themselves and the three most important reported mechanisms behind the synergistic effect of photo-chemothermal treatment are (Sugimachi *et al.*, 1994; Issels *et al.*, 2010a; 2010b; Rao *et al.*, 2010; May and Li, 2013; Angele *et al.*, 2014):

1. Inhibition of DNA repair of the chemically induced lethal or sublethal damages, and acceleration of the cytotoxic chemical reaction.

2. Improvement of intercellular uptake and accumulation of the anti-cancer drugs in tumor cells due to increased cell membrane permeability.

3. Interaction of the two modalities at a common target level (not well-understood yet).

TEM was used to monitor the GNShells+SH-P(PEGMA)100 dispersion and dose internalisation in MiaPaCa- 2 cells. In addition, preparation of TEM samples by chemical-fixation and resin embedding enable the investigation of the *in vitro* cellular responses to the photothermal effects of GNShells+SH-P(PEGMA)100 on cellular uptake and their correlation to the amount of internalised particles, intracellular position and number of NPs within a cell, identification of any degradation of the NPs within intracellular compartments and the impact of GNShells+SH-P(PEGMA)100 on cell morphology and viability.

TEM images of MiaPaCa-2 cells after 18 h of incubation with 100 µL of GNShells+SH-P(PEGMA)100 is shown in Figure 4.16. The results demonstrated by TEM showed that with or without laser irradiation (λ = 640 nm, 0.9 W cm^{-2}, 60 min):

- The exposure to GNPs did not alter morphology of MiaPaCa-2 cells
- GNPs were traced into cytoplasmic compartments and since they were mostly found in vesicles, it has been assumed that they were engulfed into cellular vesicles by energy dependent endocytic pathways, which is one of the possible uptake mechanisms for GNPs.

- There was no sign of GNPs aggregation in the cell compartments.
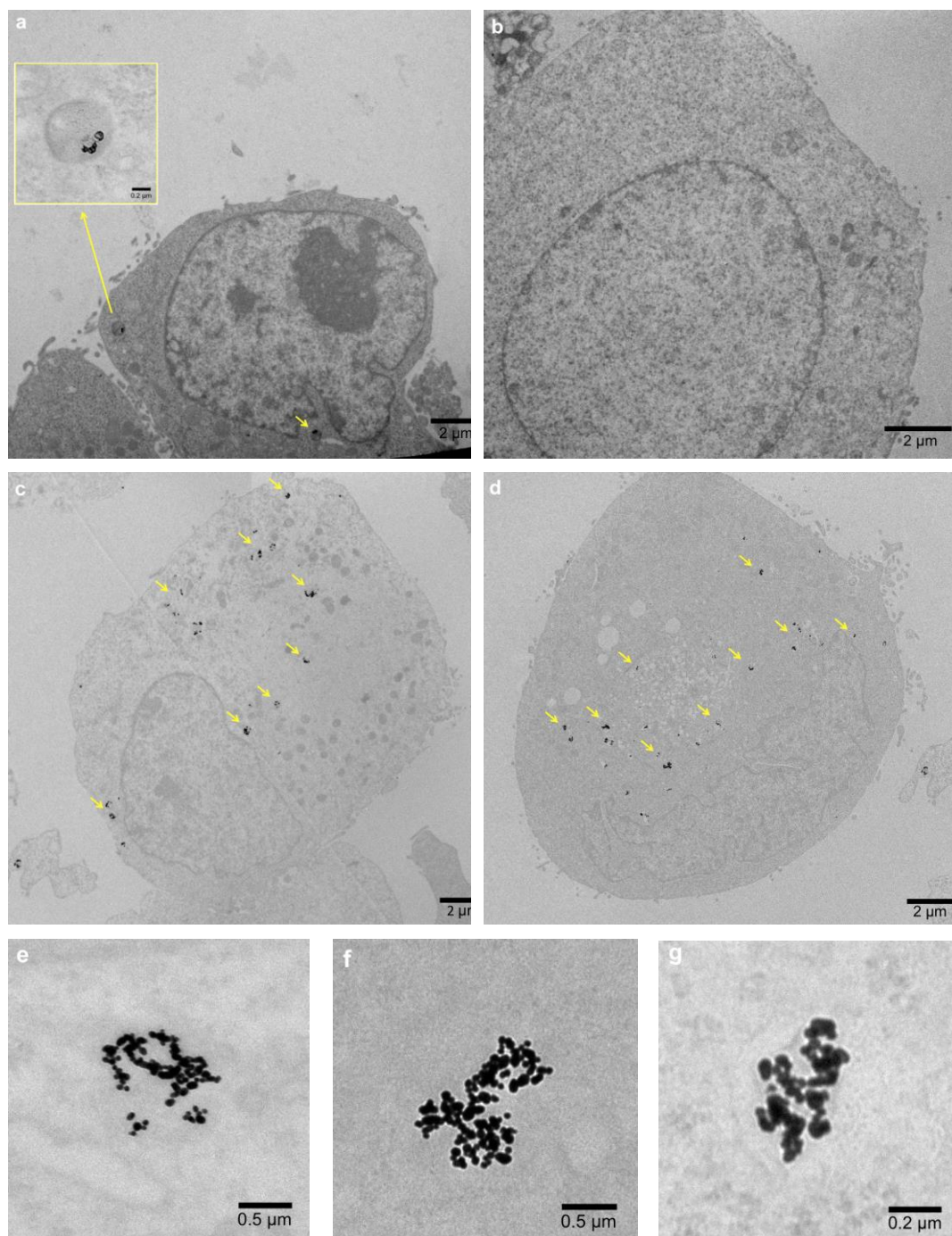
Figure 4.16. TEM images of MiaPaCa-2 cells after 18 h of incubation with GNShells+SH-P(PEGMA)100 (a-b) without laser irradiation, (c-g) with laser irradiation (λ = 640 nm, 0.9 W cm^{-2}, 60 min). The arrows show the GNShells+SH-P(PEGMA)100 inside the cells.

TEM images presented in Figure 4.16 showed that MiaPaCa-2 cells without photothermal treatment internalised into the cytoplasmic vesicles composed of very few (a) or no GNShells+SH-P(PEGMA)100 (b).

In contrast, irradiation of MiaPaCa-2 cells with red laser light resulted in accumulation of larger number of nanoparticles within larger vesicles, with diameters of 1–2 μm (Figure 4.16 c-g). These results indicated that after photothermal application, the cellular uptake of the nanoparticles increased, which could potentially affect the overall treatment efficiency, as was demonstrated by the in vitro cytotoxicity results.

Alexander group showed that the polymer-conjugated GNPs were located into MCF7 cells treated at 40 °C (12000 AuNP/cell) with more than 80-fold greater up-take compared to cells treated at 34 °C with the same particles (140 AuN/cell) (Salmaso *et al.*, 2009). To the best of my knowledge, this is the first demonstration of the laser-induced HT effect on cellular internalisation of GNPs .

Furthermore, a clonogenic assay was conducted to evaluate the longer-term cytotoxicity potential of free Gem, GNShells+SH-P(PEGMA)100 and GNShells+SH-P(PEGMA)100+Gem with and without laser irradiation by monitoring the proliferative ability of the survived cells 14 days post treatment. Formation of colonies is indicative that cells have retained their capacity to reproduce a large colony or a clone. Digital photographs of the colonies and the calculated survival fractions (%) of the treated MiapaCa-2 cells are presented in Table 4.5 and Figure 4.17, respectively.

After counting the number of colonies (n = 3), the SF (%) of MiaPaCa-2 cells was calculated for a series of different concentrations of all the three treated groups with and without laser irradiation. The results showed that the SF (%) decreased as the concentration of the drugs increased in Gem and GNShells+SH-P(PEGMA)100+Gem treated groups with and without laser irradiation.

The statistical improvement of cytotoxicity of Gem with laser-induced hyperthermia (*p<0.01-0.05, **p<0.001-0.01) clearly showed the thermal potentiation of Gem against MiaPaCa-2 cells.

As shown in Figure 4.17, GNShells+SH-P(PEGMA)100 did not exert cytotoxic effects on MiaPaCa-2 cells at any concentrations, which again highlighted the cytotoxic action of Gem in the therapeutic performance of GNShells+SH-P(PEGMA)100+Gem. In addition, hyperthermia induced by irradiation of cells treated with GNShells+SH-P(PEGMA)100 at concentrations of 1 µmol L^{-1} to 0.001 µmol L^{-1} (Gem equivalent) did not affect the cellular viability.

However, the SF (%) decreased significantly (**p<0.001-0.01 and ***p<0.0001-0.001) for MiaPaCa-2 cells treated with photothermal agent GNShells+SH-P(PEGMA)100 at higher concentrations (10 µmol L^{-1} and 100 µmol L^{-1} Gem equivalent doses), which showed the concentration-dependent thermal effect of GNShells+SH-P(PEGMA)100 under laser irradiation.

After irradiating the cells treated with GNShells+SH-P(PEGMA)100+Gem for 60 min, the number of colonies and the SF (%) in all the concentrations decreased significantly (*p<0.01-0.05, **p<0.001-0.01 and ***p<0.0001-0.001) indicating that combinational photo-chemothermal treatment significantly compromised the metabolic activity and the reproductive integrity of the cells in the long-term, 14 days post-treatment.
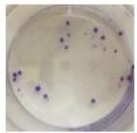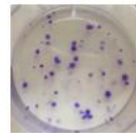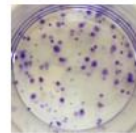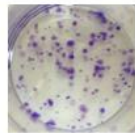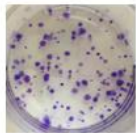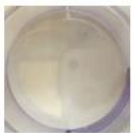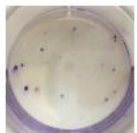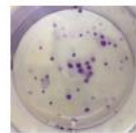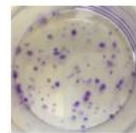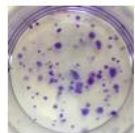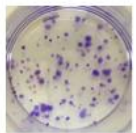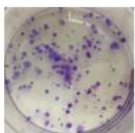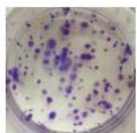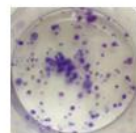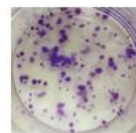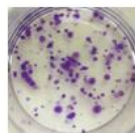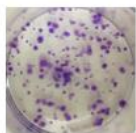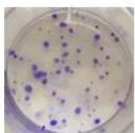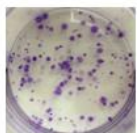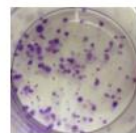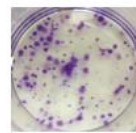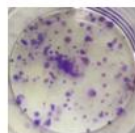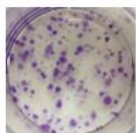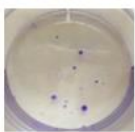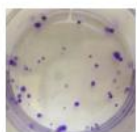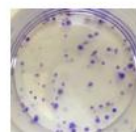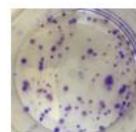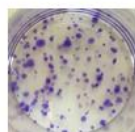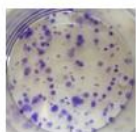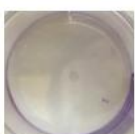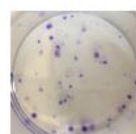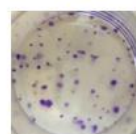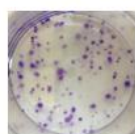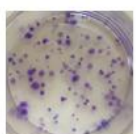
The SF (%) of cells treated with both chemo and photothermal treatments was significantly lower than that of cells treated with either treatment administered alone (*p<0.01-0.05, **p<0.001-0.01 and ***p<0.0001-0.001).

However, the SF (%) of GNShells+SH-P(PEGMA)100+Gem treated cells was very close to the values for the free drugs at lower concentrations (0.1 µmol L^{-1} to 0.001 µmol L^{-1} Gem equivalent).

In summary, the presented *in vitro* results provide strong evidence to support GNShells+SH-P(PEGMA)100+Gem as an effective therapeutic multifunctional platform with a promising potential for photo-chemothermal therapy. The results confirmed that combination of chemo- and phototherapy augmented the therapeutic outcomes of GNShells+SH-P(PEGMA)100+Gem by enhancing the accumulation, release and cytotoxicity efficacy of Gem along with lowering the effective dose and side effects of this potent anti-cancer drug.

Table 4.5. Digital photographs of the clonogenic assay of MiaPaCa-2 cells performed with the incubation of cells with free Gem, GNShells+SH-P(PEGMA)100 and GNShells+SH-P(PEGMA)100+Gem with and without laser irradiation (λ = 640 nm, 0.9 W cm^{-2}, 60 min) as a function of Gem concentration.

Figure 4.17. The percentage survival fraction of MiaPaCa-2 cells post-treatment with free Gem, GNShells+SH-P(PEGMA)100 and GNShells+SH-P(PEGMA)100+Gem with and without laser irradiation (λ = 640 nm, 0.9 W cm^{-2}, 60 min) as a function of Gem concentration after 14 days. Error bars were based on standard deviations of three different samples at each data point. Asterisks denote statistical significance level (*p<0.01-0.05, **p<0.001-0.01 and ***p<0.0001-0.001).

4.5. Conclusion

In this chapter, GNShells+SH-P(PEGMA)100+Gem as a multifunctional nanoformulation for multimodal therapeutic was demonstrated *in vitro*. Through the synergistic chemical and photothermal effect under the activation of a single wavelength laser (λ = 640 nm, 0.9 W cm^{-2}), GNShells+SH-P(PEGMA)100+Gem showed significantly higher cell-killing ability than the chemotherapeutic efficiency of Gem and the photothermal therapeutic efficiency of GNShells+SH-P(PEGMA)100 at the equivalent drug concentration.

Combination of the two therapeutic modes resulted in reduction of cellular viability of a model pancreatic cancer cell line by efficient photothermal effects of GNShells, thermal-chemopotentiation of Gem, acceleration of drug release and cellular internalisation enhancement.

This combinational approach could be used to develop a new delivery system based on gold nanostructured platforms for precision cancer medicine.

Chapter 5
General conclusion

Nanotechnology drug delivery applications occur through the use of designed nanoformulations in order to increase the drug concentration at site of action by overcoming the barriers such as unstability of therapeutic agents in the blood stream. Gem is a pyrimidine analogue that has long been considered as a well-established treatment for unresectable and metastatic pancreatic cancers. However, Gem molecules undergoe rapid and extensive inactivation in plasma and lose their antiproliferative action. This work was aimed to design and develop a nanoformulation for stable and effective drug delivery of the anti-cancer drug Gem.

Since GNPs have the ability to participate in noncovalent and covalent bonding, they undergo surface functionalisation with polymers and small moleculues and beside; they also have the capability to be used in photothermal therapy. Therefore, GNPs-based chemotherapeutics was used in order to enhance the potency of a therapeutic agent after its conjugation to polymer-stabilised GNPs.

One of the major objectives of this study was to promote the therapeutic efficacy of the designed nanosystem by incorporating both laser-induced hyperthermia mediated by GNShells and Gem and to demonstrate the potentially superior efficacy of this combination in treating pancreatic cancer compared to either photothermal agents or chemotherapeutic agent as standalone therapies.

This study elicited the synthesis and formulation of suitably nanosized samples: GNShells+SH-P(PEGMA)10+Gem, GNShells+SH-P(PEGMA)50+Gem and GNShells+SH-P(PEGMA)100+Gem, with excellent physicochemical parameters such as acceptable PDI, zeta potential, colloidal stability, loading efficiency, drug release profile, etc., which was obtained by sequential optimisation of the formulation parameters. The cytotoxic performance of the system was established by conducting *in vitro* assays,

which confirmed that GNShells+SH-P(PEGMA)10+Gem, GNShells+SH-P(PEGMA)50+Gem and GNShells+SH-P(PEGMA)100+Gem effectively killed the cancer cells in a time- and concentration-dependent manner. However, this study has provided valuable insight into the effects of type and length of the coated polymers for the application of GNShells in the delivery of Gem that should be considered when designing polymer structures as well as reproducible formulation conditions. The data showed that GNShells coated with the synthesised SH-PEGMA with longer chain length (lower grafting density and dilute brush conformation) were taken up by the MiaPaCa-2 cells with greater efficiency compared to all other nanoformulations.

Furthermore, results showed that GNShells+SH-P(PEGMA)100+Gem of ~ 70 nm are perfect photothermal agents when irradiated with a red laser. (photoconversion efficiency of 20% was attained). Chemptherapy was potentiated when used in combination with Photothermal therapy. The epxerimental data showed pronounced therapeutic action of this nanomedicinal approach than that of free drug upon red laser irradiation. Overall, GNShells+SH-P(PEGMA)100+Gem showed promising potential as a new laser based treatment modality for pancreatic cancer and overcome the serious challenges faced by monothearpy for exmaple by reducing the systemic dose of Gem and improve its therapeutic index with laser radiation of low-power density.

Chapter 6
Future work

The quantitative evaluation of the cellular uptake of GNShells+SH-P(PEGMA)100 with and without laser irradiation can be determined by the inductively coupled plasma-mass spectroscopy (ICP-Mass). This method will allow the exact quantification of the cellular uptake of the formulations in order to confirm the qualitative findings of TEM microscopy.

To evaluate the exact mode of cell death mechanism of GNShells+SH-P(PEGMA)100 and GNShells+SH-P(PEGMA)100+Gem under 640 nm laser irradiation, the evaluation of apoptosis/necrosis ratio of treated MiaPaca-2 cells can be studied by determining the cell number and cell morphology using confocal microscopy. The necrotic cells will be stained with red fluorescence ethidium homodimer III (excitation/emission: 528/617 nm), while apoptotic cells will be stained with annexin V conjugated to green fluorescence CF^{TM} 488A (excitation/emission: 490/515 nm). The fractions of apoptotic or necrotic cells are determined using five random microscopic images with at least 1×10^3 cells per group using Zen2009.

Motivated by the promising *in vitro* results, human tumor xenograft in a nude mouse model can be used to assess the effects of anti-tumor efficacy and augmentation of inhibitory potential of GNShells+SH-P(PEGMA)100+Gem in combination with photothermal therapy.. To investigate the optimal chemo and photothemal therapy dosing schedule, laser treatment can be conducted 24 h after intravenous injection of GNShells+SH-P(PEGMA)100+Gem via the tail vein. The tumor volume can be measured using a caliper and calculated as length × width)^2/2. (Li *et al*, 2014; Cao *et al.,* 2017).

A.1. Theoritical M_n calculation from ^{1}HNMR monomer conversion.

Monomer conversion (%)	Expected DP	Units of monomers	M_n of monomers (g mol^{-1})	Calculated M_n +CTA (M_n = 403 g mol^{-1})	Atomic weight of cleaved CTA (g mol^{-1})	M_n of polemers after aminolysis (g mol^{-1})
92	10	9.2		3 200		3 000
87	50	44	300	13 600	246	13 400
94	100	94		28 600		28 000

A.2. Colloidal stability of the PEGylated GNShells throughout 14 days by monitoring the hydrodynamic size of the nanoformulations.

Days	GNShells+SH-PEG6000	GNShells+SH-P(PEGMA)10	GNShells+SH-P(PEGMA)50	GNShells+SH-P(PEGMA)100
0	70.63±1.91	64.94±1.42	67.87 ± 1.20	70.58 ± 0.46
2	69.22±0.14	65.73±1.05	67.09 ± 1.17	71.25 ± 0.86
4	70.37±0.07	65.09±1.23	65.94 ± 1.77	71.90 ± 1.48
6	69.61±0.91	64.94±0.00	66.25 ± 1.22	73.01 ± 1.41
8	69.42±0.28	64.88±0.59	66.16 ± 1.38	71.30 ± 1.15
10	68.93±0.69	65.28±1.37	66.49 ±1.18	71.78 ± 1.07
12	69.93±1.91	65.27±0.82	67.43 ± 1.34	72.18 ± 0.66
14	70.1±0.94	65.99±1.48	66.30 ± 0.08	71.82 ± 0.72

A.3. PDI of the PEGylated GNShells throughout 14 days.

PDI	GNShells+SH-PEG6000	GNShells+SH-P(PEGMA)10	GNShells+SH-P(PEGMA)50	GNShells+SH-P(PEGMA)100
0	0.206 ± 0.01	0.232 ± 0.01	0.226 ± 0.02	0.204 ± 0.02
2	0.191 ± 0.01	0.232 ± 0.03	0.21 ± 0.02	0.21 ± 0.03
4	0.218 ± 0.04	0.226 ± 0.02	0.21 ± 0.03	0.214 ± 0.02
6	0.213 ± 0.01	0.251 ± 0.02	0.237 ± 0.01	0.209 ± 0.02
8	0.225 ± 0.01	0.23 ± 0.02	0.231 ± 0.01	0.214 ± 0.01
10	0.23 ± 0.01	0.233 ± 0.02	0.229 ± 0.01	0.223 ± 0.03
12	0.232 ± 0.00	0.233 ± 0.02	0.228 ± 0.01	0.227 ± 0.03
14	0.237 ± 0.01	0.232 ± 0.01	0.218 ± 0.01	0.214 ± 0.01

A.4. Representative DLS graphs of the PEGyalted GNShells throughout 14 days.

Days	GNShells+SH-PEG6000	GNShells+SH-P(PEGMA)10	GNShells+SH-P(PEGMA)50	GNShells+SH-P(PEGMA)100
0				
2				
4				
6				
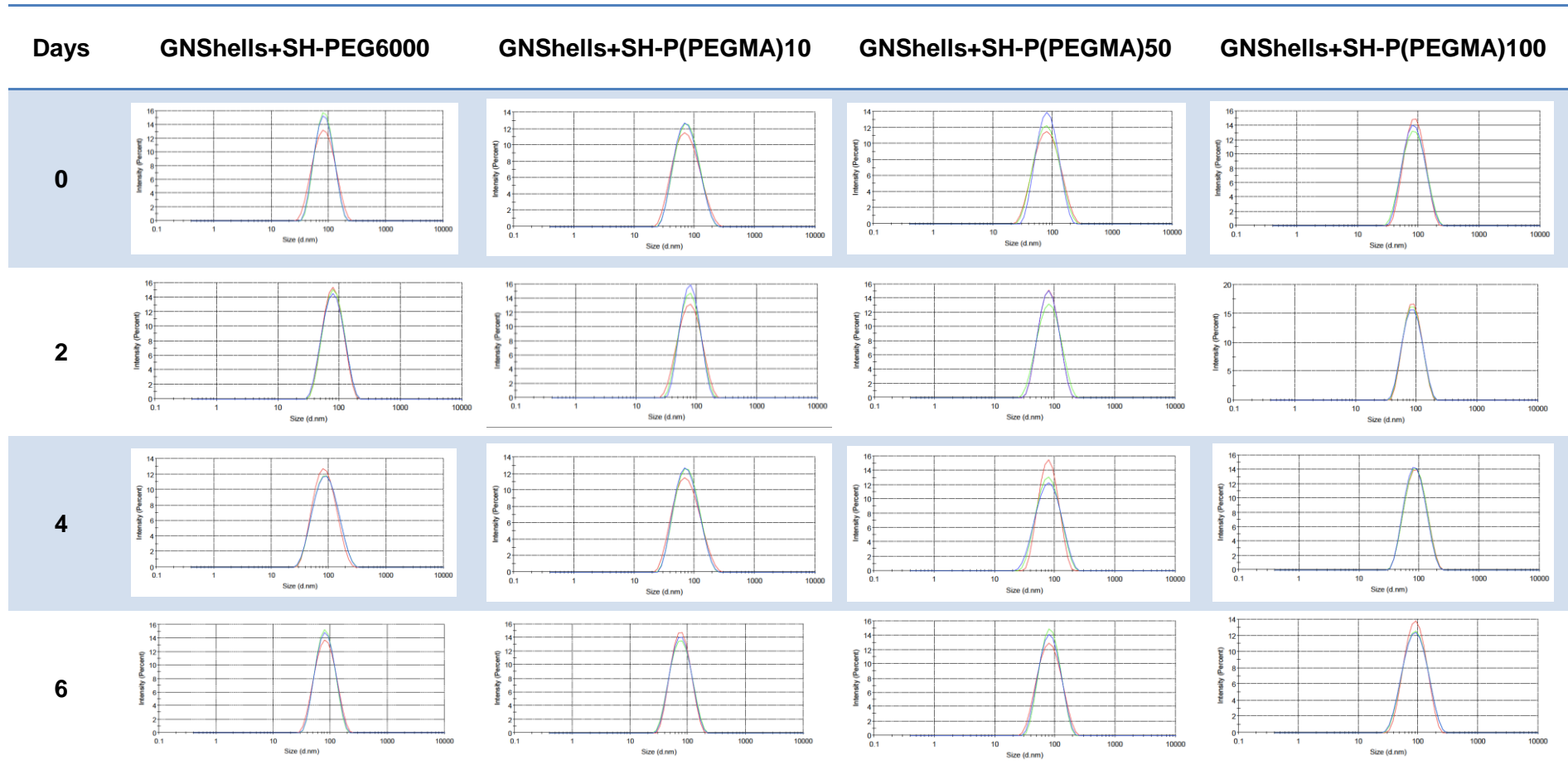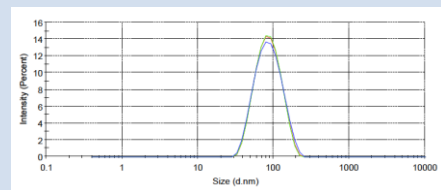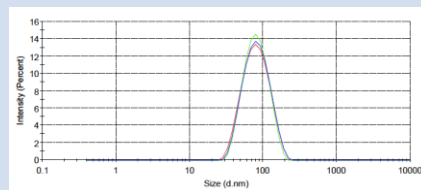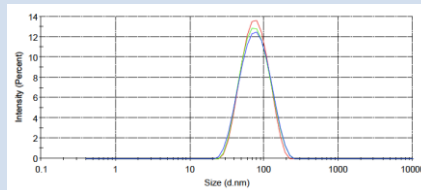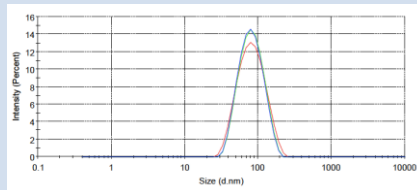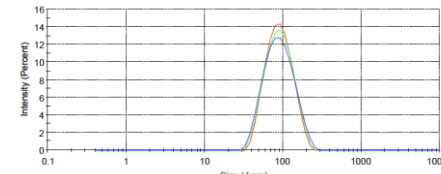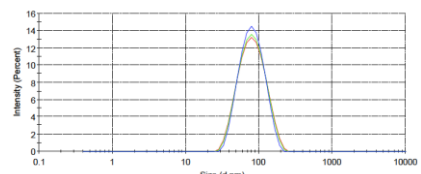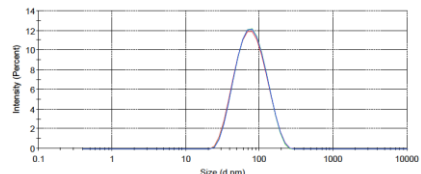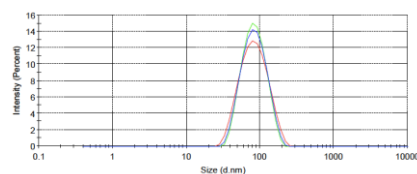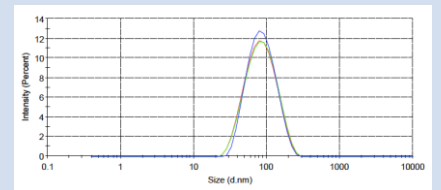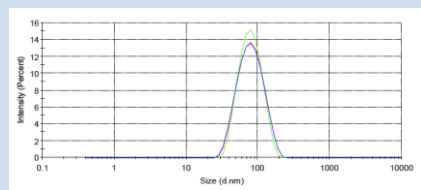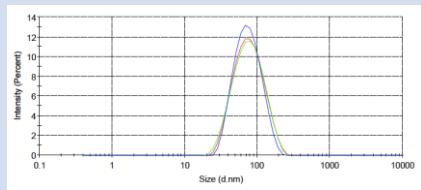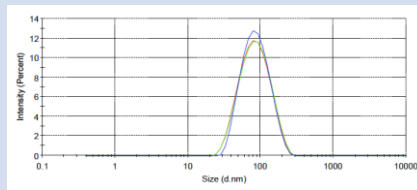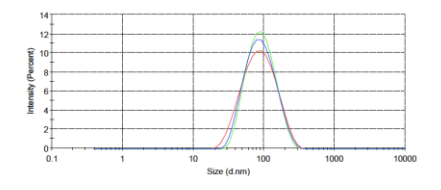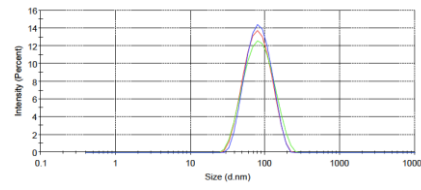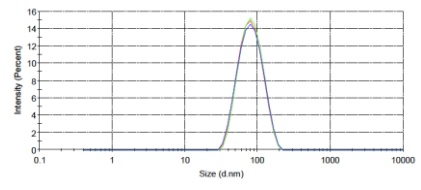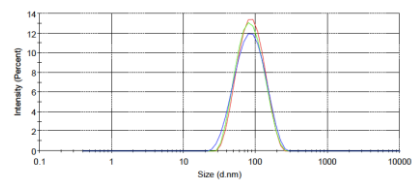
A.5. ζ-potential values of GNShells coated with thiol-terminated polymers over the period of 14 days.

Days	GNShells+SH-PEG6000	GNShells+SH-P(PEGMA)10	GNShells+SH-P(PEGMA)50	GNShells+SH-P(PEGMA)100
0	-21.6	-34	-30.5	-26.3
2	-20.7	-35.6	-29.6	-25.2
4	-21.5	-36.4	-29.9	-24.9
6	-19.2	-37.2	-33.1	-26.5
8	-19.1	-34.8	-24.2	-24.8
10	-18.2	-34.7	-29.2	-25.1
12	-18.1	-35.8	-26.5	-26.3
14	-20.1	-35.7	-27.3	-26.7

A.6. Colloidal stability of the Gem-loaded GNShells throughout 14 days by monitoring the hydrodynamic size of the nanoformulations.

Days	GNShells+SH-PEG6000+ Gem	GNShells+SH-P(PEGMA)10+ Gem	GNShells+SH-P(PEGMA)50+ Gem	GNShells+SH-P(PEGMA)100+ Gem
0	69.98 ± 0.28	65.56 ± 0.05	66.72 ± 0.83	70.81 ± 1.03
2	69.53 ± 0.51	67.34 ± 0.68	66.44 ± 0.80	71.14 ± 1.23
4	68.69 ± 1.44	66.17 ± 0.86	65.06 ± 1.14	71.45 ± 0.85
6	70.79 ± 1.28	66.00 ± 0.06	66.42 ± 0.59	73.15 ±1.08
8	69.35 ± 1.65	64.80 ± 1.22	66.75 ± 1.15	71.10 ± 1.52
10	69.53 ± 1.06	64.81 ± 0.84	66.99 ± 0.55	72.08 ± 0.24
12	69.64 ± 1.28	64.89 ± 1.45	67.62 ± 0.97	71.77 ± 0.71
14	69.74 ± 1.31	66.00 ± 1.85	67.93 ± 0.45	73.07 ± 1.09

A.7. PDI of the Gem-loaded GNShells throughout 14 days to indicate the width of the overall distribution.

Days	GNShells+SH-PEG6000+ Gem	GNShells+SH-P(PEGMA)10+ Gem	GNShells+SH-P(PEGMA)50+ Gem	GNShells+SH-P(PEGMA)100+ Gem
0	0.203 ± 0.01	0.212 ± 0.00	0.201 ± 0.01	0.22 ± 0.00
2	0.184 ± 0.01	0.221 ± 0.01	0.219 ± 0.01	0.206 ± 0.00
4	0.244 ± 0.01	0.229 ± 0.02	0.199 ± 0.00	0.204± 0.02
6	0.196 ± 0.03	0.213 ± 0.00	0.221 ± 0.00	0.224 ± 0.01
8	0.227 ± 0.03	0.228 ± 0.01	0.225 ± 0.01	0.235 ± 0.01
10	0.217 ± 0.03	0.223 ± 0.02	0.22 ± 0.00	0.241 ± 0.00
12	0.216 ± 0.02	0.247 ± 0.00	0.209 ± 0.01	0.216 ± 0.03
14	0.205 ± 0.01	0.205 ± 0.01	0.217 ± 0.01	0.214 ± 0.03

A.8. Representative DLS graphs of the Gem-loaded GNShells throughout 14 days.

Days	GNShells+SH-PEG6000+Gem	GNShells+SH-P(PEGMA)10+Gem	GNShells+SH-P(PEGMA)50+Gem	GNShells+SH-P(PEGMA)100+Gem
0				
2				
4				
6				
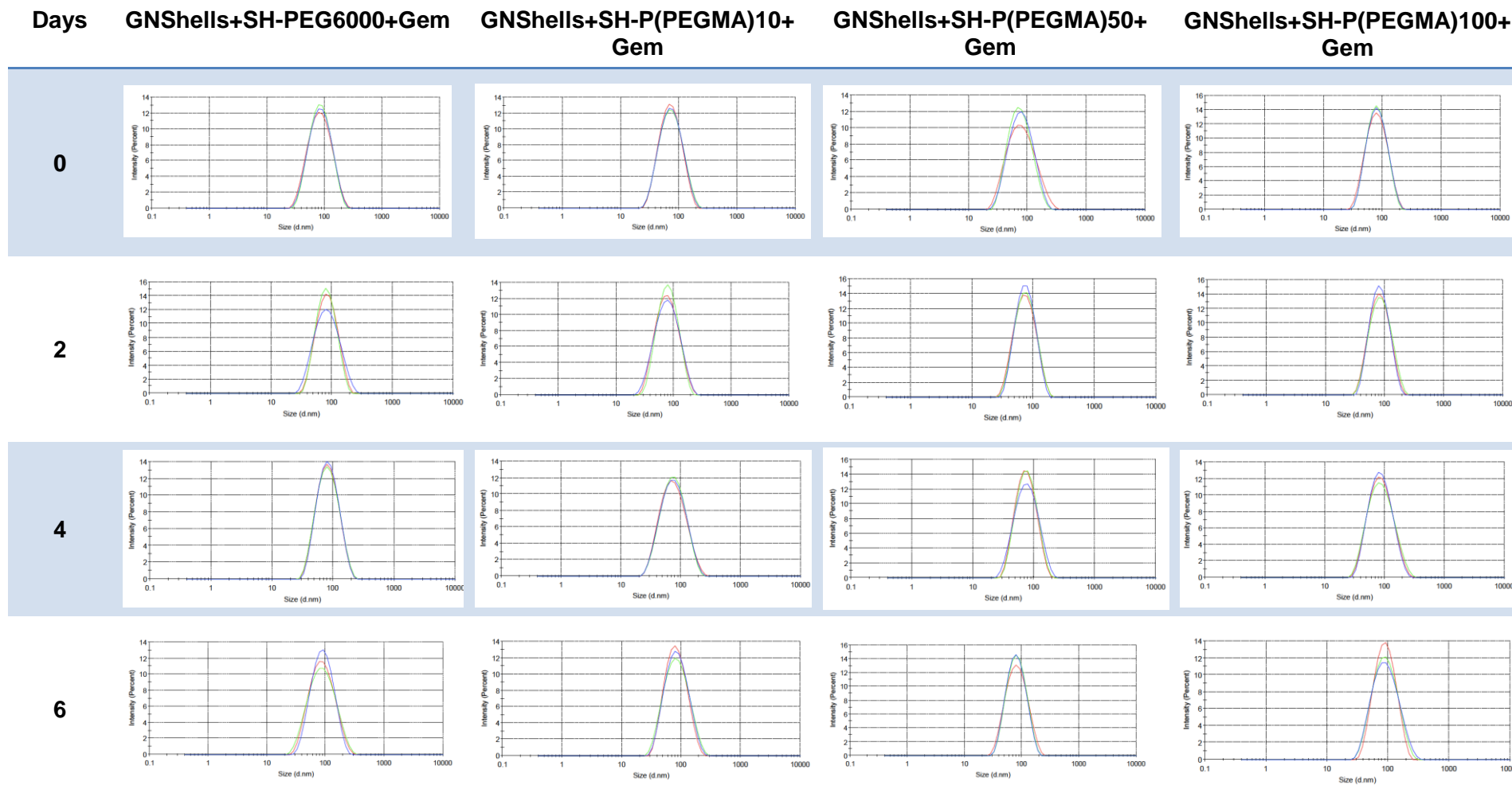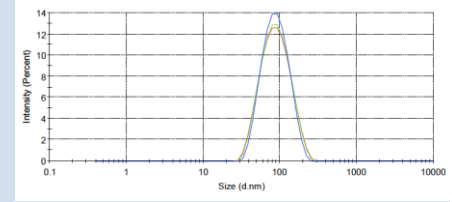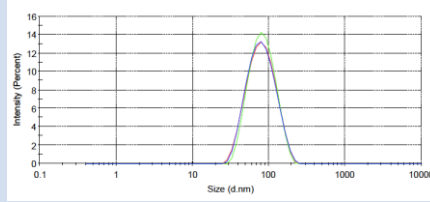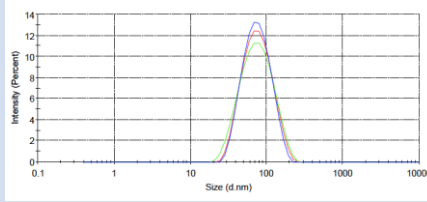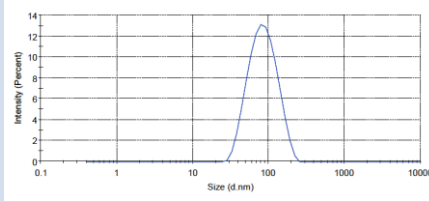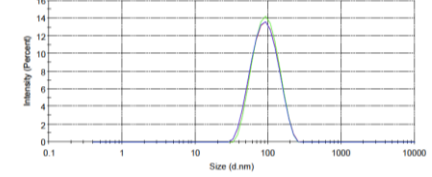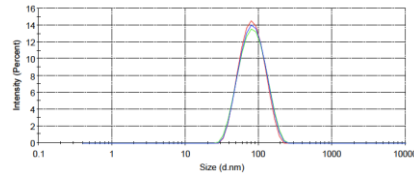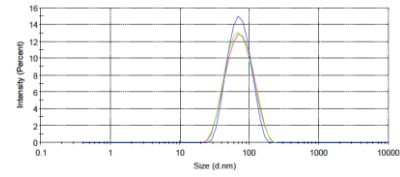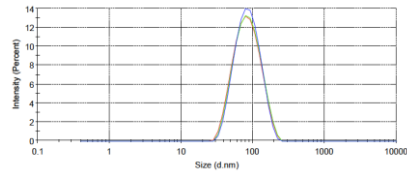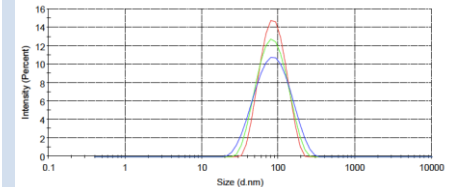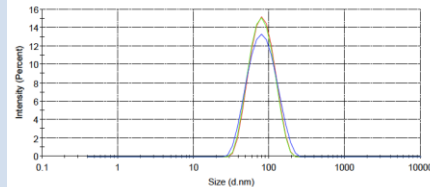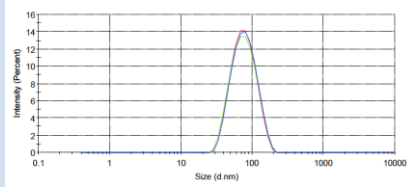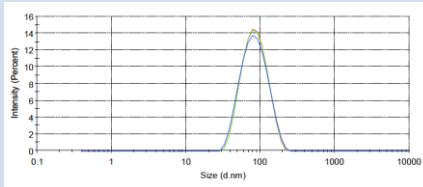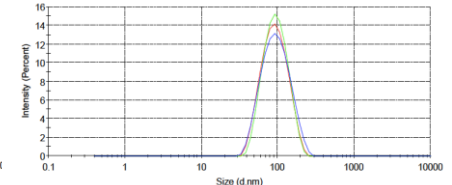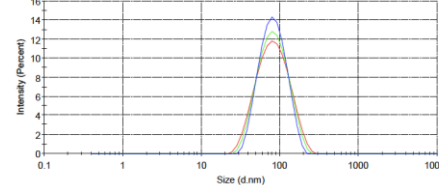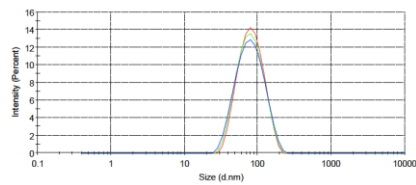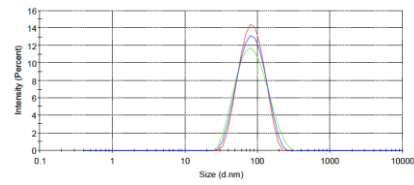
A.9. ζ-potential values of Gem-loaded GNShells over the period of 14 days.

Days	GNShells+SH-PEG6000+ Gem	GNShells+SH-P(PEGMA)10+ Gem	GNShells+SH-P(PEGMA)50+ Gem	GNShells+SH-P(PEGMA)100+ Gem
0	-15.8	-29.6	-26.3	-20.36
2	-16.23	-26	-23.7	-19.74
4	-15.14	-26.8	-24.8	-20.6
6	-15.86	-32.1	-26.7	-20.4
8	-12.8	-29.5	-24.4	-18.9
10	-15.28	-34.4	-23.6	-19.4
12	-15.31	-31.4	-22.2	-19.5
14	-16.11	-30.6	-22.1	-18.92

A.10. HPLC calibration curves and linear regression analysis by plotting peak area versus nominal concentrations of Gem in different media.

Gem in dH$_2$O

Chart: $y = 40.3x - 21.688$, $R^2 = 0.99894$. Peak area (a.u.) versus Gem concentration (µg ml^{-1}).

Gem in PBS (pH 7.4)

Chart: $y = 39.116x - 7.7873$, $R^2 = 0.99947$. Peak area (a.u.) versus Gem concentration (µg ml^{-1}).

Gem in Na. acetate buffer (pH 5.2)

Chart: $y = 42.053x + 11.64$, $R^2 = 0.99973$. Peak area (a.u.) versus Gem concentration (µg ml^{-1}).

Gem in medium

Chart: $y = 39.854x + 10.311$, $R^2 = 0.9996$. Peak area (a.u.) versus Gem concentration (µg ml^{-1}).

A.11. Selective chromatograms of Gem in different media.

Concentration (µg)	Gem in dH2O	Gem in PBS (pH 7.4)	Gem in Na. acetate buffer (pH 5.2)	Gem in medium
75 µg				
50 µg				
25 µg				
10 µg				
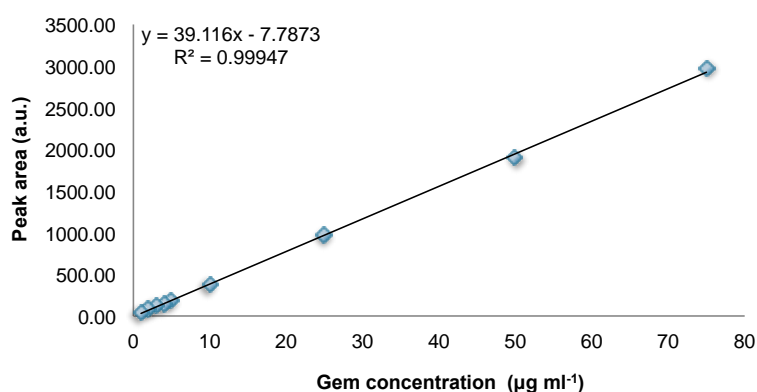
5 µg				
4 µg				
3 µg				
2 µg				
1 µg				
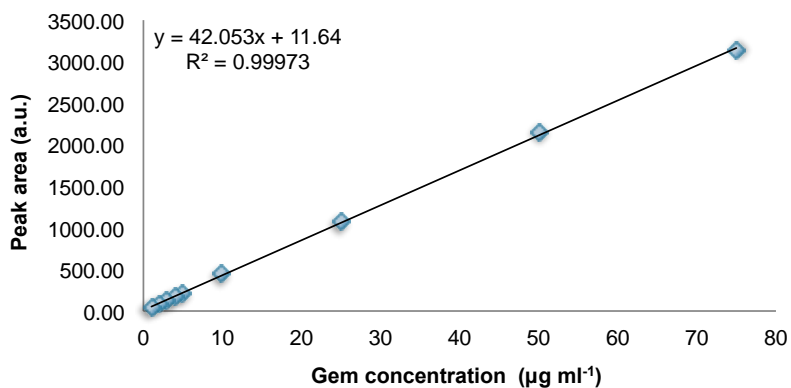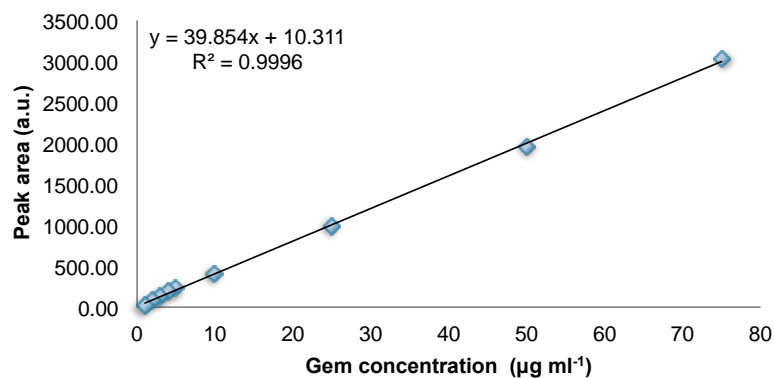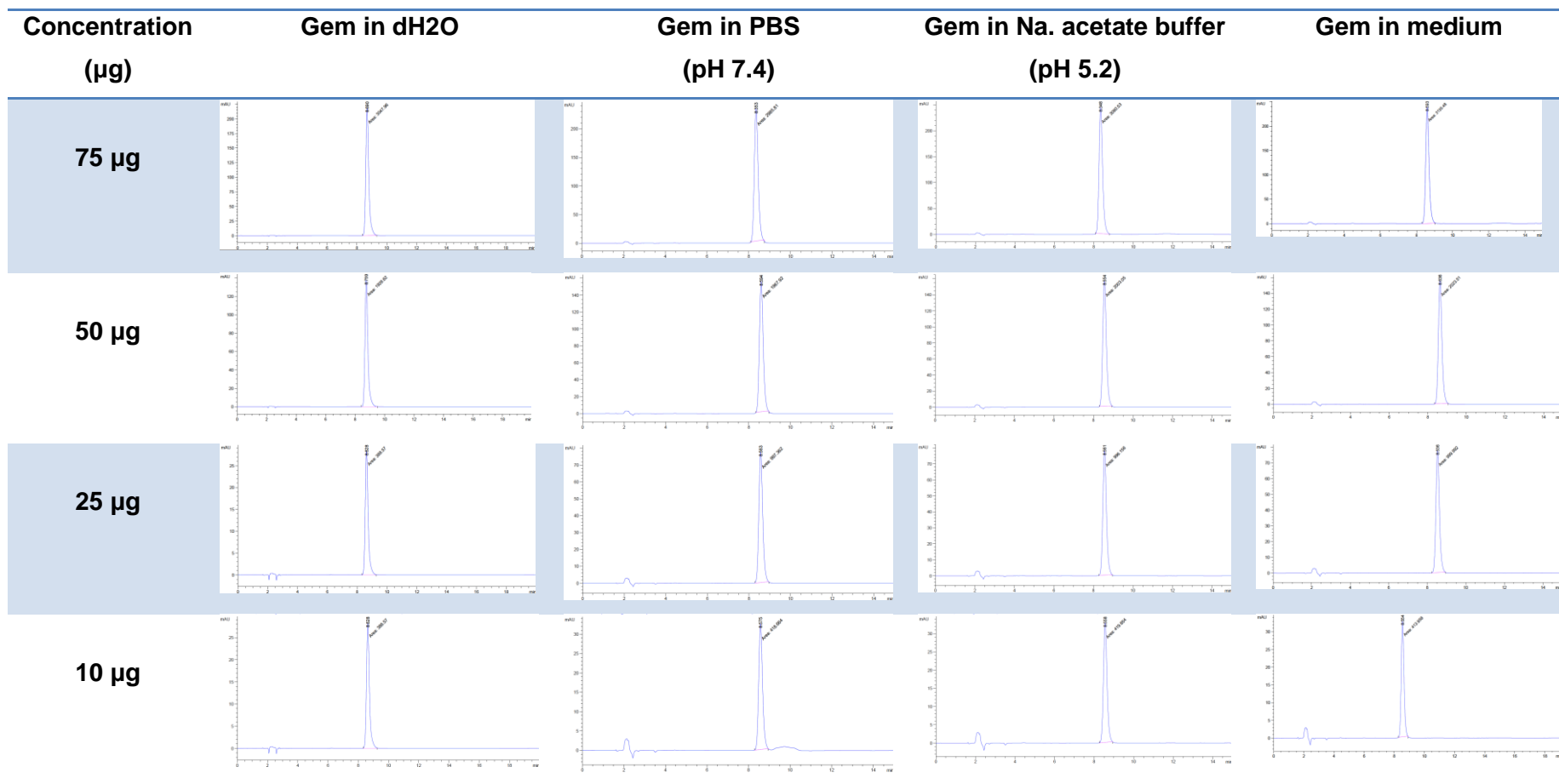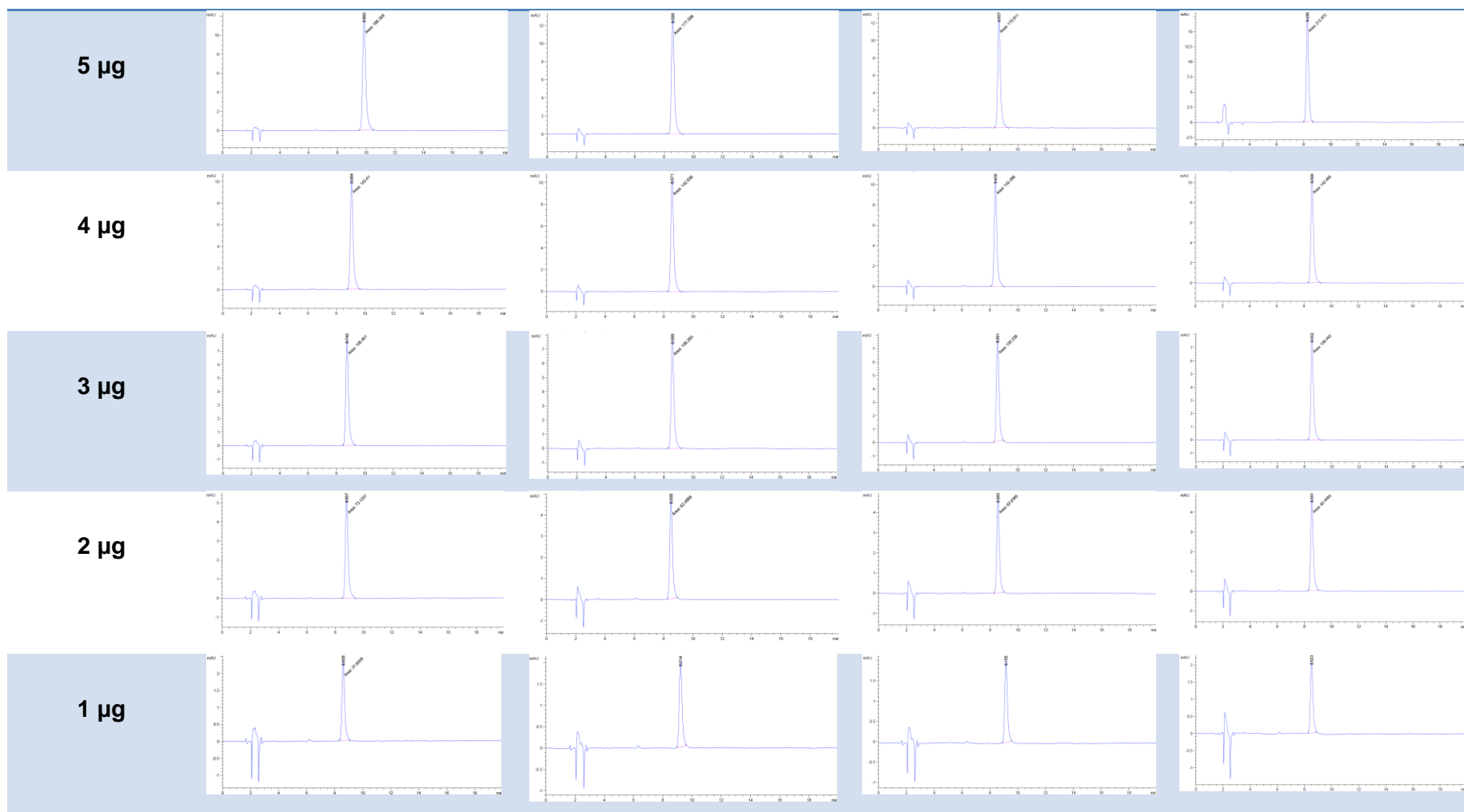
A.12. Cytotoxicity profiles of GNShells+SH-PEG6000+Gem GNShells+SH-P(PEGMA)10+Gem GNShells+SH-P(PEGMA)50+Gem and GNShells+SH-P(PEGMA)100+Gem for MiaPaCa-2 cells as a function of Gem concentration after 48h (a) and 72 h (b) incubation, measured by MTT cytotoxicity assay.

	Incubation time (h)	
	48 h	**72 h**
	a	**b**
GNShells+SH -P(PEGMA)10-50100+Gem		
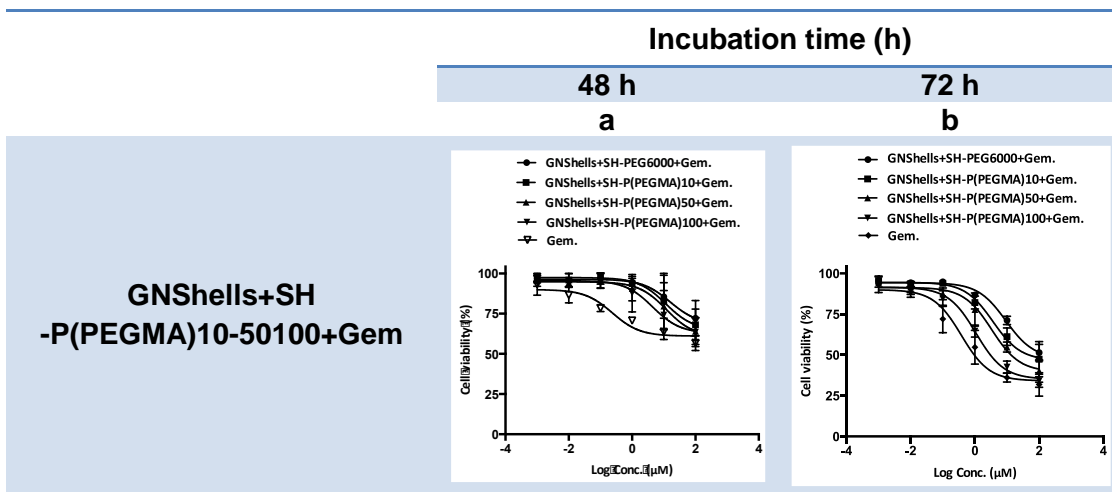
A.13. Cytotoxicity profiles of Gem, GNShells+SH-P(PEGMA)100 and GNShells+SH-P(PEGMA)100+Gem with and without laser irradiation (λ = 640 nm, 0.9 W cm^{-2}, 1-5-10 min) for MiaPaCa-2 cells as a function of Gem concentration after 48h (a) and 72 h (b) incubation, measured by MTT cytotoxicity assay.

	Incubation time (h)	
	48 h	**72 h**
	a	**b**
Gem+Laser **(λ = 640 nm, 0.9 W cm^{-2})**		
GNShells+SH-P(PEGMA)100+Laser **(λ = 640 nm, 0.9 W cm^{-2})**		
GNShells+SH-P(PEGMA)100+Gem+Laser **(λ = 640 nm, 0.9 W cm^{-2})**		
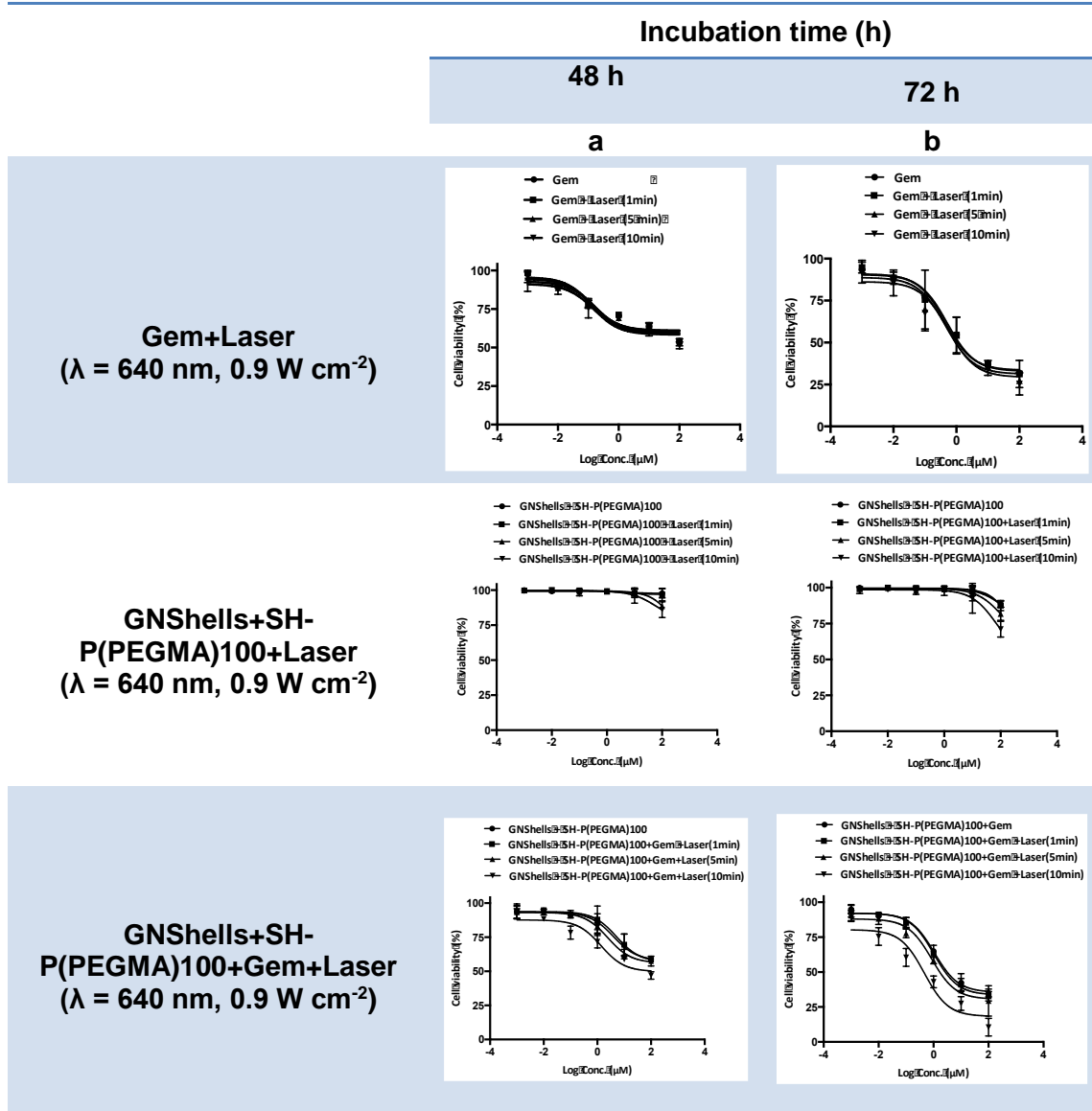
Chapter 8
References

Abadeer, N.S. and Murphy, C.J. (2016). Recent Progress in Cancer Thermal Therapy Using GoldNanoparticles. J. Phys. Chem. 120, pp. 4691-4716.

Adabi, M., Naghibzadeh, M., Adabi, M., Zarrinfard, M.A., Esnaashari, S.S., Seifalian, A.M., Faridi-Majidi, R., Tanimowo Aiyelabegan, H. and Ghanbari, H. (2016). Biocompatibility and nanostructured materials: applications in nanomedicine. Artif Cells Nanomed Biotechnol. 31, pp.1-10.

Adachi, S., Kokura, S., Okayama, T., Ishikawa, T., Takagi, T., Handa, O., Naito, Y. and Yoshikawa, T. (2009). Effect of hyperthermia combined with gemcitabine on apoptotic cell death in cultured human pancreatic cancer cell lines. Int J Hyperthermia. 25(3). pp. 210-219.

Affram, K., Udofot, O., and Agyare, E. (2015). Cytotoxicity of gemcitabine-loaded thermosensitive liposomes in pancreatic cancer cell lines. Integr Cancer Sci Ther. 2(2), pp.133-142.

Aggarwal, P., Hall, J.B., McLeland, C.B., Dobrovolskaia, M.A., McNeil, S.E. (2009). Nanoparticle interaction with plasma proteins as it relates to particle biodistribution, biocompatibility and therapeutic efficacy. Adv Drug Deliv Rev. 61, pp. 428–437.

Aguirre-ghiso, J.A. (2008). Models, mechanisms and clinical evidence for cancer dormancy. Nat Rev Cancer. 7(11), pp. 834–846.

Ahmed, K., Zhao, Q.L., Matsuya, Y., Yu, D.Y., Salunga, T.L., Nemoto, H. and Kondo, T. (2007). Enhancement of macrospheloid induced apoptosis by mild hyperthermia. Int J Hyperthermia. 23, pp. 353–361.

Ahmed, K., Hori, T., Yu, D., Wei, Z., Zhao, Q., Nakashima, M., Hassan, M.A. and Kondo, T. (2008). Hyperthermia chemo-sensitization, chemical thermo-sensitization and apoptosis. Thermal Med. 24, pp. 1-12.

Ahmad, T., Wani, I. A., Ahmed, J., Al-Hartomy, O. A. (2014). Effect of gold ion concentration on size and properties of gold nanoparticles in TritonX-100 based inverse microemulsions. Appl Nanosci. 4, pp. 491–498.

Ahmed, K., Tabuchi, Y. and Kondo, T. (2015). Hyperthermia: an effective strategy to induce apoptosis in cancer cells. Apoptosis. 20, pp. 1411–1419.

Alexiou, C., Arnold, W., Klein, R.J., Parak, F.G., Hulin, P., Bergemann, C., Erhardt, W., Wagenpfeil, S., Lubbe, A.S. (2000). Locoregional Cancer Treatment with Magnetic Drug Targeting. Cancer Res. 60, pp. 6641-6648.

Alkilany, A.M. and Murphy, C.J. (2010). Toxicity and cellular uptake of gold nanoparticles: what we have learned so far? J Nanopart Res. 12, pp. 2313–2333.
Andersson, R., Aho, U., Nilsson, B., Peters, G.J., Pastor-Anglada, M., Rasch, W. and Sandvold, M.L. (2009). Gemcitabine chemoresistance in pancreatic cancer: molecular mechanisms and potential solutions. Scand J Gastroenterol. 44(7), pp. 782-786.

Asayesh, T., Changizi, V. and Eyvazzadeh, N. (2016). Assessment of cytotoxic damage induced by irradiation combined with hyperthermia and Gemcitabine on cultured glioblastoma spheroid cells. Radiation Physics and Chemistry. 120, pp. 44–48.

Angele, M.K., Albertsmeier, M., Prix, N.J., Hohenberger, P., Abdel-Rahman, S., Dieterle, N., Schmidt, M., Mansmann, U., Bruns, C.J., Issels, R.D., Jauch, K.W. and Lindner, L.H. (2014). Effectiveness of regional hyperthermia with chemotherapy for high-risk retroperitoneal and abdominal soft-tissue sarcoma after complete surgical resection: a subgroup analysis of a randomized phase-III multicenter study. Ann Surg. 260(5), pp. 749-754.

Auguste, P., Fallavollita, L., Wang, N., Burnier, J., Bikfalvi, A. and Brodt, P. (2007). The Host Inflammatory Response Promotes Liver Metastasis by Increasing Tumor Cell Arrest and Extravasation. AJP. 170(5), 1781–1792.

Aqil, A., Qiu, H., Greisch, G.F., Jerome, R., De Pauw, E., Jerome, C. (2008). Coating of gold nanoparticles by thermosensitive poly(N-isopropylacrylamide) end-capped by biotin. Polymer. 49(5), pp. 1145-1153.

Ashwell, G.J., Williams, A.T., Barnes, S.A., Chappell, S.L., Phillips, L.J., Robinson, B.J., Urasinska-Wojcik, B., Wierzchowiec, P., Gentle, I.R., and Wood, B.J. (2011). Self-Assembly of Amino−Thiols via Gold−Nitrogen Links and Consequence for in situ Elongation of Molecular Wires on Surface-Modified Electrodes. J. Phys. Chem. C. 115(10), PP. 4200-4208.

Babu, K. and Dhamodharan, R. (2009). Synthesis of Polymer Grafted Magnetite Nanoparticle with the Highest Grafting Density via Controlled Radical Polymerization. Nanoscale Res Lett. 4, pp. 1090–1102.

Bates, D.A. and Mackillop. W.J. (1986). Hyperthermia, adriamycin transport, and cytotoxicity in drug-sensitive and -resistant Chinese hamster ovary cells. Cancer Res. 46(11), pp. 5477-81.

Bao, Z., Liu, X., Liu, Y., Liu, H. and Zhao, K. (2016). Near-infrared light-responsive inorganicnanomaterials for photothermal therapy. Asian journal of pharmaceutical science. 11, pp. 349-364.

Barford, D. (2004). The role of cysteine residues as redox-sensitive regulatory switches. Curr. Opin. Struc.Biol. 14, pp. 679-686.

Becker, E. D. (1999). High resolution NMR: Theory and chemical applications, Academic Press, US.

Beere, H.M. (2005). Death versus survival: functional interaction between the apoptotic and stress-inducible heat shock protein pathways. Journal of

Clinical Investigation. 115, pp. 2633-2639.

Benoit, D.N., Zhu, H., Lilierose, M.H., Verm, R.A., Ali, N., Morrison, A.N., Fortner, J.D., Avendano, C. and Colvin, V.L. (2012). Measuring the Grafting Density of Nanoparticles in Solution by Analytical Ultracentrifugation and Total Organic Carbon Analysis. Anal. Chem. 84, pp. 9238−9245.

Berne, B.J. and Pecora, R. (2000). Dynamic Light Scattering: With Applications to Chemistry, Biology, and Physics ; John Wiley & Sons, Inc., New York. Ed 2, Courier Dover Publications.

Berridge, M.V., Herst, P.M., Tan, A. S. (2005). Tetrazolium dyes as tools in cell biology: new insights into their cellular reduction. Biotechnol Annu Rev. 11, pp. 127-152.

Bertrand, N., Wu, J., Xu, X., Kamaly, N. and Farokhzad, O. (2014). Cancer Nanotechnology: The impact of passive and active targeting in the era of modern cancer biology. Adv Drug Deliv Rev. 66, pp. 2–25.

Bettaieb, A. and Averill-Bates, D.A. (2008). Thermotolerance induced at a fever temperature of 40 degrees C protects cells against hyperthermia-induced apoptosis mediated by death receptor signalling. Biochem Cell Biol. 86(6), pp. 521-538.

Bhattacharya, R., Mukherjee, P., Xiong, Z., Atala, A., Soker, S. and Mukhopadhyay, D. (2004). Gold Nanoparticles Inhibit VEGF165-Induced Proliferation of HUVEC Cells. Nano Lett. 4(12), pp. 2479–2481.

Bishnoi, S.W., Rozell, C.J., Levin, C.S., Gheith, M.K., Johnson, B.R., Johnson, D.H. and Halas, N.J. (2006). All-Optical Nanoscale pH meter. Nano Lett. 6 (8), pp. 1687–1692.

Binenbaum, Y., Na'ara, S. and Gil, Z. (2015). Gemcitabine resistance in pancreatic ductal adenocarcinoma. Drug Resist Updat. 23, pp. 55-68.

Bonzon, C., Bouchier-Hayes, L., Pagliari, L.J., Green, D.R. and Newmeyer, D.D. (2006) Caspase-2-induced apoptosis requires bid cleavage: a physiological role for bid in heat shock-induced death. Mol Biol Cell. 17, pp. 2150–2157.

Boisselier, E. and Astruc, D. (2009). Gold nanoparticles in nanomedicine: preparations, imaging, diagnostics, therapies and toxicity. Chem. Soc. Rev. 38, pp. 1759-1782.

Botchway, S.W., Coulter, J.A., and Currell, F.J. (2015). Imaging intracellular and systemic in vivo gold nanoparticles to enhance radiotherapy. British Journal of Radiology. 88(1054), pp.1-13.

Bouchier-Hayes, L., Oberst, A., McStay, G.P., Connell, S., Tait, S.W., Dillon, C.P., Flanagan, J.M., Beere, H.M. and Green, D.R. (2009) Characterization of cytoplasmic caspase-2 activation by induced proximity. Mol Cell. 35, pp. 830–840.

Brandon, M., Baldi, P. and Wallace, D.C. (2006). Mitochondrial mutations in cancer. Oncogene. 25, pp. 4647–4662.

Brongersma, M.L., Halas N.J. and Nordlander, P. (2015). Plasmon-induced hot carrier science and technology. Nature Nanotechnology. 10, pp. 25–34.

Brusa, P., Immordino, M.L., Rocco, F. and Cattel, L. (2007). Antitumor Activity and Pharmacokinetics of Liposomes Containing Lipophilic Gemcitabine Prodrugs. ANTICANCER RESEARCH. 27, pp. 195-200.

Brookes, P.S., Yoon, Y., Robotham, J.L., Anders, M.W. and Sheu, S.S. (2004).
Calcium, ATP, and ROS: a mitochondrial love-hate triangle, Am J Physiol Cell Physiol. 287(4), pp. 817-833.

Bull, J.M.C. (1984). An update on the anticancer effects of a combination of chemotherapy and hyperthermia. Cancer Res. 44, pp. 4853–4856.

Cai, W., Gao, T., Hong, H. and Sun, J. (2008). Applications of gold nanoparticles in cancer nanotechnology. Nanotechnol Sci Appl. 1.

Camacho. A.S. (2015). Plasmon nanolasers and Plasmon optical tweezers. J. Nano Sc. Tech. 3, pp. 10-17.

Cao, Y., Wu, Y., Wang, G., Yi, J., Yu, C., Huang, Y., Sun, L., Bao, Y. and Li, Y. (2017). Near-infrared conjugated polymers for photoacoustic imaging-guided photothermal/chemo combination therapy. J. Mater. Chem. B. 5, pp. 5479-5487.

Cao, L., Zhu, T. and Liu, Z. (2006). Formation mechanism of nonspherical gold nanoparticles during seeding growth: Roles of anion adsorption and reduction rate. J. Colloid Interface Sci. 293, pp. 69 – 76.

Cavalcante, L.D.S. and Monteiro, G. (2014). Gemcitabine: Metabolism and molecular mechanisms of action, sensitivity and chemoresistance in pancreatic cancer. European Journal of Pharmacology. 741, pp. 8–16.

Cedervall, T., Lynch, I., Lindman, S., Berggård, T., Thulin, E., Nilsson, H., Dawson, K.A., Linse, S. (2007). Understanding the nanoparticle-protein corona using methods to quantify exchange rates and affinities of proteins for nanoparticles. Proc Natl Acad Sci USA. 104, pp. 2050–2055.

Celano, M., Calvagno, M.G., Bulotta, S., Paolino, D., Arturi, F., Rotiroti, D., Filetti, S., Fresta, M. and Russo D. (2004) Cytotoxic effects of Gemcitabine-loaded liposomes in human anaplastic thyroid carcinoma cells. BMC Cancer. 4:63.

Chang, W., Willingham, B., Slaughter, L. and Dominguez-Medina, S. (2012). Radiative and Nonradiative Properties of Single Plasmonic Nanoparticles and Their Assemblies, Accounts of chemical research. 45(11), pp. 1936-45.

Chatterjee, D.K., Diagaradjane, P. and Krishnan, S. (2011). Nanoparticle-mediated hyperthermia in cancer therapy. Ther Deliv. 2(8), pp. 1001–1014.

Chaudhari, N., Talwar, P., Parimisetty, A., d'Hellencourt C.L. and Ravanan, P. (2014). A molecular web: endoplasmic reticulum stress, inflammation, and oxidative stress, Frontiers in Cellular Neuroscience. 8(213), pp. 1-15.

Chen, W.R., Adams, R.L., Higgins, A.K., Bartels, K.E. and Nordquist, R.E. (1996) Cancer Lett. 98, pp. 169–173.

Chen, J., Saeki, F., Wiley, B.J., Cang, H., Cobb, M.J., Li, Z-Y., Au, L., Zhang, H., Kimmey, M.B., Li, X. and Xia, Y. (2005). Gold Nanocages: Bioconjugation and Their Potential Use as Optical Imaging Contrast Agents. Nano Lett., 5(3), pp. 473-477.

Cherukuri, P. and Curley, S.A. (2010). Use of nanoparticles for targeted, noninvasive thermal destruction of malignant cells. In: Anonymous Cancer Nanotechnology: Springer. 624, pp. 359-373.

Chicheł, A., Skowronek, J., Kubaszewska, M. and Kanikowski, M. (2007). Hyperthermia – description of a method and a review of clinical applications. Rep Pract Oncol Radiother. 12(5), pp. 267-275.

Chiefari, J., Chong, Y.K., Ercole, F., Krstina, J., Jeffery, J., Le, T.P.T., Mayadunne, R.T.A., Meijs, J.F., Moad, C.L., Moad, G., Rizzardo, E. and Thang, S.H. (1998). Living Free-Radical Polymerization by Reversible Addition-Fragmentation Chain Transfer: The RAFT Process. Macromolecules. 31, pp. 5559-5562

Chong, B., Moad, G., Rizzardo, E., Skidmore, M., Thang, S. H. (2006). Thermolysis of RAFT-Synthesized Poly(Methyl Methacrylate) Aust. J. Chem. 59 (10), pp. 755-762.

Chong, Y.K., Moad, G., Rizzardo, E. and Thang, S.H. (2007).

Thiocarbonylthio End Group Removal from RAFT-Synthesized Polymers by Radical-Induced Reduction. Macromolecules. 40, pp. 4446-4455.

Chong, Y.K., and Thang, S.H. (2007). Thiocarbonylthio End Group Removal from RAFT-Synthesized Polymers by Radical-Induced Reduction. Macromolecules. 40, pp. 4446-4455.

Chu K.F. and Dupuy, D.E. (2014). Thermal ablation of tumours: biological mechanisms and advances in therapy. Nature Reviews Cancer. 14, pp. 199–208.

Cividalli, A., Cruciani, G., Livdi, E., Pasqualetti, P. and Tirindelli Danesi, D. (1999). Hyperthermia enhances the response of paclitaxel and radiation in a mouse adenocarcinoma. Int J Radiat Oncol Biol Phys. 44, pp. 407-412.

Clavero, C. (2014). Plasmon-induced hot-electron generation at nanoparticle/metal-oxide interfaces for photovoltaic and photocatalytic devices, Nature Photonics. 8, pp. 95–103.

Cobley, C.M. and Xia, Y. (2010). Engineering the Properties of Metal Nanostructures via Galvanic Replacement Reactions. Mater. Sci. Eng. 70(3-6), pp. 44-62.

Contreras-Sanz, A., Scott-Ward, T.S., Gill, H.S., Jacoby, J.C., Birch, R.E., Malone-Lee, J., Taylor K.M.J., Peppiatt-Wildman, K.M. and Wildman, S.S.P. (2012). Simultaneous quantification of 12 different nucleotides and nucleosides released from renal epithelium and in human urine samples using ion-pair reversed-phase HPLC. Purinergic Signalling. 8, pp. 741–751.

d'Assignies, G., Couvelard, A., Bahrami, S., Vullierme, M., Hammel, P., Hentic, O., Sauvanet, A., Bedossa, P., Ruszniewski, P. and Vilgrain, V. (2009). Pancreatic endocrine tumors: tumor blood flow assessed with perfusion CT reflects angiogenesis and correlates with prognostic factors1. Radiology. 250(2), pp. 407-416.

Dahl, O. (1988). Interaction of hyperthermia and chemotherapy. Rec Res Cancer Res. 107, pp. 157–169.

Dahl, O. (1994). Mechanisms of thermal enhancement of chemotherapeutic cytotoxicity. Hyperthermia and Oncology, edited by M. Urano and E. Douple (Utrecht, The Netherlands: VSP), pp. 9–28.

Danhier, F., Feron, O. and Préat, V. (2010). To exploit the tumor microenvironment: Passive and active tumor targeting of nanocarriers for anti-cancer drug delivery. Journal of controlled Release 148(2), pp. 135-146.

Dasanu, C.A. (2008). Gemcitabine: vascular toxicity and prothrombotic potential. Expert Opin Drug Saf. 7(6), pp. 703–706.

Davis, S.S. (2004). Coming of Age of Lipid-Based Drug Delivery Systems. Adv. Drug Delivery Rev. 56, pp. 1241–1242.

Day, E.S., Morton, J.G. and West, J.L. (2009). Nanoparticles for Thermal Cancer Therapy. J. Biomech. Eng. 131, pp. 074001-5.

Day, E.S., Thompson, P.A., Zhang, L., Lewinski, N.A., Ahmed, N., Drezek, R.A., Blaney, S.M., West, J.L. (2010). Nanoshell-mediated photothermal therapy improves survival in a murine glioma model. J. Neurooncol. 104(1), pp. 55-63.

Demers, L.M., Ostblom, M., Zhang, H., Jang, N.H., Liedberg, B. and Mirkin, C.A. (2002). Thermal desorption behavior and binding properties of DNA bases and nucleosides on gold. J Am Chem Soc. 124(38), pp. 11248-11249.

Deshpande, M.C., Davies, M.C., Garnett, M.C., Williams, P.M., Armitage, D., Bailey, L., Vamvakaki, M., Armes, S.P. and Stolnik, S. (2004). The effect of poly(ethylene glycol) molecular architecture on cellular interaction and uptake of DNA complexes. J Control Release. 97(1), pp.143-156.

Dewey, W.C.R. and Diederich C.J. (2009). Hyperthermia classic commentary: 'Arrhenius relationships from the molecule and cell to the clinic' by William Dewey, Int. J. Hyperthermia, 10:457–483, 1994. Int. J. Hyperthermia. 25(1), pp. 21–24.

DeWitt, M.R., Pekkanen, A.M., Robertson, J., Rylander, C.G. and Rylander, M.N. (2014). Influence of Hyperthermia on Efficacy and Uptake of Carbon Nanohorn-Cisplatin Conjugates. Journal of Biomechanical Engineering. 136, pp. 0210031-02100310.

Dia, J.T., Zhang, Y., Li, H-C., Deng, Y-H., Elzatahry, A., Alghamdi, A., Fu, D-L., Jiang, Y-J., Zhao, D-Y. (2017). Enhancement of gemcitabine against pancreatic cancer by loading in mesoporous silica vesicles. Chinese Chemical Letters. 28, pp. 531–536

Dickerson, E.B., Dreaden, E.C., Huang, X., El-Sayed, I.H., Chu, H., Pushpanketh, S., McDonald, J.F. and El-Sayed, M.A. (2008) Gold nanorod assisted near-infrared plasmonic photothermal therapy (PPTT) of squamous cell carcinoma in mice. Cancer Letters. 269, pp. 57–66.

Dobrovolskaia, M.A., Neun, B.W., Man, S., Ye, X., Hansen, M., Patri, A.K., Crist, R.M. and Mcneil, S.E. (2014). Protein corona composition does not accurately predict hematocompatibility of colloidal gold nanoparticles. *Nanomed. Nanotechnol. Biol. Med.* 10(7), pp.1453-1463.

Drake, R.L., Vogl, W., Tibbitts, Adam, W.M.MM. (2005). Gray's anatomy for students. 2nd Eddition. Philadelphia: Elsevier/Churchill Livingstone. pp. 288–290, 297, 303. ISBN 978-0-8089-2306-0.

Dranoff, G. (2004). Cytokines in cancer pathogenesis and cancer therapy. Nat Rev Cancer. 4(1), pp. 11-22.

Edinger, A.L. and Thompson, C.B. (2004). Death by design: apoptosis, necrosis and autophagy. Current Opinion in Cell Biology. 16, pp. 663–669.

Efficacy Study of AuroLase Therapy in Subjects With Primary and/or Metastatic Lung Tumors. https://clinicaltrials.gov/ct2/show/ NCT01679470 (accessed December 4, 2016).

Elmore, S. (2007). Apoptosis: A Review of Programmed Cell Death. Toxicol Pathol. 35(4), pp. 495–516.

El-Sayed, M.A. (2001). Some interesting properties of metals confined in time and nanometer space of different shapes. Chem Res. 34 (4), pp. 257–264.

El-Sayed, I.H., Huang, X. and El-Sayed, M.A. (2005). Surface Plasmon Resonance Scattering and Absorption of anti-EGFR Antibody Conjugated Gold Nanoparticles in Cancer Diagnostics: Applications in Oral Cancer. Nano Lett. 5 (5), pp. 829–834.

El-Orabi, N.F., Rogers, C., Edwards, H.G. and Schwartz, D.D. (2011). Heat induced inhibition of superoxide dismutase and accumulation of reactive oxygen species leads to HT-22 neuronal cell death. J Thermal Biol. 36, pp. 49–56.

Elsherbini, A.A., Saber, M., Aggag, M., El-shahawy, A. and Shokier, H.A.A. (2011). Laser and radiofrequency-induced hyperthermia treatment via gold-coated magnetic nanocomposites. Int J Nanomedicine. 6, pp. 2155–2165.

Engelhardt, R. (1987). Hyperthermia and drugs. Rec Res Cancer Res. 104, pp.136–203.

Ermak, G. and Davies, K.J. (2001). Calcium and oxidative stress: from cell signaling to cell death. Molecular Immunology. 38, pp. 713–721.

Eaton, P., Quaresma, P., Soares, C., Neves, C., de Almeida, M.P., Pereira, E., West, P. (2017) A direct comparison of experimental methods to measure dimensions of synthetic nanoparticles. Ultramicroscopy. 182, pp. 179–190.

Eustis, S. and El-Sayed, M.A. (2006). Why gold nanoparticles are more precious than pretty gold: Noble metal surface plasmon resonance and its enhancement of the radiative and nonradiative properties of nanocrystals of different shapes. Chem. Soc. Rev. 35, pp. 209-217.

Fabisiak, J.P., Tyurina, Y.Y., Tyurin, V.A., Lazo, J.S. and Kagan, V.E. (1998). Random versus selective membrane phospholipid oxidation in apoptosis: Role of phosphatidylserine. Biochemistry. 37, pp. 13781-13790.

Falk, M.H. and Issels, R.D. (2001). Hyperthermia in oncology. Int J Hyperthermia. 17, pp. 1-18.

Fan, J.H., Hung, W.I., Li, W.T. and Yeh, J.M. (2008). Biocompatibility study of gold nanoparticles to human cells 13th International Conference on Biomedical Engineering. 23, pp. 870-873.

Fang, J., Nakamura, H. and Maeda H. (2011). The EPR effect: Unique features of tumor blood vessels for drug delivery, factors involved, and limitations and augmentation of the effect. Advanced Drug Delivery Reviews 63, pp. 136–151.

Faraday, M. (1857). Experimental relations of gold (and other metals) to light. Phil. Trans. R. Soc. Lond. 147, pp. 145–181.Farhadi, S., Pourzare, K. and Sadeghinejad, S. (2013). Simple preparation of ferromagnetic Co3O4 nanoparticles by thermal dissociation of the [CoII(NH3)6](NO3)2 complex at low temperature. Journal Of Nanostructure in Chemistry. 3, pp.1-7.

Farhadi, S., Pourzare, K. and Sadeghinejad, S. (2013). Simple preparation of ferromagnetic Co3O4 nanoparticles by thermal dissociation of the [CoII(NH3)6](NO3)2 complex at low temperature. Journal Of Nanostructure in Chemistry. 3(16), pp. 1-7.

Favatier, F., Bornman, L., Hightower, L.E., Gunther, E. and Polla, B.S. (1997). Variation in hsp gene expression and Hsp polymorphism: do they contribute

to differential disease susceptibility and stress tolerance? Cell Stress Chaperones. 2(3), pp. 141-155.

Feng, J., Wang, Z., Shen, B., Zhang, L., Yang, X. and He, N. (2014). Effects of template removal on both morphology of mesoporous silica-coated gold nanorod and its biomedical application. RSC Adv. 4, pp. 28683–28690.

Ferrari, M. (2005). Cancer nanotechnology: opportunities and challenges. Nature Reviews Cancer. 5, pp. 161-171.

Filippovich, I., Sorokina, N., Khanna, K.K. and Lavin, M.F. (1994). Butyrate induced apoptosis in lymphoid cells preceded by transient over-expression of HSP70 mRNA. Biochem Biophys Res Commun. 198(1), pp. 257-265.

Fisher, D.E. (1994). Apoptosis in Cancer Therapy: Crossing the Threshold. Cell. 76, pp. 539-542.

Foufelle, F. and Fromenty, B. (2016). Role of endoplasmic reticulum stress in drug-induced toxicity. Pharmacology Research & Perspectives (PRP). 4(1), pp. 1-11.

Fridovich, I. (1995). Superoxide radical and superoxide dismutases. Annu Rev Biochem. 64, pp. 97-112.

Fulda, S., Galluzzi, L. and Kroemer, G. (2010). Targeting mitochondria for cancer therapy. Nature review Drug Discovery. 9, pp. 447-464.
Fulda, S., Gorman, A.M., Hori, O. and Samali, A. (2010). Cellular Stress Responses: Cell Survival and Cell Death. International Journal of Cell Biology. 214074, pp. 1-23.

Gabizon, A.A., Shmeeda, H. and Zalipsky, S. (2006). Pros and cons of the liposome platform in cancer drug targeting. J Liposome Res. 16(3). pp. 175–183.

Gerner, E.W., Cress, A.E., Stickney, D.G., Holmes, D.K. and Culver, P.S. (1980). Factors regulating membrane permeability alter thermal resistance. Ann N Y Acad Sci. 335, pp. 215-33.

Gesto, D.S., Cerqueira, N.M., Fernandes, P.A. and Ramos, M.J. (2012). Gemcitabine: a critical nucleoside for cancer therapy. Curr Med Chem. 19(7), pp. 1076-87.

Gewies, A. (2003). Introduction to Apoptosis. ApoReview. pp. 1-26.

Gonzalvez, F., Ashkenazi, A. (2010). New insights into apoptosis signaling by Apo2L/TRAIL. Oncogene 29, pp. 4752–4765.

Grijalba, M.T., Vercesi, A.E. and Schreier, S. (1999). Ca-induced increased lipid packing and domain formation in submitochondrial particles. A possible early step in the mechanism of Ca-stimulated generation of reactive oxygen species by the respiratory chain. Biochemistry. 38, pp. 13279–13287.

Grodzinski, P., Silver, M. and Molnar, L.K. (2006). Nanotechnology for cancer diagnostics: promises and challenges. Expert Rev Mol Diagn. 6, pp. 307–318.

Görlach, A., Bertram, K., Hudecova, S. and Krizanova, O. (2015). Calcium and ROS: A mutual interplay. Redox Biol. 6, pp. 260-271.

Habash, R.W.Y., Bansal, R., Krewski, D. and Alhafid, H.T. (2006). Thermal therapy, Part 1: an introduction to thermal therapy. Crit. Rev. Biomed. Eng., 34, pp. 459-489.

Hanahan, D. and Weinberg, R.A. (2000). The hallmarks of cancer, Cell. 100(1), pp. 57-70.

Hare, J. I., Lammers, T., Ashford, M. B., Puri, G., Storm, G. and Barry, S. T. (2017). Challenges and strategies in anti-cancer nanomedicine development: An industry perspective. Advanced Drug Delivery Reviews. 108, pp. 25–38.

Hatakeyama T. and F.X. Quinn, 1999. Thermal Analysis Fundamentals and Applications to Polymer Science: Thermogravimetry, 2nd Ed. Jhon Wiley and Sons Publications, pp. 45-71.

Hauck, T.S., Jennings, T.L., Yatsenko, T., Kumaradas, J.C. and Chan, W.C.W. (2008). Enhancing the Toxicity of Cancer Chemotherapeutics with Gold Nanorod Hyperthermia. Advanced material. 20(20). pp. 3832-3838.

Haveman, J., Rietbroek, R.C., Geerdink, A., van Rijn, J., Bakker, P.J.M. (1995). Effect of hyperthermia on the cytotoxicity of 20,20-difluorodeoxycytidine (gemcitabine) in cultured SW1573 cells. Int J Cancer. 62, pp. 627–630.

Hawker, C. J., Bosman, A. W. and Harth, E. (2001). New polymer synthesis by nitroxide mediated living radical polymerizations. Chem. Rev. 101, pp. 3661–3688.

Heinemann, V., Xu, Y.Z., Chubb, S., Sen, A., Hertel, L.W., Grindey, G.B. and Plunkett, W. (1992). Cellular elimination of 2',2'-difluorodeoxycytidine 5'-triphosphate: a mechanism of self-potentiation. Cancer Res. 52(3), pp. 533-539.

Hertel, L., Kroin, J., Misner, J. and Tustin, J. (1988). Synthesis of 2-deoxy-2, 2- difluoro-D ribose and 2-deoxy-2, 2'-difluoro-D-ribofuranosyl nucleosides. The Journal of Organic Chemistry. 53 (11), pp. 2406-2409.

Hervault, A., Dunn, A.E., Lim, M., Boyer, C., Mott, D., Maenosono, S. and Thanh, N.T.K. (2016). Doxorubicin loaded dual pH- and thermo-responsive magnetic nanocarrier for combined magnetic hyperthermia and targeted controlled drug delivery applications. Nanoscale. 8, pp. 12152-61.

Higashikubo, R., White, R.A. and Roti Roti, J.L. (1993). Flow cytometric BrdUrd-pulse-chase study of heat-induced cell-cycle progression delays. Cell Prolif. 26(4), pp. 337–348.

Hildebrandt, B., Wust, P., Ahlers, O., Dieing, A., Sreenivasa, G., Kerner, T., Felix, R. and Riess, H. (2002). The cellular and molecular basis of hyperthermia. Crit Rev Oncol Hematol. 43(1), pp. 33-56.

Hirano, H., Tabuchi, Y., Kondo, T., Zhao, Q.L., Ogawa, R. Cui, Z.G., Feril, L.B.J., Kanayama, S. (2005). Analysis of gene expression in apoptosis of human lymphoma U937 cells induced by heat shock and the effects of alpha-phenyl N-tert-butylnitrone (PBN) and its derivatives. 10(2), pp. 331-340.

Hirsch, L.R., Stafford, R.J., Bankson, J.A., Sershen, S.R., Rivera, B., Price, R.E., Hazle, J.D., Halas, N.J. and West, J.L. (2003). Nanoshell-mediated near-infrared thermal therapy of tumors under magnetic resonance guidance. PNAS. 100(23), pp. 13549-13554.

Hirsch, L.R., Gobin, A.M., Lowery, A.R., Tam, F., Drezek, R.A., Halas, N.J. and West, J.L. (2006). Metal nanoshells. Ann. Biomed. Eng. 34(1), pp.15–22.

Ho, L.H., Read, S.H., Dorstyn, L., Lambrusco, L. and Kumar, S. (2008) Caspase-2 is required for cell death induced by cytoskeletal disruption. Oncogene. 27, pp. 3393–3404.

Horn, H. F. and Vousden, K. H. (2007). Coping with stress: multiple ways to activate p53. Oncogene. 26, pp. 1306–1316.

Horvath, H. (2009). Gustav Mie and the scattering and absorption of light by particles: Historic developments and basics. Journal of Quantitative Spectroscopy & Radiative Transfer. 110, pp. 787-799.

Hou, C.H., Lin, F.L., Hou, S.M. and Liu, J.F. (2014). Hyperthermia Induces Apoptosis through Endoplasmic Reticulum and Reactive Oxygen Species in Human Osteosarcoma Cells. Int. J. Mol. Sci. 15, pp. 17380-17395.

Hou, X. and Jones B.T. (2000). Inductively Coupled Plasma/Optical Emission Spectrometry. Encyclopedia of Analytical Chemistry. R.A. Meyers (Ed.). John

Wiley & Sons Ltd, Chichester. pp. 9468–9485.

Huang, Q., Yoon, I., Villanueva, J., Kim, K. and Sirbuly, D.J. (2014). Quantitative mechanical analysis of thin compressible polymer monolayers on oxide surfaces. Soft Matter, 10, pp. 8001–8010.

Huang, X., El-Sayed, I., Qian, W. and El-Sayed, M.A. (2006). Cancer Cell Imaging and Photothermal Therapy in the Near-Infrared Region by Using Gold Nanorods. J. AM. CHEM. SOC. 128, pp. 2115-2120.

Huang, X., El-Sayed, I.H., Qian, W. and El-Sayed M.A. (2007). Cancer cells assemble and align gold nanorods conjugated to antibodies to produce highly enhanced, sharp and polarized surface Raman spectra: a potential cancer diagnostic marker. Nano Lett, 7 (6), pp. 1591–1597.

Huang, X., Jain, P.K., El-Sayed, I.H. and El-Sayed, M.A. (2007). Gold nanoparticles: interesting optical properties and recent applications in cancer diagnostics and therapy. Nanomedicine. 2(5), pp. 681-693.

Huang, X., and El-Sayed, M.A. (2010). Gold nanoparticles: Optical properties and implementations in cancer diagnosis and photothermal therapy. Journal of Advanced Research. 1, pp. 13–28.

Huang, X. and El-Sayed, M.A. (2011). Plasmonic photo-thermal therapy (PPTT). Alexandria Journal of Medicine. 47, pp. 1-9.

Hunt, C.R., Dix, D.J., Sharma, G.G., Pandita, K., Gupta, A., Funk, M. and Pandita, T.K. (2004). Genomic instability and enhanced radiosensitivity in Hsp70.1- and Hsp70.3-deficient mice. Mol Cell Biol. 24, pp. 899–911.

Hunt, C.R., Pandita, R.K., Laszol, A., Higashikubo, R., Agarwal, M., Kitamura, T., Gupta, A., Rief, N., Horikoshi, N., Baskaran, R., Lee, J-H., Lo¨brich, M., Paull, T.T., Roti Roti, J.L. and Pandita, T.K. (2007). Hyperthermia activates a subset of Ataxia-Telangiectasia mutated effectors. Cancer Res. 67(7), pp.

3010-3017.

Iancu, C. (2013). Photothermal therapy of human cancers (PTT) using gold nanoparticles. Biotechnology, Molecular biology and nanomedicine. 1(1), pp. 53-60.

Imao, M., Nagaki, M. and Moriwaki, H. (2006). Dual effects of heat stress on tumor necrosis factor-a-induced hepatocyte apoptosis in mice. Lab Invest 86, pp. 959–967.

Indran, I.R., Tufo, G., Pervaiz, Sh. and Brenner, C. (2011). Recent advances in apoptosis, mitochondria and drug resistance in cancer cells. Biochimica et Biophysica Acta. 1807, pp. 735–745.

Irani, K., Xia, Y., Zweier, J.L., Sollott, S.J., Der, C.J., Fearon, E.R., Sundaresan, M., Finkel, T. and Goldschmidt-Clermont, P.J. (1997). Mitogenic signaling mediated by oxidants in Ras-transformed fibroblasts. Science. 275, pp. 1649–1652.

Issels, R.D., Abdel-Rahman, S., Wendtner, C., Falk, M.H., Kurze, V., Sauer, H., Aydemir, U. and Hiddemann, W. (2001). Neoadjuvant chemotherapy combined with regional hyperthermia (RHT) for locally advanced primary or recurrent high-risk adult soft-tissue sarcomas (STS) of adults: long-term results of a phase II study. Eur J Cancer. 37(13), pp. 1599-608.

Issels, R.D., Lindner, L.H., Verweij, J., Wust, P., Reichardt, P., Schem, B.C., Abdel-Rahman, S., Daugaard, S., Salat, C., Wendtner, C.M., Vujaskovic, Z., Wessalowski, R., Jauch, K.W., Dürr, H.R., Ploner, F., Baur-Melnyk, A., Mansmann, U., Hiddemann, W., Blay, J.Y. and Hohenberger, P. (2010). Neo-adjuvant chemotherapy alone or with regional hyperthermia for localised high-risk soft-tissue sarcoma: a randomised phase 3 multicentre study. Lancet Oncol. 11(6), pp. 561-570.

Issels, R.D., Prenninger, S.W., Nagele, A., Boehm, E., Sauer, H., Jauch, K.W. Denecke, H., Berger, H., Peter, K. and Wilmanns, W. (1990). Ifosfamide plus

etoposide combined with regional hyperthermia in patients with locally advanced sarcomas. J Clin Oncol. 1, pp. 1818-1829.

Issels R. (1999), Hyperthermia combined with chemotherapy—biological rationale, clinical application, and treatment results. Onkologie. 22, pp. 374–381.

Issels, R.D. (2008). Hyperthermia adds to chemotherapy. EUROPEAN JOURNAL OF CANCER. 44, pp. 2546-2554.

Jackson, J.B. and Halas, N.J. (2004). Surface-enhanced Raman scattering on tunable plasmonic nanoparticle substrates. PNAS. 101(52), pp. 17931-17935.

Jackson, S.P. and Schoenwaelder, S.M. (2010). Procoagulant platelets: are they necrotic? BLOOD. 116(12), pp. 2011-2017.

Jain, P.K., Lee, K.S., El-Sayed, I.H. and El-Sayed M.A. (2006). Calculated absorption and scattering properties of gold nanoparticles of different size, shape, and composition: applications in biological imaging and biomedicine. J Phys Chem. 110(14), pp. 7238–7248.

Jain, P.K., Huang, X., El-Sayed, I.H. and El-Sayed, M.A. (2008). Noble metals on the nanoscale: optical and photothermal properties and some applications in imaging, sensing, biology, and medicine. Acc Chem Res. 41(12), pp. 1578-86.

Jakubowski, W., Min, K. and Matyjaszewski, K. (2006). Activators regenerated by electron transfer for atom transfer radical polymerization of styrene. Macromolecules. 39, pp. 39–45.

Jana, N.R., Gearheart, L. and Murphy, C.J. (2001). Evidence for Seed-Mediated Nucleation in the Chemical Reduction of Gold Salts to Gold Nanoparticles. Chem. Mater. 13, pp. 2313-2322.

Jana, N.R., Gearheart, L. and Murphy, C.J. (2008). Wet Chemical Synthesis of High Aspect Ratio Cylindrical Gold Nanorods. J. Phys. Chem. B. 105, pp. 4065-4067.

Jaracz, S., Chen, J., Kuznetsova, L.V. and Ojima, I. (2005). Recent advances in tumor-targeting anticancer drug conjugates. Bioorganic & Medicinal Chemistry. 13(17), pp. 5043–5054.

Jiang, K., Smith, D.A. and Pinchuk, A. (2013). Size-Dependent Photothermal Conversion Efficiencies of Plasmonically Heated Gold Nanoparticles. J. Phys. Chem. C. 117 (51), pp. 27073–27080.

Jones, E.L., Samulski, T.V. and Vujaskovic, Z. (2004). Hyperthermia. In: Perez CA, Brady LW, Halperin EC, Schmidt-Ullrich RK (eds.). Principles and Practise of Radiation Oncology. 4th ed. Chapter 24. Lippincott Williams & Wilkins. pp. 699–735.

Jokerst, J.V., Lobovkina, T., Zare, R.N. and Gambhir, S.S. (2011). Nanoparticle PEGylation for imaging and therapy. Nanomedicine. 6(4), pp. 715–728.

Joshi, B.P. and Wang, T.B. (2010). Exogenous Molecular Probes for Targeted Imaging in Cancer: Focus on Multi-modal Imaging. Cancers. 2, pp. 1251-1287.

Kamigaito, M., Ando, T. and Sawamoto, M. (2001). Metal-catalyzed living radical polymerization. Chem. Rev. 101, pp. 3689-3745.

Kampinga, H.H., Turkel-Uygur, N., Roti Roti, J.L. and Konings, A.W.T. (1989). The relationship of increased nuclear protein content induced by hyperthermia to killing of HeLa S3 cells. Radiation Research. 117, pp. 511–522.

Kampinga, H.H. (1993). Thermotolerance in mammalian cells. Protein denaturation and aggregation, and stress proteins. J Cell Sci. 104(1), pp. 11-7.

Kampinga, H.H. (2006). Cell biological effects of hyperthermia alone or combined with radiation or drugs: A short introduction to newcomers in the

field. Int. J. Hyperthermia. 22(3), pp. 191–196.

Kampinga, H.H. and Dikomey, E. (2001). Hyperthermic radiosensitization: mode of action and clinical relevance. Int J Radiat Biol. 77, pp. 399-408.

Kannan, K. and Jain, S.K. (2000). Oxidative stress and apoptosis. Pathophysiology. 7(27), pp. 153–163.

Kanwal, A. and Zaidi, S.F. (2013). Treating cancer with heat: hyperthermia as promising strategy to enhance apoptosis. J Pak Med Assoc. 63(4), pp. 504-508.

Karch, J. and Molkentin, J.D. (2015). Regulated Necrotic Cell Death:The Passive Aggressive Side of Bax and Bak. Circ Res. 116, pp. 1800-1809.

Kato, M., Kamigaito, M., Sawamoto, M., Higashimura, T. (1996). Polymerization of Methyl Methacrylate with the Carbon TetrachlorideIDichlorotris (triphenylphosphine)ruthedum(II)/ Methylaluminum Bis(2,6-di-tert-butylphenoxideI)n itiating System: Possibility of Living Radical Polymerization. Macromolecules. 28, pp. 1721-1723.

Ke, H., Wang, J., Dai, Z., Jin, Y., Qu, E., Xing, Z., Guo, C., Yue, X. and Liu, J. (2011). Gold-Nanoshelled Microcapsules: ATheranostic Agent for Ultrasound Contrast Imaging and Photothermal Therapy. Angew. Chem. Int. Ed. 50, pp. 3017-3021.

Khan, V.R. and Brown, I.R. (2002). The effect of hyperthermia on the induction of cell death in brain, testis, and thymus of the adult and developing rat. Cell Stress & Chaperones. 7 (1), pp. 73-90.

Kim, S.M., Lee, S.W., Moon S.Y. and Park, J.Y. (2016). The effect of hot electrons and surface plasmons on heterogeneous catalysis, J. Phys. Condens. Matter. 28, pp. 254002-2540015.

Kimling, J., Maier, M., Okenve, B., Kotaidis, V., Ballote, H. and Plech. (2006). Turkevich Method for Gold Nanoparticle Synthesis Revisited. J. Phys. Chem. 110 (32), pp. 15700-15707.

Khan, V.R. and Brown, I.R. (2002). The effect of hyperthermia on the induction of cell death in brain, testis, and thymus of the adult and developing rat. Cell Stress & Chaperones. 7 (1), pp. 73–90.

Khare, V., Alam, N., Saneja, A., Dubey, R.D. and Gupta, P.N. (2014). Targeted drug delivery systems for pancreatic cancer. J Biomed Nanotechnol. 10(12), pp. 3462-82.

Kneipp, K., Haka, A.S., Kneipp, H., Badizadegan, K., Yoshizawa, N., Boone, C., Shafer-Peltier, K.E., Motz, J.T., Dasari, R.R. and Feld, M.S. (2002). Surface-enhanced Raman spectroscopy in single living cells using gold nanoparticles. Appl. Spectrosc. 56(2), pp.150-154.

Kneipp, J., Kneipp, H., Rice, W.L. and Kneipp, K. (2005). Optical probes for biological applications based on surface-enhanced Raman scattering from indocyanine green on gold nanoparticles. Anal. Chem. 77(8), pp. 2381-2385.

Koay, E. J., Truty, M. J., Cristini, V., Thomas, R. M., Chen, R., Chatterjee, D., Fleming, J. B. (2014). Transport properties of pancreatic cancer describe gemcitabine delivery and response. The Journal of Clinical Investigation.124(4), pp. 1525–1536.

Komar, G., Kauhanen, S., Liukko, K., Seppänen, M., Kajander, S., Ovaska, J., Nuutila, P. and Minn, H. (2009). Decreased blood flow with increased metabolic activity: a novel sign of pancreatic tumor aggressiveness. Clin Cancer Res. 15(17), pp. 5511-5517.

Koo, K.M., Sina, A.A.I., Carrascosa, L.G., Shiddiky, M.J.A. and Trau, M. (2015). DNA–bare gold affinity interactions: mechanism and applications in biosensing. Anal. Methods. 7, PP. 7042-7054.

Korin, E., Froumin, N. and Cohen, S. (2017). Surface Analysis of Nanocomplexes by X-ray Photoelectron Spectroscopy (XPS). ACS Biomater. Sci. Eng. 3, pp. 882−889.

Krebs, R.A. and Feder, M.E. (1997). Deleterious consequences of Hsp70 overexpression in Drosophila melanogaster larvae. Cell Stress Chaperones. 2(1), pp. 60-71.

Kwak, H.B. (2013). Effects of aging and exercise training on apoptosis in the heart, Journal of Exercise Rehabilitation. 9(2), pp. 212-219.

Kwak, G., Hwang, J., Cheon, J.Y., Woo, M.H., Jun, K-W., Lee, J. and Ha, K-S. (2013). Preparation Method of Co_3O_4 Nanoparticles Using Ordered Mesoporous Carbons as a Template and Their Application for Fischer–Tropsch Synthesis. J. Phys. Chem. C. 117, pp. 1773−1779.

Landry, J., Chretien, P., Bernier, D., Nicole, L.M., Marceau, N. and Tanguay, R.M. (1982a). Thermotolerance and heat shock proteins induced by hyperthermia in rat liver cells. Int J Radiat Oncol Biol Phys. 8(1), pp. 59-62.

Landry, J., Bernier, D., Chretien, P., Nicole, L.M., Tanguay, R.M. and Marceau, N. (1982b). Synthesis and degradation of heat shock proteins during development and decay of thermotolerance. Cancer Res. 42(6), pp. 2457-2461.

Landry, J., Samson, S. and Chretien, P. (1986). Hyperthermia-induced Cell Death, Thermotolerance, and Heat Shock Proteins in Normal, Respiration-deficient, and Glycolysis-deficient Chinese Hamster Cells. CANCER RESEARCH. 46, pp. 324-327.

Lanz, C., Fruh, M., Thormann, W., Cerny, T., Lauterburg, B.H. (2007). Rapid determination of gemcitabine in plasma and serum using reversed-phase HPLC. J. Sep. Sci. 30, pp. 1811 – 1820.

Lecavalier, D. and Mackillop, W.J. (1985). The effect of hyperthermia on glucose transport in normal and thermal-tolerant Chinese hamster ovary cells. Cancer Lett. 29(2), pp. 223-231.

Laga, R., Janoušková, O., Ulbrich, K., Pola, R., Blažková, J., Filippov, S. K., Etrych, T. and Pechar, M. (2015). Macromolecular HPMA-Based Nanoparticles with Cholesterol for Solid-Tumor Targeting: Detailed Study of the Inner Structure of a Highly Efficient Drug Delivery System. Biomacromolecules. 16, pp. 2493–2505.

Lee, H.J., Liub, Y., Zhaoc, J., Zhouc, M., Boucharda, R.R., Mitchama, T., Wallaceb, M., Staffforda, R.J., Lic, C., Gupta, S. and Melancon, M.P. (2013). In vitro and in vivo mapping of drug release after laser ablation thermal therapy with doxorubicin-loaded hollow gold nanoshells using fluorescence and photoacoustic imaging. J Control Release. 172(1), pp. 1-17.

Lee, K.Y.J., Wang, Y. and Nie S. (2015). In vitro study of a pH-sensitive multifunctional doxorubicin–gold nanoparticle system: therapeutic effect and surface enhanced Raman scattering. RSC Adv. 5, pp. 65651-59.

Lee, K.S., El-Sayed, M.A. (2005). Dependence of the enhanced optical scattering efficiency relative to that of absorption for gold metal nanorods on aspect ratio, size, end-cap shape and medium refractive index. J Phys Chem B. 109 (43), pp. 20331–20338.

Lepock, J.R., Frey, H.E. and Ritchie, K.P. (1993). Protein denaturation in intact hepatocytes and isolated cellular organelles during heat shock. Journal of Cell Biology. 122, pp. 1267–1276.

Lepock, J.R., Frey, H.E., Heynen, M.L., Senisterra, G.A. and Warters, R.L. (2001). The nuclear matrix is a thermolabile cellular structure. Cell Stress Chaperones. 6, pp. 136–147.

Lepock, J.R. (2004). Role of nuclear protein denaturation and aggregation in

thermal radiosensitization. International Journal of Hyperthermia. 20, pp. 115–130.

Leung, A.M., Hari, D.M. and Morton D.L. (2012), Surgery for Distant Melanoma Metastasis. Cancer J. 18(2), pp. 176-184.

Li, F.J., Kondo, T., Zhao, Q.L., Tanabe, K., Ogawa, R., Li, M. and Arai, Y. (2001). Enhancement of hyperthermia-induced apoptosis by a free radical initiator, 2,2'- azobis (2-amidinopropane) dihydrochloride, in human histiocytic lymphoma U937 cells. Free Radiat Res. 35, pp. 281-299.

Li, N., Ragheb, K., Lawler, G., Sturgis, J., Rajwa, B., Melendez, J.A. and Robinson, J.P. (2003). Mitochondrial Complex I Inhibitor Rotenone Induces Apoptosis through Enhancing Mitochondrial Reactive Oxygen Species Production. THE JOURNAL OF BIOLOGICAL CHEMISTRY. 278(10), pp. 8516–8525.

Li, J., Wienties, G. and Jessie, L. (2010). Pancreatic Cancer: Pathobiology,Treatment Options, and Drug Delivery. AAPS J. 12(2), pp. 223-232.

Li, P.C., Wang, C.R., Shieh, D.B., Wei, C.W., Liao, C.K., Poe, C., Jhan, S., Ding. A.A. and Wu, Y.N. .(2008). In vivo photoacoustic molecular imaging with simultaneous multiple selective targeting using antibody-conjugated gold nanorods. Optics Express. 16(23), pp. 18605-15.

Li, W., Zhang, X., Zhou, M., Tian, B., Yu, C., Jie, J., Hao, X., Zhang, X. (2014). Functional core/shell drug nanoparticles for highly effective synergistic cancer therapy. Adv Healthc Mater. 3(9), pp.1475-1485.

Li, Z., Deen, M.J., Kumar, S., and Selvaganapathy, P.R. (2014). Raman Spectroscopy for In-Line Water Quality Monitoring—Instrumentation and Potential. Sensors. 14, pp. 17275-17303.

Liu, Y., Zhang, X., Liu, Z., Wang, L., Luo, L., Wang, M., Wang, Q., Gao, D. (2017). Gold nanoshell-based betulinic acid liposomes for synergistic chemo-photothermal therapy. Nanomedicine.13(6). pp.1891-1900.

Liao, H. and Hafner, J.H. (2005). Gold Nanorod Bioconjugates. Chem. Mater. 17, pp. 4636-4641.

Lim, E.K., Jang, E., Lee, K., Haam, S. and Huh, Y.N. (2013). Delivery of Cancer Therapeutics Using Nanotechnology. Pharmaceutics 5, pp. 294-317.

Link, S., Burda, C., Mohamed, M.B., Nikoobakht, B. and El-Sayed, M.A. (1999). Laser photothermal melting and fragmentation of gold nanorods: energy and laser pulse-width dependence. J Phys Chem A. 103 (9), pp. 1165–1170.

Link, S. and El-Sayed, M.A. (1999). Spectral properties and relaxation dynamics of surface plasmon electronic oscillations in gold and silver nanodots and nanorods. J Phys Chem B. 103 (40), pp. 8410–8426.

Link, S. and El-Sayed, M.A. (1999). Size and temperature dependence of the plasmon absorption of colloidal gold nanoparticles. J Phys Chem. B. 103(21), pp. 4212–4217.

Link, S., Burda, C., Wang, Z.L. and El-Sayed, M.A. (1999). Electron dynamics in gold and gold–silver alloy nanoparticles: the influence of a nonequilibrium electron distribution and the size dependence of the electron–phonon relaxation. J Chem Phys. 111 (3), pp. 1255–1264.

Link, S., Burda, C., Mohamed, M.B., Nikoobakht, B. and El-Sayed, M.A. (2000a). Femtosecond transient-absorption dynamics of colloidal gold nanorods: shape independence of the electron–phonon relaxation time. Phys Rev B – Condens Mat Mater Phys. 61 (9), pp. 6086–6090.

Link, S., Burda, C., Nikoobakht, B. and El-Sayed, M.A. (2000b). Laser-induced shape changes of colloidal gold nanorods using femtosecond and nanosecond laser pulses, J Phys Chem B. 104 (26), pp. 6152–6163.

Link, S. and El-Sayed, M.A. (2000). Shape and size dependence of radiative, non-radiative and photothermal properties of gold nanocrystals, Reviews in physical chemistry. 19(3), pp. 409-453.

Link, S. and El-Sayed, M.A. (2003). Optical properties and ultrafast dynamics of metallic nanocrystals. Annu Rev Phys Chem. 54, pp. 331–366.

Link, S., Furube, A., Mohamed, M.B., Asahi, T., Masuhara, H. and El-Sayed, M.A. (2002). Hot electron relaxation dynamics of gold nanoparticles embedded in $MgSO_4$ powder compared to solution: the effect of the surrounding medium. J Phys Chem B. 106 (5), pp. 945–955.

Link, S., Hathcock, D.J., Nikoobakht, B. and El-Sayed, M.A. (2003). Medium effect on the electron cooling dynamics in gold nanorods and truncated tetrahedral, Adv Mater. 15 (5), pp. 393–396.

Liossis, S.N., Ding, X.Z., Kiang, J.G. and Tsokos, G.C. (1997). Overexpression of the heat shock protein 70 enhances the TCR☐CD3- and Fas☐Apo-1☐CD95-mediated apoptotic cell death in Jurkat T cells. J Immunol. 158, pp. 5668☐5775.

Liu, K., Zheng, Y., Lu, X., Thai, T., Lee, A.N., Bach, U. and Gooding, J.J. (2015). Biocompatible Gold Nanorods: One-Step Surface Functionalization, Highly Colloidal Stability, and Low Cytotoxicity. Langmuir. 31, pp. 4973−4980.

Loo, C., Hirsch, L., Lee, M.H., Chang, E., West, J., Halas, N. and Drezek, R. (2005a). Gold nanoshell bioconjugates for molecular imaging in living cells. Opt Lett. 30(9), pp. 1012–14.

Loo, C., Lin, A., Hirsch, L., Lee, M.H., Barton, J., Halas, N. and Drezek, R. (2004). Nanoshell-enabled photonics-based imaging and therapy of cancer.

Technol Cancer Res Treat. 3(1), pp. 33–40.

Loo, C., Lowery, A., Halas, N., West, J. and Drezek, R. (2005b). Immunotargeted nanoshells for integrated cancer imaging and therapy. Nano Lett. 5(4), pp. 709–711.

Lough, W. J. ; Wainer, I. W. (1995). High performance liquid chromatography-fundamental principles and practice. London: Blaclue Academic and Professional, 276 pp.

Lu, W., Ogasawara, M.A. and Huang, P. (2008). Models of reactive oxygen species in cancer. Drug Discovery Today: Disease Models. 4(2), pp. 67-73.

Luo, J., Solimini, N.L. and Elledge, S.J. (2009). Principles of Cancer Therapy: Oncogene and Non-oncogene Addiction. Cell. 136(5), pp. 823–837.

Lynch, I. and Dawson, K.A. (2008). Protein-nanoparticle interactions. Nano Today.
3, pp. 40–47.

Ma, Y., Liang, X., Tong, S., Bao, G., Ren, Q. and Dai, Z. (2013). Gold Nanoshell Nanomicelles for Potential Magnetic Resonance Imaging, Light-Triggered Drug Release, and Photothermal Therapy. Adv. Funct. Mater. 23(7), pp. 815–822.

May, J.P. and Li, S.D. (2013). Hyperthermia-induced drug targeting. Expert Opin Drug Deliv. 10(4), pp. 511-527.

Maeda, H. (2001). The enhanced permeability and retention (EPR) effect in tumor vasculature: the key role of tumor-selective macromolecular drug targeting, in:G. Weber (Ed.), Advances in Enzyme Regulation, Elsevier Science Ltd, Oxford. pp. 189–207.

Maeda, H., Greish, K. and Fang, J. (2006). The EPR effect and polymeric drugs: a paradigmshift for cancer chemotherapy in the 21st century, Adv.

Polym. Sci. 193, pp. 103–121.

Maeda, H., Bharate, G.Y. and Daruwalla, J. (2009). Polymeric drugs and nanomedicines for efficient tumor targeted drug delivery based on EPR-effect, Eur. J. Pharm. Biopharm. 71, pp. 409–419.

Mackey, M.A. and Roti Roti, J.L. (1992). A model of heat-induced clonogenic cell death. J Theor Biol.156(2), pp. 133–146.

Mackey, M.A., Anolik, S.L. and Roti Roti, J.L.(1992). Changes in heat and radiation sensitivity during long duration, moderate hyperthermia in HeLa S3 cells. Int J Radiat Oncol Biol Phys. 24(3), pp. 543–550.

Magnusson, J.P., Khan, A., Pasparakis, G., Saeed, A.O., Wang, W. and Alexander, C. (2008). Ion-Sensitive "Isothermal" Responsive Polymers Prepared in Water. J. AM. CHEM. SOC. 130, pp. 10852–10853.

Maiti, S.N., Spevak, P., Singh, M.P., Micetich, R.G., Reddy, A.V.N. (1988). Reductive Cleavage of Symmetrical Disulfides with Hydrazines. Synth. Commun. 18, pp. 575-581.

Manfait, M., Morjani, H., Millot, J.M., Debal, V. and Angiboust, J.F. (1991). Nabiev I: Drug target interactions on a single living cell. An approach by optical microspectroscopy. Proc. Soc. Photo Opt. Instrum. Eng.-Int Soc Opt Eng. 1403, pp. 695–707.

Manfait, M., Nabiev, I. and Morjani, H. (1992). Molecular events on single living cancer cells as studied by microspectrofluorometry and micro-SERS Raman spectroscopy. J. Cell Pharm. 3(1), pp. 120–125.

Mantovani, G., Lecolley, F., Tao, L., Haddleton, D. M., Clerx, J., Cornelissen J. L. M. and Velonia, K. (2005). Design and Synthesis of *N*-Maleimido-Functionalized Hydrophilic Polymers via Copper-Mediated Living Radical Polymerization: A Suitable Alternative to PEGylation Chemistry. J. Am. Chem. Soc. 127, pp. 2966–2973.

Massignani, M., LoPresti, C., Blanazs, A., Madsen, J., , S.P. Armes, Lewis, A.L. and Battaglia, G. (2009). Controlling Cellular Uptake by Surface Chemistry, Size, and Surface Topology at the Nanoscale. Small, 5 (21), pp. 2424-2432.

Matsumura, Y. and Maeda, H. (1986). A new concept for macromolecular therapeutics in cancer chemotherapy: mechanism of tumoritropic accumulation of proteins and the antitumor agent SMANCS, Cancer Res. 46, pp. 6387–6392.

Matyjaszewski, K. and Xia, J. (2001). Atom transfer radical polymerization. Chem. Rev.101, pp. 2921–2990.

McIlwain, D.R., Berger, T. and Mak, T.W. (2013). Caspase Functions in Cell Death and Disease. Cold Spring Harb Perspect Biol. 5(4), pp. 1-28.

Michels, A.A., Nguyen, V.T., Konings, A.W., Kampinga, H.H. and Bensaude, O. (1995). Thermostability of a nuclear-targeted luciferase expressed in mammalian cells - Destabilizing influence of the intranuclear microenvironment. European Journal of Biochemistry. 234, pp. 382–389.

Michels, A.A., Kanon, B., Konings, A.W.T., Ohtsuka, K., Bensaude, O. and Kampinga, H.H. (1997). HSP70 and HSP40 chaperone activities in the cytoplasm and the nucleus of mammalian cells. Journal of Biological Chemistry. 272, pp. 33283–33289.

Mie, G. (1908), A contribution to the optics of turbid media, especially colloidal metallic suspensions. Ann Phys. 25, pp. 377–445.

Mikkelsen, R.B., Reinlib, L., Donowitz, M. and Zahniser, D. (1991). Hyperthermia effects on cytosolic [Ca2+]. Analysis at single cell level by digitized imagin. microscopy and cell survival. Cancer Res. 51, pp. 359-364.

Minegishi, S. and Mayr, H. (2003). How Constant Are Ritchie's "Constant Selectivity Relationships"? A General Reactivity Scale for n-, π-, and σ-Nucleophiles. J. Am. Chem. Soc. 125 (1), pp. 286-295.

Mini, E., Nobili, S., Caciagli, B., Landini, I. and Mazzei, T. (2006). Cellular pharmacology of gemcitabine. Ann Oncol. 17(5), pp. 7-12.

Mitsunaga, M., Ogawa, M., Kosaka, N., Rosenblum, L.T., Choyke P.L. & Kobayashi, H. (2011), Cancer cell–selective in vivo near infrared photoimmunotherapy targeting specific membrane molecules. Nature Medicine. 17, pp. 1685–1691.

Moad, G., Rizzardo, E., Thang, SH. (2005). Living Radical Polymerization by the RAFT Process. Aust J Chem. 58, pp. 379-410.

Moad, G., Rizzardo, E. and Thang, S.H. (2008a). Radical addition-fragmentation chemistry in polymer synthesis. Polymer 49, pp. 1079-1131.

Moad, G., Rizzardo, E. and Thang, S.H. (2008b). Toward Living Radical Polymerization. Account of chemical research. 41(9), pp. 1133-1142.

Moad, G., Rizzardo, E. and Thang, S.H. (2013). RAFT Polymerization and Some of its Applications. Chem. Asian J. 8, pp. 1634-1644

Moghimi, S.M., Hunter, A.C., Murray, J.C. (2001). Long-circulating and target-specific nanoparticles: theory to practice. Pharmacol Rev. 53, pp. 283–318.

Moghimi, S.M. (2003). Modulation of lymphatic distribution of subcutaneously injected poloxamer 407-coated nanospheres: the effect of the ethylene oxide chain configuration. FEBS Lett. 540, pp. 241–244.

Mohamed, M.B., Ahmadi, T.S., Link, S., Braun, M. and El-Sayed, M.A. (2001). Hot electron and phonon dynamics of gold nanoparticles embedded in a gel matrix. Chem Phys Lett. 343 (1–2), pp. 55–63.

Moore, J.C. (1964). Gel permeation chromatography. I. A new method for molecular weight distribution of high polymers. J. Polym. Sci. 2, pp. 835-843.

Morjani, H., Riou, J.F., Nabiev, I., Lavelle, F. and Manfait, M. (1993). Molecular and cellular interactions between intoplicine, DNA, and topoisomerase II studied by surface-enhanced Raman scattering spectroscopy. Cancer Res. 53, pp.4784–4790.

Mosmann, T. (1983). Rapid Colorimetric Assay for Cellular Growth and Survival: Application to Proliferation and Cytotoxicity Assays. Journal of Immunological Methods. 65, pp. 55-63.

MRI/US Fusion Imaging and Biopsy in Combination With Nanoparticle Directed Focal Therapy for Ablation of Prostate Tissue. https://clinicaltrials.gov/ct2/show/NCT02680535 (accessed December 4, 2016).

Munshi, A., Hobbs, M. and Meyn, R.E. (2005). Clonogenic cell survival assay. Methods Mol Med.110, pp. 21-28.

Murphy, C.J., Gole, A.M., Stone, J.W., Sisco, P.N., Alkilany, A.M., Goldsmith, E.C. and Baxter, S.C. (2008). Gold nanoparticles in biology: Beyond toxicity to cellular imaging. Acc. Chem. Res. 41, pp. 1721–1730.

Nabiev, I.R., Morjani, H. and Manfait, M. (1991). Selective analysis of antitumor drug interaction with living cancer cells as probed by surface-enhanced Raman spectroscopy. Eur. Biophys. J. 19(6), pp.311–316.

Natfji, A.A., Ravishankar, D., Osborn, H.M. I. and Greco, F. (2017). Parameters Affecting the Enhanced Permeability and Retention Effect: The Need for Patient Selection. Journal of Pharmaceutical Sciences. 106, pp. 3179-3187.

Negus, R.P.M. and Balkwill, F.R. (1996). Cytokines in tumour growth, migration and metastasis. World J Urol. 14, pp. 157-165.

Nesvadba, P. (2006). N-Alkoxyamines: Synthesis, properties, and applications in polymer chemistry, organic synthesis, and materials science. Chimia. 60, pp. 832–840.

Niidome, T., Yamagata, M., Okamoto, Y., Akiyama, Y., Takahashi, H., Kawano, T. Katayama, Y. and Niidome, Y. (2006). PEG-modified gold nanorods with a stealth character for in vivo applications. Journal of Controlled Release. 114(3), pp. 343-347.

Nikfarjam, M., Muralidharan, V. and Christophi, C. (2005). Focal hyperthermia produces progressive tumor necrosis independent of the initial thermal effects. J Gastrointest Surg. 9, pp. 410-417.

Nikoletopoulou, V., Markaki, M., Palikaras, K. and Tavernarakis, N. (2013). Crosstalk between apoptosis, necrosis and autophagy. Biochimica et Biophysica Acta.1833, pp. 3448–3459.

Nikoobakht, B. and El-Sayed, M.A. (2003). Preparation and Growth Mechanism of Gold Nanorods (NRs) using Seed-Mediated Growth Method. Chem. Mater. 15, pp. 1957-1962.

Nikoobakht, B., El-Sayed, M.A. (2003). Surface-Enhanced Raman Scattering Studies on Aggregated Gold Nanorods J. Phys. Chem. A. 107 (18), pp. 3372–3378.

Nishiyama, N. and Kataoka, K. (2006). Current State, Achievements, And Future Prospects of Polymeric Micelles as Nanocarriers for Drug and Gene Delivery. Pharmacol. Ther. 112, pp. 630–648.

Nunez, G., Benedict, M.A., Hu, Y. and Inohara, N. (1998). Caspases: the proteases of the apoptotic pathway. Oncogene. 17, pp. 3237-3245.

O'Hayre, M., Salanga, C.L., Handel, T.M. and Allen, S.J. (2008). Chemokines and cancer: migration, intracellular signalling and intercellular communication

in the microenvironment. Biochemical Journal. 409(3), pp. 635-649.

O'Neal, D.P., Hirsch, L.R., Halas, N.J., Payne, J.D., West, J.L. (2004). Photo-thermal tumor ablation in mice using near infrared-absorbing nanoparticles. Cancer Letters. 209(2), pp. 171-176.

Ostberg, J.R., Kaplan, K.C. and Repasky, E.A. (2002). Induction of stress proteins in a panel of mouse tissues by fever-range whole body hyperthermia. Int J Hyperthermia. 18(6), pp. 552-562.

Overgaard, J. and Horsman, MR. (1997). Hyperthermia. In: Steel GG. Basic clinical radiobiology. 2nd ed. EdwardArnold. pp. 212–221.

Pagliari, L.J., Kuwana, T., Bonzon, C., Newmeyer, D.D. and Tu, S., Beere, H.M. and Green, D.R. (2005) The multidomain proapoptotic molecules Bax and Bak are directly activated by heat. Proc Natl Acad Sci USA. 102, pp. 17975–17980.

Parsell, D.A. and Lindquist, S. (1993). The function of heat-shock proteins in stress tolerance:degradation and reactivation of damaged proteins. Annu Rev Genet. 27, pp. 437-496.

Patra, C., Bhattacharya, R., Mukhopadhyay, D. and Mukherjee, P. (2010). S of Gold Nanoparticles for targeted therapy in pancreatic cancer. Adv Drug Deliv Rev. 62(3), pp. 346–361.

Pawley J.B. (2006). Handbook of Biological Confocal Microscopy. Springer, Boston, MA. pp. 19-37. DOI: https://doi.org/10.1007/978-1-4757-5348-6-2.

Pedrosa, P., Vinhas, R., Fernandes, A. and Baptista, P.V. (2015). Gold Nanotheranostics: Proof-of-Concept or Clinical Tool? Nanomaterials. 5, pp. 1853-1879.

Pelicano, H., Carney, D. and Huanga, P. (2004). ROS stress in cancer cells and therapeutic implications. Drug Resistance Updates. 7, pp. 97–110.

Pilot Study of AuroLase Therapy in Refractory and/or Recurrent Tumors of the Head and Neck. https://clinicaltrials.gov/ show/NCT00848042 (accessed December 4, 2016).

Pitsillides, C.M., Joe, E.K., Wei, X., Anderson, R.R. and Lin, C.P. (2003). Selective Cell Targeting with Light-Absorbing Microparticles and Nanoparticles. Biophysical Journal. 84, pp. 4023–4032.

Prashant, K. and El-Sayed, M.A. (2007). Universal Scaling of Plasmon Coupling in Metal Nanostructures: Extension from Particle Pairs to Nanoshells. Nano Lett. 7 (9), pp. 2854–2858.

Prashant, K.J., Xiaohua, H., El-Sayed, I.H. and El-Sayed, M.A. (2008). Noble Metals on the Nanoscale: Optical and Photothermal Properties and Some Applications in Imaging, Sensing, Biology, and Medicine. ACCOUNTS OF CHEMICAL RESEARCH. 41(12), pp. 1578-1586.

Prevo, B.G., Esakoff, S.A., Mikhailovsky, A. and Zasadzinski, J.A. (2008). Scalable routes to gold nanoshells with tunable sizes and their response to near infrared pulsed laser irradiation. Small. 4(8), pp. 1183–1195.

Przybytkowski, E., Bates, J.H., Bates, D.A. and Mackillop, W.J. (1986). Thermal adaptation in CHO cells at 40 degrees C: the influence of growth conditions and the role of heat shock proteins. Radiat Res. 107(3), pp. 317-331.

Radenkovic ́, S., Antic ́, M., Savic ́, N.D. and Gliˇsic ́, B.Đ. (2017) The nature of the Au–N bond in gold(III) complexes with aromatic nitrogen-containing heterocycles: the influence of Au(III) ions on the ligand aromaticity. *New J. Chem.* 41, pp. 12407-12415

Rahme, K., Hobbs, R.G., Chen, L., Morris, M.A., O'Driscoll, *C.* and Holmes J.D. (2013). PEGylated Gold Nanoparticles: Polymer Quantification as a Function of PEG lengths and Nanoparticle Dimensions. RSC Adv. 3, pp. 6085-6094.

Rao, W., Deng, Z.S. and Liu, J. (2010). A review of hyperthermia combined with radiotherapy/chemotherapy on malignant tumors. Crit Rev Biomed Eng. 38(1), pp. 101-116.

Raoof, M., Zhu, C., Cisneros, B.T., Liu, H., Corr, S.J., Wilson, L.J. and Curley, S.A. (2014). Hyperthermia inhibits recombination repair of Gemcitabine-Stalled replication Forks. 106 (8), pp. 1-10.

Rau, L.R., Huang, W.Y., Liaw, J.W. and Tsai, S.W. (2016). Photothermal effects of laser-activated surface plasmonic gold nanoparticles on the apoptosis and osteogenesis of osteoblast-like cells. Int J Nanomedicine. 27(11), pp. 3461-3473.

Richter, K., Haslbeck, M. and Buchner, J. (2010). The heat shock response: life on the verge of death. Mol Cell. 40(2), pp. 253-266.

Ricci, R.W., M. Ditzler, and Nestor, L.P. (1994). Discovering the Beer-Lambert Law. Journal of chemical Education. 71(11), pp. 983.

Rodrigues, M.S., Reddy, M.M. and Sattler, M. (2008). Cell cycle regulation by oncogenic tyrosine kinases in myeloid neoplasias: from molecular redox mechanisms to health implications. Antioxid. Redox Signal. 10, pp. 1813–1848.

Rong, Y. and Mack, P. (2000). Apoptosis induced by hyperthermia in Dunn osteosarcoma cell line in vitro. Int J Hyperthermia 16, pp. 19-27.

Roper, D.K., Ahn, W. and Hoepfner, M. (2007). Microscale Heat Transfer Transduced by Surface Plasmon Resonant Gold Nanoparticles. J. Phys.

Chem. C. 111 (9), pp. 3636–3641.

Roti Roti, J.L. and Laszlo, A. (1988). The effects of hyperthermia on cellular macromolecules. In: Urano M, Douple E, editors. Thermal effects on cells and tissues. Utrecht: VSP; pp. 13–98.

Roti Roti, J.L., Kampinga, H.H., Malyapa, R.S., Wright, W.D., vanderWaal, R.P. and Xu, M. (1998). Nuclear matrix as a target for hyperthermic killing of cancer cells. Cell Stress Chaperones. 3(4), pp. 245–55.

Rudin, C.M. and Thompson, C.B. (1997). Apoptosis and disease: regulation and clinical relevance of programmed cell death. Annu. Rev. Med. 48, pp. 267–281.

Ruifork, A.C., Kanon, B. and Konings, A.W. (1987). Heat induced K2+ loss, trypan blue uptake and cell lysis in different cell lines: effect of serum. Radiat Res. 109, pp. 303-309.

Salatin, S. and Yari Khosroushahi, A. (2017) Overviews on the cellular uptake mechanism of polysaccharide colloidal nanoparticles. J Cell Mol Med. 21(9), pp.1668–1686.

Salmeen, A., Andersen, J.N., Myers, M.P., Meng, T.C., Hinks, J.A., Tonks, N.K. and Barford, D. (2003). Redox regulation of protein tyrosine phosphatase 1B involves a sulphenyl-amide intermediate. Nature. 423, pp. 769-73.

Salmaso, S., Caliceti, P., Amendola, V., Meneghetti, M., Magnusson, J.P., Pasparakis, G. and Alexander, C. (2009). Cell up-take control of gold nanoparticles functionalised with a thermoresponsive polymer. J. Mater. Chem. 19, pp. 1608–1615.

Samali, A. and Cotter, T.G. (1996). Heat shock proteins increase resistance to apoptosis. Exp Cell Res. 223(1), pp. 163-170.

Samali, A., Holmberg, C.I., Sistonen, L. and Orrenius, S. (1999).

Thermotolerance and cell death are distinct cellular responses to stress: dependence on heat shock proteins. FEBS Lett. 461(3), pp. 306-310.

Sendoel, A. and Hengartner, M.O. (2014). Apoptotic Cell Death Under Hypoxia, Physiology. 29, pp. 168-176.

Schatz, G.C. (1984), Theoretical studies of surface enhanced Raman scattering. Acc. Chem. Res. 17 (10), pp. 370–376.

Schwartzberg, A.M., Oshiro, T.Y., Zhang, J.Z., Huser, T. and Talley, C.E. (2006). Improving Nanoprobes Using Surface-Enhanced Raman Scattering from 30-nm Hollow Gold Particles. Analytical Chemistry. 78(13), pp.4732–4736.

Schwartz, J.A., Shetty, A.M., Price, R.E., Stafford, R.J., Wang, J.C., Uthamanthil, R.K., Pham, K., McNichols, R.J., Coleman, C.L., Payne, J.D. (2009). Feasibility Study of Particle-Assisted Laser Ablation of Brain Tumors in an Orthotopic Canine Model. Cancer Res. 69(4), pp. 1659-1667.

Sharma, S.V., Lee, D.Y., Li, B., Quinlan, M.P., Takahashi, F., Maheswaran, S.,McDermott, U., Azizan, N., Zou, L., Fischbach, M.A., Wong, K-K., Brandstetter, K., Wittner, B., Ramaswamy, S., Classon, M. and Settleman, J. (2011). A chromatin-mediated reversible drug tolerant state in cancer cell subpopulations. 141(1), pp. 69–80.

Shellman, Y.G., Howe, W.R., Miller, L.A., Goldstein, N.B., Pacheco, T.R., Mahajan, R.L., LaRue, S.M. and Norris, D.A. (2008). Hyperthermia Induces Endoplasmic Reticulum-Mediated Apoptosis in Melanoma and Non-Melanoma Skin Cancer Cells. Journal of Investigative Dermatology. 128, pp. 949–956.

Shen, W., Qiu, Q., Wang, Y., Miao, M., Li, B., Zhang, T., Cao, A., An. Z. (2010). Hydrazine Hydrazine as a Nucleophile and Antioxidant for Fast Aminolysis of RAFT Polymers in Air. Macromol. Rapid Commun. 31, pp. 1444–1448.

Shi, P., Qu, K., Wang, J., Li, M., Ren, J. and Qu, X. (2012). PH-responsive NIR enhanced drug release from gold nanocages possesses high potency against cancer cells. Chem. Commun. (48), pp. 7640–7642.

Shibua, E.S., Hamadaa, M., Murasea, N. and Bijua, V. (2013). Nanomaterials formulations for photothermal and photodynamic therapy of cancer. Journal of Photochemistry and Photobiology. Photochemistry Reviews. 15, pp. 53– 72.

Shil, Y., Nikulenkov, F., Zawacka-Pankau, J., Li, H., Gabdoulline, R., Xu, J., Eriksson, S., Hedstrom, E., Issaeval, N., Kel, A. Arne, E.S.J. and Selivanova, G. (2014). ROS-dependent activation of JNK converts p53 into an efficient inhibitor of oncogenes leading to robust apoptosis. Cell Death Differ. 21(4), pp. 612-623.

Shroff, R.T., Wolff, R.A. and Javle, M.M. (2011). The MD Anderson Manual of Medical Oncology. 2nd Eddition. New York: McGraw-Hill, Chap.18. ISBN 978-0-07-170106-8.

Shukla, R., Bansal, V., Chaudhary, M., Basu, A., Bhonde, R.R. and Sastry, M. (2005). Biocompatibility of gold nanoparticles and their endocytotic fate inside the cellular compartment: a microscopic overview. Langmuir. 21(23), pp. 10644-10654.

Singh, R., Shakya, A.K., Naik, R. and Shalan, N. (2015). Stability-Indicating HPLC Determination of Gemcitabine in Pharmaceutical Formulations. International Journal of Analytical ChemistrY. 2015, pp.1-12.

Skoog, D.A. (2006). Principles of Instrumental Analysis. 6th ed. Belmont, CA. Thompson Brooks/Cole, Chapter 28.

Skrabalak, S. E., Chen, J., Sun, Y., Lu, X., Au, L., Cobley, C. M. and Xia, Y. (2008). Gold Nanocages: Synthesis, Properties, and Applications. Acc. Chem. Res. 41(12), pp. 1587-1595.

Snabaitis, A.K., Hearse, D.J., and Avkiran, M. (2002). Regulation of sarcolemmal Na /H exchange by hydrogen peroxide in adult rat ventricular myocytes. Cardiovasc Res. 53, pp. 470–480.

Sneed, P.K., Stauffer, P.R., Li, G.C. and Stege, G.J.J. (2004). Hyperthermia.In: Leibel SA, Phillips TL (eds.). Textbook of Radiation Oncology. 2nd ed. Chapter 70. Saunders. pp. 1569–1596.

Sohal, R.S. and Allen R.G. (1995). Relationship between metabolic rate, free radicals,
differentiation and aging: a unified theory. Basic Life Sci. 35, pp. 75–104.

Sokolov, K., Follen, M., Aaron, J., Pavlova, I., Malpica, A., Lotan, R. and Kortum R.R. (2003). Real-time vital optical imaging of precancer using anti-epidermal growth factor receptor antibodies conjugated to gold nanoparticles. Cancer Res. 63(9), pp. 1999–2004.

Sonavane, G., Tomoda, K., Makino, K. (2008). Biodistribution of Colloidal Gold Nanoparticles After Intravenous Administration: Effect of Particle Size. Colloids Surf. 66, pp. 274−280.

Sonna, L.A., Fujita, J., Gaffin, S.L. and Lilly, C.M. (2002). Invited review: Effects of heat and cold stress on mammalian gene expression. J Appl Physiol, 92(4), pp. 1725-1742.

Sordillo, L.A., Pu, Y., Pratavieira, S., Budansky, Y. and Alfano, R.R. (2014). Deep optical imaging of tissue using the second and third near-infrared spectral windows. J Biomed Opt. 19(5), pp. 056004-056006.

Sperling, R.A. and Parak, W.J. (2010). Surface modification, functionalization and bioconjugation of colloidal inorganic nanoparticles. Phil. Trans. R. Soc. 368, pp. 1333–1383.

Spiro, I.J., Denman, D.L. and Dewey, W.C. (1982). Effect of hyperthermia on CHO DNA polymerases. Radiation Research. 89, pp. 134–149.

Subjeck, J.R., Sciandra, J.J. and Johnson, R.J. (1982a). Heat shock proteins and thermotolerance; a comparison of induction kinetics. Br J Radiol. 55(656), pp. 579-584.

Sugahara, T., Van der Zee, J., Kampinga, H.H., Vujaskovic, Z., Kondo, M., Ohnishi, T., Li, G., Park, H.J., Leeper, D.B., Ostapenko, V., Repasky, E.A., Watanabe, M. and Song, C.W. (2008). Application of thermal stress for the improvement of health. Int J Hyperthermia. 24(2), pp. 123-140.

Stern, J. M., Stanfield, J., Kabbani, W., Hsieh, J. and Cadeddu, J.A. (2008). Selective Prostate Cancer Thermal Ablation with Laser Activated Gold Nanoshells. The Journal of Urology. 179, pp. 748-753.

Studer, A. and Schulte, T. (2005). Nitroxide-mediated radical processes. Chem. Rec. 5, pp. 27–35.

Sugimachi, K., Kuwano, H., Ide, H., Toge T, Saku, M. and Oshiumi, Y. (1994). Chemotherapy combined with or without hyperthermia for patients with oesophageal carcinoma: a prospective randomized trial. Int J Hyperthermia. 10(4), pp. 485-93.

Sun, Y., Mayers, B.T. and Xia, Y. (2002). Template-Engaged Replacement Reaction: A One-Step Approach to the Large-Scale Synthesis of Metal Nanostructures with Hollow Interiors. Nano Lett. 2(5), pp. 481-485.

Sun, Y., Mayers, B.T. and Xia, Y. (2003). Metal Nanostructures with Hollow Interiors. Adv. Mater. 15(7-8), pp. 641-646.

Sun, Y. and Xia, Y. (2003). Alloying and Dealloying Processes Involved in the Preparation of Metal Nanoshells through a Galvanic Replacement Reaction. Nano Lett. 3(11), pp. 1569-1572.

Szwarc, M. (1998). Living Polymers. Their Discovery, Characterization, and Properties. Journal of Polymer Science: Part A: Polymer Chemistry. 36, pp. 9-15.

Tait, S.W.G. and Green, D.R. (2010). Mitochondria and cell death: outer membrane permeabilization and beyond. Nat Rev Mol Cell Biol. 11(9), pp. 621-632.

Tait, S.W.G. and Green, D.R. (2012). Mitochondria and cell signaling Journal of Cell. Science. 125, pp. 807–815.

Tang, H.W., Yang, X.B., Kirkham, J. and Smith, D.A. (2007). Probing Intrinsic and Extrinsic Components in Single Osteosarcoma Cells by Near- Infrared Surface-Enhanced Raman Scattering. Anal. Chem. 79(10), pp. 3646-3653.

Taruttis, A., Herzog, E., Razansky, D. and Ntziachristos, V. (2010). Real-time imaging of cardiovascular dynamics and circulating gold nanorods with multispectral optoacoustic tomography. Optics Express. 18(19), pp. 19592-602.

Toltl, L.J., Austin, R.C., Liaw, P.C. (2011). Activated protein C modulates inflammation, apoptosis and tissue factor procoagulant activity by regulating endoplasmic reticulum calcium depletion in blood monocytes. J. Thromb. Haemost. 9, pp. 582–592.

Toyama, Y., Yoshida, S., Saito, R., Kitamura, H., Okui, N., Miyake, R., Yanaga, K. (2013). Successful adjuvant bi-weekly gemcitabine chemotherapy for pancreatic cancer without impairing patients' quality of life. World Journal of Surgical Oncology, 11, 3.

Trachootham, D., Alexandre, J. and Huang, P. (2009). Targeting cancer cells by ROS-mediated mechanisms:a radical therapeutic approach? Nature Review Drug Discovery, 8, pp. 579-591.

Tran, S.E.F., Meinander, A., Holmstrom, T.H., Rivero-Muller, A., Heiskanen, K.M., Linnau, E.K., Courtney, M.J., Mosser, D.D., Sistonen, L. and Eriksson, J.E. (2003) Heat stress downregulates FLIP and sensitizes cells to Fas receptor-mediated apoptosis. Cell Death Differ 10, pp. 1137–1147.

Tsai, H.Y., Yang, Y.F., Wu, A.T., Yang, C.J., Liu, Y.P. Jan, Y.H., Lee, C.H., Hsiao, Y.W., Yeh, C.T., Shen, C.N., Lu, P.J. Huang, M.S. and Hsiao, M. (2013). Endoplasmic reticulum ribosome-binding protein 1 (RRBP1) overexpression is frequently found in lung cancer patients and alleviates intracellular stress-induced apoptosis through the enhancement of GRP78. Oncogene. 32, pp. 4921–4931.

Tu, S., McStay, G.P., Boucher, L.M., Mak, T., Beere, H.M., Green, D.R. (2006). In situ trapping of activated initiator caspases reveals a role for caspase-2 in heat shock-induced apoptosis. Nat Cell Biol. 8, pp. 72–77.

Turrens, J.F. (2003). Mitochondrial formation of reactive oxygen species. J Physiol. 552, pp. 335–344.

Urano, M., Kuroda, M. and Nishimura, Y. (1999). For the clinical application of themochemotherapy given at mild temperatures. Int J Hyperthermia. 15, pp. 79-107.

Valko, M., Rhodes, C.J., Moncola, J., Izakovic, M. and Mazura, M. (2006). Free radicals, metals and antioxidants in oxidative stress-induced cancer. Chemico-Biological Interactions. 160, pp. 1–40.

Van Bree, C., Beumer, C., Rodermond, H.M., Haveman, J. and Bakker, P.J. (1999). Effectiveness of 20,20-difluorodeoxycytidine (gemcitabine) combined with hyperthermia in rat R-1 rhabdomyosarcoma in vitro and in vivo. Int J Hyperthermia. 15(6), pp. 549-556.

Van Bree, C., Van DerMaat, B., Ceha, H.M., Franken, N.A.P., Haveman, J. and Bakker, P.J.M. (1999). Inactivation of p53 and of pRb protects human colorectal carcinoma cells against hyperthermia-induced cytotoxicity and

apoptosis. J Cancer Res Clin Oncol. 125, pp. 549-555.

Van Meerloo, J., Kaspers, G.J., Cloos, J. (2011). Cell sensitivity assays: the MTT assay. Methods Mol Biol. 731, pp. 237-245.

Vermes, I. and Haanen, C. (1994). Apoptosis and programmed cell death in health and disease. Adv Clin Chem. 31, pp. 177-246.

Vertrees, R.A., Das, G.C., Popov, V.L., Coscio, A.M., Goodwin, T.J., Logrono, R., Zwischenberger, J.B. and Boor, P.J. (2005). Synergistic interaction of hyperthermia and Gemcitabine in lung cancer. Cancer Biol Ther. 4(10). pp.1144-53.

Vilian, E.A.T., Veeramani, V., Chen, S.M., Madhu, R., Kwak, C.H., Huh, Y.S. and Han, Y.K. (2015). Immobilization of myoglobin on Au nanoparticle-decorated carbon nanotube/polytyramine composite as a mediator-free H_2O_2 and nitrite biosensor. Scientific reports. 5, pp. 18390-18400.

Von Maltzahn, G., Park, J-H., Agrawal, H., Bandaru, N.K., Das, S.K., Sailor, M.J. and Bhatia, S.N. (2009). Computationally Guided Photothermal Tumor Therapy Using Long-Circulating Gold Nanorod Antennas. Cancer Res. 69(9), pp. 3892–3900.

Von Smoluchowski, M. (1903). Contribution to the theory of electro-osmosis and related phenomena. Bull Int Acad Sci Cracovie. 3, pp. 184–199.

Wang, J.S., Matyjaszewski, K. (1995). Controlled/"living" radical polymerization. Transfer radical polymerization in thepresence of transition-metal complexes. J Am Chem Soc. 117, pp. 5614–5615.

Wang, Y., Fan, W., Dai, X., Katragadda, U., Mckinley, D., Teng, Q. and Tan, C. (2014). Enhanced Tumor Delivery of Gemcitabine via PEG-DSPE/TPGS Mixed MicellesMol. Pharmaceutics. 11 (4), pp. 1140–115.

Weissleder, R. (2001). A clearer vision for in vivo imaging. Nat.Biotechnol. 19, pp. 316-317.

Whitesides, G.M. (2003). The 'right' size in nanobiotechnology. Nat Biotechnol. 21(10), pp. 1161-5.

Wiedemann, G.J. Siemens, H.J., Mentzel, M., Wossmann, W., Knocks, D., Weiss, C. and Wagner, T. (1993). Effects of temperature on the therapeutic efficacy and pharmacokinetics of ifosfamide. Cancer Res. 53, pp. 4268–4272.

Williams, D. B. and Carter, C. B. (2009). Transmission Electron Microscopy: A Textbook for Materials Science, Springer, New York.

Willcock, H. and. O'Reilly, R.K. (2010). End group removal and modification of RAFT polymers. Polym. Chem. 1, pp. 149–157.

Won, S., Phillips, D.J., Walker, M. and Gibson M.I. (2016). Co-operative transitions of responsive-polymer coated gold nanoparticles; precision tuning and direct evidence for co-operative aggregation. J Mater Chem B Mater Biol Med. 4(34), pp. 5673–5682.

Wriedt, T. (2012). Mie Theory: A Review. Springer Series in Optical Sciences. 169, pp. 53-71.

Wu, C., Liang, X. and Jiang, H. (2005). Metal nanoshells as a contrast agent in near - infrared diffuse optical tomography . Optics Communications , 253 , pp. 214 – 21 .

Wu, Y., Zhou,Y., Zhu, J., Zhang, W., Pan, X., Zhang, Z. and Zhu, X. (2014). Fast conversion of terminal thiocarbonylthio groups of RAFT polymers to "clickable" thiol groups via versatile sodium azide. Polym. Chem. 5, pp. 5546–5550.

Wuithschick, M., Birnbaum, A., Witte, S., Sztucki, M., Vainio, U., Pinna, N., Rademann, K., Emmerling, F., Kraehnert, R. and Polte, J. (2015). Turkevich in New Robes: Key Questions Answered for the Most Common Gold

Nanoparticle Synthesis. ACS Nano, 2015, 9 (7), pp. 7052–7071.

Wust, P., Hildebrandt, B., Sreenivasa, G., Rau, B., Gellermann, J., Riess, H., Felix, R. and Schlag, P.M. (2002). Hyperthermia in combined treatment of cancer. THE LANCET Oncology. 3, pp. 487-497.

Xia, X., Wang, Y., Ruditskiy, A. and Xia, Y. (2013). 25th Anniversary Article: Galvanic Replacement: A Simple and Versatile Route to Hollow Nanostructures with Tunable and Well-Controlled Properties. Adv. Mater. 25, pp. 6313-6333.

Xiaohua, H., Prashant, K.J., El-Sayed, I.H. and El-Sayed, M.A. (2007). Gold nanoparticles: interesting optical properties and recent applications in cancer diagnostics and therapy. Nanomedicine. 2(5), pp. 681-693.

Xia, X., Yang, M., Wang, Y., Zheng, Y., Li, Q., Chen, J. and Xia, Y. (2011). Quantifying the coverage density of poly(ethylene glycol) chains on the surface of gold nanostructures. ACS. 6(1), pp. 512-522.

Xin, J.Y., Cheng, D.D., Zhang, L.X., Lin, K., Fan, H.C., Wang, Y. and Xia, C.G. (2013). Methanobactin-mediated one-step synthesis of gold nanoparticles. Int J Mol Sci. 14(11), PP. 21676-21688.

Xu, H., Gao, L., Zhang, Q., Li, J., Diwu, J., Chou, X., Tang, J., Xue, C. (2014). Preparation Method of Co3O4 Nanoparticles Using Degreasing Cotton and Their Electrochemical Performances in Supercapacitors. 2014, pp. 1-9.

Yang, H., Wang, Q., Chen, W., Zhao, Y., Yong, T., Gan, L., Xu, H. and Yang, X. (2015). Hydrophilicity/Hydrophobicity reversable and redox-sensitive nanogels for anticancer drug delivery. Mol. Pharm., 12, pp. 1636– 1647.

Yoo, J. and Lee, Y. (2007). Effect of hyperthermia on TRAIL-induced apoptotic death in human colon cancer cells: development of a novel strategy for regional therapy. J Cell Biochem. 101, pp. 619–630.

Yoon, Y., Brookes, P.S., Robotham, J.L., Anders, M.W., Sheu, S.S. (2004). Calcium, ATP, and ROS: a mitochondrial love-hate triangle, Am. J. Physiol. Cell Physiol. 287, pp. 817–833.

You, J., Zhang, G. and Li, C. (2010). Exceptionally High Payload of Doxorubicin in Hollow Gold Nanospheres for Near-Infrared Light-Triggered Drug Release. ACSNANO. 4(2), pp. 1033-1041.

Yu, DY., Matsuya, Y., Zhao, Q.L., Ahmed, K., Zheng-Li, W., Hori, T., Nemoto, H. and Kondo, T. (2008). Enhancement of hyperthermia-induced apoptosis by a new synthesized class of benzocycloalkene compounds. Apoptosis.13, pp. 448–461.

Yuguchi, T., Saito, M., Yokoyama, Y., Sait, T., Nagata, T., Sakamoto, T. and Tsukada, K. (2002). Combined use of hyperthermia and irradiation cause antiproliferative activity and cell death to human esophageal cell carcinoma cells-mainly cell cycle examination. Hum Cell. 15(1), pp. 33-42.

Zan, T., Wu, F., Pei, X., Jia, S., Zhang, R., Wu, S., Niu, Z. and Zhang, Z. (2016). Into the polymer brush regime through the "grafting-to" method: densely polymer-grafted rodlike viruses with an unusual nematic liquid crystal behavior. Soft Matter. 12(3), pp.798-805.

Zhang, W., Peng, B., Tian, F., Qin, W. and Qian, X. (2014). Facile Preparation of Well-Defined Hydrophilic Core–Shell Upconversion Nanoparticles for Selective Cell Membrane Glycan Labeling and Cancer Cell Imaging. Anal. Chem. 86, pp. 482–489.

Zhang, Z. and Lin, M. (2014). Fast Loading of PEG-SH on CTAB-protected Gold Nanorod. RSC Adv. 4, pp. 17760-17767.

Zhou, Y., Wu, X., Wang, T., Ming, T., Wang, P.N., Zhou L.W. and Chen, J.Y. (2010). A comparison study of detecting gold nanorods in living cells with confocal reflectance microscopy and two-photon fluorescence microscopy. J Microsc. 237(2), pp. 200–207.

Zou, L., Wang, H., He, B., Zeng, L., Tan, T., Cao, H., He, X., Zhang, Z., Guo, S. and Li, Y. (2016). Current Approaches of Photothermal Therapy in Treating Cancer Metastasis with Nanotherapeutics. Theranostics. 6(6), pp. 762-772.